

ISSN 1913-1844

MODERN APPLIED SCIENCE

**Vol. 3, No. 4
April 2009**



Canadian Center of Science and Education

Editorial Board

Ahmad Mujahid Ahmad Zaidi Universiti Tun Hussein Onn Malaysia, Malaysia

Hamimah Adnan Universiti Teknologi MARA, Malaysia

J S Prakash Sri Bhagawan Mahaveer Jain College of Engineering, India

Lim Hwee San Universiti Sains Malaysia, Malaysia

Musa Mailah Universiti Teknologi Malaysia, Malaysia

Stefanos Dailianis University of Patras, Greece

Sujatha. C.H Cochin University of Science and Technology, India

Sundus H Ahmed Ministry of Science and Technology, Iraq

Susan Sun Canadian Center of Science and Education, Canada

Sutopo Hadi University of Lampung, Indonesia

Wenwu Zhao Macrothink Institute, USA



Contents

Using Nonlinear Mixed Model Technique to Determine the Optimal Tree Height Prediction Model for Black Spruce	3
<i>Shongming Huang, Shawn X. Meng & Yuqing Yang</i>	
Markov Chain Monte Carlo-Based Bayesian Analysis of Binary Response Regression, with Illustration in Dose-Response Assessment	19
<i>Crispin M. Mutshinda</i>	
Two-Stage Engine Mapping for the Calibration of Carbon Monoxide Emission	30
<i>Recep Kozan & Mersin Gokce</i>	
The Statistics Properties of Orthogonal Coherent State Interacting with Two-level Atom	37
<i>Jingqiu Chen, Qiao Gu & Wenda Peng</i>	
The Isolation of α -viniferin, A Trimer Stilbene, from <i>Shorea ovalis</i> Blume	45
<i>Noviany & Sutopo Hadi</i>	
Fatigue Behaviour of Aluminum Alloy at Elevated Temperature	52
<i>Farhad B. Bahaideen, Ahmed M. Saleem, Khaleed Hussain M.T, Zaidi Mohd. RIPIN, Zainal arifin ahmad, Zahurin Samad & Nur Azam Badarulzman</i>	
New Approaches in Estimating Rubberwood Standing Volume Using Airborne Hyperspectral Sensing	62
<i>Kamaruzaman Jusoff & Malek Hj. Mohd Yusoff</i>	
Statistical Analysis and Optimization of Acid Dye Biosorption by Brewery Waste Biomass Using Response Surface Methodology	71
<i>V. Jaikumar & V. Ramamurthi</i>	
Vector Control System of Induction Motor Based on Fuzzy Control Method	85
<i>Haobin Zhou, Bo Long & Binggang Cao</i>	
Investigation on Ethylenediaminetetra-Acetic Acid as Corrosion Inhibitor for Mild Steel in 1.0M Hydrochloric Acid	90
<i>Ahmed Y. Musa, Abdul Amir H. kadhum, Mohd Sobri Takriff, Abdul Razak Daud & Siti Kartom Kamarudin</i>	
Study on the Intelligent Video Monitoring Technology and Its Applications	95
<i>Yi Wang</i>	
Distribution System Restoration Using Genetic Algorithm with Distributed Generation	98
<i>N.Shanmuga Vadivoo & S.Mary Raja Slochanal</i>	
A Numerical Simulation of the Flow in a Diffusing S-Duct Inlet	111
<i>Lifen Zhang, Zhenxia Liu & Jian Jiang</i>	
Hydrotropic Study on Furfural - Comprehensive Design Expert Plot	117
<i>C.Jaya Kumar & N. Nagendra Gandhi</i>	
Synthesis and Characterization of Novel Soluble Aromatic Polyesters with Pendant Cyano Groups	131
<i>Yikai Yu, Mingzhong Cai & Tao Wang</i>	
Experimental Investigation on the Effects of Audible Sound to the Growth of <i>Aspergillus</i> Spp	137
<i>Poopathy Muthu Karippen, Jedol Dayou & Chong Khim Phin</i>	
Extended Cesaro Operator from A_p^∞ to Bloch Space	142
<i>Mingzhu Yang</i>	



Contents

Recycling of Woven Fabric Dyeing Wastewater Practiced in Perundururai Common Effluent Treatment Plant <i>M. Ramesh Kumar, K. Saravanan & R. Shanmugam</i>	146
Chance-constrained Portfolio Selection with Birandom Returns <i>Limei Yan</i>	161
Neural Based pH System in Effluent Treatment Process <i>B. Meenakhsipriya, Dr.K.Saravanan & S.Sathiyavathi</i>	166
Catalytic Decomposition of Formaldehyde on Nanometer Manganese Dioxide <i>Xiujuan Chu & Hua Zhang</i>	177
Model Development on Disposal of Municipal Solid Waste through Experimental Studies <i>Dr.Kaliannan Saravanan, Arumugam Velumani & Kaliappan Ganesan</i>	182
Analysis of Instantaneous Center of Zero Acceleration of Rigid Body in Planar Motion <i>Haibin Sun & Tingting Liu</i>	191
A New Hybrid Optimization Method for Optimum Distribution Capacitor Planning <i>Ali Reza Seifi</i>	196
Development of TEC System for Commercial Cooling Applications <i>Wael Salah, Soib Taib & Anwar Al-Mofleh</i>	203
The Research of Inverter Welding Power Source Based on DSP for Self-shielded Flux-cored Wire <i>Xiao Li, Liangyu Li, Tianqi Wang & Xu Yang</i>	209
Synthesis, Structure and Biological Activity of Some Diorganotin(IV) with Benzamidomethionine <i>Yang Farina, Abdualbasit Graisa & Emad Yousif</i>	215



Using Nonlinear Mixed Model Technique to Determine the Optimal Tree Height Prediction Model for Black Spruce

Shongming Huang, Shawn X. Meng & Yuqing Yang

Biometrics Unit, Forest Management Branch

Alberta Department of Sustainable Resource Development

8th Floor, 9920 -108 Street, Edmonton, Alberta T5K 2M4, Canada

Tel: 1-780-422-5281 E-mail: shongming.huang@gov.ab.ca

Abstract

Based on the nonlinear mixed model technique, four base height-diameter models were evaluated for black spruce. The Chapman-Richard model was chosen. Top height and basal area were incorporated into the base model. Comparison of the base and expanded models showed that, although the goodness-of-fit measures on the modelling data were improved with the inclusion of top height and basal area, the predictive accuracy of the expanded models at the subject-specific level where the predominant interest of nonlinear mixed models lies, was reduced when tested on the model validation data. This has important practical implications because more accurate individual tree height predictions can be better achieved using the base height-diameter model without requiring the addition of other variables. It also reaffirms that determining the adequacy of a model on model fitting statistics alone can be misleading. A fitted model is best judged on separate validation data.

Keywords: Individual tree height prediction, Height-diameter model, Nonlinear mixed model, Model validation, Local prediction, Error distribution

1. Introduction

Total tree height (H) and tree diameter at breast height (DBH) are two of the most fundamental variables in forestry. The estimation of tree volume and biomass, the description of stand conditions and their changes over time, as well as the development of growth and yield projection systems all rely heavily on the availability of a complete set of tree heights and diameters.

However, since measuring tree height is time consuming and costly, typically in various data collection programs in forest management, all trees are measured for diameter but only a portion of the trees are measured for height. Predicting the “missing” tree heights is therefore routinely required in forest research and operations (Curtis 1967, Wykoff et al. 1982, Arabatzis and Burkhart 1992, Huang et al. 1992).

Although different options exist, the most commonly used method of predicting tree heights is to develop height-diameter models. From the trees that have both height and diameter measured, a height-diameter model can be developed to express tree height as a function of tree diameter. This model can then be used to predict the “missing” heights from measured DBHs.

In numerous studies related to the development of height-diameter models, it has been almost unanimously shown that the predictive ability and accuracy of the base height-diameter models can be improved if additional (statistically significant) tree and stand level variables are incorporated into the models. These variables may include tree or stand age, basal area per hectare (ha), stems per ha, crown ratio, crown competition factor, site index, dominant/co-dominant height, top height, crown class, wind speed, and different competition indices and species composition measures (e.g., Curtis 1967, Huang and Titus 1994, Huang 1999, Eerikäinen 2003, Temesgen et al. 2008, Meng et al. 2008).

The conclusions reached in previous studies were mostly derived from the goodness-of-fit measures on the modelling data, which, as will be shown later, could be unreliable and even misleading sometimes if one is not careful. Furthermore, in the cases where the nonlinear mixed model (NLMM) technique was applied (Castedo Dorado et al. 2006, Sharma and Parton 2007, Temesgen et al. 2008, Meng et al. 2008), no frequency-based comparison of the predictive performance between the base and expanded models was made on the plot-specific level where the main interest of NLMMs lie.

The prime objectives of this study were to: (1) select the optimal base height-diameter model for black spruce (*Picea mariana* (Mill.) B.S.P.); (2) compare the predictive accuracy of the base model with that of the expanded models on both the model fitting and validation data sets; and (3) evaluate the impacts of including or not including statistically

significant stand level variables into the base model. The selection, comparison and evaluation were all conducted within the NLMM framework.

2. Material and methods

2.1 Data

The black spruce data used in this study were collected by the Alberta Forest Service as a part of the provincial Permanent Sample Plots (PSP) database. The data encompass three key forest ecoregions (also called subregions) in Alberta: the lower foothills, the upper foothills, and the boreal mixedwood. The PSPs range in sizes from 200 to 2000 m², with the most common one being 1000 m². Within each plot or subplot (usually a quarter of the full PSP), diameters (always at a breast height of 1.3 m above ground) were measured for all trees taller than 1.3 m, and heights were measured for approximately 10 to 20% of the representative trees in a random or systematic fashion. A detailed description of the data collection procedures is provided in Alberta Forest Service (2000).

To avoid the potential serial correlation from repeated measurements of the same PSPs, only the initial measurements were retained in this study, which resulted in a total of 164 plots (1703 trees). The data were divided into two independent data sets by ecoregion: 93 plots (917 trees) from the lower foothills ecoregion were used as modeling data, and the other 71 plots (786 trees) from the boreal mixedwood and upper foothills ecoregions were used as model validation data. For the reasons discussed in Huang et al. (2002), we purposely avoided “random splitting” of the data. Summary statistics for the tree level variables H and DBH, and the plot level variables top height (i.e., mean height of the 100 largest DBH trees per ha) and stand basal area, are listed in Table 1. The data are also shown in Figure 1.

2.2 Specification of base height-diameter models

Based on a detailed examination of the height-diameter data shown in Figure 1, a large number of base height-diameter models were examined in preliminary analyses. Four promising candidate models were selected for further evaluation:

- (1) $H = 1.3 + \exp(\beta_1 + \beta_2 / (\text{DBH} + 1))$
- (2) $H = 1.3 + \beta_1 \text{DBH}^{\beta_2}$
- (3) $H = 1.3 + \beta_1 / (1 + \exp[\beta_2 + \beta_3 \ln(\text{DBH} + 1)])$
- (4) $H = 1.3 + \beta_1 [1 - \exp(-\beta_2 \text{DBH})]^{\beta_3}$

where H is total tree height (m), DBH is tree diameter (cm) at breast height, and β_1 , β_2 and β_3 are model parameters. These models and their slight modifications have been ranked favorably among alternative models in other relevant studies, particularly the Chapman-Richards model (4) (e.g., Wykoff et al. 1982, Huang et al. 1992, Sharma and Parton 2007, Temesgen et al. 2008).

Following the NLMM technique (Davidian and Giltinan 1995, Vonesh and Chinchilli 1997), one or more parameters in the above models were assumed to be mixed (i.e., they consist of a fixed component and a random component). Likelihood ratio tests were conducted to determine if this assumption was true (at $\alpha = 0.05$ throughout this study). It was found that the two parameters in (1) and (2) were both mixed, but parameter β_2 in (3) and (4) was fixed. Hence, the NLMM formulations of the above base models are:

- (5) $H_{ij} = 1.3 + \exp((\beta_1 + b_{1i}) + (\beta_2 + b_{2i}) / (\text{DBH}_{ij} + 1)) + \varepsilon_{ij}$
- (6) $H_{ij} = 1.3 + (\beta_1 + b_{1i}) \text{DBH}_{ij}^{(\beta_2 + b_{2i})} + \varepsilon_{ij}$
- (7) $H_{ij} = 1.3 + (\beta_1 + b_{1i}) / (1 + \exp[\beta_2 + (\beta_3 + b_{2i}) \ln(\text{DBH}_{ij} + 1)]) + \varepsilon_{ij}$
- (8) $H_{ij} = 1.3 + (\beta_1 + b_{1i}) [1 - \exp(-\beta_2 \text{DBH}_{ij})]^{(\beta_3 + b_{2i})} + \varepsilon_{ij}$

where H_{ij} and DBH_{ij} are observed height and DBH for the j th tree in the i th plot (subject), $i = 1, 2, \dots, m, j = 1, 2, \dots, n_i$, m is the total number of plots in the population, n_i is the number of trees in plot i , β_1 , β_2 and β_3 are fixed parameters common to all plots, b_{1i} and b_{2i} are random parameters specific to plot i , and ε_{ij} is a normally distributed within-plot error term. Models (5)-(8) can be expressed in matrix forms. For example, the Chapman-Richards model [8] can be written for plot i as

$$(9) \quad \mathbf{H}_i = 1.3 + (\beta_1 + b_{1i}) [1 - \exp(-\beta_2 \mathbf{DBH}_i)]^{(\beta_3 + b_{2i})} + \boldsymbol{\varepsilon}_i$$

where \mathbf{H}_i and \mathbf{DBH}_i are vectors of observed heights and DBHs, respectively, for the i th plot with n_i observations, and $\boldsymbol{\varepsilon}_i = [\varepsilon_{i1}, \varepsilon_{i2}, \dots, \varepsilon_{in_i}]'$ is a vector of the within-plot errors.

2.3 Expanded models

Individual tree height-diameter relationship could be affected by many factors. Of which, site quality and stand density were found to be most common (Huang and Titus 1994, Sharma and Parton 2007, Meng et al. 2008). Typically, site quality is represented by site index or dominant/co-dominant height (H_{dc}), with the latter appeared more common, likely due to the fact that site index is often unobservable and must be predicted from site index models, which could bring in

additional prediction errors and artificially reduce the variation in site quality. The use of H_{dc} , however, is not without its problems. The definition of “dominant”/“co-dominant” is not always clear-cut in practice, and how many “dominants” and/or “co-dominants” are needed to get a stable H_{dc} for a stand is unclear. Nicholas et al. (1991) found that the reliability of tree crown position classification was very low, and “only 38% of dominant trees and 81% of co-dominant trees were similarly re-classified” during visits in the same growing season.

In this study top height was used as an indicator of site quality. Top height is defined as the average height of the 100 largest DBH trees per ha. Given a plot size, a fixed number of the largest DBH trees corresponding to the plot size were selected and the average height of these trees was obtained to represent the site quality of the plot. The use of top height removed the inconsistencies associated with the use of H_{dc} .

For stand density, basal area per ha (BA, m²/ha) was used. Basal area per ha is a simple and objective measure of the degree of crowding within a stand. It is generally better than the stand density measure based on trees per ha because basal area combines tree number with tree size.

Top height and basal area per ha were incorporated into the base H-DBH models. Different functional forms and various combinations of the variables and their transformations were tried and evaluated based on the standard NLMM goodness-of-fit measures such as -2 times log-likelihood (-2LL), Akaike Information Criterion, Schwarz’s Bayesian Information Criterion, significance of the parameters, and studentized residual plots (Littell et al. 2006). It was found that simple linear combinations were adequate. As examples, two expanded models, one with top height incorporated and the other with both top height and BA incorporated, were formed based on the Chapman-Richards base model (9):

$$(10) \quad \mathbf{H}_i = 1.3 + (\beta_1 + \beta_4 \text{TopH}_i + b_{1i}) [1 - \exp(-\beta_2 \text{DBH}_i)]^{(\beta_3 + b_{2i})} + \boldsymbol{\varepsilon}_i$$

$$(11) \quad \mathbf{H}_i = 1.3 + (\beta_1 + \beta_4 \text{TopH}_i + \beta_5 \text{BA}_i + b_{1i}) [1 - \exp(-\beta_2 \text{DBH}_i)]^{(\beta_3 + b_{2i})} + \boldsymbol{\varepsilon}_i$$

where TopH_i is top height (m), BA_i is basal area per ha (m²/ha), and β_1 - β_5 are fixed parameters common to all plots, and b_{1i} and b_{2i} are random parameters specific to the i th plot. Attempts to relate β_4 and β_5 to additional random parameters in linear or nonlinear fashions failed to achieve convergence.

2.4 Parameter estimation

All base and expanded models can be written as a generalized NLMM of the form:

$$(12) \quad \mathbf{y}_i = f(\mathbf{x}_i, \boldsymbol{\beta}, \mathbf{b}_i) + \boldsymbol{\varepsilon}_i$$

where $\mathbf{y}_i = [y_{i1}, y_{i2}, \dots, y_{in_i}]'$ is a vector of tree height measurements in plot i , \mathbf{x}_i is a known design matrix of the covariates (DBH, and where applicable also TopH and/or BA), $\boldsymbol{\beta}$ is a vector of fixed parameters, $\mathbf{b}_i = [b_{1i}, b_{2i}]'$ is a vector of random parameters, and $\boldsymbol{\varepsilon}_i = [\varepsilon_{i1}, \varepsilon_{i2}, \dots, \varepsilon_{in_i}]'$ is the error vector. The \mathbf{b}_i and $\boldsymbol{\varepsilon}_i$ are assumed to be uncorrelated and normally distributed with mean zero and variance-covariance matrices \mathbf{D} and \mathbf{R}_i , respectively, that is:

$$E \begin{bmatrix} \mathbf{b}_i \\ \boldsymbol{\varepsilon}_i \end{bmatrix} = \begin{bmatrix} \mathbf{0} \\ \mathbf{0} \end{bmatrix} \quad \text{Var} \begin{bmatrix} \mathbf{b}_i \\ \boldsymbol{\varepsilon}_i \end{bmatrix} = \begin{bmatrix} \mathbf{D} & \mathbf{0} \\ \mathbf{0} & \mathbf{R}_i \end{bmatrix}$$

Furthermore, since no obvious pattern of unequal error variance was detected from studentized residual plots, which is typical of height-diameter models *after* the inclusion of random parameters (e.g., Castedo Dorado et al. 2006, Meng et al. 2008), \mathbf{R}_i is assumed to be $\sigma^2 \mathbf{I}_{n_i}$, where σ^2 is the error variance and \mathbf{I}_{n_i} is a $n_i \times n_i$ identity matrix, and \mathbf{D} is assumed to be an unstructured covariance matrix that is the same for all i :

$$(13) \quad \mathbf{D} = \begin{bmatrix} \sigma_{b_1}^2 & \sigma_{b_1 b_2} \\ \sigma_{b_1 b_2} & \sigma_{b_2}^2 \end{bmatrix}$$

where $\sigma_{b_1}^2$ and $\sigma_{b_2}^2$ are the variances for random parameters b_1 and b_2 , respectively, and $\sigma_{b_1 b_2}$ is the covariance between b_1 and b_2 .

The parameters of the generalized NLMM (12) can be estimated using different methods (Davidian and Giltinan 1995, Vonesh and Chinchilli 1997). In this study we used the first-order (FO) method of Beal and Sheiner (1982) and the first-order conditional expectation (FOCE) method of Lindstrom and Bates (1990). We found that the FOCE method often failed to achieve convergence, and was less stable and more prone to floating errors than the FO method. In the cases where both FO and FOCE achieved convergence, the FO method was found to give more accurate predictions with smaller mean error and error variance. Therefore, we limited ourselves in this analysis to the FO method.

The FO method employs a first-order Taylor series expansion of (12) around a $\boldsymbol{\beta}^*$ close to $\boldsymbol{\beta}$ and a \mathbf{b}_i^* set to zero, the expected value of the random-parameters (i.e., $\mathbf{b}_i^* = E(\mathbf{b}_i) = \mathbf{0}$), to approximate the nonlinear function (12), with the quadratics and cross-products dropped:

$$(14) \quad \mathbf{y}_i \approx f(\mathbf{x}_i, \boldsymbol{\beta}^*, \mathbf{b}_i^*) + \mathbf{X}_i(\boldsymbol{\beta} - \boldsymbol{\beta}^*) + \mathbf{Z}_i(\mathbf{b}_i - \mathbf{b}_i^*) + \boldsymbol{\varepsilon}_i$$

where the derivative matrices \mathbf{X}_i and \mathbf{Z}_i are defined by

$$(15) \mathbf{X}_i = \left. \frac{\partial f(\mathbf{x}_i, \boldsymbol{\beta}, \mathbf{0})}{\partial \boldsymbol{\beta}'} \right|_{\boldsymbol{\beta}^*, \mathbf{0}} \quad \mathbf{Z}_i = \left. \frac{\partial f(\mathbf{x}_i, \boldsymbol{\beta}, \mathbf{0})}{\partial \mathbf{b}_i'} \right|_{\boldsymbol{\beta}^*, \mathbf{0}}$$

Since $\mathbf{b}_i^* = \mathbf{0}$, if we define a pseudo-response function \mathbf{y}_i^* as: $\mathbf{y}_i^* = \mathbf{y}_i - f(\mathbf{x}_i, \boldsymbol{\beta}^*, \mathbf{0}) + \mathbf{X}_i \boldsymbol{\beta}^*$, eq. (14) can be written as a standard linear mixed model:

$$(16) \mathbf{y}_i^* = \mathbf{X}_i \boldsymbol{\beta} + \mathbf{Z}_i \mathbf{b}_i + \boldsymbol{\varepsilon}_i$$

Following the linear mixed model theory, the generalized least squares estimator $\hat{\boldsymbol{\beta}}$ of the fixed parameters $\boldsymbol{\beta}$ in (16) can be obtained as described in Fitzmaurice et al. (2004). The random parameters predictor $\hat{\mathbf{b}}_i$ of the \mathbf{b}_i is (Davidian and Giltinan 1995, Vonesh and Chinchilli 1997):

$$(17) \hat{\mathbf{b}}_i = \hat{\mathbf{D}} \mathbf{Z}_i' (\mathbf{Z}_i \hat{\mathbf{D}} \mathbf{Z}_i' + \hat{\mathbf{R}}_i)^{-1} [\mathbf{y}_i - f(\mathbf{x}_i, \hat{\boldsymbol{\beta}}, \mathbf{0})]$$

where $\hat{\mathbf{D}}$ and $\hat{\mathbf{R}}_i$ are estimates of \mathbf{D} and \mathbf{R}_i , respectively, and \mathbf{Z}_i is defined in (15).

It is worthwhile to point out that eq. (17) is adequate only for the FO method. Had the FOCE method been used, we must use the following equation to predict the \mathbf{b}_i and solve it iteratively (Lindstrom and Bates 1990, Schabenberger 1994, Huang 2008, Temesgen et al. 2008, Meng et al. 2008):

$$\hat{\mathbf{b}}_i = \hat{\mathbf{D}} \mathbf{Z}_i' (\mathbf{Z}_i \hat{\mathbf{D}} \mathbf{Z}_i' + \hat{\mathbf{R}}_i)^{-1} [\mathbf{y}_i - f(\mathbf{x}_i, \hat{\boldsymbol{\beta}}, \hat{\mathbf{b}}_i) + \mathbf{Z}_i \hat{\mathbf{b}}_i]$$

Unfortunately, many forest modellers used eq. (17) to predict the $\hat{\mathbf{b}}_i$ while implementing the FOCE method, without realizing that this could seriously bias the results.

All base and expanded NLMMs were estimated using the SAS macro %NLINMIX, with the keyword EXPAND = ZERO for the FO method (Littell et al. 2006).

2.5 Model prediction

Since model fitting statistics alone can sometimes be unreliable, a fitted model is more appropriately judged through cross-validation or using separate model validation data (Picard and Cook 1984, Huang et al. 2002, Yang et al. 2004). To evaluate the predictive accuracy of the base and expanded H-DBH models fitted in this study on the validation data at plot- or subject-specific level where the main interest of NLMMs lies, the random parameters \mathbf{b}_i must be predicted first based on eq. (17). Once the $\hat{\mathbf{b}}_i$ are available, predictions for \mathbf{y}_i are obtained by eq. (18), which is derived by equating (16) to the pseudo function \mathbf{y}_i^* (Davidian and Giltinan 1995, Vonesh and Chinchilli 1997):

$$(18) \hat{\mathbf{y}}_i = f(\mathbf{x}_i, \hat{\boldsymbol{\beta}}, \mathbf{0}) + \mathbf{Z}_i \hat{\mathbf{b}}_i$$

The errors (residuals) associated with the predictions are

$$\mathbf{e}_i = \mathbf{y}_i - \hat{\mathbf{y}}_i \quad \text{or} \quad e_{ij} = y_{ij} - \hat{y}_{ij}$$

where y_{ij} and \hat{y}_{ij} are the j th observed and predicted values for subject i with n_i observations. For a population of N observations from m subjects, where $N = \sum_{i=1}^m n_i$, the overall mean bias (\bar{e}) is

$$(19) \bar{e} = \frac{1}{N} \sum_{i=1}^m \sum_{j=1}^{n_i} e_{ij} = \frac{1}{N} \sum_{i=1}^m \sum_{j=1}^{n_i} (y_{ij} - \hat{y}_{ij})$$

Since in practice, many researchers (e.g., Fang and Bailey 2001, Calama and Montero 2004) have used the fixed parameters estimated as a part of a NLMM to represent the “typical” population-averaged responses, we also calculated such “typical” responses:

$$(20) \hat{\mathbf{y}}_{i_fix} = f(\mathbf{x}_i, \hat{\boldsymbol{\beta}}, \mathbf{0})$$

where $\hat{\mathbf{y}}_{i_fix}$ are the “typical” population-averaged responses based on the fixed parameters $\hat{\boldsymbol{\beta}}$ only (with the $\hat{\mathbf{b}}_i$ set to zero). The associated “typical” population-averaged residuals are:

$$(21) \mathbf{e}_{i_fix} = \mathbf{y}_i - \hat{\mathbf{y}}_{i_fix}$$

In addition to the overall mean bias averaged over all observations from all subjects (as in eq. (19)), which could be misleading sometimes because the positive and negative errors from individual subjects could cancel one another out, the mean bias (or simply bias) for each individual subject was also calculated one plot at a time, together with the standard deviation (SD):

$$(22) \bar{e}_i = \frac{1}{n_i} \sum_{j=1}^{n_i} e_{ij} = \frac{1}{n_i} \sum_{j=1}^{n_i} (y_{ij} - \hat{y}_{ij})$$

$$(23) SD_i = \sqrt{\frac{1}{n_i} \sum_{j=1}^{n_i} (e_{ij} - \bar{e}_i)^2}$$

where \bar{e}_i is the bias for subject i with n_i (or n_{ij}) observations, and all other variables are as defined before. Two other conventional goodness-of-fit statistics were also calculated by plot (subject). One is the percent bias (Bias% or $\bar{e}_i\%$) and the other is the root mean square error (RMSE):

$$(24) \text{ Bias}\%_i = \frac{\bar{e}_i}{\bar{y}_i} \times 100\%$$

$$(25) \text{ RMSE}_i = \sqrt{\frac{1}{n_i} \sum_{j=1}^{n_i} (y_{ij} - \hat{y}_{ij})^2}$$

where \bar{y}_i is the average of the observed values for subject i , and all others are as defined before.

Once the values of \bar{e}_i , $\text{Bias}\%_i$ and RMSE_i were calculated for each of the 71 plots of the validation data, their frequency distributions were examined and compared to assess the goodness-of-prediction of the base and expanded height-diameter models on the validation data.

For a comparison, the biases for each of the 93 plots of the modelling data were also calculated following the same procedures outlined above and their frequency distributions were also examined.

2.6 Maximum height-diameter relationship

Subject-specific local predictions obtained from the NLMM technique attempt to “best” mimic the local data. Sometimes, due to the scarcity and the limited range of the data, as well as the flexibility of the specified model, local predictions may be unrealistic when extrapolated beyond the original data range (especially when more covariates are present). This is illustrated in Figure 2. To prevent the potential extrapolation errors due to data limitation, a maximum height-diameter curve was developed for black spruce based on all PSP data, plus the stem analysis data from sectioned trees (Huang et al. 1992). The combined data of 14,345 trees (Figure 2) were grouped by a 2-cm DBH class and the tallest tree in each DBH class was used to fit the Chapman-Richards model (4) by the ordinary nonlinear least squares method. This produced the “mean” maximum height-diameter curve for black spruce:

$$(26) H_{\max} = 1.3 + 34.3451[1 - \exp(-0.04892\text{DBH})]^{0.9042}$$

which, if necessary, would be used to constrain the height predictions beyond the observed data range. In the cases where negative predictions are obtained, which is possible for the FO method since eq. (18) is used to predict the response variable, negative values are set to zero to be biologically meaningful.

3. Results and discussion

3.1 Choice of the base and expanded models

Table 2 lists the parameter estimates and relevant fit statistics for the base and expanded models, where all fixed parameters are highly significant at $\alpha = 0.05$. The Akaike Information Criterion (AIC) and the Schwarz’s Bayesian Information Criterion (BIC) are computed by

$$(27) \text{ AIC} = -2\text{LL} + 2P \quad \text{BIC} = -2\text{LL} + P\ln(m)$$

where -2LL is -2 times the log-likelihood function of the model, P is the total number of effective parameters (includes fixed parameters, variance-covariance components of the random parameters, plus the residual variance component), and m is the number of effective subjects.

Among the four base models, the Chapman-Richards model (9) has the smallest AIC and BIC values (Table 2), suggesting (9) is the most reasonable base model for black spruce. Therefore, only (9) is expanded to include top height and/or basal area. The two expanded models (10) and (11) have smaller AIC and BIC values than their counterparts from (9), suggesting (10) and (11) are better than the Chapman-Richards base model (9).

Between the two expanded models, model (11), which included both top height and basal area, has smaller AIC and BIC values (Table 2). Hence, model (11) is considered better than model (10). This is expected because (10) included top height only. The estimated fixed parameters related to top height (β_4) and basal area (β_5) are both positive, indicating that in general, site quality and stand density have positive impacts on black spruce height growth.

Following the standard model ranking and selection practice in regression analysis, models (9), (10) and (11) would be ranked 3, 2 and 1 (best), respectively. Model (11) would be selected as the best model among the three models. The base model (9) would be considered as the worst model.

3.2 Predictive performance of the models

To assess the predictive performance of the models in real-world applications, height predictions from the base and expanded models were made based on the validation data (as well as on the modeling data for a comparison). To illustrate the computations involved, an example plot was used. This plot has three height-diameter observations. They are listed in Table 3 and shown in Figures 3(a)-3(b).

The height predictions based on the fixed parameters only are obtained directly from the models, with the random parameters set to zero. For instance, for the base model (9):

$$\hat{H}_{i_fix} = 1.3 + \hat{\beta}_1 [1 - \exp(-\hat{\beta}_2 \text{DBH}_i)]^{\hat{\beta}_3}$$

where the estimated fixed parameters $\hat{\beta}_1 - \hat{\beta}_3$ are given in Table 2. For the FO method, the derivatives of (9) with respect to the two random parameters are calculated by

$$\text{der}_{b_1} = \partial f(\mathbf{x}_i, \hat{\boldsymbol{\beta}}, \mathbf{0}) / \partial b_1 = [1 - \exp(-\hat{\beta}_2 \mathbf{DBH}_i)]^{\hat{\beta}_3}$$

$$\text{der}_{b_2} = \partial f(\mathbf{x}_i, \hat{\boldsymbol{\beta}}, \mathbf{0}) / \partial b_2 = \hat{\beta}_1 \ln[1 - \exp(-\hat{\beta}_2 \mathbf{DBH}_i)] [1 - \exp(-\hat{\beta}_2 \mathbf{DBH}_i)]^{\hat{\beta}_3}$$

The calculated results at the given DBHs are listed in Table 3. They constitute the \mathbf{Z}_i matrix defined in (15). In addition, from Table 2, we also know the $\hat{\mathbf{D}}$ and $\hat{\mathbf{R}}_i$ matrices. Therefore:

$$\mathbf{Z}_i = \begin{bmatrix} 0.286 & -8.475 \\ 0.371 & -8.709 \\ 0.596 & -7.306 \end{bmatrix} \quad \hat{\mathbf{D}} = \begin{bmatrix} 10.7688 & 0.2834 \\ 0.2834 & 0.02546 \end{bmatrix} \quad \hat{\mathbf{R}}_i = \begin{bmatrix} 1.2931 & 0 & 0 \\ 0 & 1.2931 & 0 \\ 0 & 0 & 1.2931 \end{bmatrix}$$

Having the $\hat{\mathbf{H}}_{i_fix}$, \mathbf{Z}_i , $\hat{\mathbf{D}}$ and $\hat{\mathbf{R}}_i$ values, the random parameters can be predicted from (17):

$$\hat{\mathbf{b}}_i = \hat{\mathbf{D}} \mathbf{Z}_i' (\mathbf{Z}_i \hat{\mathbf{D}} \mathbf{Z}_i' + \hat{\mathbf{R}}_i)^{-1} (\mathbf{H}_i - \hat{\mathbf{H}}_{i_fix}) = [-2.0180, 0.06947]'$$

Once the $\hat{\mathbf{b}}_i$ are known, the predicted heights are obtained by (18): $\hat{\mathbf{H}}_i = \hat{\mathbf{H}}_{i_fix} + \mathbf{Z}_i \hat{\mathbf{b}}_i$. Results are listed in Table 3, along with the associated errors. The standard deviation of the errors and an overall accuracy measure (δ) combining bias and precision were also calculated (Cochran 1977):

$$(28) \delta = (\text{mean bias})^2 + (\text{standard deviation of the errors})^2$$

Height predictions from the other models were obtained in a similar manner. Results are also listed in Table 3. Height prediction trajectories for all 71 plots of the validation data across the possible predictive range where future predictions are likely to be made, are shown in Figures 3(c)-3(d). These trajectories, sometimes referred to as "spaghetti plots" or "chow-mein plots" (Huang 2008), can be particularly useful in assessing the predictive behaviors of NLMMs within and beyond the observed data range. All trajectories for black spruce (Figure 3) were found to be within the bounds defined by the maximum H-DBH curve shown in Figure 2, rendering the constraint unnecessary for this data set.

The results in Table 3 suggest that all three models over-predicted the height for the example plot (i.e., the mean biases are all negative). Among the three models, the expanded model (11) produced the largest bias (-0.633) and δ (1.156), whereas the base model (9) produced the smallest bias (-0.347) and δ (0.748). Note that this is completely opposite to the ranking of the models based on the goodness-of-fit measures on the modelling data (Table 2), where the expanded model (11) was the best and the base model (9) was the worst.

Following the same procedure illustrated for the example plot, random parameters were calculated and height predictions were made for each of the 71 plots of the validation data. In addition, "typical" population-averaged (PA) height predictions were also made using the estimated fixed parameters only given in Table 2. For the purpose of comparison, similar predictions were made for each of the 93 plots of the modelling data. Summary statistics of the prediction biases from different models, by different methods, and on different data sets are provided in Table 4.

For the PA predictions based on the fixed parameters only, the expanded models are more accurate with smaller values of δ and Bias% than those from the base model (Table 4). This implies that if we use the fixed parameters only to make the PA predictions, the inclusion of additional variables will improve the accuracy of the predictions. This is consistent with the traditional least squares regression, in which only fixed parameters are present, and additional variables may need to be incorporated into the base model to explain additional variations that may arise from the between-subject differences in, for instance, site quality and stand density.

However, under the NLMM framework, or whenever the NLMM technique is applied, subject-specific local predictions become the predominant focus. The fixed parameters estimated as a part of a NLMM do not fully characterize the mean responses of the population, especially when the inter-subject variability is large (Hu et al. 1998, Davidian and Giltinan 2003, Fitzmaurice et al. 2004, Young et al. 2007). As a consequence, they generally provide a biased partial representation of the true population mean responses, which, unfortunately, is hardly ever recognized in forest modelling, where many forest modellers used the predictions obtained from the fixed parameters only to represent the "unbiased" PA responses. Corrections (or separate fits by nonlinear least squares) are necessary to obtain the unbiased PA predictions unless it can be shown that the biases are of little or no practical consequence (Chiswell and Monahan 2004, Kjellsson et al. 2004, Funatogawa and Funatogawa 2007, Huang 2008). The simplest and the most effective correction procedure for obtaining the unbiased PA predictions under the NLMM framework can be derived based on the ratio estimate method of Hartley and Ross (1954), which is frequently employed in sample surveys to obtain unbiased estimates of the population and subpopulation means. Since a correctly specified and fitted NLMM possesses the ability to closely follow the population-averaged and subject-specific trends exhibited by the data, the proportionality between the observed and predicted values can be assumed and the ratio estimate method can be used to adjust the predictions. Various ratio estimators can be formed of which the most common one, when calculated for the entire population based on the fixed parameters only, is

$$(29) \quad r = \frac{\bar{y}}{\hat{\bar{y}}} = \left(\frac{1}{N} \sum_{i=1}^m \sum_{j=1}^{n_i} y_{ij} \right) / \left(\frac{1}{N} \sum_{i=1}^m \sum_{j=1}^{n_i} \hat{y}_{ij_fix} \right) = \sum_{i=1}^m \sum_{j=1}^{n_i} y_{ij} / \sum_{i=1}^m \sum_{j=1}^{n_i} \hat{y}_{ij_fix}$$

where \bar{y} and $\hat{\bar{y}}$ are the grand mean of the observed (y_{ij}) and predicted (\hat{y}_{ij_fix}) values, respectively. The r defined in eq. (29) follows that: 1) if $\hat{\bar{y}} = \bar{y}$, $r = 1$, indicating unbiased prediction; 2) if $\hat{\bar{y}} > \bar{y}$, $r < 1$, indicating over-prediction; and 3) if $\hat{\bar{y}} < \bar{y}$, $r > 1$, indicating under-prediction. Cochran (1977) showed that the expectation:

$$E(\bar{y} - r \cdot \hat{\bar{y}}) = 0$$

Therefore, in the case of over-prediction ($r < 1$), the ratio estimate will adjust the predicted values downward by the ratio $\bar{y} / \hat{\bar{y}}$ to remove the bias. When under-prediction occurs ($r > 1$), the ratio estimate will adjust the predicted values upward by the same ratio $\bar{y} / \hat{\bar{y}}$. In both cases, the adjusted (unbiased) predictor \hat{y}_{ij_adj} , can be written as

$$\hat{y}_{ij_adj} = r \cdot \hat{y}_{ij_fix}$$

Once the adjusted predictor is obtained, it can be used to generate an unbiased PA curve for the population. For the base model (9) fitted in this study, this unbiased PA curve is given by

$$\hat{H}_{i_adj} = r(1.3 + \hat{\beta}_1 [1 - \exp(-\hat{\beta}_2 \text{DBH}_i)]^{\hat{\beta}_3})$$

where \hat{H}_{i_adj} are the adjusted unbiased PA predictions, and r is ratio estimate defined in eq. (29).

For subject-specific predictions, the results in Table 4 suggest that the overall mean biases are much smaller than those for the PA predictions. This is expected because the PA predictions were based on the fixed parameters only, whereas each plot in the subject-specific predictions has its own localized curve obtained from both fixed and random parameters.

The results in Table 4 also suggest that for subject-specific predictions, the mean bias and the standard deviation of the errors from the base model (9) are smaller than those from the expanded models. The bias (-0.023) and the SD (0.870) from the base model (9) are the smallest, whereas the bias (-0.068) and the SD (0.903) from the expanded model (11) are the largest. The values of the overall accuracy (δ) are 0.757, 0.798 and 0.820 for models (9), (10) and (11), respectively, indicating that as the number of variables incorporated into the base model increases, the accuracy of the predictions decreases. A similar trend is also observed on the modeling data (Table 4). Clearly, the height predictions from the base model are the most accurate. This is again entirely opposite to the ranking of the models based on the model fitting statistics. It is unexpected because the expanded models, which included one additional variable (top height) in (10), and two additional variables (top height and basal area) in (11), were supposed to provide incrementally more accurate predictions with smaller biases and SDs (to offset the incremental time and costs associated with measuring the additional variables).

For subject-specific local predictions, the unbiasedness of the predictions is not guaranteed because, depending on many factors (e.g., number of subjects, inter-subject variability, observations per subject, approximation process, model specification, errors-in-variables, assumptions, etc.), a NLMM provides varying degrees of goodness-of-fits to individual subjects within the population (Huang 2008). In fact, the biases for many subjects of an appropriately fitted NLMM could still be substantial (e.g., |Bias%| exceeding ± 2.5 or $\pm 5.0\%$ of the observed mean, see Tables 5-6). To ensure the unbiasedness of subject-specific local predictions, a ratio estimate can also be calculated for each subject within the population:

$$(30) \quad r_i = \frac{\bar{y}_i}{\hat{\bar{y}}_i} = \sum_{j=1}^{n_i} y_{ij} / \sum_{j=1}^{n_i} \hat{y}_{ij}$$

where \bar{y}_i is the mean of y_{ij} for subject i and $\hat{\bar{y}}_i$ is the mean of \hat{y}_{ij} predicted from eq. (18). The calculated r_i can be used to adjust the \hat{y}_{ij} to obtain unbiased predictions for subject i :

$$\hat{y}_{ij_adj} = r_i \cdot \hat{y}_{ij}$$

Essentially, both the population-based and subject-specific correction procedures adjust the predicted values from a NLMM downward or upward by the calculated ratio estimates, such that the averages of the residuals (i.e., mean biases) are zero on both the population and subject-specific levels. To avoid a digression from the main objectives of this study, we did not demonstrate the correction procedures in the present study. Interested readers can find more details elsewhere (e.g., Huang 2008).

3.3 Distributions of biases from the base and expanded models

To determine the possible reasons for the lower accuracy from the expanded models, the frequency distributions of subject-specific biases from the base and expanded models were examined. Table 5 lists the summary statistics for the bias ($\bar{\epsilon}_i$), Bias%_{*i*} and RMSE_{*i*} calculated plot-by-plot. The calculations were done for 71 plots of the validation data, and as a comparison, for 93 plots of the modelling data as well. The plots where the Bias%_{*i*} exceeded $\pm 2.5\%$ of the observed mean were identified and listed separately, where the $\pm 2.5\%$ threshold was chosen by dividing the one-sided 5% significance level commonly used in statistical inferences into two-sides.

The frequency distributions of the biases, Bias%*s* and RMSEs were examined. Here we only show the distributions of the Bias%*s* from the base model (9) and the expanded model (11) (Figure 4), as the distribution from the expanded model (10) was similar to that of (11), and the distributions of the other statistics showed similar patterns to those of Figure 4. Actual values and additional information related to the distributions are available, but here we only list those (Table 6) relevant to the validation data.

The contrasts between the base and expanded models are obvious. For instance, when (9) was used, 18 out of 71 plots of the validation data produced biases exceeded $\pm 2.5\%$ of the observed mean (Tables 5-6). When (10) and (11) were used, 23 and 27 plots produced biases exceeded $\pm 2.5\%$ of the observed mean. The results on the modelling data were similar: 15 out of 93 plots had biases exceeded $\pm 2.5\%$ when (9) was used, and 30 and 37 plots had biases exceeded $\pm 2.5\%$ when (10) and (11) were used. The frequencies of poor predictions from the expanded models are greater than those from the base model.

The poorer performance of the expanded models can also be seen in Figure 4, where the biases are centered around zero but those from the expanded models are spread out more than those from the base model, suggesting larger prediction variations and lower accuracies from the expanded models. On the validation data, the standard deviations of the biases for (10) and (11) are 0.612 and 0.664, respectively (Table 5). Both are larger than that (0.399) for the base model (9). The δ value (0.159) of the base model is less than half of the δ values (0.386 and 0.447) of the expanded models, suggesting that the base model is more than twice as accurate as the expanded models. The same conclusion can also be reached on the modelling data (Table 5).

It was generally taken for granted that the predictive accuracy of a base model would be improved if additional tree and stand level variables were incorporated into the model. This is true in the traditional least squares regression, and it may also be true in the biased PA predictions using only the fixed parameters under the NLMM framework. However, in terms of subject-specific predictions that the NLMM technique was developed for, we found that the addition of top height in (10), and top height and basal area in (11) both produced lower accuracy than the base model (9). In fact, judging from the results in Tables 4-5, the overall accuracy (δ) of the predictions is reduced as additional variables are added into the base model. This is true on the validation data, as well as on the modelling data.

The possible reason that caused the base model to perform better in local predictions than the expanded models likely originated from the inclusion of subject-specific random parameters in the base model. Under the NLMM framework, the random parameters in the base model already allowed the plot level variations associated with different site-specific factors to be accounted for without actually requiring that they be identified or measured. This renders in a statistical sense (as oppose to biological) that the addition of other plot level variables such as top height and stand density, which also represent the same differences in site factors that the random parameters already represent, unnecessary.

For the purpose of evaluating the biological implications of top height and basal area on black spruce height growth under the NLMM framework, it is still useful to look at the significance of these variables when entered into the base model. However, for subject-specific local predictions, the results of this study show that the addition of other variables beyond the base height-diameter model is unwarranted. Apparently, the random parameters in an aptly specified base model can take into account all or most of the other known and unknown factors on a given site, thereby eliminating the need to measure or to include other variables when subject-specific local predictions are made.

4. Conclusions

We examined four base height-diameter models for black spruce under the NLMM framework. We found that the Chapman-Richards base model was the best. We compared this base model with the expanded models that included top height and/or basal area as the additional predictors through the evaluation of the overall biases and the frequency distributions of the biases from individual plots. We found that the base model produced the most accurate subject-specific height predictions. For black spruce, optimal, subject-specific tree height predictions can be achieved using a simple height-diameter model fitted by the NLMM technique without including any other additional variables. We also found that the frequency distributions of the biases from individual plots where the main interest of a NLMM lies are more powerful in revealing the adequacy of the fitted NLMM than many other statistics. Such frequency distributions should be routinely examined in any future study involving NLMMs.

Acknowledgements

This research was supported by the Alberta Government and Forest Resource Improvement Association of Alberta (the FRIAA-GYPSY project). Special thanks are given to our industry partners, and to Mr. R. Briand, Dr. W.R. Dempster and Mr. D.J. Morgan for their help and contributions to this project. The constructive suggestions from Dr. K. McClain are appreciated.

References

Alberta Forest Service. (2000). Permanent sample plots field procedures manual. Forest Management Branch, Alberta

- Sustainable Resource Development, Edmonton, Alberta, Pub. FMOPC 83-03, 106 p.
- Arabatzis, A.A., & Burkhart, H.E. (1992). An evaluation of sampling methods and model forms for estimating height–diameter relationships in loblolly pine plantations. *For. Sci.* 38: 192–198.
- Beal, S. L., & Sheiner, L.B. (1982). Estimating population kinetics. *Critical Reviews in Biomedical Engineering* 8: 195-222.
- Calama, R., & Montero, G. (2004). Interregional nonlinear height–diameter model with random coefficients for stone pine in Spain. *Can. J. For. Res.* 34: 150–163.
- Castedo Dorado, F., Diéguez-Aranda, U., Barrio Anta, M., Rodríguez, M.S., & Gadow, K.V. (2006). A generalized height–diameter model including random components for radiate pine plantations in northwestern Spain. *For. Ecol. Manage.* 229: 202–213.
- Chiswell, K., & Monahan, J. F. (2004). Dealing with model bias in a nonlinear mixed model. In *Proc. of the 2004 American Statistical Association*, Alexandria, VA, pp. 2419-2426.
- Cochran, W.G. (1977). *Sampling techniques* (3rd ed.). Wiley, New York, 428 p.
- Curtis, R.O. (1967). Height-diameter and height-diameter-age equations for second growth Douglas-fir. *For. Sci.* 13: 365-375.
- Davidian, M., & Giltinan, D.M. (1995). *Nonlinear models for repeated measurement data*. Chapman & Hall, New York, 360 p.
- Davidian, M., & Giltinan, D.M. (2003). Nonlinear models for repeated measurement data: an overview and update. *J. Agricultural, Biological, and Environmental Statistics* 8: 387–419.
- Eerikäinen, K. (2003). Predicting the height–diameter pattern of planted *Pinus kesiya* stands in Zambia and Zimbabwe. *For. Ecol. Manage.* 175: 355–366.
- Fang, Z., & Bailey, R.L. (2001). Nonlinear mixed effects modeling for slash pine dominant height growth following intensive silvicultural treatments. *For. Sci.* 47: 287–300.
- Fitzmaurice, G.M., Laird, N.M., & Ware, J.H. (2004). *Applied longitudinal analysis*. Wiley, New York, 506 p.
- Funatogawa, T., & Funatogawa, I. (2007). The Bayesian bias correction method of the first-order approximation of nonlinear mixed-effects models for population pharmacokinetics. *Jour. of Biopharmaceutical Statistics* 17: 381-392.
- Hartley, H.O., & Ross, A. (1954). Unbiased ratio estimators. *Nature* 174: 270-271.
- Hu, F.B., Goldberg, J., Hedeker, D., Flay, B.R., & Pentz, M.A. (1998). Comparison of population- averaged and subject-specific approaches for analyzing repeated binary outcomes. *American Journal of Epidemiology* 147: 694-703.
- Huang, S. (1999). Ecoregion-based individual tree height-diameter models for lodgepole pine in Alberta. *Western J. Applied For.* 14: 186-193.
- Huang, S. (2008). A generalized procedure for bias-free predictions at population and local levels. A discussion paper, Pub-Feb-22-2008, Forest Management Branch, ASRD, Edmonton, Alberta, 61 p.
- Huang, S., & Titus, S.J. (1994). An age-independent individual tree height prediction model for boreal spruce-aspen stands in Alberta. *Can. J. For. Res.* 24: 1295–1301.
- Huang, S., Titus, S.J., & Wiens, D.D. (1992). Comparison of nonlinear height–diameter functions for major Alberta tree species. *Can. J. For. Res.* 22: 1297–1304.
- Huang, S., Yang, Y., & Wang, Y. (2002). A critical look at procedures for validating growth and yield models. In *Modelling Forest Systems*. CAB Publishing, Wallingford, UK, pp. 243-250.
- Kjellsson, M.C., Jönsson, S., & Karlsson, M.O. (2004). The back-step method – method for obtaining unbiased population parameter estimates for ordered categorical data. *The AAPS Journal* 6: Article 19 (<http://www.aapsj.org>).
- Littell, R.C., Milliken, G.A., Stroup, W.W., Wolfinger, R.D., & Schabenberger, O. (2006). *SAS system for mixed models* (2nd ed.), SAS Institute Inc., Cary, NC, 814 p.
- Lindstrom, M.J., & Bates, D.M. (1990). Nonlinear mixed effects models for repeated measures data. *Biometrics* 46: 673–687.
- Meng, X.S., Huang, S., Lieffers, V.J., Nunifu, T., & Yang, Y. (2008). Wind speed and crown class influence the height–diameter relationship of lodgepole pine: nonlinear mixed effects modeling. *For. Ecol. Manage.* 256: 570-577.
- Nicholas, N.S., Gregoire, T.G., & Zedaker, S.M. (1991). The reliability of tree crown position classification. *Can. J. For. Res.* 21: 698-701.

- Picard, R.R., & Cook, R.D. (1984). Cross-validation of regression models. *J. Am. Stat. Assoc.* 79: 575-583.
- Schabenberger, O. (1994). Nonlinear mixed effects growth models for repeated measures in ecology. In *Proc. of ASA, Section on Stats. & Environment*, Toronto, Canada, pp. 156-161.
- Sharma, M., & Parton, J. (2007). Height-diameter equations for boreal tree species in Ontario using a mixed-effects modeling approach. *For. Ecol. Manage.* 249: 187-198.
- Temesgen, H., Monleon, V.J., & Hann, D.W. (2008). Analysis and comparison of nonlinear tree height prediction strategies for Douglas-fir forests. *Can. J. For. Res.* 38: 553-565.
- Vonesh, E.F., & Chinchilli, V.M. (1997). *Linear and nonlinear models for the analysis of repeated measurements*. Marcel Dekker, New York, 560 p.
- Wykoff, W.R., Crookston, N.L., & Stage, A.R. (1982). User's guide to the stand prognosis model. USDA For. Serv. Gen. Tech. Rep. INT-133. 122 p.
- Yang, Y., Monserud, R.A., & Huang, S. (2004). An evaluation of diagnostic tests and their roles in validating forest biometric models. *Can. J. For. Res.* 34: 619-629.
- Young, M.L., Preisser, J.S., Qaqish, B.F., & Wolfson, M. (2007). Comparison of subject-specific and population averaged models for count data from cluster-unit intervention trials. *Statistical Methods in Medical Research* 16: 167-184.

Table 1. Summary statistics for black spruce model fitting and validation data

Data type	Level	Variable	N	Mean	Min	Max	SD
Model fitting	Tree	DBH (cm)	917	14.040	1.300	39.400	5.292
		H (m)	917	13.092	2.300	26.200	3.997
	Plot	BA (m ² /ha)	93	14.418	0.643	54.608	12.030
		TopH (m)	93	15.759	5.500	23.550	3.986
Validation	Tree	DBH (cm)	786	12.291	1.400	35.800	5.301
		H (m)	786	10.673	2.000	27.400	4.277
	Plot	BA (m ² /ha)	71	15.896	0.515	45.344	12.269
		TopH (m)	71	15.350	7.067	27.400	4.605

Note: DBH is tree diameter at breast height (1.3 m above ground), H is total tree height, BA is basal area per hectare, TopH is top height (i.e., average height of the 100 largest DBH trees per ha), N is sample size (i.e., number of trees at tree level, or number of plots at plot level). Min, max, and SD are minimum, maximum, and standard deviation, respectively.

Table 2. Parameter estimates and fit statistics for the base and expanded height-diameter models

Parameter	Base models				Expanded models	
	(5)	(6)	(7)	(9)	(10)	(11)
β_1	3.2418	1.6320	33.0854	25.4440	9.1617	8.9909
β_2	-11.5278	0.7401	3.8144	0.04734	0.07668	0.07127
β_3			-1.1826	1.0748	1.2266	1.1617
β_4					0.6745	0.6752
β_5						0.03388
$\sigma_{b_1}^2$	0.04409	0.3556	1053.65	10.7688	0.8135	1.1145
$\sigma_{b_1b_2}$	-0.4310	-0.05916	18.8578	0.2834	0.08974	0.1277
$\sigma_{b_2}^2$	6.2356	0.01046	0.3426	0.02546	0.03450	0.02895
σ^2	1.2736	1.3557	1.2704	1.2931	1.2864	1.2923
P	6	6	7	7	8	9
m	93	93	93	93	93	93
-2LL	3094.6	3104.2	3079.9	3075.5	2959.3	2948.7
AIC	3106.6	3116.2	3093.9	3089.5	2975.3	2966.7
BIC	3121.8	3131.4	3111.6	3107.2	2995.5	2989.5
Ranking	[5]	[6]	[4]	[3]	[2]	[1]

Note: β_1 - β_5 are fixed parameters, $\sigma_{b_1}^2$ and $\sigma_{b_2}^2$ are the variances for random parameters b_1 and b_2 , respectively, $\sigma_{b_1b_2}$ is the covariance between b_1 and b_2 , σ^2 is the residual (error) variance, P is the total number of parameters (includes fixed parameters, variance-covariance components of the random parameters, plus the residual variance component), m is the number of subjects (plots), -2LL is -2 times log-likelihood of the model, AIC is Akaike information criterion, and BIC is the Schwarz's Bayesian information criterion (AIC and BIC are defined in eq. (27)), and ranking refers to the rank of the model by the AIC and BIC values (smaller is better).

Table 3. Height predictions for an example plot with three height-diameter (H-DBH) observations

Model	Observed		Predicted						δ	Bias%
	DBH	H	H _{fix}	e _{fix}	der _{b1}	der _{b2}	H _{ss}	e _{ss}		
(9)	7.9	7.8	8.577	-0.777	0.286	-8.475	7.411	0.389	0.748	-3.41
	10.7	8.2	10.738	-2.538	0.371	-8.709	9.384	-1.184		
	20.3	14.5	16.455	-1.955	0.596	-7.306	14.745	-0.245		
	Mean	10.167	11.923	-1.756			10.513	-0.347		
	SD	3.758	4.071	0.897			3.796	0.792		
(10)	7.9	7.8	8.497	-0.697	0.380	-5.678	7.589	0.211	1.111	-5.68
	10.7	8.2	10.597	-2.397	0.491	-5.394	9.730	-1.530		
	20.3	14.5	15.467	-0.967	0.748	-3.355	14.914	-0.414		
	Mean	10.167	11.520	-1.354			10.744	-0.577		
	SD	3.758	3.575	0.913			3.767	0.882		
(11)	7.9	7.8	8.454	-0.654	0.376	-6.029	7.731	0.069	1.156	-6.23
	10.7	8.2	10.479	-2.279	0.482	-5.767	9.804	-1.604		
	20.3	14.5	15.244	-0.744	0.732	-3.741	14.862	-0.362		
	Mean	10.167	11.392	-1.226			10.799	-0.633		
	SD	3.758	3.486	0.913			3.668	0.869		

Note: H_{fix} is height prediction from fixed parameters, H_{ss} is height prediction from fixed and random parameters, e_{fix} and e_{ss} are associated residuals, der_{b1} and der_{b2} are derivatives with respect to b₁ and b₂, SD is the standard deviation, δ is defined in eq. (28), and Bias% = 100 × mean bias / mean H.

Table 4. Summary statistics for the overall height prediction biases

Data	Parameters used	Model	N	Bias				δ	Bias%
				Mean	Min	Max	SD		
Validation	Fixed & random	(9)	786	-0.023	-3.342	4.198	0.870	0.757	-0.216
		(10)	786	-0.045	-3.799	4.183	0.892	0.798	-0.422
		(11)	786	-0.068	-3.793	4.177	0.903	0.820	-0.637
	Fixed only	(9)	786	-0.804	-8.584	7.450	1.990	4.607	-7.533
		(10)	786	-0.223	-4.910	4.490	1.221	1.541	-2.089
		(11)	786	-0.350	-5.261	4.312	1.197	1.555	-3.279
Modelling	Fixed & random	(9)	917	-0.004	-5.247	4.140	1.074	1.153	-0.031
		(10)	917	-0.002	-5.703	4.408	1.091	1.190	-0.015
		(11)	917	-0.002	-5.643	4.403	1.097	1.203	-0.015
	Fixed only	(9)	917	0.451	-4.559	7.462	1.838	3.582	3.445
		(10)	917	0.284	-6.109	4.706	1.395	2.027	2.169
		(11)	917	0.109	-5.883	5.007	1.336	1.797	0.833

Note: N is sample size, SD is standard deviation, δ is defined in eq. (28), and Bias% = 100 × mean bias / mean H (equals to 10.673 for the validation data, and 13.092 for the modelling data, see Table 1).

Table 5. A summary of plot-based height prediction biases from the base and expanded models.

Model	Type	Variable	Validation data				Modelling data			
			Freq	Mean	SD	δ	Freq	Mean	SD	δ
(9)	All	\bar{e}_i	71	-0.013	0.399	0.159	93	-0.011	0.270	0.073
		$\bar{e}_i\%$	71	-0.615	3.304		93	-0.404	1.961	
		RMSE _i	71	0.913	0.459		93	0.924	0.572	
	$\bar{e}_i\%$ > 2.5	\bar{e}_i	18	-0.097	0.759		15	-0.001	0.598	
		$\bar{e}_i\%$	18	-2.088	6.236		15	-1.317	4.275	
		RMSE _i	18	1.105	0.581		15	0.729	0.329	
(10)	All	\bar{e}_i	71	-0.105	0.612	0.386	93	-0.054	0.442	0.198
		$\bar{e}_i\%$	71	-1.148	5.240		93	-0.286	2.952	
		RMSE _i	71	0.990	0.563		93	1.002	0.605	
	$\bar{e}_i\%$ > 2.5	\bar{e}_i	23	-0.277	1.038		30	-0.185	0.735	
		$\bar{e}_i\%$	23	-3.200	8.811		30	-1.161	4.897	
		RMSE _i	23	1.265	0.712		30	1.111	0.667	
(11)	All	\bar{e}_i	71	-0.076	0.664	0.447	93	0.005	0.472	0.223
		$\bar{e}_i\%$	71	-1.039	5.514		93	0.105	3.170	
		RMSE _i	71	1.024	0.562		93	1.018	0.601	
	$\bar{e}_i\%$ > 2.5	\bar{e}_i	27	-0.154	1.060		37	-0.028	0.726	
		$\bar{e}_i\%$	27	-2.223	8.767		37	-0.095	4.860	
		RMSE _i	27	1.247	0.672		37	1.066	0.626	

Note: \bar{e}_i , $\bar{e}_i\%$ and RMSE_i are plot-specific bias, Bias% and root mean square error defined in eqs. (22), (24) and (25), respectively, freq refers to the number of plots, SD is standard deviation, and δ is an overall measure of accuracy defined in eq. (28).

Table 6. Frequency distributions of Bias% from the base and expanded models on the validation data

Class	Range		Mid-point	Base model		Expanded models			
	From	To		(9)		(10)		(11)	
				Mean	Freq	Mean	Freq	Mean	Freq
1	-∞	-10.5		-19.93	1	-23.85	2	-19.06	3
2	-10.5	-9.5	-10			-9.64	1	-10.42	1
3	-9.5	-8.5	-9			-8.89	2	-9.26	1
4	-8.5	-7.5	-8			-7.58	1	-8.27	1
5	-7.5	-6.5	-7	-7.08	3				
6	-6.5	-5.5	-6			-5.88	3	-6.04	2
7	-5.5	-4.5	-5	-5.17	2			-5.00	2
8	-4.5	-3.5	-4	-3.68	1	-3.97	2	-4.05	2
9	-3.5	-2.5	-3	-3.13	3	-3.21	2	-2.82	3
11	-2.5	-1.5	-2	-2.03	3	-1.91	8	-2.00	7
12	-1.5	-0.5	-1	-0.87	17	-0.97	12	-1.01	14
13	-0.5	0.5	0	-0.13	19	-0.01	13	-0.05	14
14	0.5	1.5	1	1.16	13	0.91	10	0.94	3
15	1.5	2.5	2	2.15	1	1.98	5	2.04	6
16	2.5	3.5	3	2.92	5	2.93	5	2.98	2
17	3.5	4.5	4	3.72	2	3.78	3	4.05	3
18	4.5	5.5	5	4.96	1	4.93	1	5.06	3
19	5.5	6.5	6					5.55	2
20	6.5	7.5	7					6.77	1
21	7.5	8.5	8						
22	8.5	9.5	9						
23	9.5	10.5	10			10.22	1		
24	10.5	∞						12.61	1
Total					71		71		71
No. of plots where Bias% > 2.5					18		23		27
% of plots where Bias% > 2.5					25.4		32.4		38.0

Note: mean and freq refer to the mean bias and frequency (number of plots) associated with the defined class. The frequencies are displayed in Figures 4(a)-4(b).

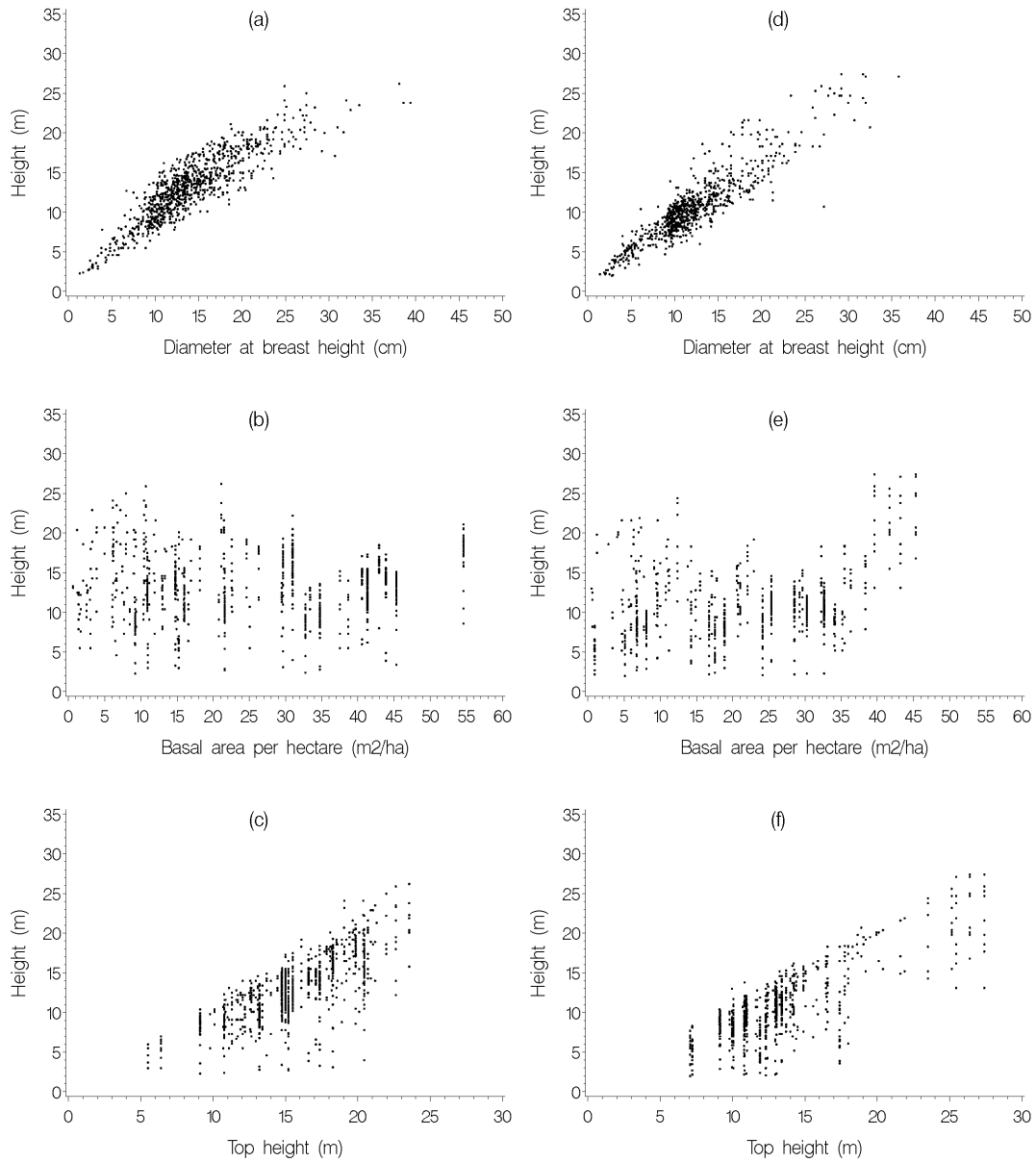


Figure 1. Model fitting (a, b, c) and validation data (d, e, f). Summary statistics are listed in Table 1.

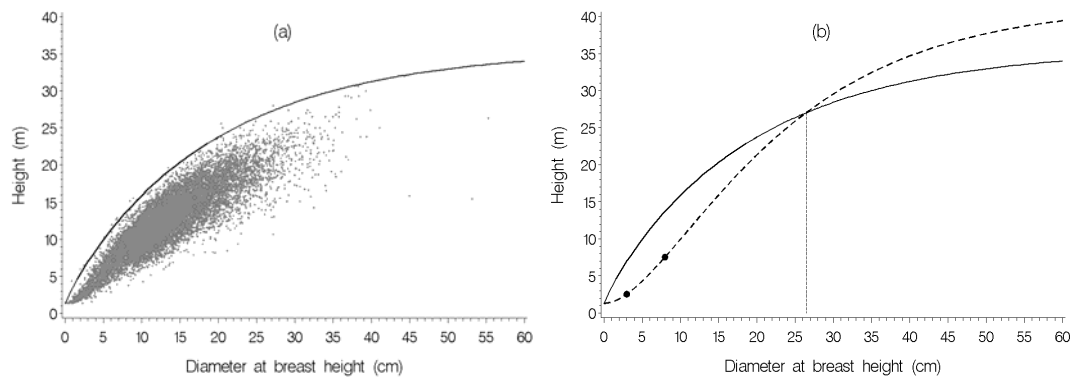


Figure 2. Maximum height-diameter relationship (solid line in a and b) for black spruce. The relationship is defined by eq. (26). The localized curve (dashed line) from the two data points in (b) gives unrealistic predictions when extrapolated beyond a DBH of 26.5 (cm). Therefore, for DBH > 26.5, height predictions are constrained by the maximum relationship.

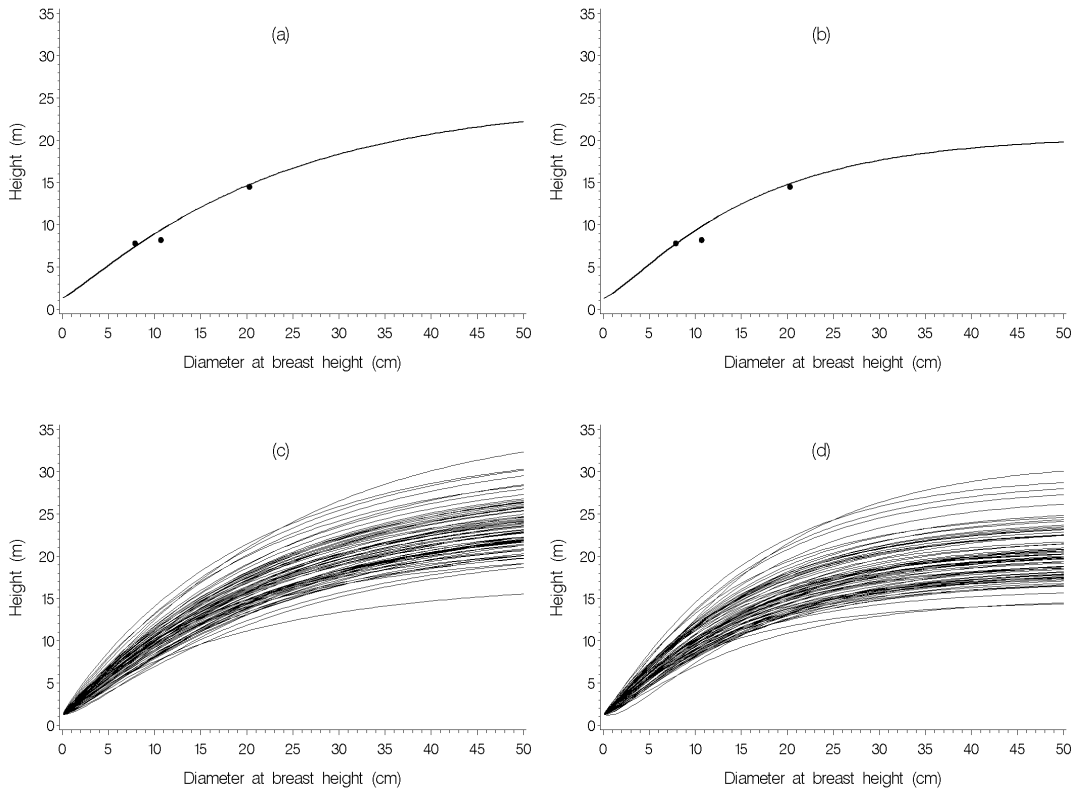


Figure 3. Height prediction curves from the base model (9) (a, c) and expanded model (11) (b, d), for an example plot (a, b) and for all 71 plots (c, d). Actual values for the example plot are listed in Table 3.

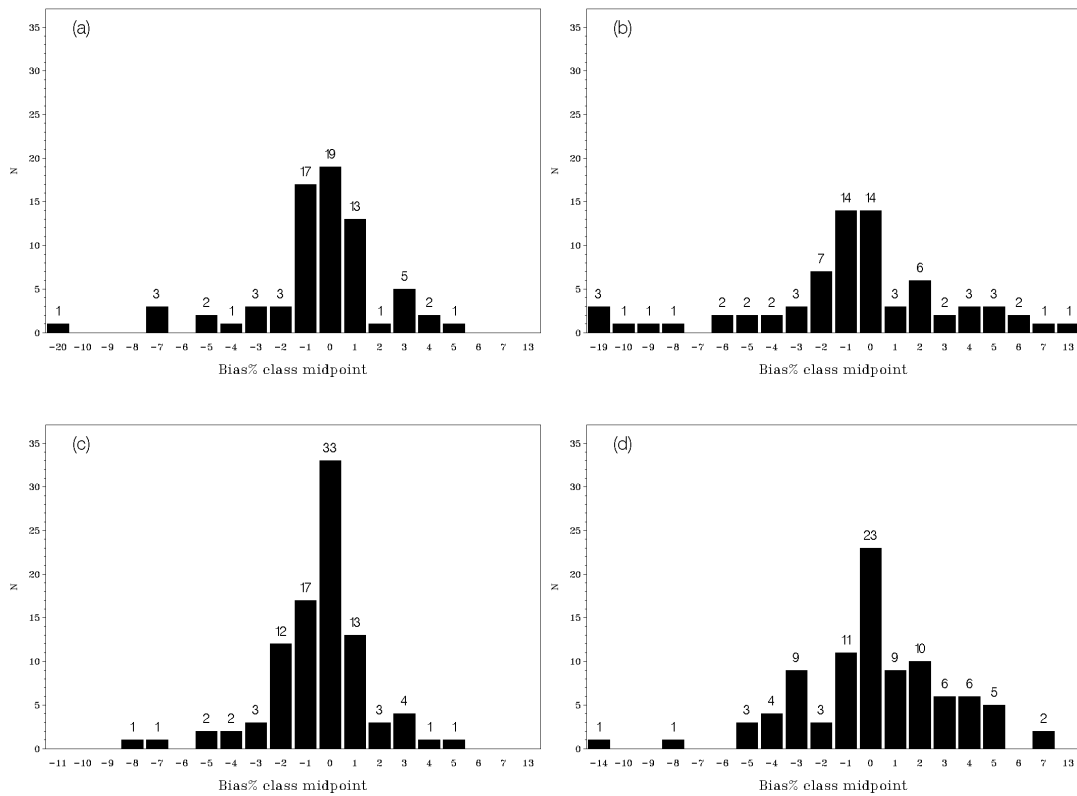


Figure 4. Frequency distributions of Bias% from models (9) (a, c) and (11) (b, d) on the validation data (a, b) and modelling data (c, d). Actual values related to (a) and (b) are given in Table 6.



Markov Chain Monte Carlo-Based Bayesian Analysis of Binary Response Regression, with Illustration in Dose-Response Assessment

Crispin M. Mutshinda

Department of Mathematics and Statistics (Gustaf Hällströmin katu 2b)

University of Helsinki

P.O. Box 68, FIN-00014, Helsinki, Finland

Tel: 3-58-9191-51439 E-mail: mutshinda@gmail.com

Abstract

This paper deals with the Bayesian analysis of binary response regression using Markov chain Monte Carlo (MCMC) methods, more specifically the Metropolis sampler, for posterior simulation. The methodology is illustrated with real-world data from a bioassay experiment. Inference about quantities of typical interest in the dose-response setting such as the lethal dose is discussed as well. MCMC are routinely implemented through popular Bayesian software such as Win-/Open-BUGS. However, these remain black boxes which provide no insight in the estimation procedure. This paper exemplifies that developing and implementing an MCMC sampler may, in many practical situations, be relatively straightforward. The R code for the Metropolis sampler is also provided in an appendix to the paper.

Keywords: Bayesian logistic regression, Generalized linear models, LD50, Metropolis sampler, Toxicological analysis

1. Introduction

Dose-response (D-R) analyses represent an important pillar upon which toxicological analyses regarding drugs and putative environmental contaminants are built. They allow identifying a range of intakes (doses) encompassing an appropriate benefit-to-risk ratio. Acute toxicity of drugs and various chemical compounds is typically assessed through bioassay (biological assay) experiments. These consist of measuring the effects of a substance on living organisms under controlled conditions. Typically, batches of animals are administered various doses of a drug or a chemical (e.g., an insecticide), and the outcomes are usually recorded on a dichotomous scale: dead/alive, tumor/no tumor, etc. The same type of data may arise from observational studies on environmental contamination involving humans, animals or plants, by relating a health defect outcome to the level of exposure to an alleged contaminant, using appropriate proxies for exposure. Such an experiment or observational study typically yields data of the form (x_i, n_i, y_i) where y_i denotes the number of individuals with positive outcome at dose x_i out of a total of n_i individuals.

Developing D-R models is central to determining “safe” and “hazardous” levels and dosages of drugs, potential pollutants and other substances to which humans, animals and plants are exposed. Conclusions of D-R analyses often serve as basis for public health regulations that limit exposure to hazardous substances (e.g., Mutshinda et al. 2008).

Statistical analyses of D-R data have mainly revolved around the maximum-likelihood method (e.g. Metz et al. 1982 amongst many others). However, the steady increase in popularity of the Bayesian methodology (Clark 2005) has prompted substantial interest in implementing it in the D-R and exposure risk assessment settings (e.g., French et al. 2002; Teunis et al. 2002; Englehardt 2004; Englehardt & Swartout. 2004, 2006; Mutshinda et al. 2008). Bayesian inference offers attractive options whereby available information such as results from previous studies or experts’ opinion in the form of a prior distribution can rationally be combined with information conveyed by empirical data and encoded in the likelihood function to boost the power of estimation. Owing to advances in sampling-based methods such as Markov chain Monte Carlo (MCMC) (Gilks et al. 1996) and the spread of related software in the vein of Win-/Open-BUGS (Spiegelhalter et al. 2003; Thomas et al. 2006), the computational burden that has long hampered the broad adoption of the Bayesian approach, or limited its application to the computationally convenient conjugate analysis should overall no longer be an issue in itself.

This paper discusses the Bayesian analysis of binary response regression using MCMC, more specifically the (random walk) Metropolis sampler for posterior simulation. The methodology is illustrated in a practical example using real-world data from a bioassay experiment. In spite of the relatively large body of literature on Bayesian dose-response assessment, the subject is worthy of additional attention, in particular as numerical methods such as the MCMC

implemented here are concerned. Indeed, the principles of these methods still need to be made broadly accessible to applied scientists. Notwithstanding the user-friendliness of available Bayesian software packages, these remain black boxes which provide no insight in the estimation process. This paper exemplifies that, in many practical cases, developing and implementing a MCMC sampler may be relatively straightforward once the underlying principles are well understood. In addition to a concise tutorial on generalized linear models under the umbrella of which falls binary response regression, this paper contributes to the literature by providing a handy explanation of the MCMC algorithm known as the Metropolis sampler, along with an illustration of its implementation in the increasingly popular R environment.

This paper is structured as follows. Section 2 presents the materials and methods. Section 3 deals with the analysis of the bioassay data, and section 4 is devoted to some conclusions.

2. Materials and methods

2.1 Description of data

We use real data from a bioassay experiment as presented Table 1. The data were reproduced (with permission) from Gelman et al. (2003), and are used here solely for illustrative purposes. The dichotomous outcomes are death/survival, and y_i denotes the number of animals with positive outcome at dose x_i (on the log-scale) out of n_i . Gelman et al. (2003) analyzed the same dataset with a Bayesian approach by approximating the posterior distribution in two ways: (i) using crude simulations, and (ii) using the normal approximation to the posterior. Here we use MCMC to directly simulate samples from the joint posterior of the model parameters. By using the same dataset, we have the opportunity to compare the results across different methods, including the method of maximum likelihood which is briefly carried out in section 2.2.2.

2.2 Methods

The probability of positive outcome is related to the dose level through a logit (logistic regression) model. Logistic regression falls into the category of generalized linear models (GLMs) which underlie most of the statistical analyses in applied research. We revisit GLMs in subsection 2.2.1 without any attempt to presenting an exhaustive discussion. Readers interested in more details are referred to appropriate literature which includes McCullough & Nelder (1989), Lindsey (1997), and Dobson (2002). In subsection 2.2.2 we fit the model to the bioassay data using the maximum likelihood method, and in subsection 2.2.3, we perform a MCMC-aided Bayesian analysis, simulating samples from the joint posterior of interest through a Metropolis sampler.

2.2.1 Generalized linear models: an overview

GLMs extend the ordinary linear regression (OLR) model to settings where assumptions of the latter are not met. This is so when: (i) the relation between, $\mu = E(Y)$ and X is not linear (in GLMs, it is rather a transformation of $\mu = E(Y)$ through a function $g(\cdot)$ called link function which linearly related to X as we discuss below), (ii) the variance is not constant across responses (OLR assumes constant variance across the responses), and (iii) the response variables are not Gaussian. This last assumption is nonetheless not critical. Indeed, in the OLR setting, $Y = X\beta + \varepsilon$, where Y is a (column) vector of n iid Gaussian responses, X is a design matrix with n rows and $(p+1)$ columns where p is the number of explanatory variables and the first column of X corresponds to the intercept. β is a (column) vector of the $(p+1)$ regression parameters (including the intercept), and ε is a (column) vector of the n residuals which are assumed to be normally distributed with mean zero and variance σ^2 i.e. $\varepsilon \sim N(0, \sigma^2 I_n)$. The ordinary least squares (OLS) estimator of β is given by $\tilde{\beta} = (X^T X)^{-1} X^T Y$, and its covariance matrix is $Var(\tilde{\beta}) = \{(X^T X)^{-1} X^T\} Var(Y) \{X(X^T X)^{-1}\} = \sigma^2 \{(X^T X)^{-1} X^T\} \{X(X^T X)^{-1}\}$ since $Var(Y) = \sigma^2 I_n$. Moreover, $\tilde{\beta}$ is Gaussian as a linear transformation of Y which is Gaussian by assumption in the OLR setting. Nevertheless, even if the responses, Y_i , are not normal, the OLS estimator $\tilde{\beta}$, which coincides with the MLE $\hat{\beta}$ is still asymptotically normal as long as the variance is constant, by virtue of the renowned central limit theorem.

A GLM consists of the following three components. First, a sequence of independent responses y_1, y_2, \dots, y_n assumed to be realizations of random variables Y_1, Y_2, \dots, Y_n which share the same form of parametric distribution from the exponential dispersion family. That is, the probability density function (pdf) of Y_i or the probability mass function (pmf) Y_i if is discrete can be written in the form

$$f(y_i) = \exp \{w_i [y_i \theta_i - b(\theta_i)] / \phi + c(y_i, \phi)\}, \quad (1)$$

where θ_i is the so-called natural (or canonical) parameter, ϕ is a scale parameter and the w_i 's are known weights which in the usual case are all equal to 1. Second, a systematic part or linear predictor $\eta_i = x_i^T \beta$, where

$X_i^T = (X_{i,1}, \dots, X_{i,p})$ is the i^{th} row of the design matrix $X_{n \times p}$, and β is a (column) vector of the $(p+1)$ regression parameters. The systematic part η_i is still linear (in the parameters!). And third, a monotonic and differentiable function $g(\cdot)$ called link function through which the systematic part $X_i^T \beta$ is related to the mean value $\mu_i = E(Y_i)$. More specifically $\theta_i(\mu_i) = g(\mu_i) = X_i^T \beta$ or equivalently, $\mu_i = g^{-1}(X_i^T \beta)$.

The exponential family includes a wide range of common distributions such as the normal, the binomial, the Poisson, and the gamma distributions. Below we derive the canonical forms of the three first distributions.

The normal pdf is $f(y_i) = 1 / (2\pi\sigma^2)^{1/2} \exp(-(y_i - \mu_i)^2 / 2\sigma^2)$, $-\infty < y < \infty$, which can be written as $f(y_i) = \exp[(y_i \mu_i - \mu_i^2 / 2) / \sigma^2 - y_i^2 / 2\sigma^2 - (1/2) \log(2\pi\sigma^2)]$ which is in the canonical form (1) with $\theta_i = \mu_i$, $b(\theta_i) = \theta_i^2 / 2$, $\phi = \sigma^2$, $w_i = 1$, and $c(y_i, \phi) = -y_i^2 / 2\phi - (1/2) \log(2\pi\phi)$.

The binomial pmf is $f(y_i | \pi_i) = k \pi_i^{y_i} (1 - \pi_i)^{n_i - y_i}$ where $k = n_i! / y_i! (n_i - y_i)!$ which can be written in the canonical form as $\exp\{y_i \log(\pi_i / [1 - \pi_i]) + n_i \log(1 - \pi_i) + \log(k)\}$, where $\theta_i = \log(\pi_i / [1 - \pi_i])$, i.e. $\pi_i = \exp(\theta_i) / [1 + \exp(\theta_i)]$, $b(\theta_i) = -n_i \log(1 - \pi_i) = n_i \log(1 + \exp(\theta_i))$, $\phi = 1$, $c(y_i, \phi) = \log(k)$, and $w_i = 1$.

The Poisson pmf is $f(y_i | \lambda_i) = e^{-\lambda_i} \lambda_i^{y_i} / y_i! = \exp(y_i \log \lambda_i - \lambda_i - \log y_i!)$ which is in the canonical form with $\theta_i(\lambda_i) = \log \lambda_i$, $b(\theta_i) = \exp(\theta_i)$, $\phi = 1$, $w_i = 1$, and $c(y_i, \phi) = -\log(y_i!)$.

It is worth emphasizing that for distributions belonging to the exponential family, the mean $\mu_i = E(Y_i)$, is related to the variance $\text{Var}(Y_i | \eta_i)$ through a special relationship, $V(\mu_i)$, called the variance function. Moreover, It can be shown that $\mu_i = E(Y_i) = \partial b(\theta_i) / \partial \theta_i$, and $\text{Var}(Y_i) = (\phi / w_i) \partial^2 b(\theta_i) / \partial \theta_i^2$. ϕ is usually a nuisance parameter. The variance function is defined as $V(\mu_i) = \partial^2 b(\theta_i(\mu_i)) / \partial \theta_i^2$. These relations can be easily derived in the following way (e.g. Lindsey 1997, p. 12 -13). For any likelihood function $L(\theta_i, \phi; Y_i)$, the quantity $U_i = \partial \log L(\theta_i, \phi; Y_i) / \partial \theta_i$ is commonly known as the score function, and in standard inference, it is known that $E(U_i) = 0$ and $\text{Var}(U_i) = E(-\partial U_i / \partial \theta_i)$. For distributions that belong to the exponential family, $U_i = w_i [Y_i - b'(\theta_i)] / \phi$. Hence, $E(U_i) = 0$ implies $E(Y_i) = b'(\theta_i)$ as required. Moreover, $\text{Var}(U_i) = (w_i / \phi)^2 \text{Var}(Y_i)$, and $E(\partial U_i / \partial \theta_i) = -(w_i / \phi) b''(\theta_i)$. The requirement $\text{Var}(U_i) = E(-\partial U_i / \partial \theta_i)$ yields $\text{Var}(Y_i | \eta_i) = b''(\theta_i) (\phi / w_i)$. Consequently, $V(\mu_i) = b''(\theta_i)$.

The function $b(\theta)$ is very important in GLMs as its first and second derivatives *with respect to the natural parameter* provide the mean and the variance functions, respectively. In the binomial case for instance, $E(Y_i) = b'(\theta_i) = n_i [\exp(\theta_i) / (1 + \exp(\theta_i))] = n_i \pi_i$, and $b''(\theta_i) = n_i [\exp(\theta_i) / (1 + \exp(\theta_i))^2]$ which is nothing but $n_i \pi_i (1 - \pi_i)$ in agreement with what we know about the binomial distribution. It can be easily checked that $V(\mu) = \mu$ for Poisson regression (with log link), $V(\mu) = \mu(1 - \mu)$ for logistic regression, $V(\mu) = \phi \mu^2$ for gamma (with inverse link $g(\mu) = 1 / \mu$), and $V(\mu) = \text{constant}$ for ordinary linear regression with identity as link function.

2.2.2 Maximum likelihood estimation of the binary response regression model, and application to the bioassay dose-response data

Let $f_\theta(X)$ be a statistical model (i.e. a family of distributions indexed by the unknown parameter θ) describing a process of interest, and let $X = X_1, \dots, X_n$ be independent and identically distributed (iid) random variables with density f_θ . The maximum likelihood method estimator (MLE) of θ is the value $\hat{\theta}$ which maximizes the likelihood $L(\theta; X) = p_\theta(X_1, \dots, X_n) = \prod_{i=1}^n f_\theta(X_i)$ of the observed data, which is the joint distribution of X evaluated viewed as a function of θ . Since the log function is monotonic and increasing, $L(\theta; x)$ and $l(\theta; X) = \log L(\theta; X)$ take their maximum at the same point, and it is often more convenient to work with the logarithm of the likelihood function $l(\theta; X) = \sum_{i=1}^n \log f_\theta(X_i)$ known as the log-likelihood function. The maximum likelihood estimator (MLE) $\hat{\theta}(X)$ is a random variable, since its value (the estimate) depends on a realization $x = (x_1, \dots, x_n)$ i.e. the data at hands. $\hat{\theta}(x)$ is then called the maximum likelihood estimate based on x . Maximum likelihood estimates have desirable large sample properties: as the sample size increases, they become unbiased,

efficient, and normally distributed with the “true” value as mean and asymptotic covariance matrix given by the inverse of the Fisher information matrix (the negative of the Hessian matrix of log-likelihood evaluated at the maximum likelihood estimate). Moreover, MLEs are re-parameterization invariant (see below), and the likelihood function can be used to construct confidence intervals and to test hypotheses about models and parameters. More details on maximum likelihood estimation can be found in many statistical books such as Casella & Berger (2001) or Garthwaite et al. (2002). Finding MLEs is an optimization problem which often requires iterative procedures.

In a dose-response setting, the outcomes of different trials are assumed to be (conditionally) independent given the level of dose. Hence, under controlled conditions, the dose-response relationship can be described by a logistic regression model. That is,

$$y_i | x_i \sim \text{Bin}(n_i, \pi_i), \text{ where } \eta_i = \text{logit}(\pi_i) = \beta_1 + \beta_2 x_i, \quad (i = 1, \dots, k) \quad (2)$$

where k is the number of dose levels, β_1 and β_2 are real-valued regression parameters. Consequently, the probability of positive outcome at dose level x_i is given by $\pi_i = \exp(\beta_1 + \beta_2 x_i) / [1 + \exp(\beta_1 + \beta_2 x_i)]$.

The regression parameters are often interpreted in terms of odds ratios. The log (odds) for the probability of positive response at dose level x is $\text{logit} \pi = \beta_1 + \beta_2 x$. If the dose increases by one unit from x to $(x + 1)$, the log (odds) becomes $\beta_1 + \beta_2 x + \beta_2$. By taking the exponential of the log (odds) to return to the odds scale, it turns out that the odds are multiplied by a factor of $\exp(\beta_2)$. Therefore, $\exp(\beta_2)$ is interpretable as an odds ratio; it is the multiplicative increase in the odds of positive response due to one unit increase (on the log-scale) in the level of dose. If the log is in base 2, each one unit increase corresponds to a doubling of the dose. A negative β_2 would suggest that increasing the dose does not increase the probability of having a positive response. In the case of a categorical explanatory variable with two categories $\exp(\beta_2)$ is just the odds ratio for one category compared with the other. Let $Z_i = 1 / [1 + \exp(\beta_1 + \beta_2 x_i)]$. Then the likelihood function (up to a constant of proportionality) is $L(\beta) \propto \prod_i (1 - Z_i)^{y_i} Z_i^{(n_i - y_i)}$, and the log-likelihood is $l(\beta) = \sum_i y_i \log(1 - Z_i) + (n_i - y_i) \log(Z_i)$.

The maximum likelihood estimator (MLE), $\hat{\beta} = (\hat{\beta}_1, \hat{\beta}_2)$ is obtained by (numerically) maximizing the (log)-likelihood with respect to each component of β . Presumably all standard software packages include functions for fitting GLMs. We used the *glm(.)* function built-in to the R statistical package (R script in appendix A) to carry out the ML model fitting to the bioassay data which yielded the ML estimate $\hat{\beta} = (0.847, 7.75)$. Elements of the asymptotic covariance matrix, C , of $\hat{\beta}$ were estimated to be $C_{1,1} = 1.04$, $C_{1,2} = 3.54$, and $C_{2,2} = 23.74$. The maximum likelihood estimate is pretty close to $(0.88, 7.93)$, the mean of Gelman et al.’s normal approximation to the posterior.

With mortality data, a typical quantity of interest is the so-called lethal dose which represents the level of dose resulting in the death of a specific proportion of experimental subjects (typically animals in a preclinical experiment). The cure effective dose is similarly defined as the dose resulting in the cure of a specific proportion of experimental subjects. Usually, the dose resulting in the death of half of the subjects, the so-called *LD50* henceforth denoted by φ is reported.

The formula $\varphi = -\beta_1 / \beta_2$, ($\beta_2 \neq 0$) is easily derived by solving $(1 + \exp(\beta_1 + \beta_2 * \varphi))^{-1} = 0.5$ for φ .

A handy feature of MLEs is their re-parameterization invariance property, by which the MLE of a function of parameters is just the same function of the appropriate MLE. It follows from this property that the MLE for φ is simply given by $\hat{\varphi} = -\hat{\beta}_1 / \hat{\beta}_2$, ($\hat{\beta}_2 \neq 0$). To derive a confidence interval for $\hat{\varphi}$, however, one needs to estimate its variance through what is known as the delta method (e.g., Casella & Berger 2002), which can be stated as follows. Let $\hat{\beta} = (\hat{\beta}_1, \dots, \hat{\beta}_d)$ be the maximum likelihood estimator of a d -dimensional parameter $\beta = (\beta_1, \dots, \beta_d)$ based on a sufficiently large-sample, with $\text{Var}(\hat{\beta}) = V$, and let $\varphi = g(\cdot)$ be a scalar and differentiable function of β . Then $\hat{\varphi} = g(\hat{\beta})$ is the MLE of φ . In addition, $\hat{\varphi}$ is asymptotically Gaussian with a distribution centred at the true value, φ , and approximate covariance variance matrix W given by $W = (\nabla \hat{\varphi})^T V (\nabla \hat{\varphi})$, where $\nabla \hat{\varphi} = (\partial \varphi / \partial \beta_1, \dots, \partial \varphi / \partial \beta_d)^T |_{\hat{\beta}}$ and T denotes matrix transposition. So, an expression for $\text{Var}(\hat{\varphi})$ can be derived via the delta method. Below we consider a MCMC-aided Bayesian approach.

2.2.3 Bayesian estimation of the binary response regression model via random walk Metropolis sampling

In the Bayesian paradigm, information conveyed by empirical data y through the likelihood function $p(y | \theta)$ is combined with prior information about the model parameter θ , encoded in a prior distribution $p(\theta)$, into a posterior

distribution $p(\theta|y)$ deriving from the joint distribution $p(y, \theta) = p(y|\theta)p(\theta)$ according to the celebrated Bayes' theorem as

$$p(\theta|y) = p(y|\theta)p(\theta) / p(y) \propto p(y|\theta)p(\theta) \tag{3}$$

where $p(y) = \int_{\Theta} p(\theta) p(y|\theta) d\theta$, and Θ the range of all possible values of θ .

The posterior distribution is the legitimate tool for Bayesian inference whose conclusions are essentially made in terms of probabilistic statements about plausible parameter values or outcomes of future observations.

The derivation of the posterior distribution may be difficult to impossible, owing to integration involved in the normalizing constant $p(y)$. Historically, Bayesian analyses were confined to trivial situations where the integral can be ignored. These situations involve the use of the so-called conjugate priors where the likelihood and the prior combine in a nice fashion so that the posterior can be determined without integration because the posterior and the prior have the same form. For example, a binomial likelihood coupled with a beta prior yield a beta posterior, a Poisson likelihood coupled with a gamma prior yield a gamma posterior. The advent of the computationally intensive methods known as Markov Chain Monte Carlo (MCMC) methods has made Bayesian analysis feasible for a wide class of models. This simulation-based approach greatly simplifies Bayesian analysis. The two most popular MCMC algorithms are the Gibbs sampler (e.g. Gelfand & Smith 1990) and the Metropolis-Hastings (M-H) algorithm (Hastings, 1970; Chib & Greenberg 1995)

For the purpose of our analysis, we first revisit M-H algorithm, which is an extension of the original Metropolis algorithm introduced by Metropolis et al. (1953). Like any other MCMC method, the principle of the M-H sampler is to generate (dependent) samples $\beta^{(1)}, \dots, \beta^{(N)}$ whose distribution converges to a target distribution $\pi(\beta)$. In Bayesian estimation of β , based on likelihood $p(y|\beta)$ and prior distribution $p(\beta)$, the target distribution is the posterior $\pi(\beta) = p(\beta|y)$. Starting from an arbitrary point in the parameter space, new states β^* are generated from a proposal (or instrumental) distribution $q(\beta^*|\beta^{(i)})$ giving the probability density of moving to state β^* from the current state $\beta^{(i)}$ of the chain at step i . Each proposal is either accepted (meaning that the chain moves to the new state) or rejected (i.e. the chain remains in the same state), depending on the value of a test ratio. A description of the M-H algorithm is given below.

1. Pick $\beta^{(1)}$ arbitrarily in the support of $\pi(\beta) = p(\beta|y)$
2. Draw β^* from $q(\beta^*|\beta^{(i)})$
3. Compute $r(\beta^{(i)}, \beta^*) = \pi(\beta^*) q(\beta^{(i)}|\beta^*) / \pi(\beta^{(i)}) q(\beta^*|\beta^{(i)})$

Generate $u \sim Uni(0,1)$

If $u < r(\beta^{(i)}, \beta^*)$ then set $\beta^{(i+1)} = \beta^*$

otherwise, set $\beta^{(i+1)} = \beta^{(i)}$

Repeat 2 -3 until "convergence"

The proposal density q can be anything, but a symmetric proposal, meaning that $q(\beta^{(i)}|\beta^*) = q(\beta^*|\beta^{(i)})$ yields the simpler form $r(\beta^{(i)}, \beta^*) = \pi(\beta^*) / \pi(\beta^{(i)})$ for the test ratio. A common symmetric choice is the random walk proposal which corresponds to the original Metropolis algorithm which is implemented here. Conditionally on the state, $\beta^{(k)}$, of the chain at step k , a random walk Metropolis sampler proposes a move to $\beta^* = \beta^{(k)} + \sigma \epsilon$ where $\epsilon \sim MVN(\mathbf{0}, \Sigma)$, and $\sigma > 0$ is a tuning constant usually selected in such a way that roughly 20%-40% of the proposals are accepted. The pre-convergence part of the MCMC called "burn-in" is usually discarded, and the remaining part might be thinned to say every j^{th} observation, for an integer $j > 1$ in order to reduce the correlation between consecutive draws. The thinning factor j is therefore the frequency with which successive parameter values are stored. After the burn-in and thinning of the MCMC, distributional summaries of the parameters of interest are produced from the stored samples.

3. Application to the bioassay data

We placed on the components of β independent and diffuse (with variance 1.0E+6) centered Gaussian priors. A random walk Metropolis was subsequently implemented, generating at step k proposals of the form $\beta^* = \beta^{(k)} + \sigma Az$,

where z is a random draw from the bivariate standard Gaussian, and A is the Cholesky factor of the ML asymptotic covariance matrix C i.e., means $C = A^T A$. Any symmetric and positive definite (SPD) matrix (all covariance matrices are indeed SPD) has a Cholesky decomposition (see e.g. Gentle, 1998 for more details).

We initially ran 5000 iterations of the MCMC for a couple of times in order to select a suitable tuning factor σ . The value $\sigma = 2$ was retained as it yielded a roughly 32% acceptance probability. After the tuning constant was set, we ran 5000 burn-in iterations of the MCMC followed by a further 20000 iterations, and thinned the MCMC to every 10th draw. A commented version of the R script implementing the sampler is provided in appendix B, where the variable *nacc* contains the number of accepted proposal and *acc_prob* contains the acceptance probability.

The MCMC reached the target distribution quite fast, and then proved to move freely over the parameter space. This good mixing is illustrated by the trace plots in Figure1 which display 1000 posterior samples for each component of the parameter β .

The sensitivity of the results to the prior inputs was assessed by varying the range of the priors by order of magnitudes, while starting the MCMC from dispersed points in the parameter space, but the results remained broadly robust to these changes.

All our results are reported on the scale of the log dose. The posterior mean, $\bar{\beta}$ was (1.35, 12.37), which is relatively close to Gelman et al.'s approximate posterior (1.37, 11.93) obtained through simulations. The components of the posterior covariance matrix of $\hat{\beta}$ were estimated to be $\text{Var}(\hat{\beta}_1) = 1.12$,

$$\text{Cov}(\hat{\beta}_1, \hat{\beta}_2) = 3.92, \text{ and } \text{Var}(\hat{\beta}_2) = 32.76.$$

Contour plots generally provide a better approach to displaying three-dimensional continuous data than the three-dimensional hidden-line plots. The un-normalized posterior was estimated at a 100 by 100 grid: $(\beta_1, \beta_2) \in [-5, 8] \times [-5, 35]$ and contour lines of the posterior surface were drawn at levels 0.922, 0.815, 0.701, 0.4, 0.1, 0.01, and 0.005 around the value at the mode. 1000 samples from the joint posterior of β_1 and β_2 were subsequently plotted on top of the contour plot as shown in Figure 2 (R code in appendix C). It can also be seen from this graph that the posterior mode is roughly equal to the ML estimate as expected under non-informative prior. However, the Bayesian approach allows for an effective handling of uncertainty through the posterior distribution. This is particularly important when it comes to predictions and risk assessment where a suitable accommodation of uncertainty is crucial.

As already pointed out, $\varphi = LD50$, as a function of the parameters, is defined by $\varphi = \varphi(\beta_1, \beta_2) = -\beta_1 / \beta_2, (\beta_2 \neq 0)$. A sample from the posterior distribution, $p(\varphi | y)$, of $LD50$ is straightforwardly obtained from the joint posterior of β , and an approximate $100 \times (1 - \alpha)\%$ credibility interval for φ is determined by the $\alpha/2$ and $(1 - \alpha/2)$ percentiles of the simulated $p(\varphi | y)$. For the bioassay data, the posterior mean and an approximate 95% credible interval for φ (on the log-scale) were respectively -0.101 and [-0.280, 0.091]. Figure 3 displays a histogram of the posterior distribution $p(\varphi | y)$.

4. Conclusions

In this paper we have discussed the Bayesian analysis of binary response regression using MCMC, more specifically the Metropolis sampler, for posterior simulation. We illustrated the methodology with real-world data from a bioassay experiment. The results were compared across different methods of posterior approximation and compared to their maximum likelihood counterparts. It is worth emphasizing that the bioassay dataset analyzed here was selected solely for illustration. There were only 5 replicates by level of dose, which resulted in low estimation precision as reflected by the large standard errors of the estimates.

In biological control, pest organisms may evolve over time with some characteristics that allow them to buffer the effect of say, pesticides or insecticides. Sequential replication over specific time-periods is necessary in order to track possible evolution of the dose-response relationship. This can be done by including random effects for different time periods. Combining link functions and exponential family variation with random effects leads to the cutting edge generalized linear mixed models (GLMMs) (e.g., Skrondal & Rabe-Hesketh 2004). GLMMs can easily be fitted with a Bayesian approach using MCMC.

References

- Casella, G., Berger, Roger L. (2002). *Statistical Inference*, 2nd edn. Duxbury Press, Belmont, CA.
- Chib, S., & Greenberg, E. (1995). Understanding the Metropolis-Hastings algorithm, *The American Statistician* 49, 327-335.

- Clark, J. S. (2005). Why environmental scientists are becoming Bayesians *Ecology Letters*, Vol. 8: 2-14.
- Dobson, A. J. (2002). An introduction to generalized linear models, 2nd edn. Chapman & Hall/CRC, London
- Englehardt, J. (2004). Predictive Bayesian dose-response assessment for appraising absolute health risk from available information Human and Ecological Risk Assessment, The Association for Environmental Health and Sciences, 10(1), 69–78.
- Englehardt, J., and Swartout, J. (2004). Predictive population dose-response assessment for *Cryptosporidium parvum*: Infection end point. *Journal of Toxicology and Environmental Health Part A: Current Issues*, 67(8–10), 651–666.
- Englehardt, J., and Swartout, J. (2006). “Predictive Bayesian Microbial Dose-Response Assessment Based on Suggested Self-Organization in Primary Illness Response: *C. Parvum*,” *Risk Analysis*, vol. 26, no. 2, pp. 543-554.
- French, N. P., Kelly, L., Jones, R. & Clancy, D. (2002). Dose-response relationships for foot and mouth disease in cattle and sheep *Epidemiology and Infection* 128: 325-332 Cambridge University Press.
- Garthwaite, P. H., Joliffe, I. T. & Jones, B. (2002). Statistical inference 2nd Edition Oxford University Press, Oxford, UK.
- Gelfand, A., & Smith, A. F. M. (1990). Sampling-based approaches to calculating marginal densities, *JASA* 85, 398-409.
- Gelman, A., Carlin, J. B., Stern, H. S. & Rubin, D. B. (2003). *Bayesian Data Analysis* Chapman & Hall/CRC.
- Gentle, J. E. (1998). *Numerical Linear Algebra for Applications in Statistics*. Springer-Verlag, Berlin.
- Gilks, W. R., Richardson, S. & Spiegelhalter, D. J., eds. (1996). *Markov Chain Monte Carlo in practice* Chapman and Hall, London, UK
- Hastings, W. K. (1970). Monte Carlo Sampling Methods Using Markov Chains and Their Applications *Biometrika*, 57(1):97-109.
- Lindsey, J. K. (1997). *Applying Generalized Linear Models* Springer-Verlag New York
- McCullagh, P. & Nelder, J. A. (1989). *Generalized Linear Models*. Chapman and Hall, New York.
- Metropolis, N., Rosenbluth, A. W., Rosenbluth, M. N, Teller, A. H., & Teller, E. (1953). Equations of State Calculations by Fast Computing Machines *Journal of Chemical Physics* 21(6):1087-1092.
- Metz, C. E., Tokars, R. P., Kronman, H. B, and Griem, M. L. (1982). Maximum likelihood estimation of dose-response parameters for therapeutic operating characteristic (TOC) analysis of carcinoma of the nasopharynx. *Int J Radiat Oncol Biol Phys*. 8 (7):1185-92.
- Mutshinda, C.M., Antai, I., O'Hara R.B. (2008). A probabilistic approach to exposure risk assessment. *Stochastic Environmental Research & Risk Assessment* 22: 441-449
- Skrondal, A. & Rabe-Hesketh, S. (2004). *Generalized latent variable modeling: Multilevel, longitudinal and structural equation models*. Boca Raton, FL: Chapman & Hall/CRC.
- Spiegelhalter, D., Thomas, A., Best, N. & Lunn, D. (2003). WinBUGS version 1.4 User manual <http://www.mrc-bsu.cam.ac.uk/bug>
- Teunis, P., Chappell, C., & Okhuysen, P. (2002). *Cryptosporidium* dose response studies: Variation between hosts. *Risk Analysis*, 22(3), 475–485.
- Thomas, A., O'Hara, R. B., Ligges, U., and Sturtz, S. (2006). Making BUGS Open. *R News* 6: 12-17.

Table 1. The bioassay data reproduced (with permission) from Gelman et al. (2003).

x : Dose (log g/ml)	y : Number of Deaths	n : Number of Animals
-0.86	0	5
-0.30	1	5
-0.05	3	5
0.73	5	5

y_i denotes the number of animals with positive response at dose x_i out of n_i .

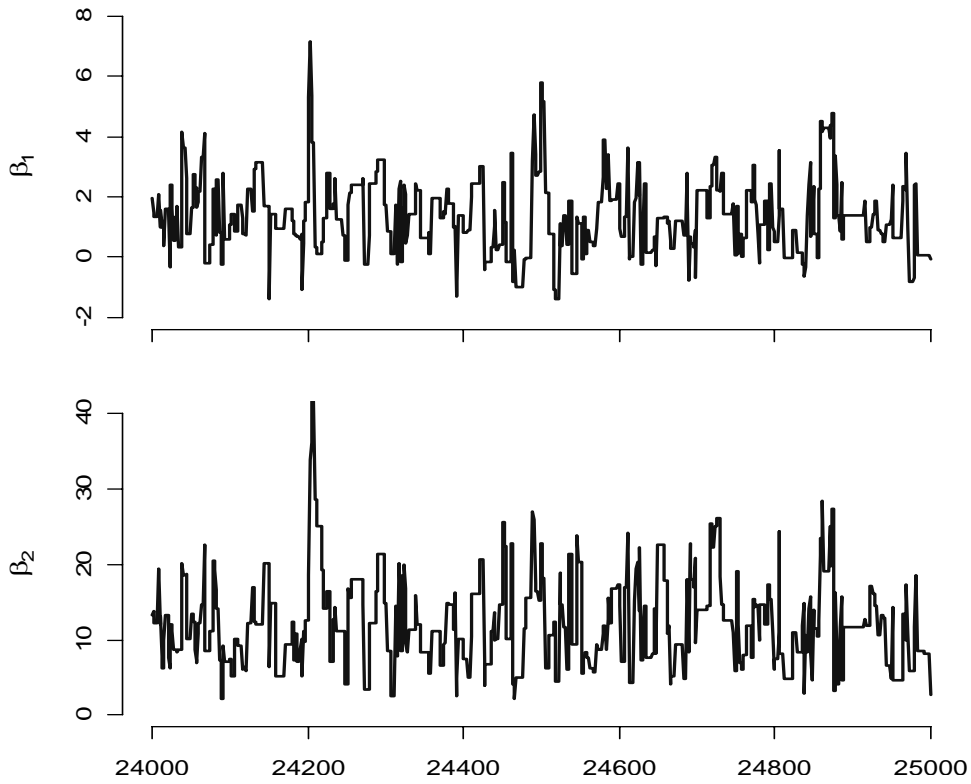


Figure 1. Trace plot of 1000 draws from the joint posterior of β_1 (top) and β_2 (bottom)

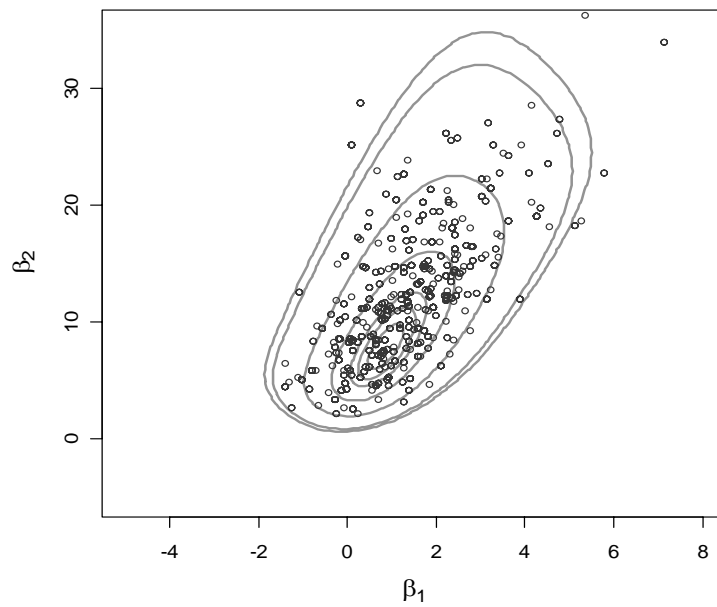


Figure 2. 1000 simulated samples from the joint the joint posterior of β_1 and β_2 plotted on top of a contour plot for the joint posterior density of the two parameters.

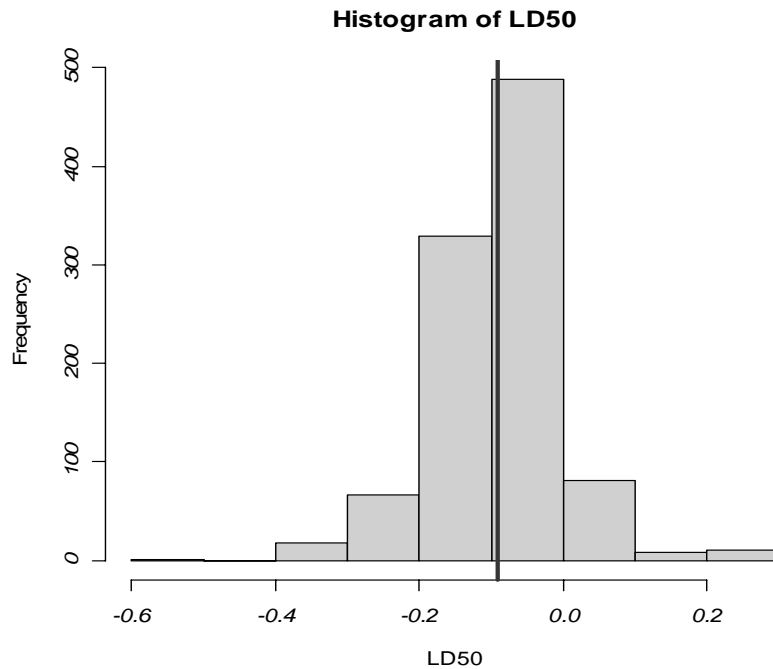


Figure 3. Histogram of simulated samples from the posterior of $LD50$. The solid vertical line is drawn at the posterior mean estimated to be -0.101 . A 95% credible interval for $LD50$ is $[-0.280, 0.091]$

Appendix A: R script for model fitting with the ML method

```
x<-c(-0.86, -0.3, -0.05, 0.73); n<-c(5, 5, 5, 5); y<-c(0, 1, 3, 5)
myfit<-glm(cbind(y, n-y)~x, family=binomial)
# Getting the covariance matrix of the parameter vector
C<-summary(myfit)$cov.unscaled
```

Appendix B: Annotated R script for the Metropolis sampler

```
###functions for loglik and (unnormalized) prior and posterior
loglik<-function(theta)
sum(y*(theta[1] + theta[2]*x - log(1 + exp(theta[1]+ theta[2]*x)))-(n-y)*log(1 + exp(theta[1] + theta[2]*x)))
logprior<-function(theta){
lp1<-dnorm(log=TRUE, theta[1], mean=0, sd=1000)
lp2<-dnorm(log=TRUE, theta[2], mean=0, sd=1000)
lp1+lp2}
## function for (unnormalized) log-posterior
logpost<-function(theta)
loglik(theta)+logprior(theta)
```

```
#### Data
x<- c(-0.86, -0.3, -0.05, 0.73); n<-c(5,5,5,5); y<-c(0,1,3,5)
## ML cov matrix, C, and its Cholesky factor A
C<-matrix(c(1.038,3.546,3.546, 23.744),nrow=2, byrow=T)
A<-t(chol(C))
### Setting the number B of MCMC iterations
B=25000
beta<-matrix(0,nrow=B, ncol=2)
beta[1,]<-c(0.5, 6)####initializing beta
sigma<-2.0 ## setting the tuning factor
nacc<-0 ##initializing number of accepted proposals
for (b in 2:B){
current<-beta[b-1,]
###Generating a proposal state
proposal<-current + sigma*A%%rnorm(2)
log_alpha<- logpost(proposal)-logpost(current)#log of the MH test ratio
alpha<-exp(log_alpha) ### the MH test ratio
u<-runif(1)
### accept or reject, that is the question
if(u<alpha){beta[b,]<-proposal; nacc=nacc+1}
  else{beta[b,]<-current}
}
## Acceptance rate
acc_prob<-nacc/B; print(acc_prob)
```

Appendix C: R script for displayed plots

```
## Plotting (1000) samples from the posterior (Figure 1)
par(mfrow=c(2,1))
par(oma=c(0,0,0,0)); par(mar=c(2,4,1,1))
t<-24000:25000
plot(t,beta[24000:25000,1],type="l", ylab=expression(beta[1]), axes=F,cex.lab=1.2, col="blue",lwd=2, font.lab=3,
xlab= " ", ylim=c(-2,8))
axis(2, lwd=1) ; axis(1, labels=NA)
par(mfg=c(2,1))
plot(t,beta[24000:25000,2],type="l",ylab=expression(beta[2]), axes=F, ylim=c(0,40), cex.lab=1.2, font.lab=3,
col="blue", lwd=2)
axis(2, lwd=1) ; axis(1, lwd=1)

### Contour plot (Figure 2)
par(mfcol=c(1,1))
### Setting a grid for contour plot
grid1 = seq(-5,8,len=100); grid2 = seq(-5, 35,len=100)
postg<-matrix(0,nrow=length(grid1),ncol=length(grid2))
```

```
for(i in seq(along=grid1)){
  for(j in seq(along=grid2)){
# Computing the (unnormalized posterior) over the grid
    postg[i,j]<-exp(logpost(c(grid1[i], grid2[j])))
  }
}
maxp<-max(postg)
lev<-c(0.922, 0.815, 0.701, 0.4, 0.1, 0.01, 0.005)*maxp
contour(grid1, grid2, postg, levels=lev, col=3, drawlabels=F, lwd=2, xlab=expression(beta[1]),ylab=expression(beta[2]),
cex.lab=1.3)
points(beta[24000:25000,1],beta[24000:25000,2], col=2)

## Histogram for LD50 (Figure 3)
LD50<- -beta[24000:25000,1]/ beta[24000:25000,2]
hist(LD50, bg="grey", col="lightblue", xlab="LD50",
font=3)
abline(v=mean(LD50),col=2,lwd=3)
-----
```



Two-Stage Engine Mapping for the Calibration of Carbon Monoxide Emission

Recep Kozan

Sakarya University, Faculty of Engineering,

Esentepe Kampüsü, 54187, Adapazarı-Turkey

Tel: 90-262-311-4351 E-mail: kazan@sakarya.edu.tr

Mersin Gokce (Corresponding author)

Faculty of Engineering, Sakarya University

Esentepe Kampüsü, 54187, Adapazarı-Turkey

Tel: 90-262-311-4351 E-mail: mersingokce@yahoo.com

Abstract

The calibration of a model's parameters due to desired objectives is the main definition of model-based calibration. The calibration of a diesel engine's two-stage model to get minimum carbon monoxide (CO) emission is described in this paper.

The data used in this study is collected in an engine test bench which can measure CO emission of the engine for different cam angle, engine speed and torque values. The different two-stage models are created by different local and global model functions. The best model among these models is chosen by statistical parameters.

Afterwards, this model is used for the calibration. The optimization of cam angle to minimize CO emissions is described. At the end of the calibration, the look-up table can be filled up with optimum cam angle values to be used in an electronic control unit of a diesel engine (ECU).

Keywords: Engine mapping, Two-stage modelling, Calibration

1. Introduction

Engine mapping is the process of modelling engine behaviour as a function of adjustable engine parameters. A primary application of engine mapping is the calibration of electronic engine controllers used to optimize the fuel efficiency of the engine subject to legislative limits on the emission of exhaust gases (Holliday T., Lawrence A.J., Davis T.P., 1998).

Engine maps consisting of three- dimensional contour plots of engine performance parameters such as break specific fuel consumption (bsfc) in the engine speed- break mean effective pressure (bmep) plane give a large amount of information in a very concise manner (Darda M., Sable A., Sastry G.V.J.).

The objective of this study is calibrating the diesel engine's cam angle for different operating conditions to get minimum CO emission by using the engine mappings created by two-stage modelling method with the help of model-based calibration toolbox which is supported by MATLAB. The cam angle term is used as the start of fuel injection according to the position of No:1 piston in the cylinder.

Model-based calibration refers to the process of using modern design of experiments, statistical modelling and optimization techniques and tools to define a methodology for efficiently producing high quality calibrations for complex engine applications, and model-based calibration provides a way to break down the calibration process into manageable subtasks(Sampson D.J.M., Sheridan L.A.D.). Including these advantages, the model-based calibration toolbox in MATLAB allows extracting calibrations directly from the models, and makes analysis possible without taking extra time (Maloney P., 2003).

2. Two-Stage Modelling

Using large polynomials for engine modelling causes the interpretation of the fitted model (Holliday T. 1995), and the number of parameters is too much which increases both the time and the cost for the tests, and it is also not so easy to extend the model, because of the difficulty to figure out how to add extra parameters (Esenturk E., 2004).

These problems started a new approach to engine modelling which is called two-stage modelling because of the nature of data collecting. This new approach improves the accuracy of the model, takes account of variability in the data, and

easily identifies the outliers (Sameer M.P., Maloney P., 2003)(Dr.Morton T.M. 2004). The previous studies about two-stage modelling are described in details in reference (Kazan R., Taymaz I., Gokce M.).

The cam angle is swept from maximum to minimum values for two-stage modelling, while the engine speed, torque, and vs. are fixed within each test group and CO emission is recorded for each test group after enough time is given for the stabilization of the diesel engine. The specification of the diesel engine, which is used for this study, is presented at Table-1.

The local models are formed independently for each test group, and then global model is constructed by these local models. That is why this approach of modelling is called two-stage modelling. Once the global model has been estimated it can be used to calculate the local models' parameters for any engine speed and torque.

There are different functions for both local and global model in the model-based calibration toolbox, which can be chosen by the user.

The algorithm of two-stage modelling in the toolbox is presented in Fig.1. In this figure, ' S (degree)' stands for cam angle which is the local input, and ' T (Nm)' stands for torque and ' N (rpm)' is engine speed which are the global inputs in this figure. Since the cam is swept from minimum to maximum within each test group, it shall be chosen as local input whereas engine torque and engine speed shall be global inputs, because they are fixed within each test group. It is not possible to choose the local and global inputs other than these parameters because of the capability of test facility.

The linear least square method is used to form both local and global models in the toolbox. It is assumed that the error follows a normal distribution with zero mean and constant variance. To clarify the modelling procedures in the toolbox, quadratic function for both local and global model is chosen and examined.

The mathematical definition of quadratic local model is presented below;

$$CO = \beta_1 + \beta_{s1} * S + \beta_{s2} * S^2 \quad (1)$$

where,

CO: CO emission,

S : cam angle,

β_1 , β_{s1} , and β_{s2} are the coefficients of the quadratic function.

In order to evaluate the values of β_1 , β_{s1} , and β_{s2} , the equation is transformed into matrix form as shown below.

$$A = (X' * X)^{-1} * (X' * Y) \quad (2)$$

where,

$X(:,1)$: identity vector

$X(:,2)$: normalized cam angle

$X(:,3)$: square of normalized cam angle

Y : measured CO emission for the chosen local model

A : β_1, β_{s1} , and β_{s2} are the coefficients vector for the chosen test group.

The number of the local models is equal to the number of measured test groups, which is 89 for this study. The fitted quadratic function that belongs to test group number 3 is displayed in Fig.2. The points in this figure show the measured CO emission for each cam angle while the curve is the fitted quadratic function.

After the coefficients of each local model are estimated, the next step will be to express these coefficients in terms of global inputs, which is the second stage of two-stage modelling. The coefficients of global model in terms of engine speed and torque are shown below

$$\beta_1 = a1 + b1 * N + c1 * T + d1 * N^2 + e1 * N * T + f1 * T^2 \quad (3)$$

$$\beta_{s1} = a2 + b2 * N + c2 * T + d2 * N^2 + e2 * N * T + f2 * T^2 \quad (4)$$

$$\beta_{s2} = a3 + b3 * N + c3 * T + d3 * N^2 + e3 * N * T + f3 * T^2 \quad (5)$$

The matrix solution of equation (3) by using linear least square method is displayed below;

$$B = (X1' * X1)^{-1} * (X1' * Y1) \quad (6)$$

where,

$X1$: calculated coefficients for each local model

$Y1$: vector of calculated β_1 value of equation (1) for each local model

B : vector of coefficient values of β_1 for global model

This solution method in equation (6) is identical for the other coefficients of global model. The predicted versus observed values for β_1 are plotted in Fig-3. In this figure, the points in circle are the outliers and these points can be removed to improve the model. Once these coefficients are found it is very easy and simple to find CO emission of the engine for any combination of engine speed and torque.

During the modelling, five different combinations of local and global models for CO emission are investigated, and it is decided that the combination of 'cubic' as local model and 'multiquadratic radial basis function (RBF)' as global model is the best model for CO emission by comparing two-stage root mean squared error (RMSE) and predicted sum of squares (PRESS) RMSE values of the models. The RMSE and PRESS RMSE values of the examined models are displayed in Table-2. The fitted curve for test group number 3 after two-stage modelling is shown in Fig-4. The curve with empty circles present fitted two-stage model, whereas the curve with dots is the fitted curve for local model.

The best-chosen model's surface response is displayed in Fig-5. This figure can be used just for general idea about the model, it does not provide any cam angle value corresponding to engine speed and torque.

RMSE is the basic parameter to figure out how close the model is fitted, and it estimates the average mismatch between each test, whereas PRESS RMSE measures the predictive of each point in the data if it was not included in modelling process.

The model fit is getting better as RMSE is getting closer to zero. On the other hand, considering RMSE as the only measure for the model fit can cause skipping overfit problem. That is why PRESS RMSE shall be also considered for deciding the model fit. If PRESS RMSE is much bigger than RMSE, then there is an over fitting problem.

3. Calibration

After the models are built up, the second step is the calibration of the models in order to get minimum CO emission by using 'CAGE' browser of the model-based calibration toolbox.

After CO emission model is imported to 'CAGE' browser, the size and the parameters of the look-up table are chosen. The x-axis of the look up table is engine speed whereas the y-axis is torque. The inside of the look-up table will be filled by the cam angle, which satisfies the minimum CO emission. The size of the look-up table is up to the engineer; however the axes of the look-up table must be the global inputs of the two-stage model.

The combination of engine speed and torque values depends on the size of the look-up table. CO emission for each combination is calculated for the cam angle sweep by using the global model equation evaluated during modelling, and displayed as graph in the toolbox as shown in Fig-6. Once the graph is drawn, the engineer can easily choose the minimum cam angle for CO emission. It can be easily observed in Fig-6 that the cam angle for minimum CO emission shall be -4.44° for 1193 rpm and 1213 Nm. The CO emission at this cam angle is evaluated as 8.40 ppm. The optimal cam angle for CO emission can be found for random 4 or 5 combinations, and the rest of the table can be extrapolated. But as it is stated in the toolbox manual [10], the result of extrapolation cannot always satisfy the desired value for each combination. That is why each point must be checked manually, which consumes time depending on the size of the look-up table.

4. Results and Discussions

The model-based calibration is performed for a diesel engine by using real data to minimize CO emission. The calibration process consists of mainly two steps. The first step is creating engine mapping of the diesel engine by two-stage modelling, and the second step is importing this model into 'CAGE' browser to find the optimum cam angle for minimum CO emission.

One of the experienced advantages of model-based calibration toolbox is the ability to observe and remove away the outliers in modelling stage to improve the model.

It is always necessary to consider both RMSE and PRESS RMSE values at the same time during the selection of best model. As it is observed, model 'D' has the smallest two-stage RMSE value, but there is a big difference between the model's two-stage RMSE and PRESS RMSE values. That is why model 'E' is chosen as the best model instead of model 'D'.

The calibration is very fast, simple, and needs no statistical information after the models are created which are the advantages of 'CAGE' browser. On the other hand, the results must be always checked after the calibration to be sure about it. Because it is experienced that the extrapolation does not always give the correct values.

The original cam angle of the diesel engine used in this study is -10° . The measured CO emission at this cam angle is 75 ppm for 1198 rpm and 1202 Nm. However the CO emission value evaluated after modelling is approximately 85 ppm for 1193rpm and 1213 Nm at this cam angle as shown in Fig-6.

Even though there is 10% percent error between the measured and modelled CO emission values, the decrease of CO emission can be easily observed by changing only the cam angle from -10° from -4.44° for the same engine speed and torque as presented in Fig-6

It will be very helpful to consider also specific fuel consumption during the calibration of exhaust emissions for a diesel engine for further studies.

References

- Darda M., Sable A., Sastry G.V.J., Chandra H., ‘Detailed Engine Mapping Using E-DACS for Thorough Performance Analysis, SAE Technical Paper Series, 950012
- Dr. Morton T.M., (2004). ‘Model-Based Optimal Calibration of A Dual Independent Variable Valve-Timing Engine’, *The Mathworks*, 2004.
- Esenturk E., (2004). ‘Improving Two-Stage Statistical Engine Mapping Models For The Performance Of Diesel Engine, MSc Thesis, Istanbul Technical University, April 2004.
- Holliday T., (1995). ‘The Design And Analysis of Engine Mapping Experiments: A Two-Stage Approach’, PhD Thesis, University of Birmingham, December 1995.
- Holliday T., Lawrence A.J., Davis T.P., (1998). ‘Engine-Mapping Experiments: A Two-Stage Regression Approach’, *Technometrics*, 40, Pg. 120-126, May 1998.
- Kazan R., Taymaz I., Gokce M., ‘The comparison of Two-Stage and One-Stage Engine Mapping, *European Journal of Scientific Research*, Vol.20, No 1, pp 24-36
- Maloney P., (2003). ‘Overview Of Empirical And Analytic Calibration Processes’, *The Mathworks*, June 24, 2003.
- Model Browser User’s Guide, Model-Based Calibration Toolbox, MATLAB
- Sameer M.P., Maloney P., (2003). ‘Overview of Empirical And Analytic Calibration Processes’, *The Mathworks*, August 2003.
- Sampson D.J.M., Sheridan L.A.D., ‘Engine Calibration: A Model-Based Approach’

Table 1. The specification of the diesel engine

Cylinder Number	10
Cylinder Inner Diameter	165 mm
Stroke	175 mm
Compression Ratio	1:18 – 1:19.5
Maximum Power	2200 rpm, 610 KW (830 HP)
Maximum Engine Speed	2400 rpm without load

Table 2. The statistics of the investigated models

Model	Local Model	Global Model	Local RMSE	Two-stage RMSE	PRESS RMSE
A	Quadratic	Quadratic	47.3107	40.0458	41.7179
B	Cubic	Quadratic	43.5171	38.2866	40.7443
C	Cubic	Cubic	43.5171	33.4403	36.9629
D	Cubic	Cubic-RBF	43.5171	28.6917	39.3304
E	Cubic	RBF	43.5171	33.2511	35.9234

Table Caption

Table 1. The specification of the diesel engine

Table 2. The statistics of the investigated models

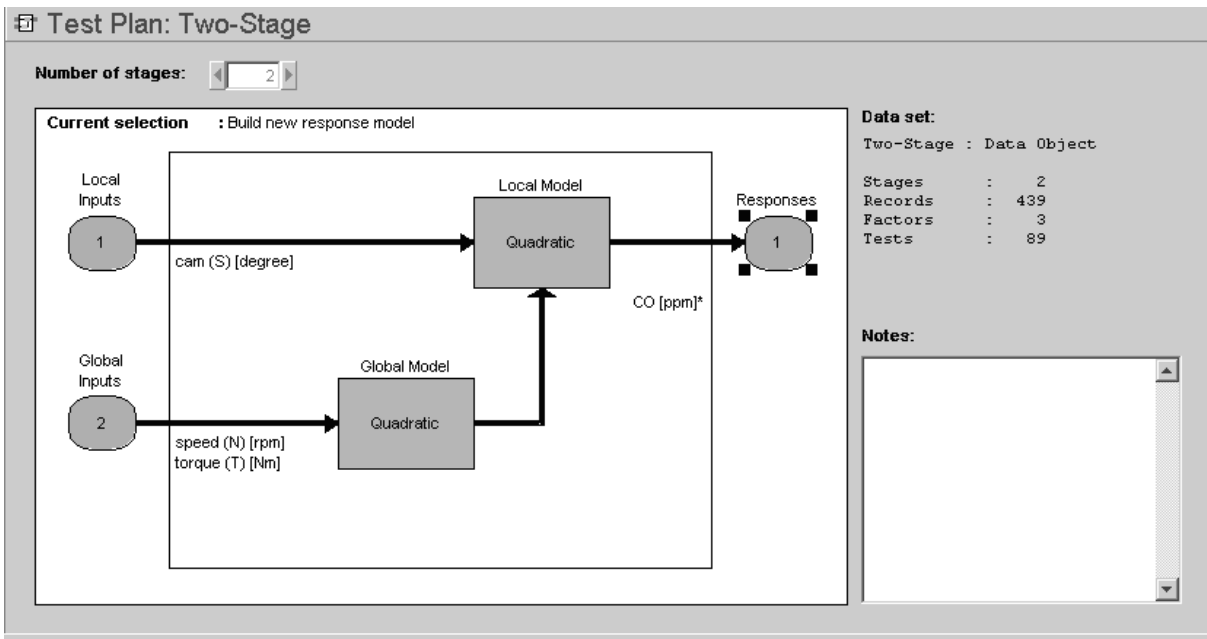


Figure 1. The algorithm for two-stage modelling

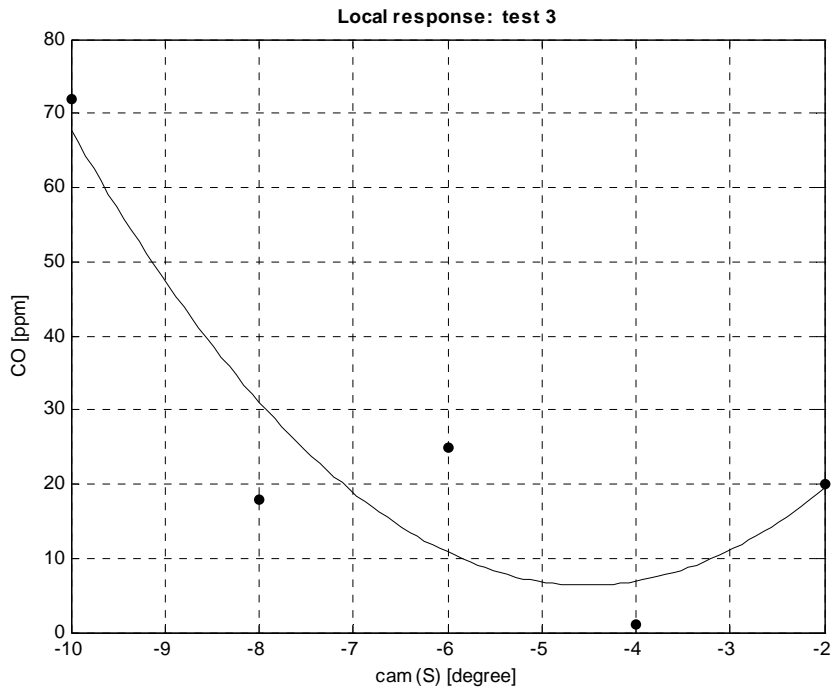


Figure 2. The fitted local quadratic function for test no:3

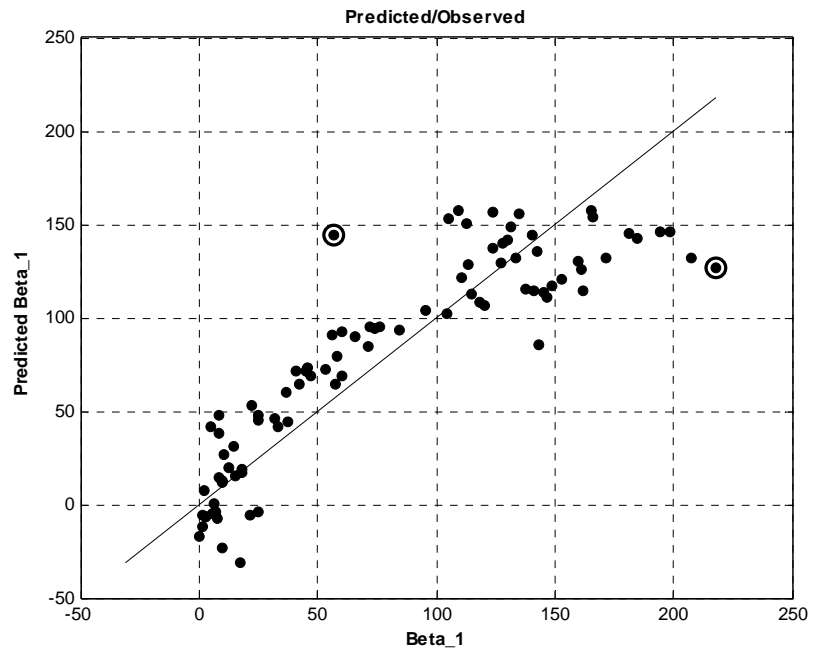


Figure 3. The predicted versus observed values of 'beta_1

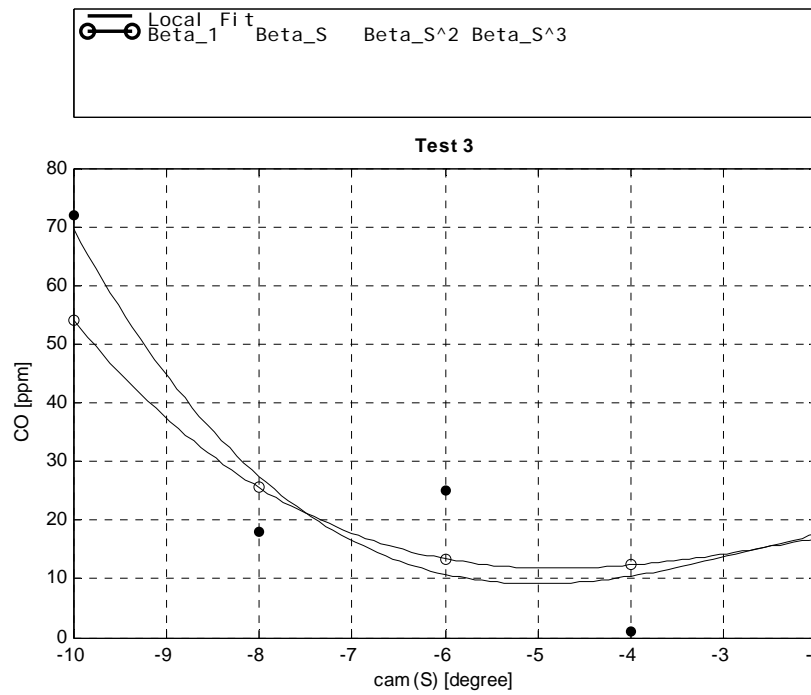


Figure 4. Two-stage modelling of test no: 3

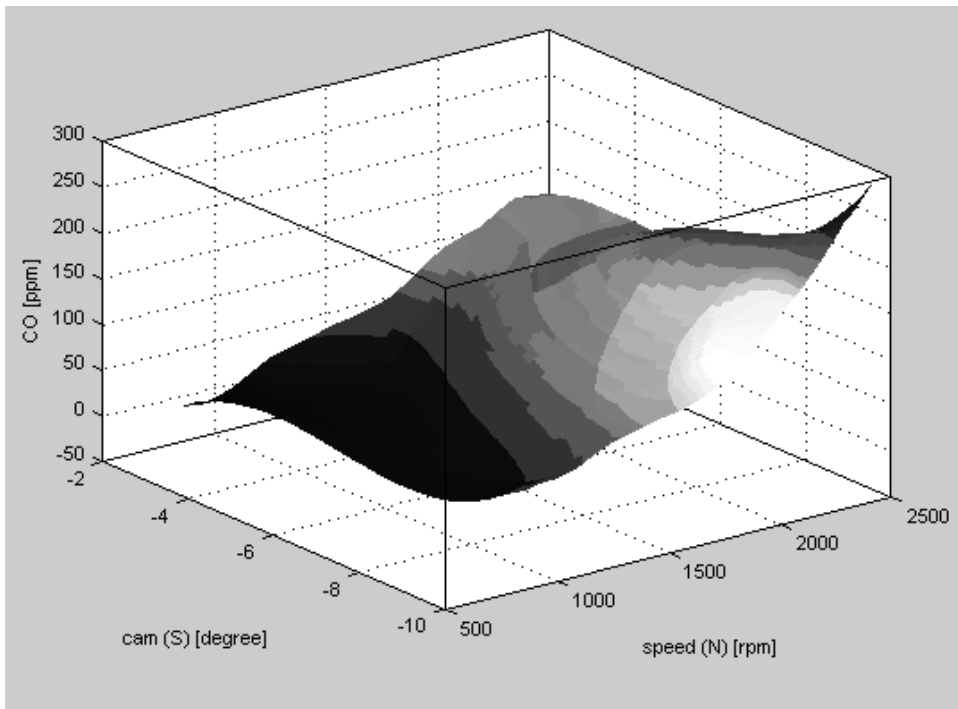


Figure 5. The response surface of the best-chosen model

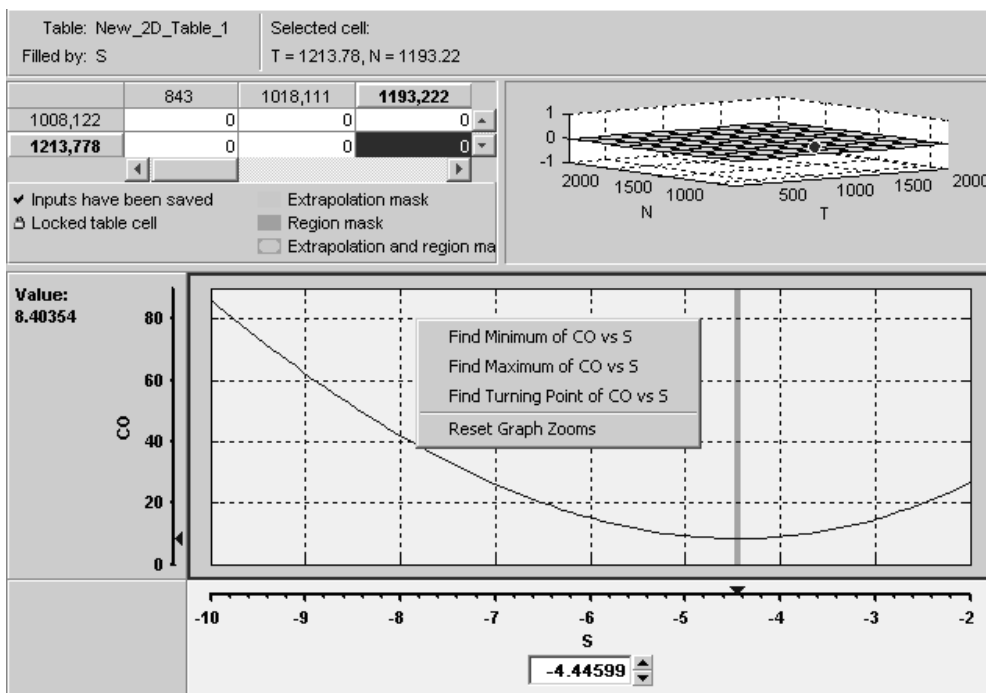


Figure 6. The calibration for CO emission

Figure Caption

- Figure 1. The algorithm for two-stage modelling
- Figure 2. The fitted local quadratic function for test no:3
- Figure 3. The predicted versus observed values of 'beta_1
- Figure 4. Two-stage modelling of test no: 3
- Figure 5. The response surface of the best-chosen model
- Figure 6. The calibration for CO emission



The Statistics Properties of Orthogonal Coherent State

Interacting with Two-level Atom

Jingqiu Chen (Corresponding author)

Institute of Optoelectronics Science and Engineering

Huazhong University of Science and Technology

Wuhan 430074, China

College of Physics Science and Technology

Shenzhen University

Guangdong 518060, China

E-mail: chenjq@szu.edu.cn

Qiao Gu

International Institute of Biophysics

Kaiserslautern100004, Germany

Wenda Peng

Institute of Optoelectronics, Shenzhen University

Guangdong 518060, China

Abstract

In this paper, the statistics properties of the statistics properties of orthogonal coherent state Interacting with two-level atom have been discussed, the statistics properties of both atom and field have been discussed. A set of conclusion have been gotten that atom inversion exit the collapse, calm, revival and chaotic behavior. The filed exit several unclassical effect: Sub-poisson photon distribution, Antibunching effect and $(\Delta x)^2$ squeezing effect.

Keywords: Orthogonal coherent state, Antibunching effect, Sub-poisson photon distribution, Squeezing effect

1. Introduction

Jayness-Cummings model(JCM)(F.W.CUMMINGS, 1965) has been studied many times because the relatively realistic way that it represents the quantum physics of a resonant interact ion .It is the simplest fully quantized model of quantum optics, quantum electronics, and resonance physics .From this model one hopes to know more properties of single mode filed interaction with a two level atom. For example, the coherent–state Jaynes-cummings model has been studied by J.H.Eberly, *et al* (J.H.Eberly, N.B.Narozhny And J.J.Sanchez-Mondragon, 1980).a set of equations characterizing the Jaynes-Cummings model ,which can be used to describe the dynamic and statistical aspect of the system ,have presented by Qiao.Gu(QIAO QU, 2003).

In general, when people study the statistics properties of JCM ,both atom and field should be discussed.

(1)The atomic inversion is given by expectation value of atomic inversion operator σ_z . $\langle \sigma_z \rangle$ which its scale between -1 and +1 represents the degree of excitation of a two-level system.

$$\langle \sigma_z \rangle = \begin{cases} = -1 & \text{(downer level)} \\ = 1 & \text{(upper level)} \end{cases} \quad (1.1)$$

(2) Squeezed characteristic statistics

Based on the definition the quadrature operators x and p

$$x = a^+ + a \quad (1.2a)$$

$$p = i(a^+ - a) \quad (1.2b)$$

The fluctuations of the radiation field are represented by (QIAO GU, J.ZHANG, 1989).

$$\left(\frac{(\Delta x)^2}{(\Delta p)^2} \right) = 1 + 2\langle a^\dagger a \rangle \pm 2\text{Re}\langle a^2 \rangle - 4 \left(\frac{\text{Re}^2\langle a \rangle}{\text{Im}^2\langle a \rangle} \right) \tag{1.3}$$

If $(\Delta x)^2$ or $(\Delta p)^2 < 1$, the field has squeezed effect, which is an unclassical effect.

(3) Photon statistical properties.

The photon statistical properties of the field if characterized by the Mandel factor can be written by

$$Q = \frac{(\Delta N)^2 - \langle N \rangle}{\langle N \rangle} \tag{1.4}$$

where $(\Delta N)^2 = \langle N^2 \rangle - \langle N \rangle^2$, $\langle N \rangle = \langle a^\dagger a \rangle$.

$$Q = \begin{cases} > 0 & \text{(super - poisson)} \\ = 0 & \text{(non - poisson)} \\ < 0 & \text{(sub - poisson)} \end{cases} \tag{1.5}$$

Sub-poisson is an unclassical effect.

(4) Bunching characteristic statistics.

The Second-order Coherence degree is defined below:

$$g^2(0) = \frac{\langle N^2 \rangle - \langle N \rangle^2}{\langle N \rangle^2} \tag{1.6}$$

$$g^2_{(0)} = \begin{cases} > 1 & \text{(bunching photon)} \\ = 1 & \text{(coherent state photon)} \\ < 1 & \text{(antibunching photon)} \end{cases} \tag{1.7}$$

Antibunching -effect is unclassical effect.

The property of the coherent state and the squeezing state field has been discussed (QIAO QU, 2003). The Orthogonal Coherent state (PENG SHI AN, GUO GUANG CAN, 1990) interacting two-level atom has never been reported. We will discuss its statistical properties.

The arrangement of this paper is as follows. We first introduced general solution of the Jaynes-Cummings Model (QIAO QU, 2003), then we discussed the statistical properties of the orthogonal coherent state interacting with two-level atom

2. General Solution of the Jaynes-Cummings Model

A two-level atom description is valid in Fig.1. if the two atomic levels involved are resonant or nearly resonant with driving field, while all other levels are highly detuned.

The two-level atom is characterized by the ground state $|b\rangle$ and an excited state $|a\rangle$.

The Hamiltonian system of Jaynes-Cummings model is

$$H = \hbar\omega a^\dagger a + \frac{1}{2}\hbar\omega_0\sigma_z + \hbar g(a\sigma^+ + a^\dagger\sigma^-) \tag{2.1}$$

where a and a^\dagger are annihilation and creation operators of the field mode, σ_z is the atomic inversion operator and σ^\pm are the atomic raising and lowering operators. ω and ω_0 are the frequencies of the field mode and of the two level atom, respectively, g is a coupling constant, and \hbar is Planck's constant divided by 2π .

where

$$\sigma_z = \sigma^+ \sigma - \sigma \sigma^+ \tag{2.2a}$$

$$\sigma = |b\rangle\langle a| \tag{2.2b}$$

$$\sigma^+ = |a\rangle\langle b| \tag{2.2c}$$

$$\sigma\sigma^+ = |b\rangle\langle b| \tag{2.2d}$$

$$\sigma^+\sigma = |a\rangle\langle a| \tag{2.2e}$$

We can solve the eigenequation of H :

$$H|\phi\rangle = E|\phi\rangle \tag{2.3}$$

where E and $|\phi\rangle$ represent the eigenvalue and the corresponding eigenstate. We assume that $|\phi\rangle$ be written as a linear combination of the states $|n, a\rangle$ and $|n+1, b\rangle$, in the form

$$|\phi\rangle = A|n, a\rangle + B|n+1, b\rangle \tag{2.4}$$

Where $|n, a\rangle$ corresponds to n photons in the field atom at the upper state $|a\rangle$, and $|n+1, b\rangle$ corresponds to $n+1$ photons in the field with atom at the downer $|b\rangle$ state. A and B are the probability amplitudes of finding the system in the states $|n, a\rangle$ and $|n+1, b\rangle$ respectively, we obtain

$$[\hbar\omega n + \frac{1}{2}\hbar\omega_0 - E]A + \hbar g\sqrt{n+1}B = 0 \tag{2.5 a}$$

$$[\hbar\omega(n+1) - \frac{1}{2}\hbar\omega_0 - E]B + \hbar g\sqrt{n+1}A = 0 \tag{2.5 b}$$

Eq.(2.5) display a set of the linear and homogeneous equations on A and B , and the necessary and sufficient condition for occurring of the non-zero solution is that the coefficient determinant is equal to zero, its results is the eigenvalues

$$E^\pm = \hbar[\omega(n + \frac{1}{2}) \pm \Omega_n] \tag{2.6a}$$

where

$$\Omega_n = \sqrt{(\frac{\Delta}{2})^2 + g^2(n+1)} \tag{1.6b}$$

with $\Delta = \omega - \omega_0$ being the detuning. substituting (2.6) into (2.5) and using (2.4), we obtain the coefficients

$$A^+ = \sin \theta_n, B^+ = \cos \theta_n \tag{2.7}$$

$$A^- = \cos \theta_n, B^- = -\sin \theta_n \tag{2.8}$$

where θ_n is defined by

$$\tan 2\theta_n = \frac{g\sqrt{n+1}}{\Delta/2} \quad (0 \leq 2\theta_n \leq \pi) \tag{2.9}$$

We have then the eigenstates

$$|\phi_n^\pm\rangle = \begin{pmatrix} \sin \theta_n \\ \cos \theta_n \end{pmatrix} |n, a\rangle + \begin{pmatrix} \cos \theta_n \\ \sin \theta_n \end{pmatrix} |n+1, b\rangle \tag{2.10}$$

Which are usually called ‘‘dresses states’’. we observe that

$$\langle \phi_n^+ | \phi_n^- \rangle = 0 \tag{2.11 a}$$

$$\langle \phi_n^+ | \phi_n^+ \rangle = \langle \phi_n^- | \phi_n^- \rangle = 1 \tag{2.11 b}$$

There is another states that is not included, namely. no photon in the field with atom at the downer state

$$|\phi_g\rangle = |0, b\rangle \tag{2.12}$$

It is the lowest energy and is called ground state. The corresponding eigenvalue E_g is calculated from the eigenequation $H|\phi_g\rangle = E_g|\phi_g\rangle$, result in

$$E_g = -\frac{1}{2}\hbar\omega_0 \tag{2.13}$$

Each of the dressed states $|\phi_n^\pm\rangle$ is orthogonal to the ground state $|\phi_g\rangle$, and all of them are complete so that

$$\sum_{n=0}^{\infty} (|\phi_n^+\rangle\langle\phi_n^+| + |\phi_n^-\rangle\langle\phi_n^-|) + |\phi_g\rangle\langle\phi_g| = 1 \tag{2.14}$$

We now consider an arbitrary field-atom system described by a time dependent state vector

$$\frac{\partial}{\partial t}|\Phi(t)\rangle = -\frac{i}{\hbar}H|\Phi(t)\rangle \tag{2.15}$$

Assume that the system is initially in state $|\Phi(0)\rangle$, which can be expanded by using the completeness relation (2.14)

$$|\Phi(0)\rangle = \sum_{n=0}^{\infty}(\alpha_n|\phi_n^+\rangle + \beta_n|\phi_n^-\rangle) + \gamma_g|\phi_g\rangle \tag{2.16}$$

where

$$\alpha_n = \langle\phi_n^+|\Phi(0)\rangle, \tag{2.17 a}$$

$$\beta_n = \langle\phi_n^-|\Phi(0)\rangle, \tag{2.17b}$$

$$\gamma_g = \langle\phi_g|\Phi(0)\rangle. \tag{2.17c}$$

(2.17) are the expanding coefficients ,which satisfy the normalized condition

$$\sum_{n=0}^{\infty}(|\alpha_n|^2 + |\beta_n|^2) + |\gamma_g|^2 = 1 \tag{2.18}$$

Since the Hamiltonian (2.1) does not contain the time explicitly, we can write the solution of the Schrödinger equation (2.15) as

$$|\Phi(t)\rangle = \exp(-\frac{i}{\hbar}Ht)|\Phi(0)\rangle \tag{2.19}$$

Substituting (2.16)into (2.19)and using the eigenequation(1.2),we have

$$|\Phi(t)\rangle = \sum_{n=0}^{\infty} \left(\begin{array}{l} \alpha_n |\phi_n^+\rangle \exp(-\frac{i}{\hbar} E_n^+ t) + \\ \beta_n |\phi_n^-\rangle \exp(-\frac{i}{\hbar} E_n^- t) \end{array} \right) + \gamma_g |\phi_g\rangle \exp(-\frac{i}{\hbar} E_g t) \tag{2.20}$$

Eq. (2.20) displays a general solution [5]of the Jaynes_Cummings model in terms of the dressed states $|\phi_n^\pm\rangle$ and the ground state $|\phi_g\rangle$.

3. Orthogonal Coherent State Interact with Two-Level Atom

For convenient our work, we briefly review the orthogonal coherent state .the orthogonal coherent state is one of the eigenstates of the operator of square of annihilation a^2 (PENG SHI AN, GUO GUANG CAN, 1990).

Because coherent state $|\alpha\rangle$ and the $|\alpha\rangle$ are not orthogonal .So Peng Shi An *et al* (WILLIAM H.LOUISELLI, 1982) by use the Gram-Schmidt method, gained a new state $|\alpha_\perp\rangle$ which it is orthogonal to $|\alpha\rangle$.

So

$$|\alpha\rangle_\perp = \frac{-\exp(-|\alpha|^2)|\alpha\rangle + \exp(|\alpha|^2)|-\alpha\rangle}{2S^{1/2}C^{1/2}} \tag{3.1a}$$

$$S = \sinh|\alpha|^2, C = \cosh|\alpha|^2 \tag{3.1 b}$$

By representation of number state we can get that:

$$|\alpha_\perp\rangle = \frac{[-\exp(-\frac{3}{2}|\alpha|^2)\sum_{n=0}^{\infty}\frac{(\alpha)^n}{\sqrt{n!}} + \exp(\frac{1}{2}|\alpha|^2)\sum_{n=0}^{\infty}\frac{(-\alpha)^n}{\sqrt{n!}}]}{2S^{1/2}C^{1/2}}|n\rangle \tag{3.2}$$

We now consider a system with initial state that atom is in the upper level $|a\rangle$.and the field is orthogonal coherent state describing by (3.2).so the initial state can be written as:

$$|\Phi(0)\rangle = \sum_{n=0}^{\infty} p_n |n, a\rangle \tag{3.3}$$

where

$$p_n = \frac{[-\exp(-\frac{3}{2}|\alpha|^2) \frac{(\alpha)^n}{\sqrt{n!}} + \exp(\frac{1}{2}|\alpha|^2) \frac{(-\alpha)^n}{\sqrt{n!}}]}{2S^{1/2}C^{1/2}} \tag{3.4}$$

is the probability amplitude of finding n photons in thermal equilibrium state.

After expanding $|n, a\rangle$ in term of the dress states (2.10), (3.2) takes the form as (2.16) with the coefficients

$$\alpha_n = p_n \sin \theta_n, \beta_n = p_n \cos \theta_n, \gamma_n = 0. \tag{3.5}$$

Under the resonant condition, substitute (3.5) into (2.20) .we have wave function of the Orthogonal Coherent State interacting with the two level atom which can be represent as

$$|\Phi(t)\rangle = \sum_{n=0}^{\infty} \begin{pmatrix} p_n \sin \theta_n |\phi_n^+\rangle \exp(-\frac{i}{\hbar} E_n^+ t) + \\ p_n \cos \theta_n |\phi_n^-\rangle \exp(-\frac{i}{\hbar} E_n^- t) \end{pmatrix} \tag{3.6}$$

So we can get:

$$W(t) = \langle \sigma_z \rangle = \langle \Phi(t) | \sigma_z | \Phi(t) \rangle \tag{3.7}$$

Substitute (3.15) into (3.16), using (2.2).

We get the result (QIAO QU, 2003):

$$W(t) = \sum_{n=0}^{\infty} |p_n|^2 \cos(2\sqrt{n+1}gt), \tag{3.8}$$

As the same process, we can get:

$$\langle N \rangle = \langle a^+ a \rangle = \sum_{n=0}^{\infty} |p_n|^2 [n + \sin^2(\sqrt{n+1}gt)] \tag{3.9}$$

$$\begin{aligned} \langle N^2 \rangle &= \langle (a^+ a)^2 \rangle \\ &= \sum_{n=0}^{\infty} |p_n|^2 [n^2 + (2n+1)\sin^2(\sqrt{n+1}gt)] \end{aligned} \tag{3.10}$$

$$\begin{aligned} Q(t) &= \frac{(\Delta N)^2 - \langle N \rangle}{\langle N \rangle} \\ &= \frac{\sum_{n=0}^{\infty} |p_n|^2 [n^2 + (2n+1)\sin^2(\sqrt{n+1}gt)]}{\sum_{n=0}^{\infty} |p_n|^2 [n + \sin^2(\sqrt{n+1}gt)]} \\ &\quad - \sum_{n=0}^{\infty} |p_n|^2 [n + \sin 2(\sqrt{n+1}gt)] - 1. \end{aligned} \tag{3.11}$$

$$\begin{aligned} g_{(0)}^2(t) &= \frac{\langle N^2 \rangle - \langle N \rangle}{\langle N \rangle^2} \\ &= 1 - \frac{\sum_{n=0}^{\infty} |p_n|^2 [n + \sin^2(\sqrt{n+1}gt)]}{\sum_{n=0}^{\infty} |p_n|^2 [n^2 + (2n+1)\sin^2(\sqrt{n+1}gt)]} \end{aligned} \tag{3.12}$$

From (3), and deriving as the same method, we get:

$$\begin{aligned}
\left(\frac{(\Delta x)^2(t)}{(\Delta p)^2(t)} \right) &= 1 + 2 \sum_{n=0}^{\infty} |p_n|^2 [n + \sin^2(\sqrt{n+1}gt)] - \\
&\left\{ \left(\begin{array}{l} \text{Re} \\ \text{Im} \end{array} \right) \sum_{n=0}^{\infty} p_n^* p_{n+1} \left[\begin{array}{l} (\sqrt{n+1} + \sqrt{n+2}) \cos(\sqrt{n+1} - \sqrt{n+2})gt \\ + (\sqrt{n+1} - \sqrt{n+2}) \cos(\sqrt{n+1} + \sqrt{n+2})gt \end{array} \right] \right\}^2 \\
&\pm \text{Re} \sum_{n=0}^{\infty} p_n^* p_{n+2} \left[\begin{array}{l} (\sqrt{(n+1)(n+2)} + \sqrt{(n+2)(n+3)}) \cos(\sqrt{n+1} - \sqrt{n+3})gt \\ + (\sqrt{(n+1)(n+2)} - \sqrt{(n+2)(n+3)}) \cos(\sqrt{n+1} - \sqrt{n+2})gt \end{array} \right]
\end{aligned} \tag{3.13}$$

4. Discussing the results

We plot expression (3.8) of $W(t)$, show in Fig.2 ,Fig.3,

When $\alpha = 1$, it exhibits chaotic behaviour of the atom inversion .however ,when $\alpha = 3$,it exhibits an ordered behaviour, this is so-called the quantum ‘collapse and revival’(PENG SHI AN, GUO GUANG CAN, 1990),and it also exhibits chaotic behaviour after a longer time.

Display (3.11) of $Q(t)$,show in Fig.4

The time dependence of Mandel parameter is shown in Fig.4, where the collapse ,calms, revivals, and chaos occur again ,similarly to $W(t)$. we also found that there are main part of the data under zero, form(5),it imply that there exit a sub-Poisson photon statistics in the system.

Plot expression (3.12) of $g_{(0)}^2(t)$,show in Fig.5

The $g_{(0)}^2(t)$ of the system is shown in Fig.5, we found that there are different shape with vary α .We also simple calculate that $g_{(0)}^2(t)=0$.when $\alpha = 0$, or $\alpha \geq 5$.

From Fig.5, we know that $g_{(0)}^2 \leq 1$ for all time and for all α , from (1.7) we can get that there exit Antibunching effect in its system.

We plot expression (3.13)of $(\Delta x)^2$ and $(\Delta p)^2$,show in Fig.6 and Fig.7

From the Fig.6 show that: in first valley exit $(\Delta x)^2 \leq 1$. from this we can get that the fluctuation $(\Delta x)^2$ have squeezing effect .but it last a very little time .it is a unclassical effect.

But from Fig.7, we find that $(\Delta p)^2 \geq 1$ for all time, so there do not exit squeezing effect.

5. Conclusion

In our paper, we discussed the Orthogonal Coherent state interacting two-level atom, the statistics properties of both atom and field will be discussed. There are several results after we study:

5.1 Atom inversion exit the collapse, calm, revival and chaotic behaviour.

5.2 The field of the system have unclassical effect.

The photon distribution exit sub-Poisson statistics; there exists Antibunching effect .The fluctuation of $(\Delta x)^2$ have squeezing effect, at the mean time, the fluctuation of $(\Delta p)^2$ do not exit squeezing effect.

6. Acknowledgements

I am grateful to professor Gu Qiao, this work was supported by professor Gu Qiao.

References

- F.W.Cummings. (1965). *Phys.Rev.*140, A1051.
- J.H.Eerly, N.B.Narozhny and J.J.Sanchez-Mondragon. (1980). *Phys.Rev.lett.*44, 20.
- Peng Shi An, Guo Guang Can. (1990). Generated a None-Classical Filed by Orthogonal Symmetry method. *Science Report.* 1990(8):579~583.
- Qiao Gu, J.Zhang. (1989). A possible way for generating sub-poissonisn field,*Acta Optical Sinica* 9,478-480.
- Qiao Qu. (2003). *Radiation and Bioinformation*,BeiJing:Scince Press, 2003.10.
- Willam, H. Louisell, (1982). *Quantum statistical Properties of Radiation*. BeiJing:Scince Press,1982.9.

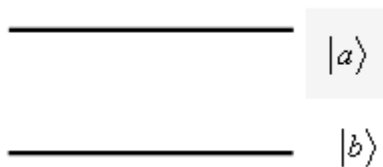


Figure 1. a two-level atom model

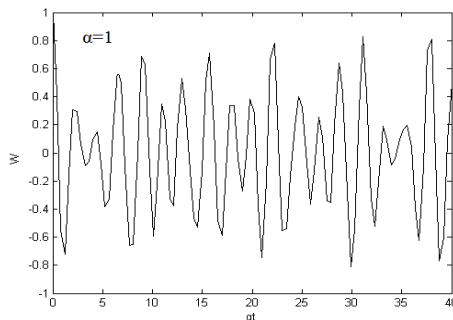


Figure 2. the chaotic behavior of $W(t)$ as $\alpha = 1$

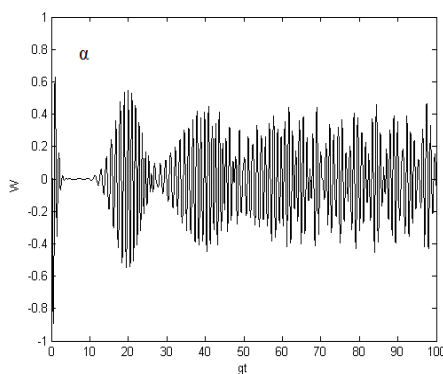


Figure 3. the collapse, calm, revival and chaotic behavior of $W(t)$ as $\alpha = 3$

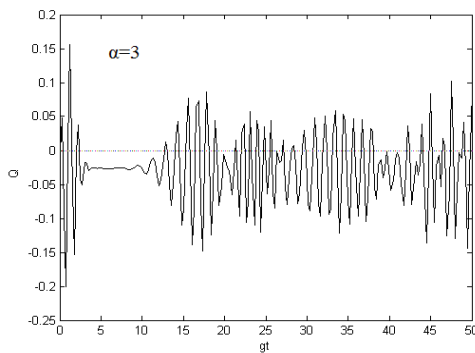


Figure 4. the collapse, calm, revival and chaotic behavior of $Q(t)$ as $\alpha = 3$

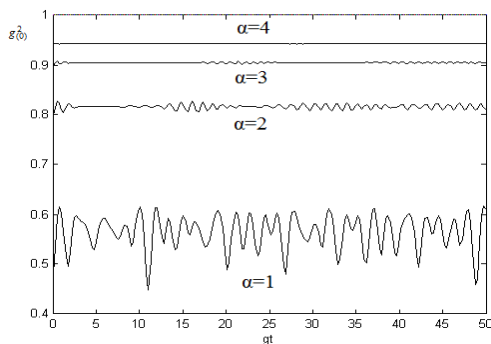


Figure 5. second order coherence degree when $\alpha = 1 \cdot 4$

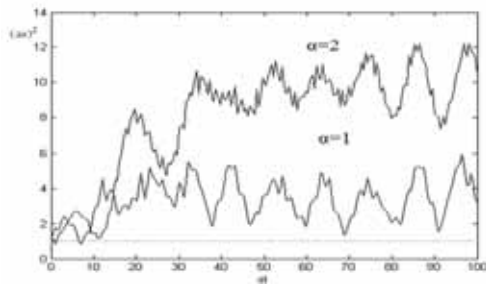


Figure. 6 $(\Delta x)^2$ when $\alpha = 1$ and 2

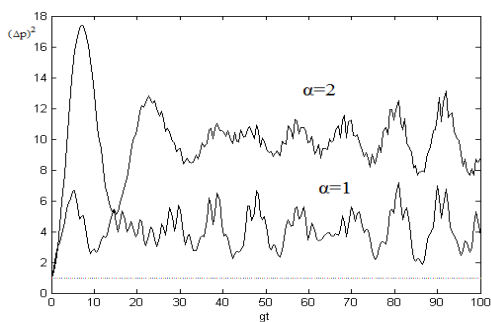


Figure 7. $(\Delta p)^2$ when $\alpha = 1$ and 2



The Isolation of α -viniferin, A Trimer Stilbene, from *Shorea ovalis* Blume

Noviany

Department of Chemistry, University of Lampung, Bandar Lampung 35145, Indonesia

E-mail: nv_any@yahoo.com

Sutopo Hadi (Corresponding author)

Department of Chemistry, University of Lampung, Bandar Lampung 35145, Indonesia

Tel: 62-813-69059733 E-mail: sutopohadi@unila.ac.id

Abstract

The derivative of oligomeric stilbene compound which was identified as α -viniferin, a trimer stilbene, was successfully isolated from acetone extract of stem bark of *Shorea ovalis* Blume (Dipterocarpaceae). The isolation of this trimer stilbene from this *Shorea* plant has never been done previously. The purification methods included extraction, partition, and fractionation with vacuum liquid chromatography and then followed by gravity column chromatography. The structure of the compound isolated was determined based on the analyses of physical data, UV and IR spectroscopies and compared to the standard compound of α -viniferin.

Keywords: α -viniferin, Dipterocarpaceae, *S. ovalis* Blume

1. Introduction

The human lives are always related to their surround environment including plants. Plants for human being are not only used as sources of food, clothes, or medicine but also used as a source of knowledge. It is predicted that in the world, there are about more than 250,000 of plant species, in which 60% of them are tropical plants. Of the whole plants, there was only 0.4 % which has been chemically researched, while most of them (99%) has never been explored their chemical content (Achmad et al., 1995). Indonesia as the second richest country, after Brazil, in the biological diversity is a leading country in the tropical forest. However this advantage has not been fully investigated, although the presence of the tropical forest as the natural resources of chemical substances is invaluable and potentially to be much more developed (Achmad, 1995)

One of the biological diversities of Indonesian plants is the family of Dipterocarpaceae which is widespread throughout Indonesia. The Dipterocarpaceae is a very large family comprising of 16 genera and about 600 species (Cronquist, 1981; Heyne, 1987). The two biggest genera of Dipterocarpaceae family are *Shorea* and *Dipterocarpus* having 150 and 75 species, respectively.

Dipterocarpaceae plant groups, locally known as Meranti, Keruing or Tengkawang, produce variety of compounds such as volatile oil, triterpenoid, flavonoid, arylpropanoid, and oligomeric resveratrol (Heyne, 1987; Sotheeswaran and Pasupathy, 1993). These plants are mainly growth in tropical areas. The chemical research on these plants has long been done (Dai et al., 1998; Ito et al., 2000; Noviany et al., 2002; Saraswathy, et al., 1992; Sultanbawa et al., 1987; Zheng et al., 1994), but for such big family plants, the chemistry of Dipterocarpaceae is relatively less known. This is because the initial research on Dipterocarpaceae was mainly focused on chemical compounds of their resins such as terpenoid, sesquiterpen and triterpen.

Since the finding of hopeaphenol, a polyphenol of oligomeric resveratrol, from two different species of Dipterocarpaceae, *i.e* *Hopea odorata* and *Balanocarpus heimii*, in the last two decades, the phytochemical research on Dipterocarpaceae has shifted rapidly. This is due to the fact that oligomeric resveratrol compounds are the main polyphenol which shows variety of important bioactivities, such as anti inflammation, antibacterial, antifungal, cytotoxicity, chemo preventive, hepatoprotective, and inhibit topoisomerase II, gastric ATPase and 5 α -reduktase reactions (Hakim, 2002).

Of the 17 *Shorea* species which have been researched on, about 11 of them have been mainly researched in Indonesia (Aminah et al., 2001; Aminah et al., 2002; Hakim, 2002; Muharini et al., 2001; Noviany, 2002; Noviany et al., 2002). From the previous researches carried out, the results showed that the phenolic compounds isolated were generally those

of oligomeric stilbenes. Based on this knowledge, the chemical research on *Shorea* genera in Indonesia which have not previously been done must be continued as they have high potential as sources of modern medicines. In this research, *Shorea ovalis* Blume is chosen, as the chemical contents of this species has not been previously reported.

2. Experiment

2.1 General

Melting points were determined on a Fisher Johns micro-melting point apparatus and are uncorrected. Vacuum liquid chromatography (VLC) was carried out using Merck Si-gel 60, TLC analysis on pre-coated Si-gel plates (Merck Kieselgel 60 F₂₅₄, 0.25 mm). The UV lamp of Spectroline, Model ENF-240 C/F was used to see the spot in TLC. UV and IR spectra were measured with Varian Cary 100 Conc. and Shimadzu FT-IR 8501 Scientific spectrophotometers respectively.

2.2 Plant Material

Samples of the stem bark of *Shorea ovalis* Blume were collected in April 2004 from Way Kambas National Park, East Lampung, Indonesia and were identified by the staff at the Herbarium Bogoriense, Research Centre for Biology, Indonesia Institute of Sciences Bogor, Indonesia and a voucher specimen has been deposited at the herbarium.

2.3 Extraction and Isolation

The stem bark which has been dried and ground (3 kg) was macerated with acetone for 3 x 24 hours. After the removal of acetone under reduced pressure, the gummy brown residue of acetone extract (80 g) was obtained. The acetone extract was dissolved in methanol then partitioned with *n*-hexane. Upon evaporation of the solvent, the methanol extract (50 g) as brown residue was obtained. The methanol extract was then again dissolved in acetone and fractioned twice using VLC (200 g, 7 cm x 10 cm) by increasing polarity (*n*-hexane, *n*-hexane-ethyl acetate, ethyl acetate, methanol) to give 26 fractions which were grouped into 8 major fractions by combining fractions with similar TLC profiles. The main fraction obtained by combining fraction 22-25 (9 g) was further fractioned with gravity column chromatography and was eluted with mixture of chloroform-ethyl acetate-methanol in increasing polarity. On repeated chromatographic purification, pale yellow crystalline (compound **A**, 8 mg) mp 231-233 °C was obtained. The TLC of this compound showed a single spot when it was eluted with three different solvent systems, *i.e.* *n*-hexane-acetone (1 : 1); chloroform : methanol (85 : 15) and methanol-dichloromethane (25 : 75) with R_f of 0.3, 0.5, and 0.8 respectively.

3. Results and Discussion

The isolated compound (**A**) was obtained as pale yellow crystalline (8 mg). The UV spectrum of this compound showed λ_{\max} (MeOH) (log ϵ): 204 (1.09), 226 (0.66), 285 (0.15) nm. Upon addition of NaOH (MeOH + NaOH) showed λ_{\max} (log ϵ): 209 (2.47), 250 (0.55), 295 (0.19) nm. The IR spectrum (in KBr) showed vibration bands on 3414, 2920, 1616, 1515, 1440, 1364, 1241, 1171, 1112, 996, and 831 cm⁻¹.

The UV spectrum (Figure 1) exhibited absorptions (λ_{\max} MeOH) (log ϵ) 204 (1.09), 226 (0.66), 285 (0.15) nm, which indicated a typical of phenolic chromophore (Mattivi et al., 1996). On addition of NaOH the bathochromic shift is not occurred. The IR spectrum (Figure 2) showed absorptions at 3414 cm⁻¹, 2920, 1616, 1515, 1440, 1364, 1241, 1171, 1112, 996, 831 cm⁻¹ and in the finger print area. The stretch vibration at 3414 cm⁻¹ is the typical of hydroxyl (OH) stretch, and vibration at 2920 cm⁻¹ is characteristic of aliphatic stretch, while absorptions at 1616, 1515, 1440, 1364, and 1241 cm⁻¹ are due to presence of aromatic group of **A** (Table 1), and adsorption at 831 cm⁻¹ is indication by the presence of 1,4-disubstituted benzene. The UV and IR showed a typical and characteristic of unconjugated phenolic derivative of oligomeric resveratrol (Mattivi et al., 1996).

The isolated compound **A** has similar spectroscopies data to that of compound which has previously been identified from some different genus of *Shorea*, thus the structure determination of the isolated compound **A** was done by comparing to the UV and IR data as shown in Table 1 and 2, respectively and by matching the UV and IR spectra as in Figure 1 and 2, respectively. To strengthen the structure determination of the compound **A**, the TLC spot of the isolated compound **A** was eluted with three different solvent systems *i.e.* *n*-hexane-acetone (1 : 1); chloroform : methanol (85 : 15) and methanol-dichloromethane (25 : 75) and the R_f results were compared with the R_f of the standard compound, α -viniferin, in which the results on the three different solvents showed the same R_f values, *i.e.* 0.3, 0.5, and 0.8 respectively (Aminah et al., 2001).

Based on the spectroscopies data above and the physical data in Table 3, the values obtained are similar to α -viniferin previously reported by Aminah et al. (2001), therefore it was suggested that the compound **A** is α -viniferin (Table 1, 2 and 3) with the molecule structure as shown in Figure 3. α -viniferin, a trimer stilbenoid, is oligomeric stilbene which is always almost present in all *Shorea* genus. Thus based on chemotaxonomy, *S. ovalis* Blume also produced oligomeric stilbene compound as expected like other species of *Shorea*.

The biological activity of the compound isolated (α -viniferin) has been tested against brine shrimp *Artemia salina* assay (Meyer et al., 1982) and the lethal concentration 50% (LC₅₀) was found to be 66.9 $\mu\text{g/ml}$. This oligoresveratrol has also been previously reported to have antifungal and anti inflammation activities (Ohyama et al., 1999).

4. Conclusion

A trimer stilbene, α -viniferin has successfully been isolated from *Shorea ovalis* Blume. Based on chemotaxonomy, *S. ovalis* Blume has also produced the oligomeric stilbene similar to other species of *Shorea*. This finding supports the botany taxonomy which shows the close family relation of *S. ovalis* with other *Shorea* genus and this report also provides new compound obtained in *S. ovalis* Blume. The chemical research on *S. ovalis* Blume is still on progress in order to find other oligomeric stilbenes which might present.

Acknowledgements

The authors would like to thank to The State Ministry for Research and Technology of Republic of Indonesia that provides fund for this project to be undertaken through Basic Science Research Grant Scheme 2004 (PRSD) with contract number of 30/SK/PKRM/II/2004. Thanks also go to Polmer Sinaga, S.Si. and Ardi Fanta Yuda who have helped us in the preparation of the samples. We are also grateful to the Herbarium Bogoriense Bogor, Indonesia, for the assistance in identification of the plant specimen.

References

- Achmad, S.A., Hakim, E.H., Juliawaty, L.D., Kasuma, S., Makmur, L., and Syah, Y.M. (1995). Eksplorasi Kimia Tumbuhan Hutan Tropis Indonesia, Prosiding Seminar Etnobotani dalam Kelompok Penelitian Kimia Bahan Alam, Publikasi dan Presentasi Ilmiah 1993-1995, Bandung. (Indonesian).
- Achmad, S.A. (1995). Tiga Periode dalam Revolusi Industri Bahan Kimia Alami, Ceramah Ilmiah, Seminar Nasional Industri Kimia Indonesia dalam Kelompok Penelitian Kimia Bahan Alam, Publikasi dan Presentasi Ilmiah 1993-1995, Bandung. (Indonesian).
- Aminah, N.S., Aimi, N., Hakim, E.H., Syah, Y.M., Makmur, L., Juliawaty, L.D., Kitajima, M., Mujahidin, D., Takayama, H. (2001). Oligomer stilbenoids: α -viniferin, Hopeaphenol, and Related Compounds from *Shorea seminis* V.S1. (Dipterocarpaceae), Padang Indonesia, *Abstr.* P A06. 77.
- Aminah, N.S., Achmad, S.A., Aimi, N., Ghisalberti, E.L., Hakim, E.H., Kitajima, M., Syah, Y.M. and Takayama, H. (2002). Diptoinonesin A, a new C-glucoside of α -viniferin from *Shorea seminis* (Dipterocarpaceae). *Fitoterapia*, 73 (6), 501-507.
- Cronquist, A. (1981). An Integrates System of Classification of Flowering Plants, Columbia Univ. Press., New York. 316-318.
- Dai, J.R., Hallock, Y.F., Cardellina, J.H.H., Boyd, M.R. (1998). HIV-Inhibitory and Cytotoxicity Oligostilbenes from the Leaves of *Hopea malibato*, *Journal of Natural Products*, 61, 351-353.
- Hakim, E.H. (2002). Oligostilbenoid dari Tumbuh-Tumbuhan Dipterocarpaceae, *Buletin of the Indonesia Society of Natural Products Chemistry*, 2(1), 1-19.
- Heyne, K. (1987). Tumbuhan Berguna Indonesia, Vol.II, Balai Kehutanan Indonesia, 1432. (Indonesian).
- Ito, T., Tanaka, T., Ido, Y., Nakaya, K., Iinuma, M., Riswan, R. (2000). Stilbenoids Isolated from Stem Bark of *Shorea hemsleyana*, *Chemistry and Pharmacy Bulletin*, 48(7), 1001-1005.
- Mattivi, F., Reneiro, F., (1996). Relationship between UV spectra and molecular structure of resveratrol oligomers, in Vercauteren, J., Cheze, C. Dumon, M.C., Weber J.F. (Eds). *Polyphenols Communication*. p.125-126.
- Meyer B.N., Mc Laughlin, J.L and Ferrigni, N.R. (1982). Brine Shrimp: a Convenient General Bioassay for Active Natural Plant Compounds, *Planta Medica*, 45, 31-34.
- Muharini, R., Hakim, E.H., Achmad, S.A., Aimi, N., Makmur, L., Syah, Y.M., Juliawaty, L.D., Kitajima, M., Mujahidin, D., Takayama, H. (2001). (-)- α -viniferin, a Trimer Stilbenoid and Related Compounds from *Shorea guiso* Blume. Third International Seminar on Tropical Rainforest Plants and Their Utilization for Development, Padang, Indonesia, *Abstr.*, P A12, 83.
- Noviany, (2002). Eksplorasi Senyawa Oligomer Stilbenoid dari Tumbuhan *Shorea multiflora* Burck, Thesis, Bandung Institute of Technology, Indonesia (Indonesian).
- Noviany, Hakim, E.H., Achmad, S.A., Aimi, N., Syah, Y.M., Juliawaty, L.D., Ghisalberti E.L., Choudhary I.M. (2002). Beberapa Oligomer Stilbenoid dari Tumbuhan *Shorea multiflora* Burck. *Jurnal Matematika dan Sains*, 125-132 (Indonesian).

Ohyama, M., Tanaka, T., Ito, T., Iinuma, M., Bastow, K.F., Lee, K-H. (1999) Antitumor Agents 200.1 Cytotoxicity of Naturally Occurring Resveratrol Oligomers and Their Acetate Derivatives, *Bioorganic Medical Chemistry Letters*, 9, 3057-3060.

Sotheeswaran, S. and Pasupathy, V. (1993). Distribution of Resveratrol Oligomer in Plants, *Phytochemistry*, 32, 1083-1092.

Sultanbawa, M.U.S., Surendrakumar, S., Bladon, P. (1987). Distichol, An Antibacterial Polyphenol from *Shorea disticha*, *Phytochemistry*, 26(3), 799-801.

Zheng, Z., Zhao, S., Deng, J., Zhao, H., Ye, W., and Wang, M. (1994). Triterpenes from Root Bark of *Shorea wangiashuea*. *Zhongguo Yaoke Daxue Xuebao*, 25(5), 262-264.

Table 1. The comparison of UV Spectra data between the compound isolated and standard α -viniferin

Isolated Compound		Standard α -viniferin	
λ_{max} . (MeOH)	λ_{max} . (NaOH+MeOH)	λ_{max} . (MeOH)	λ_{max} . (NaOH+MeOH)
204 nm	209 nm	206 nm	209 nm
226 nm	250 nm	266 nm	293 nm
285 nm	295 nm	342 nm	344 nm

Table 2. The comparison of IR spectra data between the isolated compound and standard α -viniferin

No.	Vibration	Isolated compound (cm^{-1})	Standard α -viniferin (cm^{-1})
1	OH Strech	3414	3387.2
2	-CH aliphatic	2920	-
3	C=C aromatic	1616,1515,1486,1364,1243	1616,1515,1440,1364,1241
4	1,4 disubstitution of benzene	831	834

Table 3. The comparison of physical data between the isolated compound and standard α -viniferin

Physical data	Isolated compound	Standard α -viniferin
Physical character	Pale yellow crystalline	Pale yellow crystalline
Melting point	231-233°C (decomposed)	230°C (decomposed)
$[\alpha]_{\text{D}}^{20}$ (0.1 M in MeOH)	-61°	-58°

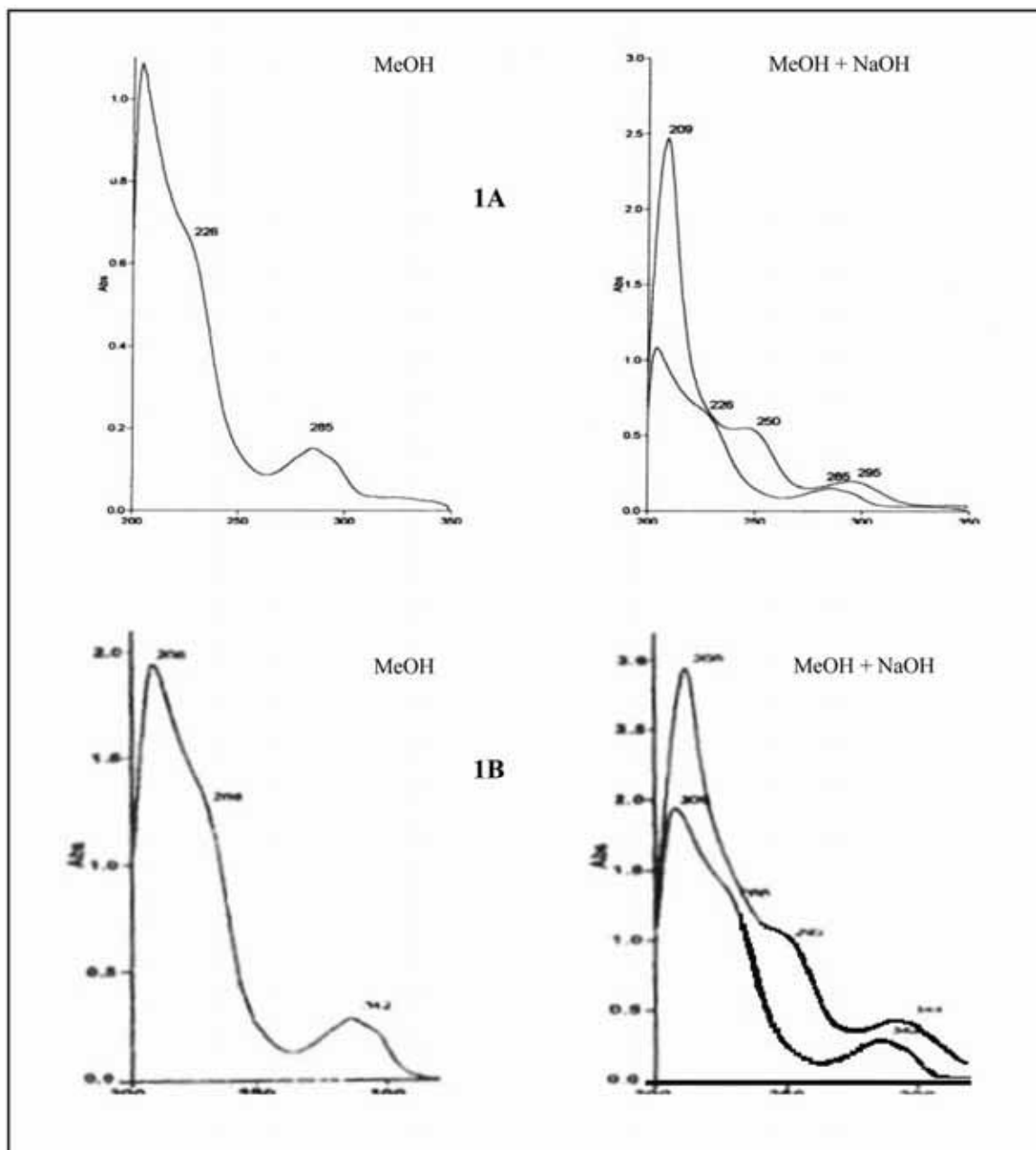


Figure 1. The comparison of UV Spectra between the isolated compound (1A) and standard α -viniferin (1B)

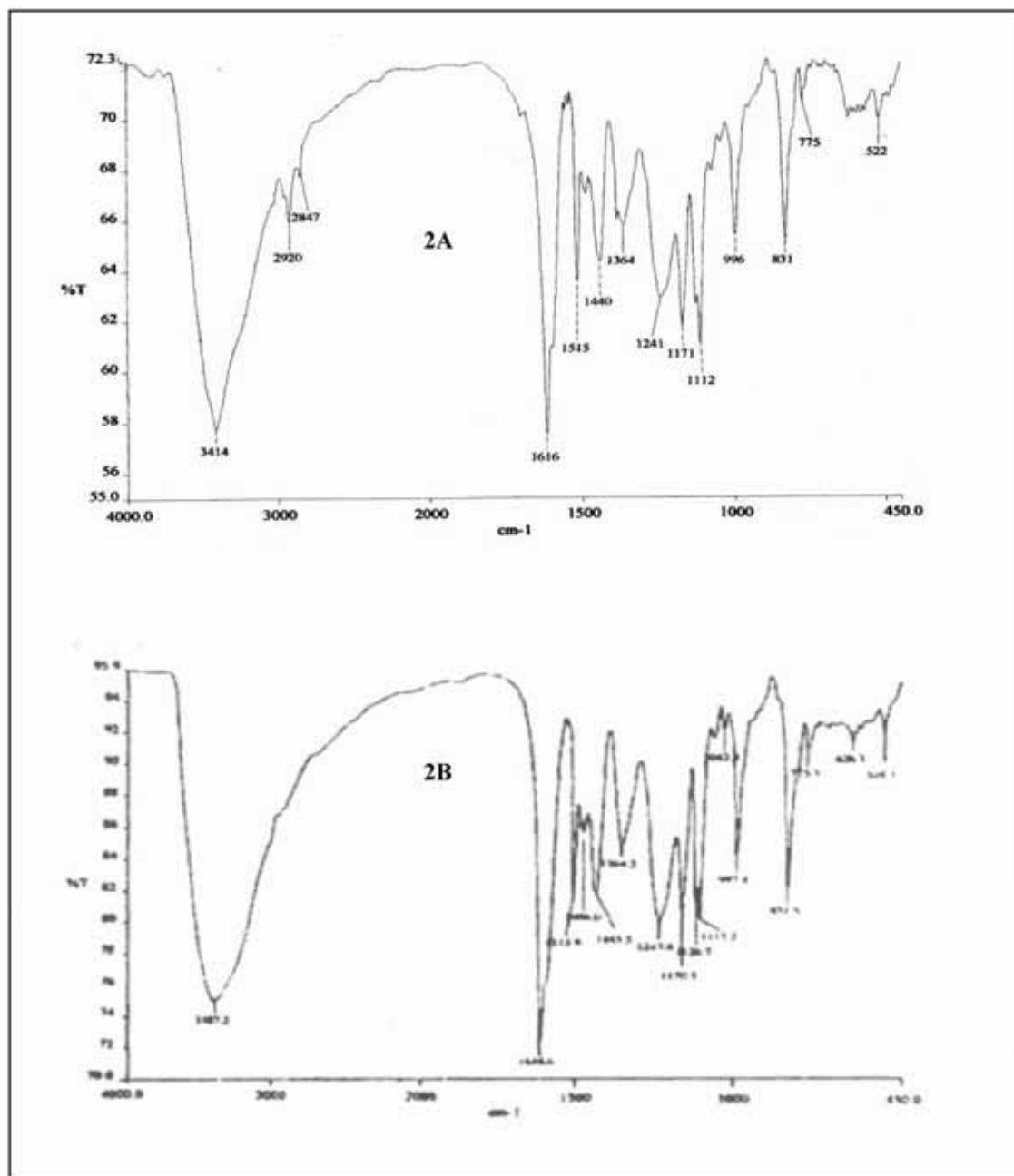


Figure 2. The comparison of IR spectra between the isolated compound (2A) and standard α -viniferin (2B)

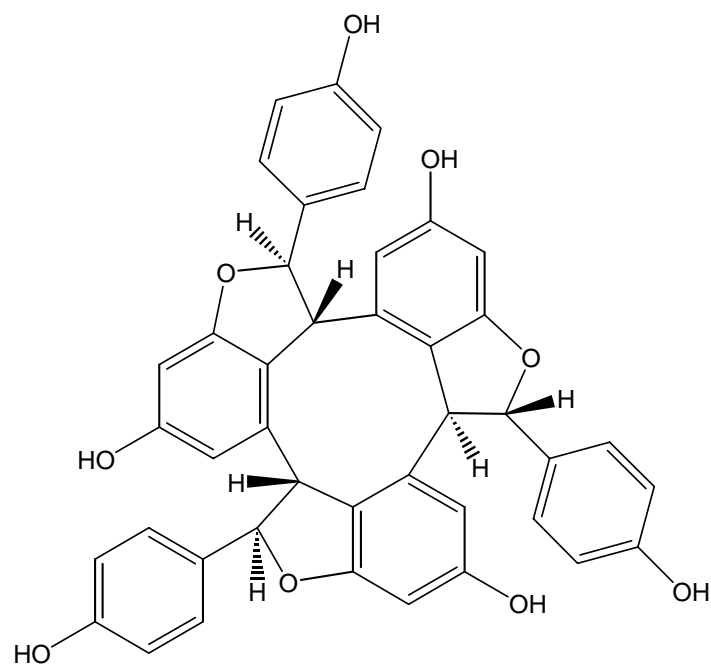


Figure 3. The molecule structure of α -viniferin



Fatigue Behaviour of Aluminum Alloy at Elevated Temperature

Farhad B. Bahaideen

School of Mechanical Engineering, Universiti Sains Malaysia

14300 Nibong Tebal, Penang, Malaysia

E-mail: farhadbilal62@yahoo.com

Ahmed M. Saleem

Technical College, Mosul, Iraq

E-mail: ah_ms1971@yahoo.com

Khaleed Hussain M.T (Corresponding Author)

School of Mechanical Engineering, Universiti Sains Malaysia

14300 Nibong Tebal, Penang, Malaysia

E-mail:Khalid_tan@rediffmail.com

Zaidi Mohd. RIPIN

School of Mechanical Engineering, Universiti Sains Malaysia

14300 Nibong Tebal, Penang, Malaysia

E-mail: mezaidi@eng.usm.my

Zainal arifin ahmad

School of Materials and Mineral Resources Engineering, Universiti Sains Malaysia

14300 Nibong Tebal, Penang, Malaysia

Zahurin Samad

School of Mechanical Engineering, Universiti Sains Malaysia

14300 Nibong Tebal, Penang, Malaysia

E-mail: zahurin@eng.usm.my

Nur Azam Badarulzman

School of Mechanical and manufacturing Engineering, Universiti Tun Hussein Onn Malaysia

86400Parit Raja, Johor, Malaysia

Abstract

In this article fatigue behavior of aluminum alloy at elevated temperature is studied. Fatigue failure is a major failure mode of failure where the cyclic load is applied to the machine element. Hence certainly it is important to know the fatigue behavior of the machine element at elevated temperature, aluminum alloy is excessively used in industry like in aerospace automobile and miniatures industries etc, because of its non corrosive property and light in weight. The fatigue behavior of 2024 – T4 Aluminum alloy is investigated under room and elevated temperatures and it is observed that the fatigue strength of 2024 – T4 Aluminum alloy at elevated temperature is reduced by a factor 1.2 – 1.4 compared with dry fatigue strength.

Keywords: Dry fatigue, Elevated fatigue, Aluminum, Aerospace

1. Introduction

The increasing use of engineering materials in severe environments requires that the materials have good mechanical properties in these environments. Fatigue is one of the principle damage mechanisms for materials operating at elevated temperatures. Fatigue at elevated temperature produces larger strain deformation, crack initiation and growth. Finally the material or structure may fail in different modes, fatigue, rupture, loss and large deformation etc.... For the material under elevated fatigue there is serious influence on the properties and fatigue life of the material (H. Mao and S.

Mahadevan, 2000). Figure 1 Fracture of an Aluminium Crank Arm. Dark area: slow crack growth. Bright area: sudden fracture. Damage initiation and propagations properties for aluminum alloys structures is increased with elevated temperature fatigue compared with dry fatigue (Bilal M. Ayub et al, 2002). This investigation was initiated with the objective of fatigue and the effect of elevated temperatures on the fatigue resistance and fatigue properties. The behavior of aluminum alloy 2024 T4 was tested under dry fatigue and elevated fatigue in order to compare the characteristics of this alloy in the both conditions. This paper discusses the behavior of damage accumulation in dry and elevated fatigue (T. Hanlon, et al, 2005).

2. Parameter for non-linear region:

- 1) Strength
- 2) Ductility
- 3) Strain Hardening properties

The flow properties of a metal may be greatly altered by repeated plastic strains.

2.1 A metal deformation resistance may increase cyclic hardening and the stress required to enforce the strain limit on successive reversals increases. In general annealed metals and aluminum is decreases cyclic softening. The stress required to enforce the strain limit decreases with successive reversals. In general cold worked metals having unchanged cyclic stability.

2.2 The ideal fatigue resistant material for structural applications could be achieved with the following characteristics

- 1) A strain hardening exponent of about 0.1 to insure cyclic stability.
- 2) A high fracture strength to resist the imposed loads
- 3) High fracture ductility to accommodate large plastic strains at critical locations (notches, inclusions, voids, etc.).

2.3 Increased strength is not necessarily synonymous with increased fatigue resistance.

- 1) In light of the large changes in flow properties that may result from cycling, it should not be surprising that monotonic fracture properties are more indicative of a metal's fatigue resistance than either yield or ultimate strength.
- 2) Monotonic fracture properties are sensitive to many of the internal defects which are known to affect fatigue behavior (predicted by σ_f and ϵ_f values).

2.4 Total strain resistance

- 1) Metal's resistance to total strain cycling summation of elastic and plastic strain resistance is given by equation. (Tot strain amp/2) = (Elastic strain amp/2) + (Plastic strain amp/2).

$$= (\sigma_f/E)(2N_f)^b + \epsilon_f(2N_f)^c \quad \text{-----(9)}$$

At short lives the plastic strain component predominates importance of ductility. At long lives the elastic component predominates role of strength. Transition fatigue life, $2N_t$ life where the total strain amplitude consists of equal elastic and plastic component. Whereas, $2N_t$ varies $1e5$ reversals at low hardness normalized steel will display appreciable plastic strain even at very long lives. In 10 reversals at the highest hardness, highly strengthened steels resist cyclic strains largely on the basis of strength over the entire life range. Rule of thumb is that most metals when subjected to a strain amplitude of 0.01 will fail in approximately 2000 reversals. Consideration of local stress-strain response suggests that in many engineering structures the material at the critical location experiences essentially reversed strain cycling, thus emphasizing the importance of strain-based fatigue data. Total strain cycling resistance will depend on a high $(\epsilon_f)'$ at short lives, a high σ_f at long lives, and a combination of high strength and ductility at intermediate lives.

Literature Survey:

H. Moa and S. Mahadevan (H. Mao and S. Mahadevan, 2000) derived probabilistic model for the reliability analysis of the creep and fatigue of materials based on experimental data and a linear damage accumulation rule was used. The main concluded remarks were that the scatter of different random variables on the creep fatigue life is very important.

Bilal M. Ayub et al (Bilal M. Ayub et al, 2002) studied the fatigue behavior of material structures subjected to fatigue loadings under the effect of sea water waves and sea environment. The objective of this paper was to develop reliability based methods for determining the fatigue life of structural details associated with conventional displacement type surface monohull ships based on the S – N approach and on the assumption that the fatigue damage accumulation is a linear phenomenon (i.e; that follows Miner's rule).

T. Hanlon, E. D. Tabahnkova, and S. Suresh (T. Hanlon, et al, 2005) studied the stress – life fatigue behavior and fatigue crack growth characteristics of pure Ni were studied as a function of grain size. This study concluded that the fatigue resistance of engineering structures by recourse to grain refinement down to the nanocrystalline regime.

Levon Minnetyan (Levon Minntyan, 2005) studied damage progression sequence during different degradation stages was made. This study showed that the number of cycles to failure at different temperatures using computational simulation data in the assessment of damage tolerance.

Ali F. Hamide Al – amiri (Ali F. Hamide Al – Amiri, 2006) studied the fatigue behavior of Aluminum alloy at elevated temperature was investigated using random cyclic loading at zero mean stress. The results showed that the mechanical and fatigue properties are decreased at elevated temperature compared with the results of dry fatigue.

Svjetlana Stekovic (Svjetlana Stekovic, 2007) investigated high strength nickel – base super alloys have been used under dry and elevated fatigue (high temperature). The focus of this work was on a study of the low cycle fatigue and thermo mechanical fatigue behavior of a polycrystalline. The main conclusions were that the presence of the coatings was, in most cases, detrimental to low cycle fatigue lives of the super alloys at 500 °C while the coatings do improve the low cycle fatigue lives of the super alloys at 900 °C.

Experimental Work:

Material:

Aluminum alloy specimen is taken as sample article and the average of chemical composition for three specimens is analyzed and compared them with the standard specification as shown in table (1).

Tensile test machine of maximum capacity (1000 kN) is used to determine the mechanical properties of the material as per the standard Germany specification (DIN 5025) and compared with the standard specification as shown in table (2). The standard material specification for Aluminum 2024 alloy has given in table (3).

Test Rig:

Rotating bending test machine: A cantilever type, load controlled type machine of constant load ratio of (-1) is used for experimental work. The specimen is subjected to load at its free end perpendicular to its axis while rotating. This will develop a bending moment which can be calculated by using the following equations:

$$\sigma_b = MY/I \quad (1)$$

$$\sigma_b = P * L / (\pi * d^3 / 32) \quad (2)$$

Where:

L: Arm of the applied force (L = 125.7 mm)

σ_b : Bending stress

Y : Radius of the specimen = d/2

I : Moment of inertia = $\pi d^4/64$

The specimen dimensions are given in figure (1).

Experimental Results and Discussion:

Table (4) shows the S – N curve fatigue data for specimens tested reversed bending and (R = -1, stress ratio) at room temperatures. It is observed that as the applied bending stress is increases the life cycle of the specimen is go on decreased for the all the three group of specimen. It is generally accepted that as the applied stress is go on increases the life cycle of the material decreases, hence it is observed that for a different group of materials, the fatigue life varies as applied stress varies.

Figure (2) shows nature of curve for applied stress to the number cycle ,it observed from the graphe that as decrease in applied stress range the life cycle is go on decreases. This curve shows the relationship between bending stress at failure and number of fatigue cycle. In this study 21 specimens have been tested and computed the life cycle for each specimen for various stress range for three groups of materials. From figure (2) it is observed that the curve is exponentially decreases, hence from this curve the equation for fatigue life of the S - N curve is obtained as equation (3).

$$\sigma_f = 1479 * (N_f)^{-0.147} \quad (3)$$

Similarly 21 specimens at different stress range are tested for three groups of materials at elevated temperature as 180 °C. The loading condition is as applied to specimens at room temperature. It is observed from the table (5) is that as the

stress range increases the fatigue life go on decreases as in the specimen tested in room temperature .it also observed that at elevated temperature the life cycle is comparatively less for same loading condition applied to the specimen at room temperature for all three groups...

Figure (3) shows the behavior of the AL – alloy under high temperatures. It is evident that the life cycle goes on increases exponentially as decreasing in the stress range, hence from the curve, the equation of life of the S - N curve is developed as (4).

$$\sigma_f = 524 * (N_f)^{-0.0858} \quad (4)$$

Figure (4) shows a comparison between the S – N curve for dry fatigue and elevated temperature.

It is evident that specimen at elevated temperature is having less life cycle as compared to the specimen tested at room temperature for the same loading conditions . Al – Kaisee (Rasha Hussam AL – Kiasee, 2002) studied the 2024 AL – alloy material and a comparison between the published result and the current result is given in figure (5).

AL – Amiri (Ali F. Hamide Al – Amiri, 2006), Yaseen (Yassen Mohammed Kalook, 2007), and AL – Naimy (W. R. Al – Naimy, 1997) studied the 2024 AL – alloy material and a comparison between the published result and the current result is given in figure (6).

3. Conclusions

In this study the fatigue life cycle of the for AL– Alloy 2024 – T4 is carried out for three group of materials for the different stress range ,this specimen have been tested at room temperature and elevated temperature that is 180 °C and it observed that the life cycles are significantly reduce at elevated temperature comparative to specimen tested at room temperature at same applied stress range. The equations have developed for fatigue life for AL– Alloy 2024 – T4 at room temperature and elevated temperature. It is observed that the fatigue strength in elevated temperature is reduced compared to ambient temperature by a factor 1.2-1.4.

1) The fatigue behaviour of the AL – Alloy 2024 – T4 of dry fatigue at constant amplitude load may be described by the following formula:

$$\sigma_f = 1479 * (N_f)^{-0.147}$$

2) While the behaviour of the AL- Alloy under 180 °C may be taken the formula:

$$\sigma_f = 524 * (N_f)^{-0.0858}$$

3) The fatigue strength under elevated temperature is reduced by a factor of 1.2 – 1.4 compared with the strength at dry fatigue.

Abbreviations

L	Arm of the applied force ($L = 125.7$ mm)
σ_b	Bending stress
Y	Radius of the specimen
I	Moment of inertia
R	Stress ratio
σ_f	Fatigue stress
N_f	Fatigue Life
S	Stress Range
N	Number of Cycle

References

- Ali F. Hamide Al – Amiri. (2006). “Cumulative Fatigue Damage Application to Estimating Parts Under High Temperature with Using Learning System”, Ms. C. Thesis, Department of Technical Education, University of Technology, Iraq.
- Bilal M. Ayuub et al. (2002). “Reliability - Based Design Guide lines for Fatigue of Ship Structures”, *The American Society of Naval Engineers Journal*,.

H. Mao and S. Mahadevan. (2000). "Creep Fatigue Reliability of High Temperature Materials", 8th ASCE Specially Conference on Probabilistic Mechanics and Structural Reliability,

Levon Minntyan. (2005). "Computational Simulation of Composite Structural Fatigue", NASA Glenn Research center,.

Rasha Hussam AL – Kiasee. (2002). "Effect of Pipe – Stress on Al – Alloy Structural Fatigue life", Ph. D. Thesis, Mechanical Engineering Department, University of Technology, Iraq,.

Svetlana Stekovic. (2007). "Low Cycle Fatigue and Thermo – Mechanical Fatigue of Uncoated and Coated Nickel – Base Super alloys", Ph. D. Thesis, Linkoping University, Sweeden,.

T. Hanlon, et al. (2005). "Fatigue Behavior of Noncrystalline Metals and alloys", *International Journal of Fatigue*, Vol. 27, pp. 1147 – 1158.

W. R. Al – Naimy. (1997). "Cumulative Multi axial Fatigue Damage on Aircraft Alloy 2024 – T4 Under complex Loading", M. Sc. Thesis, Mechanical Engineering Department, University of Technology,.

Yassen Mohammed Kalook. (2007). "The concept of cumulative fatigue damage as a tool to elevate the residual stresses for 2024 – Al alloy", *Journal of Engineering and Technology*.

Table 1. Experimental chemical composition for 2024 – T4 AL– alloy

Element	Cu	Mg	Mn	Si
%wt	4	0.244	0.43	0.12
Element	Fe	Ni	Zn	Al
%wt	0.28	0.1	0.43	94.396

Table 2. Experimental mechanical properties

AL - alloy	σ_y (Mpa.)	σ_{ult} (Mpa.)	Elong. %	Hardness (Brinell)
2024	352	502	15.4	117
G	μ	Average of (3) specimens		
26.86	0.29			

Table 3. Standard material specification 2024 – T4 AL - alloy ^{[3], [4]}.

Chemical composition (% w) =
Al 92.05; Cu 4.5; Mn 0.6; Cr 0.1; Mg 1.5; Zn 0.25; Si 0.5; Fe 0.5

Physical properties	
Melting Range (°C)	502 – 638
Density (kN/m ³), (20 °C)	1.366
Thermal Expansion (1/°C *10 ⁻⁶)	24.66 (20 – 300 °C)

Mechanical properties - temperature = HT	
Tensile strength (MN/mm ²)	482.3
Yield strength (MN/mm ²)	344.5
Elongation (%)	18
Hardness (Brinell)	120
Elastic modulus (Gpa.) / tension	69.3

Table 4. S – N curve fatigue data for 2024 – T4 AL– alloy at room temperatures.

σ_b (bending stress) Mpa	Life to failure (cycles) (N_f)		
	Group One	Group Two	Group Three
140	$9.4 \cdot 10^6$	$8.2 \cdot 10^6$	$10.1 \cdot 10^6$
160	$3.5 \cdot 10^6$	$4 \cdot 10^6$	$3.7 \cdot 10^6$
170	$2.65 \cdot 10^6$	$3.01 \cdot 10^6$	$2.88 \cdot 10^6$
180	$1.94 \cdot 10^6$	$1.77 \cdot 10^6$	$1.82 \cdot 10^6$
200	$9.25 \cdot 10^5$	$8.88 \cdot 10^5$	$9.2 \cdot 10^5$
250	$3.2 \cdot 10^4$	$3.07 \cdot 10^4$	$2.92 \cdot 10^4$
300	$4.2 \cdot 10^3$	$4 \cdot 10^3$	$3.87 \cdot 10^3$

Table 5. S – N curve fatigue data for 2024 – T4 AL – alloy at (180 °C).

σ_b (bending stress) or stress at failure Mpa	Life to failure (cycles) (N_f)		
	Group Four	Group Five	Group Six
140	$5.2 \cdot 10^6$	$4.45 \cdot 10^6$	$4.9 \cdot 10^6$
160	$1.1 \cdot 10^6$	$0.9 \cdot 10^6$	$1.07 \cdot 10^6$
170	$8.1 \cdot 10^5$	$9.02 \cdot 10^5$	$8.4 \cdot 10^5$
180	$5 \cdot 10^6$	$4.45 \cdot 10^5$	$5.07 \cdot 10^5$
200	$1.2 \cdot 10^5$	$1.09 \cdot 10^5$	$1.7 \cdot 10^5$
250	$1.2 \cdot 10^4$	$1.09 \cdot 10^4$	$1.11 \cdot 10^4$
300	$1.2 \cdot 10^3$	$0.9 \cdot 10^3$	$0.85 \cdot 10^3$



Figure 1. Fracture of an Aluminium Crank Arm. Dark area: slow crack growth. Bright area: sudden fracture

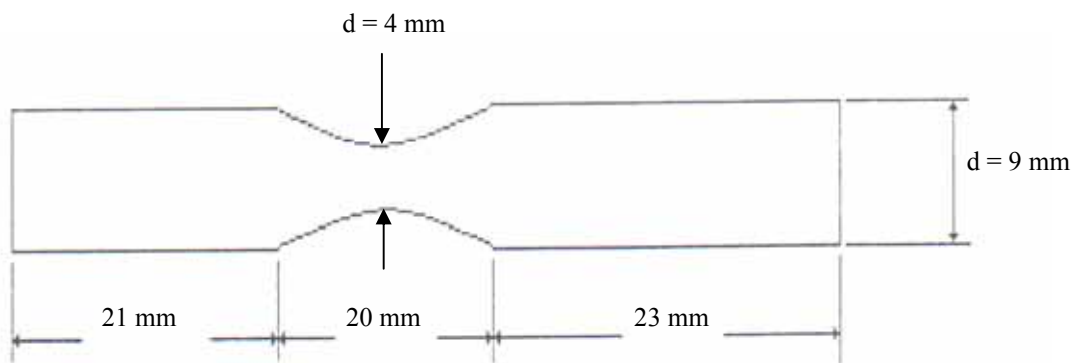


Figure 2. Dimensions of rotating bending fatigue test specimens

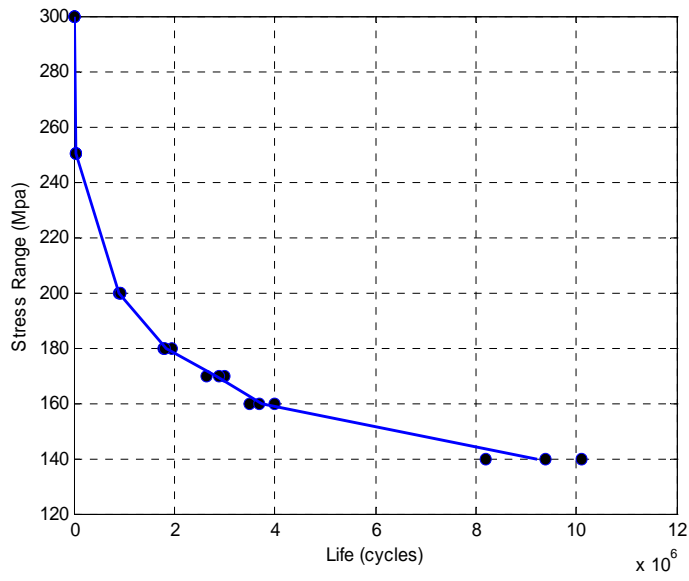


Figure 3. (S – N) curve for 2024 AL – Alloy material for dry fatigue

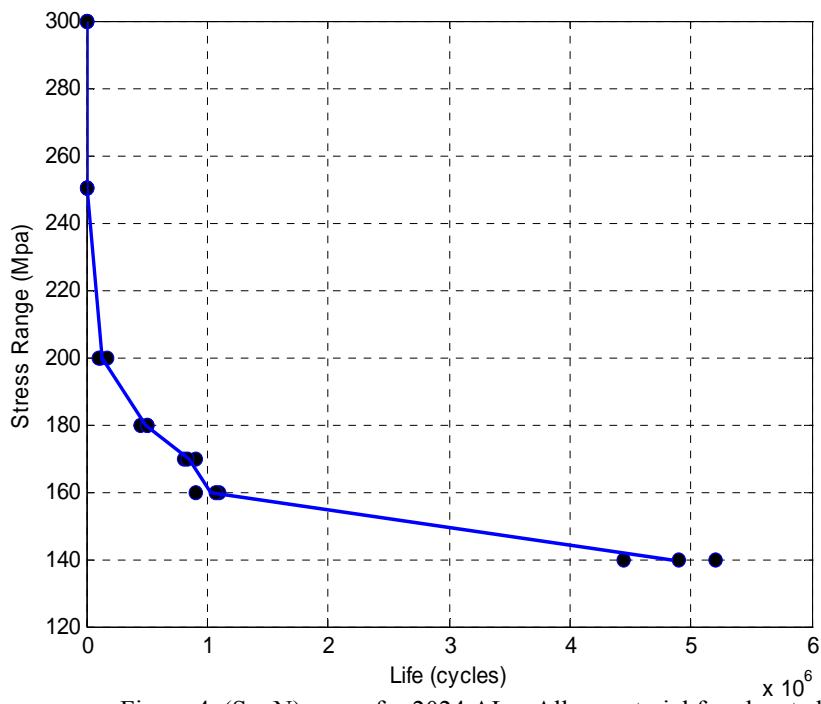


Figure 4. (S – N) curve for 2024 AL – Alloy material for elevated fatigue

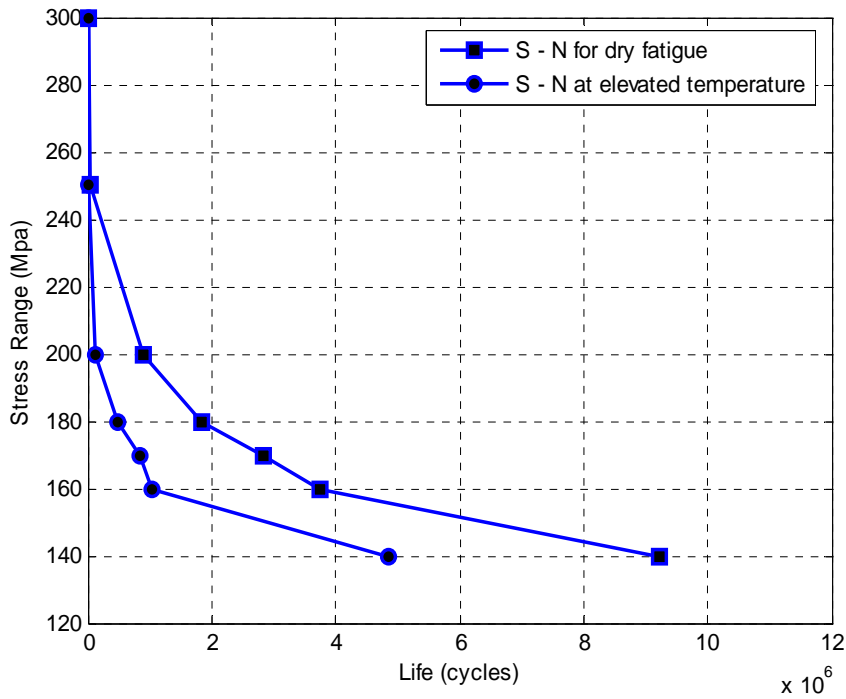


Figure 5. Comparison between the S – N curve for dry fatigue and elevated temperature

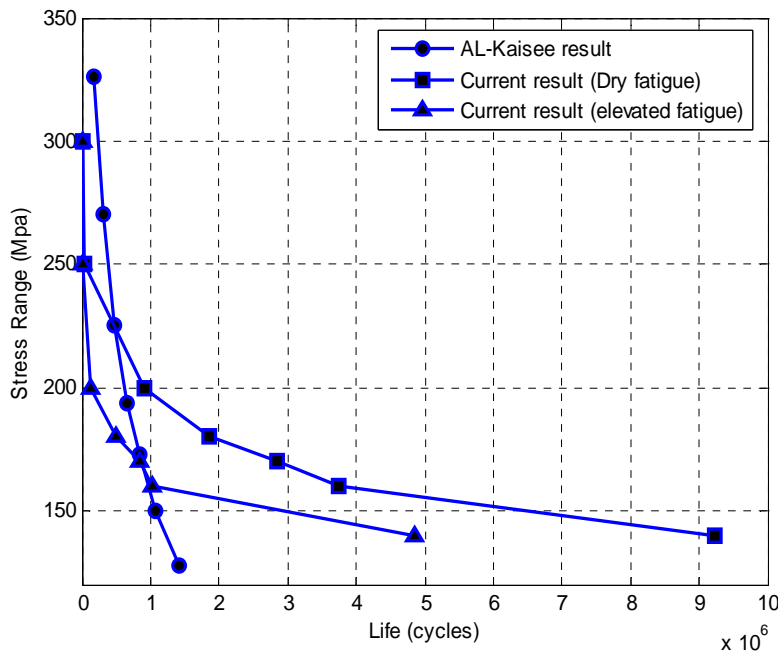


Figure 6. Comparison between present results and AL – Kaisee result

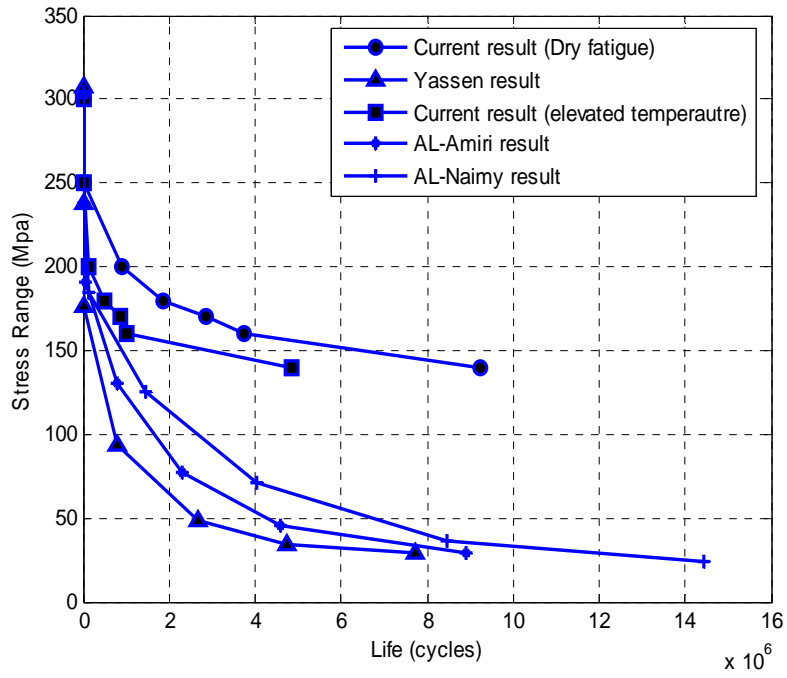


Figure 7. Comparison between present results and AL – Amiri, Yassen , and AL – Naimy Results



New Approaches in Estimating Rubberwood Standing Volume Using Airborne Hyperspectral Sensing

Kamaruzaman Jusoff (Corresponding author)

Yale University, Yale's Tropical Resources Institute

370 Prospect St, New Haven, CT 06511, USA

Tel: 20-3-676-7761 E-mail: jusoff.kamaruzaman@yale.edu

Malek Hj. Mohd Yusoff

Universiti Teknologi MARA, UiTM Arau, 02600 Perlis, Malaysia

Tel: 60-4-986-8077 E-mail: malek_uitm@yahoo.com

Abstract

This paper focuses on mapping and quantifying the rubberwood plantation's volume by using the UPM-APSB's AISA airborne hyperspectral sensor in Lebuah Silikon, Universiti Putra Malaysia, Serdang, Malaysia. The image and field spectral knowledge of the individual standing rubber tree was obtained by image analysis and field work, respectively. The correlations between the different crown area of rubber trees and the diameter at breast height with the ancillary data were obtained. A supervised classification method based on Spectral Angle Mapper (SAM) and spectral matching knowledge was presented and applied to classify the entire image leading towards an estimation of rubberwood volume for the study area. It shows that the rubberwood volume of an old matured unmanaged rubber plantation can easily be predicted with high accuracy obtained through this approach. A total of 20 rubber tree samples were identified, quantified and mapped representing a standing rubberwood volume of 91.44 m³ /ha and a mapping accuracy of 89.84%. The study demonstrated that UPM-APSB's AISA airborne hyperspectral sensor is capable of mapping individual rubber trees and estimate the standing rubberwood volume with an acceptable accuracy.

Keywords: Rubber (*Hevea brasiliensis*), Rubberwood volume, Airborne hyperspectral sensing, Mapping, Universiti Putra Malaysia

1. Introduction

Airborne hyperspectral remote sensing has recently become popular in agricultural resources assessment, planning, management and monitoring in Malaysia (Jusoff and Malek, 2008; Jusoff and Pathan, 2009). The system acquires images from airborne remote sensors, pre-processed data on-board and later the images analysed to provide the necessary information and assessment. It enables spatial and temporal assessment of agricultural land use and cover. It has been successfully used not only for assessment and classification of major agricultural resources, but also for mapping and estimating individual plantation tree crop production such as the oil palm (Jusoff and Pathan, 2009; Jusoff, 2009b, 2009c) and rubber plantations. It is very important in the planning, management and sustainable utilization of these agricultural resources.

Inventory of rubber plantation resources in Malaysia is still in an initial phase of development. Ground inventory is rather accurate, but may be costly in time and resources. Remote sensing alone cannot compete with ground methods in accuracy and scope, but can provide an excellent framework for field inventories and can save on cost. In combination with limited field samples, remote sensing can produce excellent results at a reasonable and competitive price (Jusoff and Malek, 2008). It can be especially useful in the monitoring and analysis of rubber cover changes and timber volume estimation and inventory. It is not easy to apply remote sensing techniques to rubber, especially a wild unmanaged old rubber plantation compared with other plantation crop species. Given that the individual crowns of rubber is often scattered and overlapped throughout the plantation, it might be difficult to separate it from other tree crowns and would require field validation.

Malaysia has now become the centre (and model) for the processing and utilization of rubberwood worldwide. In Peninsular Malaysia, about 2.0 mil.m³ are utilized by the timber and wood-based industries annually even though about 3.2 mil.m³ are suitable for conversion into sawn timber. This leaves 1.2 mil.m³ yet to be exploited for processing into sawn timber. In Malaysia the estimated volume available annually up to the year 2005 is between 8-10 mil.m³. The available wood volume per hectare is dependent upon numerous factors such as clone, site, management etc. In general between 163-185 m³ / ha for diameter above 15 cm. is obtained. Usable log volume from 9 cultivars studied has been

estimated to range from 52-162 m³/ha. Although sawn timber recovery from logs is about 25-45% studies on the 9 cultivars have shown a range from 8.9-27.9 m³ /ha (Gan *et al.*, 1985). Lacking of complete information of rubberwood plantations had urged more research on getting the accurate data about their timber volume. Estimation of standing timber volume is important to obtain the quantitative amounts of various forest products that are available in pre-harvest (Jusoff, 2007; and Jusoff and Lisa, 2009). Nowadays, sales of timber in Malaysia are based on volume. Most of the information of the rubberwood plantations comes from three sources such as National Forest Inventory (NFI), Post-F Inventory and Special Inventory.

Using airborne hyperspectral imaging gain many advantages such as data collection can be collected on demand with high spatial and spectral resolution, real-times processing of images and GIS ready data (Jusoff and Lisa, 2009; Jusoff and Skidmore, 2009; Jusoff, 2008a; 2008b; 2008c and Jusoff, 2006). Using this technique, one can save the time of monitoring and mapping the crop cover. In addition, it also can be used to estimate the standing timber volume and crown area of the rubber. The objective of this study is therefore to map and estimate the standing rubberwood timber volume in a matured unmanaged rubber plantation in Lebu Silikon UPM, Selangor.

2. Methods and materials

2.1 Description of study area

Universiti Putra Malaysia's main campus is located in Serdang, Selangor that is approximately 23 km to the south Kuala Lumpur (Figure 1). Serdang Campus covers an area of 1,214 ha and approximately 121 ha are used for administration buildings, lecture halls, student's dormitories, staff housing, sports fields and the rest of the area are used for plantation. The study area is located in Lebu Silikon, UPM in the state of Selangor Darul Ehsan at latitude 2°59'58"N and longitude 101°43'30"E. The total rubber plantation area of 1 ha was an unmanaged old stand (Figure 2). The climate of Lebu Silikon, UPM is characterized as humid and hot in the whole year with mean daily temperature of 27°C. The peak temperature could reach 32.3°C and the lowest at 21°C. The hot and humid climate of Lebu Silikon, UPM is accompanied by an average rainfall of 2,500 mm per annum with the highest of 290 mm per month and the lowest at 130 mm per month. The humidity level is constant at 80% throughout the year.

2.2 Equipments and software

UPM-APSB'S AISA airborne hyperspectral system is a commercial hyperspectral sensor product (15 kg in total weight), a complete push-broom system, consisting of a hyperspectral sensor head, miniature Global Position System (GPS) sensor, and data acquisition unit in a rugged PC with display unit and power supply, operated by Tropical Forest Airborne Observatory (TropAIR)/Forest Geospatial Information & Survey Lab in collaboration with Aeroscan Precision (M) Sdn. Bhd. in Block C3, UPM-MTDC Tech Centre, Lebu Silikon, Universiti Putra Malaysia. It is a proven hyperspectral system that has been designed to collect accurate and reliable information of the earth surface (Jusoff, 2008a; 2008b; 2008c; 2009a; 2009b; 2009c; Jusoff and Norsuzila, 2008). It is quick to install and remove from any aircraft and provide timely, accurate and reliable information. The systems include an in-flight configuration setting, which allows alterations to be made easily for each exercise. Auxiliary components include a mount to connect the sensor head to the GPS or INS unit, regulated power supply and CaliGeo post-processing software that produces calibrated geo-referenced images and image mosaics of the acquired data with an ENVI header. It is a ready-to-use system to produce radiometrically calibrated and geo-referenced hyperspectral data and measures up to 244 bands of contiguous visible and IR wavelengths at up to 100 images. UPM-APSB's AISA is capable of collecting data within a spectral range of 430 to 900 nm. Although UPM-APSB's AISA is capable of collecting up to 286 spectral channels within this range, the data rate associated with the short integration times (sampling rates) required of the sensor in most operational or flight modes, limits the number of channels. The operational collection configuration used for this study is 20 spectral bands depending on the aircraft speed, altitude and mission goals.

Hyperspectral image of the rubber plantation was acquired using UPM-APSB's AISA hyperspectral sensor. The sensor was flown at an altitude of 1000 m from the ground at a spatial resolution of 1.0 m. The aircraft flying speed was 120 knots or 60 ms⁻¹. The entire image capturing process was taken by the Aeroscan Precision (M) Sendirian Berhad (APSB) which is located at the Tropical Forest Airborne Observatory (TropAIR)/Forest Geospatial Information and Survey Lab, Block C3, UPM-MTDC Tech Centre, Lebu Silikon, UPM. Image pre-processing was done on-board automatically with the Caligeo software to increase the accuracy and the interpretability of the image prior to image classification. This process involves correcting images to reduce the magnitude of unwanted effects to improve the quality of the image data for subsequent processing in addition to correct for sensor and platform-specific radiometric and geometric distortions of data (Jusoff, 2007). Image enhancement using the contrast and optimum band combinations were later performed using ENVI 4.2 to edit the original image data to increase the amount of information for visually interpreted data to create a "new" image. In order to automatically extract the individual species pixels, the spectral signatures of the individual tree species must be analysed and pixels were then assigned to categories based on similar spectral signatures. A supervised classification using Spectral Angle Mapper (SAM) was finally applied to separate the end members for each tree crown species and later verified on the ground by the field survey team members from Aeroscan

Precision (M) Sdn Bhd using a handheld Global Positioning System (GPS). The supervised classification was done using the Spectral Angle Mapper (SAM), which is a physically-based spectral classification that uses an n-dimensional angle to match pixels to reference spectra. The end-member of the tree crowns were derived from the archived spectral library, which were collected during the ground sampling using a handheld spectroradiometer. The radian used in this study was 0.10, which is the most suitable radian to classify the species-species crowns of trees in the study area. A post classification using the Clump Classes was used to clump adjacent similar classified pixels together using morphological operators. The selected classes were then clumped together by first performing a dilate operation following by erode operation on the classified image using a kernel of the size specified in the parameters dialog. Sieve classes removed isolated classified pixels in classification image using blob grouping. The sieve classes at the neighboring 4 or 8 pixels were to determine that the pixel is grouped with pixels of the same class. The number of pixels in a class that were grouped less than the neighboring pixels value was removed away from the class. For the purpose of mapping accuracy assessment, a ground verification plot of 0.25 ha in size at latitudes 2°59'58.17"N and 3°00'00.25"N, and longitudes 101°43'29.16"E and 101°43'31.91"E was chosen. The mapping accuracy was calculated using following formula:

$$\begin{aligned} \text{\% of Accuracy} &= 100\% - \text{error\%} \\ &= 100\% - \frac{\text{Average of the differences between crown size}}{\text{Average of crown size for each tree at ground truth}} \times 100 \end{aligned}$$

Finally, an output thematic map of individual rubber tree crowns in UPM Lebu Silikon was developed. It can be used to estimate the rubberwood standing volume in Lebu Silikon, UPM and the future sivilcultural prescription to manage the stand for better productivity. This information will definitely aid the rubberwood pre-harvest estimation based industry in Malaysia and elsewhere.

3. Results and discussion

Sobel edge detection filter showed the best effect on the image in detecting edges of canopy of *Hevea brasiliensis* compared to other convolution and morphology filter. The tree crown image (Figure 3) of rubber plantations in the study area was selected randomly from the image to estimate the crown area. Table 1 showed the result of the individual tree crowns of rubber plantation from the image using the ENVI 4.2 software.

Spectral reflectance of *H. brasiliensis* in the study area was selected randomly from the image to check the curve of spectral reflectance. This step was done to confirm the classes that have been mapped out were belonged to the *H. brasiliensis*. Figure 4 showed several similar spectral reflectances of *H. brasiliensis*. Since the pattern and curve of spectral reflectances were almost the same, the spectral reflectances were therefore being concluded to belong to the same species. However, the value of spectral library plots had a different range between 800 – 1000 due to the condition of the age and stress levels of the rubber's leaves. The differences of colour (red, green and yellow) in image were perhaps due to factors of age, healthy or disease affected trees.

In the ground verification, 20 of *H. brasiliensis* were selected for the sample. Ground verification was conducted on 26 March 2007 to define the relationship between the *H. brasiliensis* canopies against their respective rubberwood volumes. Tree diameter, height and crown diameter were measured and data collected were recorded. The rubberwood volume and rubber canopies of all the sampled trees were calculated. Table 2 showed the data collected during the ground verification. From the ground verification data, the calculations of height, basal area, volume, and canopy are shown as below:

$$\begin{aligned} \text{Height} &= (\tan \text{ up} + \tan \text{ down}) * \text{distance} \\ &= (\tan 55^\circ + \tan 3^\circ) * 15 \text{ m} \\ &= 22.21 \text{ m} \end{aligned}$$

$$\begin{aligned} \text{Basal Area} &= \pi (\text{DBH})^2 / 4 \\ &= \pi (0.356)^2 / 4 \\ &= 0.0995 \text{ m}^2 \end{aligned}$$

Volume = Height * Basal Area

$$\begin{aligned} &= 22.21 \text{ m} * 0.0995 \text{ m}^2 \\ &= 2.21 \text{ m}^3 \end{aligned}$$

$$\begin{aligned} \text{Canopy} &= \pi (\text{Crown Diameter})^2 / 4 \\ &= \pi (12.4)^2 / 4 \\ &= 121 \text{ m}^2 \end{aligned}$$

Table 2 showed the result of crown area from the image and crown area from the ground verification. The mapping accuracy of this study was 89.84% as calculated below:

$$\begin{aligned}
 \text{\% of Accuracy} &= 100\% - \text{error\%} \\
 &= 100\% - \frac{\text{Average of the differences between crown size}}{\text{Average of crown size for each tree at ground truth}} \times 100 \\
 &= 100\% - \frac{(162 / 20)}{(1594 / 20)} \times 100 \\
 &= 100\% - 10.16\% \\
 &= 89.84\%
 \end{aligned}$$

The mapping accuracy seems to be reasonably accurate and acceptable (over 80%) probably due to the capability of such sensor's spatial resolutions to map rubber canopy in the study area. However, some differences between image and ground measurement exist in this study. Crown size measured on the airborne images are more clearly defined than those measured on the ground, even though crown size measured on the hyperspectral images are smaller than those measured on the ground. This is due to some parts of the overlapping crowns are not resolved on the image. Nevertheless, the airborne hyperspectral sensor measurement is probably a better measure of the functional growing space of a tree and is better correlated with tree and stand volume. Figure 5 showed the relationship between crown area and volume of all the 20 sampled *H. brasiliensis*. The x-axis is crown area (m²) units and y-axis is timber volume (m³) units. The equation for regression between crown area and volume is $y = 0.0147x$ with $R^2 = 0.64$. The crown area was increasing proportionally to the volume, and *vice versa*. The estimated standing timber volume of rubber plantations in Lebu Silikon, UPM was 91.44 m³ / ha. The calculations are shown as below:

$$\begin{aligned}
 \text{Volume/ha} &= \frac{\text{Total Timber Volume}}{\text{Total Area}} \\
 &= 22.86 \text{ m}^3 / 0.25 \text{ ha} \\
 &= 91.44 \text{ m}^3 / \text{ha}
 \end{aligned}$$

4. Conclusions

It can be concluded from the study that the UPM-APSB's AISA airborne hyperspectral sensor is capable of quantifying and mapping the individual crowns of the rubber trees with an accuracy of 89.84%. The estimated standing timber volume of rubber plantations in the study area was 91.44 m³/ha. It is highly recommended that future work should be tested with a higher spatial resolution image of below 1 m² to improve the accuracy of mapping and the tree crown area-volume relationship estimates.

References

- Gan L.T., Ho C.Y., and Chew O.K., (1985). Heveawood: Sawntimber Production and Recovery Studies. International Rubber Conference 1985, Kuala Lumpur.
- Jusoff, K. (2007). Advanced processing of UPM-APSB's AISA airborne hyperspectral images for individual timber species identification and mapping. *International Journal of Systems Applications, Engineering & Development* 2(1): 21-26.
- Jusoff, K and Hj. Malek M.Y. (2008). Airborne Hyperspectral Imagery for Agricultural Businesses in Malaysia. *Journal of International Business Research, Canadian Center of Science & Education, (CCSE), Canada. The Issue of Vol. 1, No.3, July 2008: 54-62.*
- Jusoff, K and L. Curran. (2009). Precision forestry using airborne hyperspectral imaging sensor. *J. Agricultural Science (In Press: The issue of Vol. 1, No. 1, in June 2009).*
- Jusoff, K and M. Pathan. (2009). Mapping of individual oil palm trees using airborne hyperspectral sensing: An overview. *Applied Physics Research (In Press: The issue of Vol. 1, No. 1, in May 2009).*
- Jusoff, K and Norsuzila, Y. (2008). Mapping of power transmission lines on Malaysian highways using UPM-APSB's AISA airborne hyperspectral imaging system. *Journal of Computer & Information Science.* 1(1):88-94.
- Jusoff, K. (2006). Individual mangrove species identification and mapping in Port Klang using airborne hyperspectral imaging. *Journal of Sustainability Science and Management* 2006 1(2): 27-36.
- Jusoff, K. 2008a. Development of geographic information system database for town planning of Sri Serdang, Malaysia using UPM-APSB's AISA airborne hyperspectral imaging data. The National Mapping & Spatial Data Committee (JPDSN), Malaysian National Survey & Mapping Department. *Bulletin GIS.* ISSN 1394-5505. July 2008. 1/2008:1-22.

Jusoff, K. 2008b. Search-and-Rescue (SAR) operations for the missing Bell 206 Long Ranger helicopter in Sarawak, Malaysia using near real-time airborne hyperspectral imaging systems. *Disaster Prevention & Management: An International Journal*.17 (1):94-103.

Jusoff, K. 2008c. Geospatial information technology for conservation of coastal forest and mangroves environment in Malaysia. *Journal of Computer & Information Science*. Issue of Vol.1, No.2. May 2008: 129-134.

Jusoff, K. 2009a. Mapping of Sabah Islands using airborne hyperspectrometer. *J Geography and Geology (In Press: The issue of Vol. 1, No. 1, in May 2009)*.

Jusoff, K. 2009b. Mapping of individual oil palm trees using airborne hyperspectral sensing. *Journal of Applied Physics Research (In Press: The issue of Vol. 1, No. 1, in May 2009)*.

Jusoff, K. 2009c. Land Use and Cover Mapping with Airborne Hyperspectral Imager in Setiu, Malaysia. *Journal Agricultural Science. (In Press: The issue of Vol. 1, No. 2, in December 2009)*.

Jusoff, K., and A.K. Skidmore. (2009). Geo-information science for sustainable development of Mount Stong F.R., Kelantan, Malaysia. *Journal Sustainability Development (In Press: The issue of Vol. 2, No. 1, in March 2009)*.

Table 1. The GPS locations and crown size measurement of the individual *H. brasiliensis* based from the UPM-AOSB's AISA data

Crown No	Latitude	Longitude	Crown Size (m ²)
1	2°59'58.45"	101°43'31.59"	133
2	2°59'58.68"	101°43'31.26"	69
3	2°59'59.11"	101°43'31.36"	99
4	2°59'59.46"	101°43'31.36"	95
5	2°59'59.73"	101°43'30.52"	78
6	3°00'00.08"	101°43'31.66"	112
7	2°59'59.33"	101°43'31.65"	80
8	2°59'58.75"	101°43'31.75"	79
9	2°59'59.07"	101°43'31.04"	121
10	2°59'59.40"	101°43'30.72"	103
11	3°00'00.14"	101°43'29.65"	85
12	2°59'59.73"	101°43'30.17"	81
13	2°59'59.14"	101°43'29.94"	70
14	2°59'59.37"	101°43'29.49"	81
15	3°00'00.05"	101°43'29.33"	92
16	2°59'58.62"	101°43'29.32"	82
17	2°59'58.30"	101°43'29.32"	57
18	2°59'58.26"	101°43'30.49"	55
19	3°00'00.11"	101°43'31.07"	105
20	2°59'59.72"	101°43'30.94"	59

Table 2. GPS readings and crown size variations between image and ground truth

No.	Latitude	Longitude	Crown Size (Image) (m ²)	Crown Size (Ground Truth) (m ²)	Differences Crown Size (m ²)
1	2°59'58.45"	101°43'31.59"	133	121	12
2	2°59'58.68"	101°43'31.26"	69	64	5
3	2°59'59.11"	101°43'31.36"	99	100	1
4	2°59'59.46"	101°43'31.36"	95	83	12
5	2°59'59.73"	101°43'30.52"	78	72	6
6	3°00'00.08"	101°43'31.66"	112	104	8
7	2°59'59.33"	101°43'31.65"	80	75	5
8	2°59'58.75"	101°43'31.75"	79	68	11
9	2°59'59.07"	101°43'31.04"	121	109	12
10	2°59'59.40"	101°43'30.72"	103	95	8
11	3°00'00.14"	101°43'29.65"	85	74	11
12	2°59'59.73"	101°43'30.17"	81	72	9
13	2°59'59.14"	101°43'29.94"	70	66	4
14	2°59'59.37"	101°43'29.49"	81	69	12
15	3°00'00.05"	101°43'29.33"	92	95	3
16	2°59'58.62"	101°43'29.32"	82	88	6
17	2°59'58.30"	101°43'29.32"	57	50	7
18	2°59'58.26"	101°43'30.49"	55	48	7
19	3°00'00.11"	101°43'31.07"	105	88	17
20	2°59'59.72"	101°43'30.94"	59	53	6
Total				1594	162

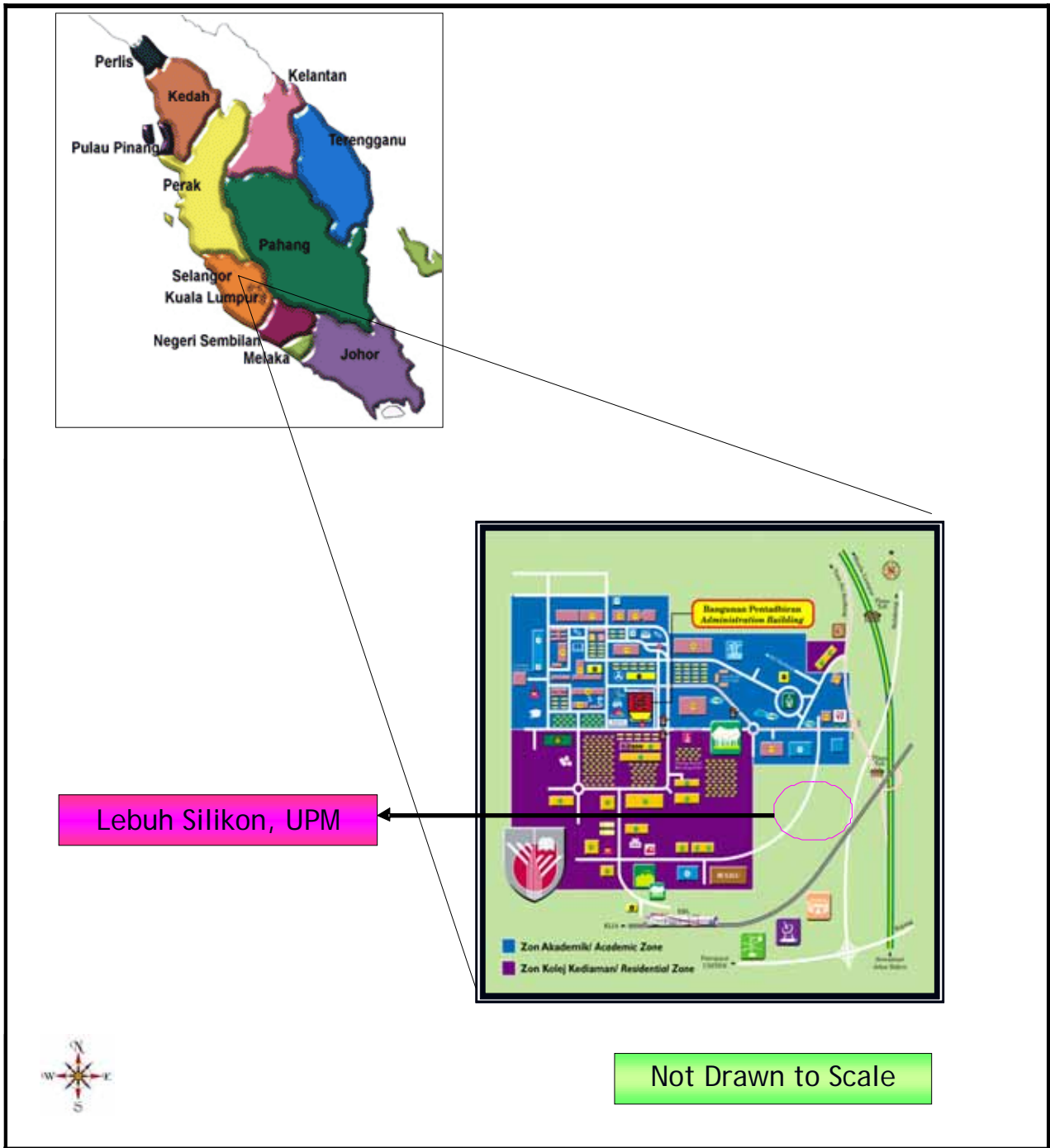


Figure 1. A map of Peninsular Malaysia showing the study area



Figure 2. The unmanaged old rubber plantation under study

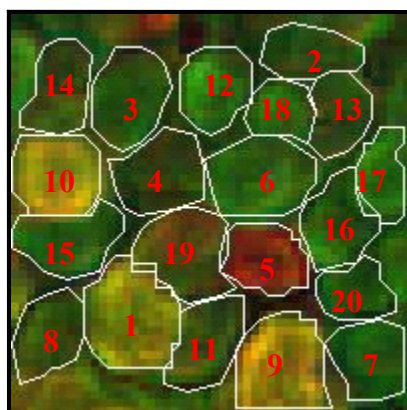


Figure 3. Tree crown image delineation of rubber plantations, Lebu Silikon

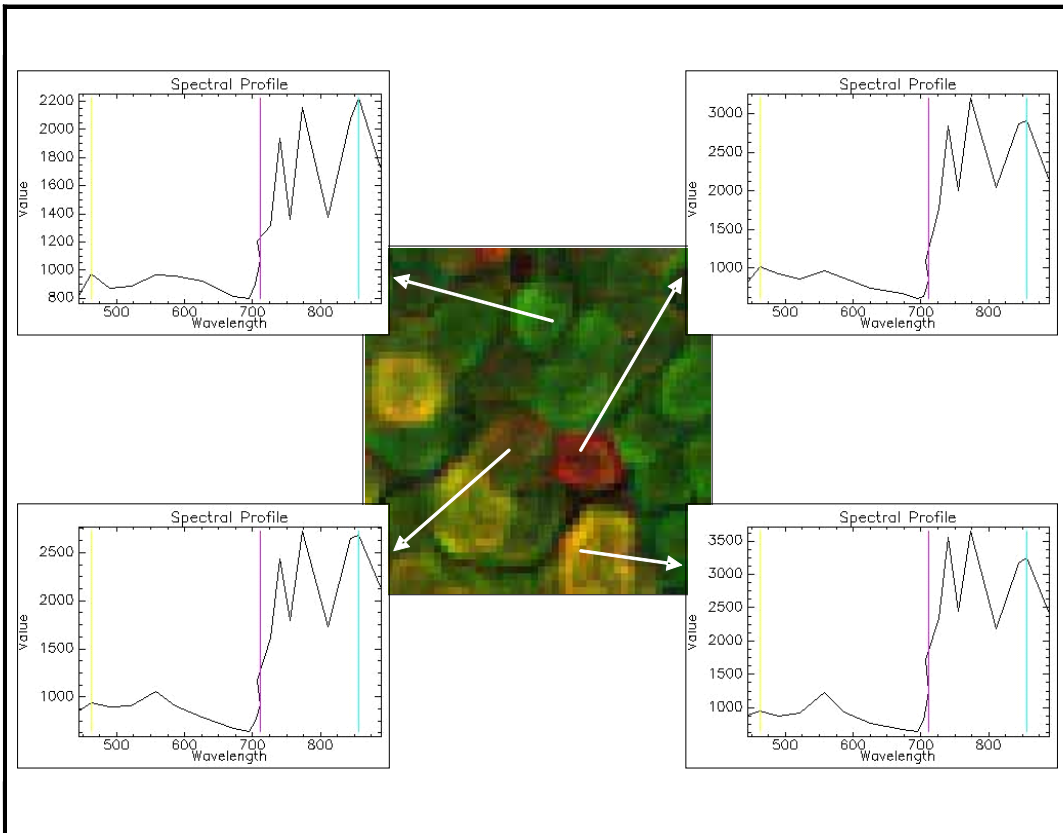


Figure 4. Spectral reflectance of *H. brasiliensis* in study area

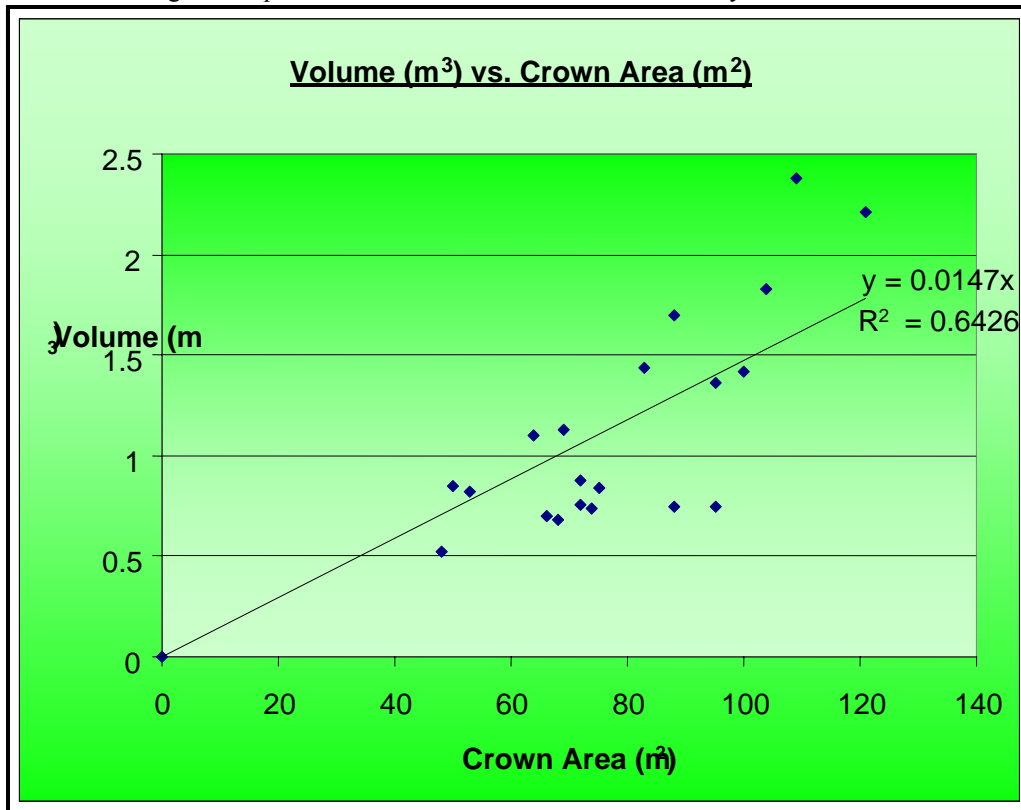


Figure 5. Relationship between crown area and volume of the 20 sampled *H. brasiliensis*



Statistical Analysis and Optimization of Acid Dye Biosorption by Brewery Waste Biomass Using Response Surface Methodology

V. Jaikumar

Department of Chemical Engineering

SSN College of Engineering, Rajiv Gandhi Salai (OMR), Kalavakkam, Chennai 603110, India

Tel: 91-44-2747-5063 Ext 416 E-mail: jaikumarv@ssn.edu.in

V. Ramamurthi (Corresponding author)

Department of Chemical Engineering, Alagappa College of Technology

Anna University Chennai, Chennai 600025, INDIA

Tel: 91-44-2220-3523 E-mail: vramamurthi@yahoo.co.in

The research is financed by Council of Scientific and Industrial Research (CSIR), New Delhi, India, grant number CSIR Lr. No. 9/468(371)/2007-EMR-1 dated 30.03.2007.

Abstract

Biosorption of Acid Yellow (AY 17) and Acid Blue (AB 25) were investigated using a biomass obtained from brewery industrial waste spent brewery grains (SBG). A 2^4 full factorial response surface central composite design with seven replicates at the centre point and thus a total of 31 experiments were employed for experimental design and analysis of the results. The combined effect of time, pH, adsorbent dosage and dye concentration on the dye biosorption was studied and optimized using response surface methodology. The optimum contact time, pH, adsorbent dosage and dye concentration were found to be 45min, 6, 0.5g, 75 mg/L respectively for the maximum decolorization of AY 17(97.2%) and 40 min, 2, 0.4g and 75 mg/L respectively for the maximum decolorization of AB 25(97.9%). A quadratic model was obtained for dye decolorization through this design. The experimental values were in good agreement with predicted values and the model developed was highly significant, the correlation coefficient being 0.89 and 0.905 for AY 17 and AB 25 respectively. Experimental results were analyzed by Analysis of variance (ANOVA) statistical concept.

Keywords: Biosorption, Response surface methodology, Acid dyes, Spent brewery grains, Statistical analysis

1. Introduction

Dyes are intensely coloured substance used for the dyeing of various materials such as textiles, paper, leather, hair, foods, drugs, cosmetics, plastics and many more substances. They are retained on these materials by physical adsorption, salt or metal complex formation, solution mechanical retention, or by the formation of covalent chemical bonds. The colour of the dye is due to electronic transitions between various molecular orbital, the probability of these transitions determining the intensity of the colour. Textile dyes are also designed to be resistant to fading by chemicals and light. They must also be resilient to both high temperatures and enzyme degradation resulting from detergent washing. For these reasons, degradation of dyes is typically a slow process.

The effluents arising out of textile and dyeing industries are the most problematic to be treated not only for their high chemical and biological oxygen demands, suspended solids in toxic compounds but also for colour, which is the first contaminant to be recognized by human eye. Dye wastewater is usually treated by physical or chemical treatment processes for colour removal. These include chemical coagulation/flocculation, precipitation, ozonation, adsorption, oxidation, ion exchange, membrane filtration and photo degradation. These methods for colour removal from effluents have high operating costs and limited applicability (Cooper, 1993). In recent years, biological decolorization method has been considered as an alternative and eco-friendly economical method. This has led many researchers to search for the use of effective, economical and eco-friendly alternative materials such as Chitin (McKay *et al.*, 1983); Silica

(McKay, 1984); the hardwood sawdust (Asfour et al., 1985); Bagasse pith (McKay et al., 1987); Fly ash (Khare et al., 1987); Paddy straw (Deo, 1993); Rice husk (Lee & Low, 1997); Slag (Ramakrishna & Viraraghavan, 1997); Chitosan (Juang et al., 1997); Palm fruit bunch (Nasser, 1997); Bone char (Ko et al., 2000). Thus research is still going on to develop alternative low cost adsorbents to activated carbon which is used mostly in industries. So in the present study spent brewery grains (SBG) which is present in abundant as waste in brewery industry is tried and tested as biosorbent.

Except a few studies in the literature for colour removal only traditional methods of experimentation were followed to study the effects of all variables which are lengthy, random processes and also require large number of experimental combinations to obtain the desired results. In addition, obtaining the optimum conditions i.e., the point at which maximum % colour removal could be achieved is almost beyond the scope. The traditional step-by-step approach, although widely used, involves a large number of independent runs and does not enable us to establish the multiple interacting parameters. This method is also time consuming, material consuming and requires large number of experimental trials to find out the effects, which are unreliable. So, specifically designed experiments to optimize the system with lesser number of experiments are the need of the hour. These limitations of the traditional method can be eliminated by optimizing all the affecting parameters collectively by statistical experimental design (Montgomery, 1991).

So, in this present study, experiments were designed by incorporating all important process variables namely time, pH, adsorbent dosage, and initial dye concentration using Statistical Design Software Minitab 14 (USA). Experimental design allows a large number of factors to be screened simultaneously to determine which of them has a significant effect on % colour removal. A polynomial regression response model shows the relationship of each factor towards the response as well as the interactions among the factors. Those factors can be optimized to give the maximum response (% colour removal) with a relatively lower number of experiments. In this context, a new approach using statistically designed experiments for finding optimum conditions for maximum % colour removal was discussed in detail. The corresponding interactions among the variables were studied and optimized using central composite design and response surface and contour plots.

2. Materials and Methods

2.1 Biosorbent and Adsorbate

The Brewery Industry waste Spent Brewery grain was obtained from Mohan breweries and distilleries Limited, Chennai, India and dried at 60°C for 12 hours. Synthetic textile dye acid yellow and acid blue was obtained from Sigma-Aldrich Chemicals Private Ltd., India and was used without further purification their chemical structures are shown in Fig.1 and Fig.2. All chemicals and reagents used for experiments were of analytical grade and supplied by Qualigens fine chemicals.

2.2 Preparation of biomass

Spent Brewery Grains, taken from Mohan breweries and distilleries Limited, Chennai, India, was suspended in 1M sulphuric acid solution (20g of SBG per 100mL of acid solution) for one hour. Then it was filtered and the acid solution was discarded. The biomass was washed with distilled water many times until it is completely free from the acid and dried at 60°C for 24 hours. The dried biomass was ground, sieved to 270 mesh size and stored for further use in the experiments. As seen from the Fig.3 the scanning electron micrograph (SEM) image shows the porous structure of the biosorbent.

2.3 Batch Experiments

Stock solution 1000mg/L of dye (AY 17 and AB 25) were prepared in double distilled water and was diluted as required according to the working concentration. The required pH was adjusted by 0.1N HCl or 0.1N NaOH. pH was measured using a pH meter (Elico, model LI 120, Hyderabad, India). Dye concentration was measured using UV-Vis Spectrophotometer (HITACHI U 2000, spectrophotometer) at a wavelength corresponding to the maximum absorbance of each dye $\lambda_{\max} = 401.5$ nm for AY 17 and $\lambda_{\max} = 600$ nm for AB 25. The dye solution (50 mL) at desired concentration, pH and adsorbent dosage taken in 250 ml Erlenmeyer flasks was contacted. The flasks were kept under agitation in a rotating orbital shaker at 150 rpm for desired time. Experiments were performed according to the central composite design (CCD) matrix given in Table 2. The response was expressed as % color removal calculated as

$$\% \text{ Colour removal} = \left[\frac{C_0 - C_t}{C_0} \right] \times 100 \quad (1)$$

2.4 Factorial experimental design

The parameters contact time, pH, adsorbent dosage and dye concentration were chosen as independent variables and the output response, removal efficiency of dye. Independent variables, experimental range and levels for AY 17 and AB 25 removal are given in Table 1 and Table 2. A 2^4 full-factorial experimental design, with seven replicates at the center point and thus a total of 31 experiments were employed in this study. The center point replicates were chosen to verify any change in the estimation procedure, as a measure of precision property. Experimental plan showing the coded value

of the variables together with dye removal efficiency are given in Table 3. The analysis focused on how the colour removal efficiency is influenced by independent variables, i.e., time (X_1), pH(X_2), adsorbent dosage(X_3) and dye concentration(X_4). The dependent output variable is maximum removal efficiency. For statistical calculations, the variables X_i were coded as x_i according to the following relationship:

$$x_i = \left[\frac{X_i - X_0}{\delta X} \right] \tag{2}$$

The behavior of the system was explained by the following quadratic equation

$$Y = \beta_0 + \sum \beta_i x_i + \sum \beta_{ii} x_i^2 + \sum \beta_{ij} x_i x_j \tag{3}$$

The results of the experimental design were studied and interpreted by statistical software, MINITAB 14 (PA, USA) to estimate the response of the dependent variable.

3. Results and Discussion

3.1 Response Surface Methodology (RSM)

The most important parameters, which affect the efficiency of a biosorption process are contact time, pH, adsorbent dosage and dye concentration. In order to study the combined effect of these factors, experiments were performed at different combinations of the physical parameters using statistically designed experiments.

The main effects of each parameter on dye removal are given in Fig.4 and Fig.5 for AY 17 and AB 25 respectively. From the figure, it was observed that the maximum removal was found to occur at 60 min for AY 17 and 45 min for AB 25. This indicates that higher the contact time between the dye and adsorbent, higher is the equilibrium removal efficiency. Maximum adsorption occurred at acidic pH range for both the acid dyes. This may be due to high electrostatic attraction between the positively charged surface of the SBG and anionic dyes AY 17 and AB 25. Acid dyes are also called as anionic dyes because of the negative electrical structure of the chromophore group. As the initial pH increases, the number of negatively charged sites on the biosorbent surfaces increases and the number of positively charged sites decreases. A negative surface charge does not favor the biosorption of dye anions due to electrostatic repulsion (Namasivayam and Kavitha, 2002). In general, the acidic dye uptakes are much higher in acidic solutions than those in neutral and alkaline conditions.

It was observed that the removal efficiency of both the dyes AY 17 and AB 25 increases as the adsorbent dosage increases. This may be due to the increase in the available active surface area of the adsorbent. It is observed that the removal efficiency of AY 17 decreases with the increase in dye concentration due to unavailability of surface area of the adsorbent to the increasing number of dye molecules and for AB 25 it is increasing in the studied range up to 175 mg/L with increase in initial dye concentration. Using the experimental results, the regression model equation (second order polynomial) relating the removal efficiency and process parameters was developed and is given in Equ. (4). and Equ. (5) for AY 17 and AB 25 respectively.

The regression equation for the determination of output response for AY17 is

$$\eta = (62.7143) + (2.5590X_1) + (-2.6632X_2) + (12.5382X_3) + (-5.4092X_4) + (-0.2117(X_1^2)) + (-4.4617X_2^2) + (0.2883X_3^2) + (1.9609X_4^2) + (0.1823X_1 X_2) + (0.5469X_1 X_3) + (0.8073 X_1 X_4) + (-0.3906 X_2 X_3) + (0.5990 X_2 X_4) + (-0.9115 X_3 X_4) \tag{4}$$

The regression equation for the determination of output response for AB 25 is

$$\eta = (96.8571) + (0.9867X_1) + (-1.8254X_2) + (-0.3079X_3) + (0.5308X_4) + (-2.1964(X_1^2)) + (-0.5897X_2^2) + (0.1089X_3^2) + (0.0909X_4^2) + (-1.5768X_1 X_2) + (0.5658X_1 X_3) + (-0.0163 X_1 X_4) + (-0.0653 X_2 X_3) + (0.4310 X_2 X_4) + (-0.0572 X_3 X_4) \tag{5}$$

Apart from the linear effect of the parameter for the dye removal, the RSM also gives an insight into the quadratic and interaction effect of the parameters. These analyses were done by means of Fisher's 'F'-test and Student't'-test. The student't'-test was used to determine the significance of the regression coefficients of the parameters. The P-values were used as a tool to check the significance of each of the interactions among the variables, which in turn may indicate the patterns of the interactions among the variables. In general, larger the magnitude of t and smaller the value of P , the more significant is the corresponding coefficient term (Montgomery, 1991). The regression coefficient, t and P values for all the linear, quadratic and interaction effects of the parameter are given in Table 4 and Table 5 for AY 17 and AB 25. It was observed that the coefficients for the linear effect of adsorbent dosage, dye concentration ($P=0.000, 0.001$) was highly significant and coefficient for the linear effect of time was the least significant for AY 17 and pH, time ($P = 0.000, 0.004$, respectively) was highly significant and coefficient for the linear effect of adsorbent dosage was the least significant for AB 25. The coefficient of the quadratic effect of pH and dye concentration ($P = 0.002, 0.130$) was highly significant and the coefficient of the quadratic terms of time ($P = 0.865$) was least significant for AY 17. The coefficient of the quadratic effect of time and pH ($P = 0.000, 0.042$) was highly significant and the coefficient of the quadratic terms of dye concentration ($P = 0.737$) was least significant for AB 25.

The coefficients of the interactive effects of AY 17 among the variables did not appear to be very significant in comparison to the interactive effects of AB 25. However, the interaction effect between time and pH ($P = 0.000$) and time and adsorbent dosage ($P = 0.131$) were found to be significant for AB 25. The significance of these interaction effects between the variables would have been lost if the experiments were carried out by conventional methods.

The optimum values of the process variables for the maximum removal efficiency for both the dyes AY 17 and AB 25 are shown in Table 6. These results are in close agreement with those obtained from the response surface analysis, confirming that the RSM could be effectively used to optimize the process parameters in complex processes using the statistical design of experiments. Although few studies on the effects of parameters on adsorption have been reported in the literature, only a few attempts has been made to optimize them using statistical optimization methods. The predicted values (using the model equation) were compared with experimental result and the data are shown in Table 3.

3.2 Analysis of Variance (ANOVA)

The statistical significance of the ratio of mean square due to regression and mean square due to residual error was tested using analysis of variance (ANOVA). ANOVA is a statistical technique that subdivides the total variation in a set of data into component parts associated with specific sources of variation for the purpose of testing hypothesis on the parameters of the model (Seguro et al., 1999). According to the ANOVA Table 7 and Table 8 for AY 17 and AB 25, the $F_{\text{Statistics}}$ values for all regressions were higher. The large value of F indicates that most of the variation in the response can be explained by the regression model equation. The $F_{\text{statistics}}$ value of 9.24 is greater than tabulated $F_{14, 16}$ (2.38) which indicates that the second order polynomial equation (4) is highly significant and adequate to represent the actual relationship between the response and the variables with a high value of coefficient of determination ($R = 0.9433$; $R^2 = 0.89$) for AY 17. The $F_{\text{statistics}}$ value of 10.9 is greater than tabulated $F_{14, 16}$ (3.14) which indicates that the second order polynomial equation (5) is highly significant and adequate to represent the actual relationship between the response and the variables with a high value of coefficient of determination ($R = 0.9513$; $R^2 = 0.905$) for AB 25.

The associated P -value is used to judge whether F Statistics is large enough to indicate statistical significance. A P -value lower than 0.05 indicates that the model is considered to be statistically significant (Kim et al., 2003). The P -values for almost all of the regressions for both the acid dyes AY 17 and AB 25 were lower than 0.01. This means that at least one of the terms in the regression equation has a significant correlation with the response variable. The ANOVA table also shows a term for residual error, which measures the amount of variation in the response data left unexplained by the model. The form of the model chosen to explain the relationship between the factors and the response is correct.

The response surface and contour plots to estimate the removal efficiency over independent variables adsorbent dosage, pH and pH, dye concentration for the dyes are shown in Fig.6 and 7 for AY 17 and Fig.8 and 9 for AB 25 respectively. The contour plots given in figures show the relative effects of any two variables when concentration of the remaining variables is kept constant. The maximum predicted yield is indicated by the surface confined in the smallest curve of the contour diagram (Gopal et al., 2002).

Figs. 10 - 13 depict the experimental and model predicted removal efficiencies. The predictive capacity of the models was also evaluated in terms of the relative deviations $(RE_{\text{Exp}} - RE_{\text{Pred}}) / RE_{\text{Exp}}$ for the model. With a few exceptions, the values of the variables showed a good agreement (within 3% error) with the experimental data shown in Table 3.

4. Conclusions

The present investigation clearly demonstrated the applicability of SBG as biosorbent for AY 17 and AB 25 dye removal from aqueous solutions. Experiments were carried out covering a wide range of operating conditions. The influence of time, pH, adsorbent dosage and initial dye concentration was critically examined. It was observed from this investigation that the percentage removal efficiency is significantly influenced by time, pH, adsorbent dosage and initial dye concentration. A 2^4 Full factorial central composite experimental design was applied. The experimental data were analyzed using response surface methodology and the individual and combined parameter effects on colour removal efficiency were analyzed. Regression equations were developed for removal efficiency using experimental data and solved using the statistical software Minitab 14. It was observed that model predictions are in good agreement with experimental observations. Under optimal values of process parameters around 97.2% and 97.9% colour removal was achieved for AY 17 and AB 25 dye respectively using the SBG. This study clearly showed that response surface methodology was one of the suitable methods to optimize the best operating conditions to maximize the dye removal.

Acknowledgements

The financial support for this investigation given by Council of Scientific and Industrial Research (CSIR), New Delhi, India under the grant CSIR Lr. No. 9/468(371)/2007-EMR-1 dated 30.03.2007 is gratefully acknowledged.

References

Asfour, H.M., Fadel, O.A., Nasser, M.M., & El-Geundi, M.S. (1985). Colour removal from textile effluents using hardwood sawdust as adsorbent. *J. Chem. Technol. Biotechnol.* 35, 21-27.

- Cooper, P. (1993). Removing colour from dye house wastewaters - a critical review of technology available. *J Soc Dyers Colour.* 109, 97-108.
- Deo, N., & Ali, M. (1993). Adsorption by a new low cost material Congo red 2. *Ind. J. Environ. Protect.* 13, 496-508.
- Gopal, M., Pakshirajan, K., & Swaminathan, T. (2002). Heavy metal removal by biosorption using phanerochaete chrysosporium. *Appl. Biochem. Biotechnol.* 102, 227-237.
- Juang, R.S., Tseng, R.K.L., Wu, F.C., & Lee, S.H. (1997). Adsorption behaviour of reactive dyes from aqueous solution on chitosan. *J. Chem. Technol.* 70, 391-399.
- Khare, S.K., Panday, S.K., Srivastava, R.M., & Singh, V.N. (1987). Removal of Victoria Blue from aqueous solutions by fly ash. *J. Chem. Technol. Biotechnol.* 38, 99-104.
- Kim, H.M., Kim, J.G., Cho, J.D., & Hong, J.W. (2003). Optimization and characterization of UV-curable adhesives for optical communication by response surface methodology. *Polym. Test.* 22, 899-906.
- Ko, D.C.K., Porter, J.F., & McKay, G. (2000). Optimized correlations for the fixed bed adsorption of metal ions on bone char. *Chem. Eng. Sci.* 55, 5819-5829.
- Lee, C.K., & Low, K.S., (1997). Quaternized rice husk as sorbent for reactive dyes. *Bioresour. Technol.* 61, 121-125.
- McKay, G., Blair, H.S., & Gardner, J.S. (1983). Rate studies for the adsorption of dyestuffs on chitin. *J. Colloid Interface Sci.* 95, 108-119.
- McKay, G. (1984). Analytical solution using a pore diffusion model for a pseudo irreversible isotherm for the adsorption of basic dye on silica. *J. AIChE.* 30, 692-697.
- McKay, G., Geundi, E.I., & Nasser, M.M. (1987). Equilibrium studies during the removal of dyestuff's from aqueous solutions using bagasse pith. *Water Resour.* 21, 1513-1520.
- Montgomery, D.C. (1991). Design and analysis of experiments. New York: Wiley.
- Namasivayam, C., & Kavitha, D. (2002). Removal of Congo Red from water by adsorption onto activated carbon prepared from coir pith, an agricultural solid waste. *Dyes and pigments.* 54, 47-58.
- Nasser, M.M., (1997). Intraparticle diffusion of Basic red and basic yellow dyes on Palm fruit Bunch. *Water Sci. Technol.* 40, 133-139.
- Ramakrishna, K.R. & Viraraghavan, T. (1997). Use of slag for dye removal. *Waste Manage.* 17, 483-488.
- Segurola, J., Allen, N.S., Edge, M., & Mahon, A.M. (1999). Design of eutectic photo initiator blends for UV/visible curable acrylated printing inks and coatings. *Prog. Org. Coat.* 37, 23-37.

Nomenclature

C_0	initial concentration of dye solution (mg/L)
C_t	concentration of dye solution at the desired time, t (mg/L)
$RE_{Exp.}$	Removal Efficiency experimental value
$RE_{Pred.}$	Removal Efficiency predicted value
RE	Removal Efficiency
x_i	dimensionless coded value of the variable, X_i
X_0	value of the X_i at the center point
X_1	time (min)
X_2	pH
X_3	adsorbent dosage(g)
X_4	dye concentration (mg/L)
δX	step change
Y	predicted response
<i>Greek letters</i>	
β_0	offset term
β_i	linear effect
β_{ii}	squared effect
β_{ij}	interaction effect
η	removal efficiency

Table 1. Experimental range and levels of independent process variables for AY 17 removal

Independent variable	Range and level				
	$-\alpha$	-1	0	+1	$+\alpha$
Time(X_1 ,min)	15	30	45	60	75
pH(X_2)	4	6	8	10	12
Adsorbent dosage(X_3 ,g)	0.125	0.25	0.375	0.5	0.625
Dye concentration(X_4 ,mg/L)	75	100	125	150	175

Table 2. Experimental range and levels of independent process variables for AB 25 removal

Independent variable	Range and level				
	$-\alpha$	-1	0	+1	$+\alpha$
Time(X_1 ,min)	15	30	45	60	75
pH(X_2)	2	4	6	8	10
Adsorbent dosage(X_3 ,g)	0.2	0.4	0.6	0.8	1.0
Dye concentration(X_4 ,mg/L)	75	100	125	150	175

Table 3. Full factorial central composite design matrix for AY 17 and AB 25 removal

Observations	Time (X_1 ,min)	pH (X_2)	Adsorbent dosage (X_3 ,g)	Dye concentration (X_4 ,mg/L)	Removal Efficiency (η , %)			
					AY 17		AB 25	
					RE _{Exp.}	RE _{Pred.}	RE _{Exp.}	RE _{Pred.}
1	-1	-1	-1	-1	53.75	54.10	97.94	98.19
2	1	-1	-1	-1	57.50	56.14	94.55	92.93
3	-1	1	-1	-1	53.75	47.99	96.07	94.51
4	1	1	-1	-1	57.50	50.77	94.11	93.01
5	-1	-1	1	-1	80.00	80.69	93.52	92.66
6	1	-1	1	-1	82.50	84.92	96.47	96.85
7	-1	1	1	-1	78.75	73.02	98.62	98.47
8	1	1	1	-1	80.00	77.98	91.50	90.04
9	-1	-1	-1	1	44.17	42.29	98.58	98.14
10	1	-1	-1	1	46.67	47.57	97.94	98.95
11	-1	1	-1	1	45.83	38.58	98.23	99.00
12	1	1	-1	1	49.17	44.58	90.44	91.15
13	-1	-1	1	1	63.33	65.23	90.29	90.65
14	1	-1	1	1	70.83	72.69	96.23	96.85
15	-1	1	1	1	62.50	59.96	96.23	96.85
16	1	1	1	1	73.33	68.15	97.52	96.67
17	$-\alpha$	0	0	0	51.00	56.75	93.13	92.93
18	α	0	0	0	64.00	66.99	89.41	90.84
19	0	$-\alpha$	0	0	57.00	50.19	83.64	86.09
20	0	α	0	0	24.00	39.54	96.17	95.01
21	0	0	$-\alpha$	0	30.00	38.79	97.52	96.85
22	0	0	α	0	89.00	88.94	97.52	96.85
23	0	0	0	$-\alpha$	76.67	81.38	91.17	91.17
24	0	0	0	α	55.71	59.74	96.47	96.85
25	0	0	0	0	61.00	62.71	92.64	92.66
26	0	0	0	0	63.00	62.71	96.06	97.90
27	0	0	0	0	63.00	62.71	96.38	98.28
28	0	0	0	0	63.00	62.71	97.52	96.85
29	0	0	0	0	63.00	62.71	94.11	94.16
30	0	0	0	0	63.00	62.71	97.05	96.15
31	0	0	0	0	63.00	62.71	93.30	92.78

Table 4. Estimated Regression Coefficients and corresponding T- and P- values for AY 17

Term	Coefficient	Standard error	T	P
Constant	62.7143	2.484	25.247	0.000
X₁	2.5590	1.342	1.908	0.075
X₂	-2.6632	1.342	-1.985	0.065
X₃	12.5382	1.342	9.346	0.000
X₄	-5.4092	1.342	-4.032	0.001
X₁X₁	-0.2117	1.229	-0.172	0.865
X₂X₂	-4.4617	1.229	-3.630	0.002
X₃X₃	0.2883	1.229	0.235	0.817
X₄X₄	1.9609	1.229	1.596	0.130
X₁X₂	0.1823	1.643	0.111	0.913
X₁X₃	0.5469	1.643	0.333	0.744
X₁X₄	0.8073	1.643	0.491	0.630
X₂X₃	-0.3906	1.643	-0.238	0.815
X₂X₄	0.5990	1.643	0.365	0.720
X₃X₄	-0.9115	1.643	-0.555	0.587

Table 5. Estimated Regression Coefficients and corresponding T- and P- values for AB 25

Term	Coefficient	Standard error	T	P
Constant	96.8571	0.5380	180.027	0.000
X₁	0.9867	0.2906	3.396	0.004
X₂	-1.8254	0.2906	-6.282	0.000
X₃	-0.3079	0.2906	-1.060	0.305
X₄	0.5308	0.2906	1.827	0.086
X₁X₁	-2.1964	0.2662	-8.251	0.000
X₂X₂	-0.5897	0.2662	-2.215	0.042
X₃X₃	0.1089	0.2662	0.409	0.688
X₄X₄	0.0909	0.2662	0.342	0.737
X₁X₂	-1.5768	0.3559	-4.431	0.000
X₁X₃	0.5658	0.3559	1.590	0.131
X₁X₄	-0.0163	0.3559	-0.046	0.964
X₂X₃	-0.0653	0.3559	-0.184	0.857
X₂X₄	0.4310	0.3559	1.211	0.243
X₃X₄	-0.0572	0.3559	-0.161	0.874

Table 6. Optimum values of the process parameter for maximum efficiency for AY 17 and AB 25

Parameter	Optimum Values	
	AY 17	AB 25
η (Removal Efficiency, %)	97.2	97.9
X₁ (Time, min)	45	45.00
X₂ (pH)	6	2.00
X₃ (Adsorbent Dosage, g)	0.5	0.4
X₄ (Dye Concentration, mg/L)	75	75

Table 7. ANOVA of removal efficiency for AY 17: Effect of time, pH, adsorbent dosage and Dye concentration

Source	Degree of freedom	Sum of Squares	Mean of Squares	F _{statistics}	P
Model	14	5588.78	399.2	9.24	0.000
Linear	4	4802.57	1200.64	27.8	0.000
Square	4	748.99	187.25	4.34	0.015
Interaction	6	37.22	6.20	0.14	0.988
Residual Error	16	691.08	43.19	-	-
Lack of fit	10	687.65	68.77	120.34	0.000
Pure Error	6	3.43	0.57	-	-
Total	30	6279.86	-	-	-

Table 8. ANOVA of removal efficiency for AB 25: Effect of time, pH, adsorbent dosage and Dye concentration

Source	Degree of freedom	Sum of Squares	Mean of Squares	F _{statistics}	P
Model	14	309.256	22.0897	10.90	0.000
Linear	4	112.373	28.0933	13.86	0.000
Square	4	148.881	37.2203	18.37	0.000
Interaction	6	48.002	8.0003	3.95	0.013
Residual Error	16	32.420	2.0262	-	-
Lack of fit	10	29.992	2.9992	7.41	0.012
Pure Error	6	2.428	0.4047	-	-
Total	30	341.676	-	-	-

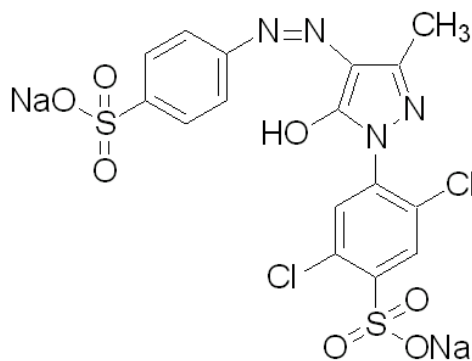


Figure 1. The chemical structure of AY 17 dye

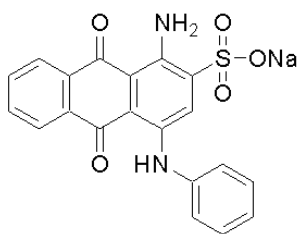


Figure 2. The chemical structure of AB 25 dye

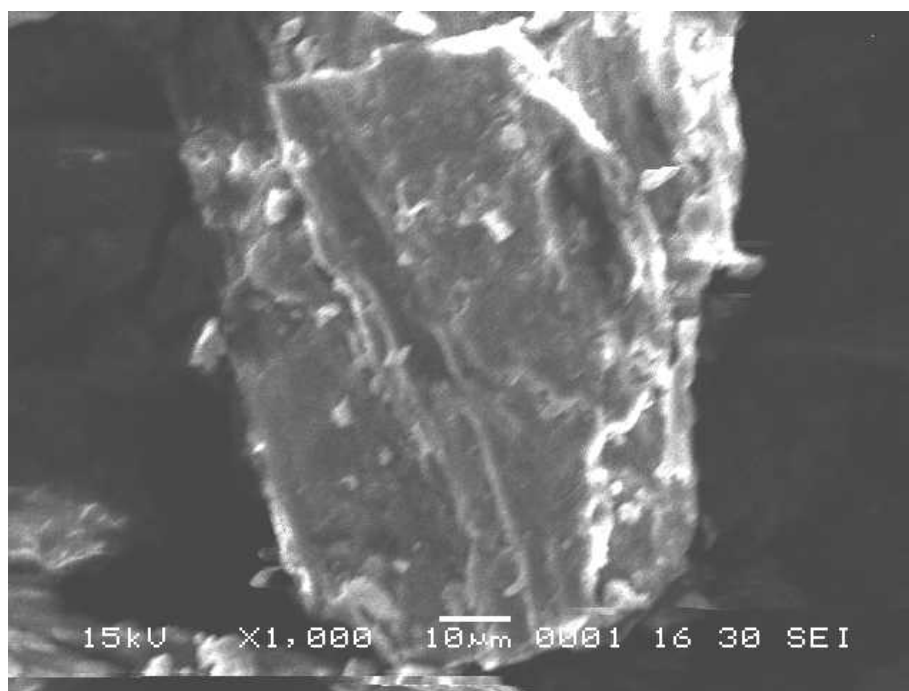


Figure 3. SEM image of the biomass SBG

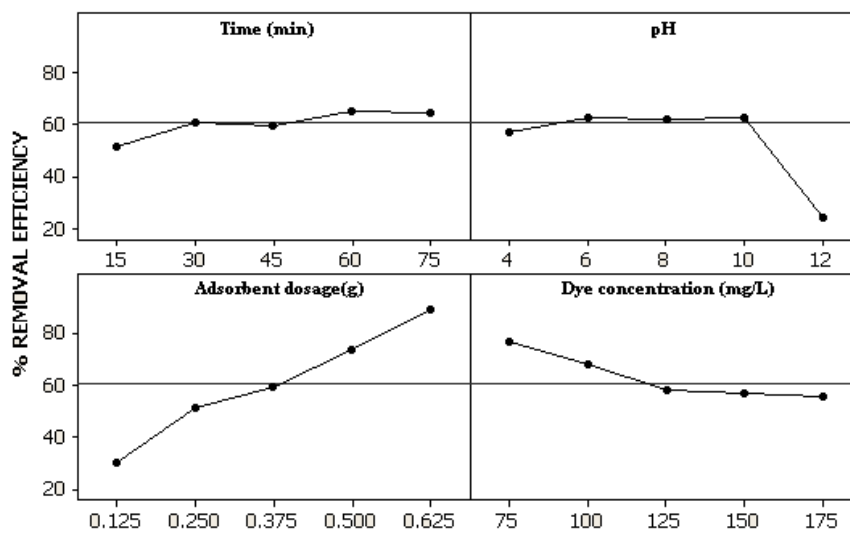


Figure 4. Main effects plot of parameters for AY 17 removal

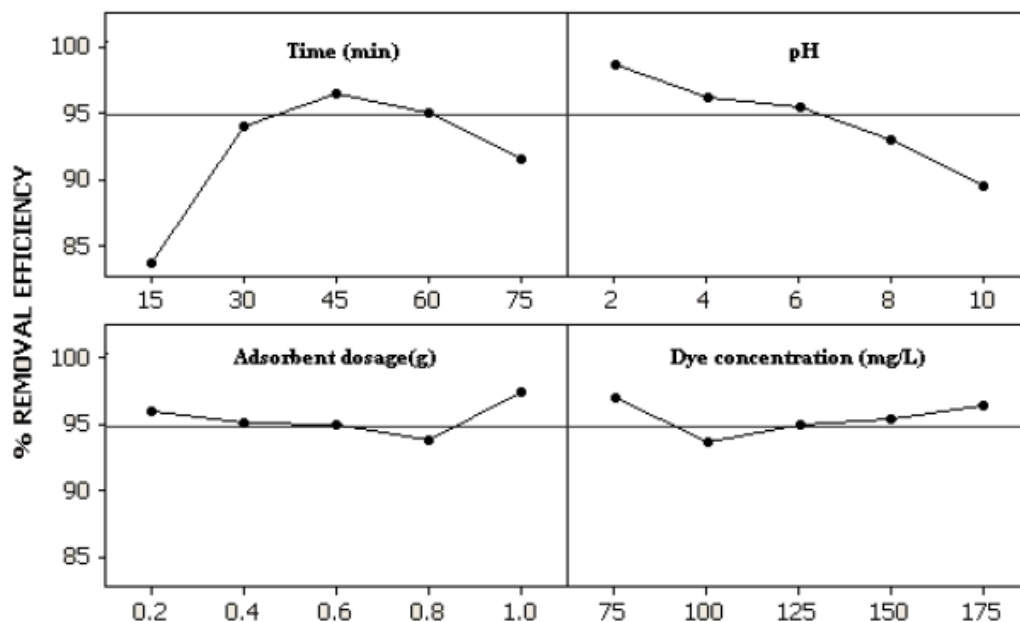


Figure 5. Main effects plot of parameters for AB 25 removal

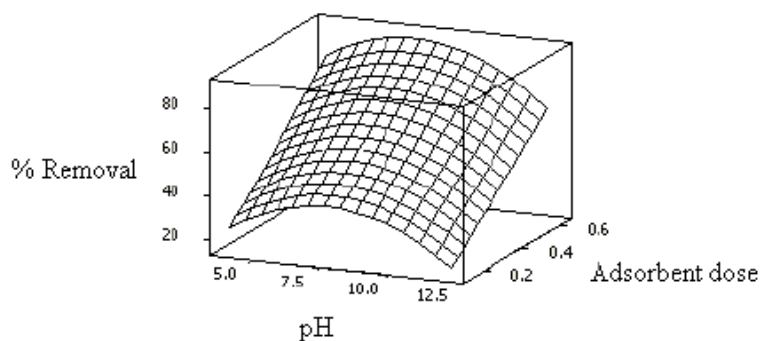


Figure 6. Response surface plot of AY 17 dye removal (%) showing interactive effect of adsorbent dose and pH

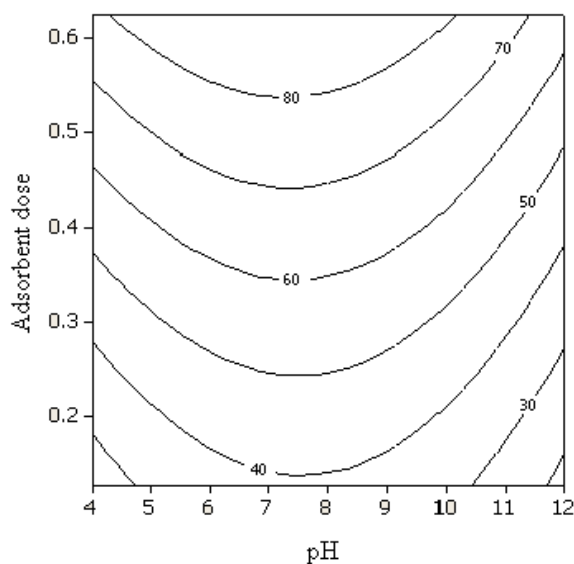


Figure 7. Response contour plot of AY 17 dye removal (%) showing interactive effect of adsorbent dose and pH.

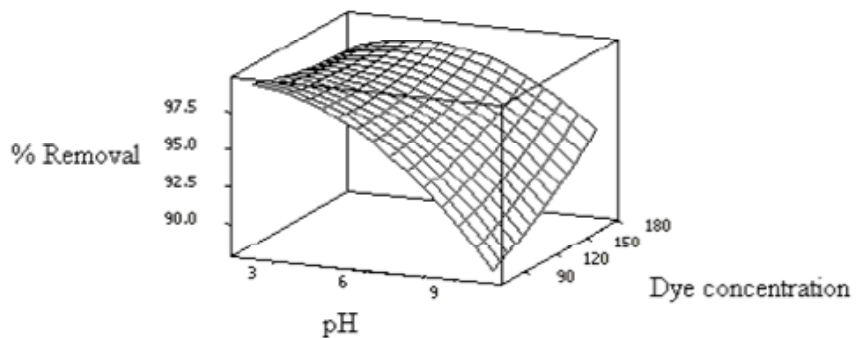


Figure 8. Response surface plot of AB 25 dye removal (%) showing interactive effect of pH and dye concentration

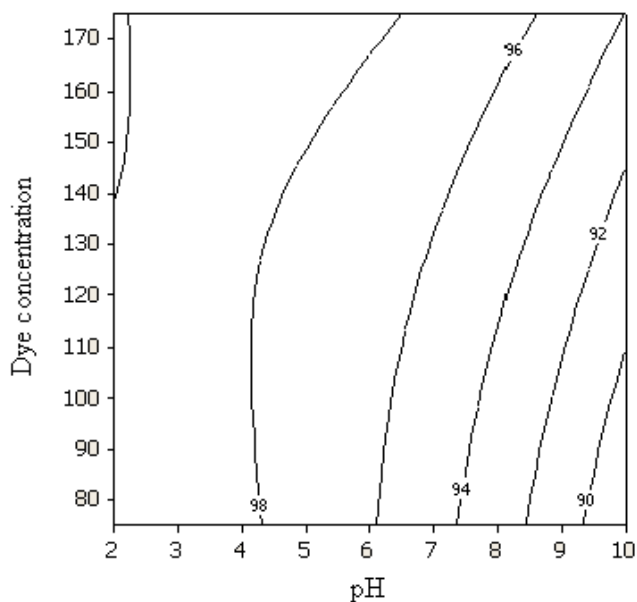


Figure 9. Response contour plot of AB 25 dye removal (%) showing interactive effect of pH and dye concentration

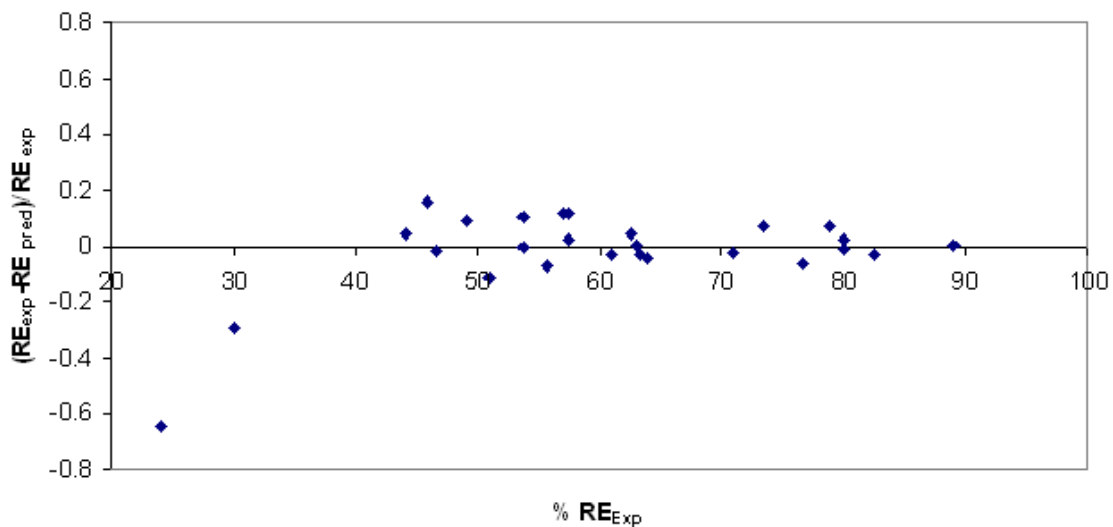


Figure 10. Comparison of experimental and predicted removal efficiency for AY 17

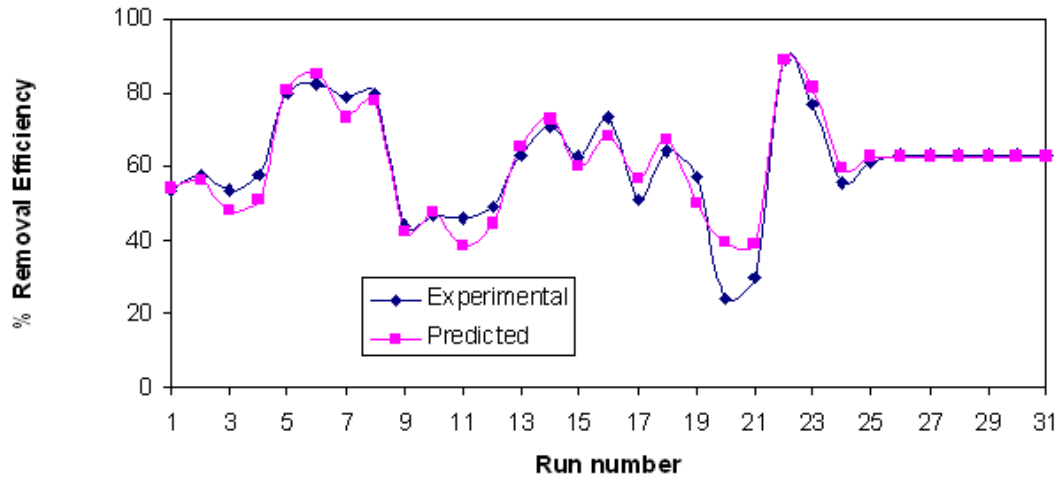


Figure 11. Relative deviation between experimental and predicted removal efficiency for AY 17

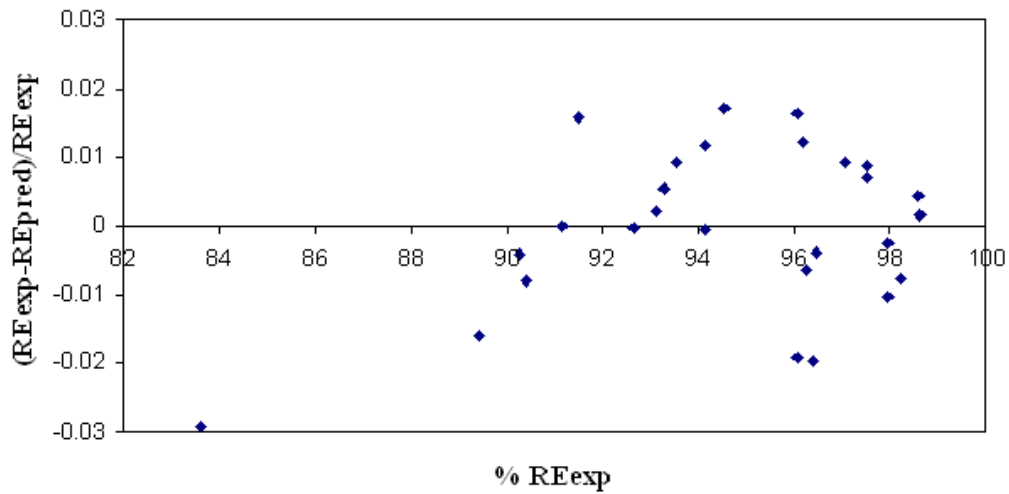


Figure 12. Comparison of experimental and predicted removal efficiency for AB 25

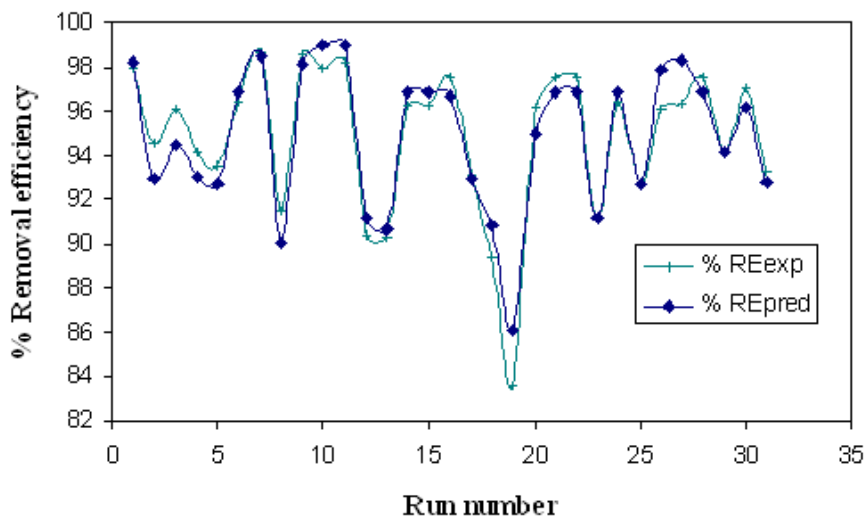


Figure 13. Relative deviation between experimental and predicted removal efficiency for AB 25



Vector Control System of Induction Motor Based on Fuzzy Control Method

Haobin Zhou, Bo Long & Binggang Cao
School of Mechatronic Engineering
Xi'an JiaoTong University, Xi'an 710049, China
E-mail: hbzhou@xysu.edu.cn

Abstract

Aiming at non-linear model of multivariable induction motor, traditional PI method is hard to achieve satisfactory control purpose. Fuzzy control can carry the real-time control on system without the accurate mathematical model of induction motor. This paper elaborates induction motor vector control system and the basic principle of the fuzzy PI, making use of fuzzy reasoning, automatically adjusting the controller's parameters. Simulation results prove that fuzzy PI controller is superior to traditional PI controller in the aspect of response speed, steady state accuracy and disturbance attenuation.

Keywords: Fuzzy control, Vector control, Adjustment parameter

1. Introduction

PI control algorithm is simple, realized easily, used in traditional induction motor speed regulating system usually. With the demand of save energy performance and technical and economic target of speed regulating system, PI control have some limitation. For complex model of induction motor, the parameter of the controller is hard auto adjust to adapt outside conditional variety, making the control of motor inaccuracy. To have better adaptability, realize the automatic adjustment of the controller parameter, can adopt the method of the fuzzy control theories. The fuzzy control can realize the automatic adjustment of the control parameter, with strong adaptability and good speed governing. This paper apply vector control method on induction motor, use the decoupling of rotor flux linkage and torque, practice a continuous control, comparatively width speed governing scope. Electric current loop use space vector pulse width modulation, and design a kind of controller of self- adaptation fuzzy control, proceed simulation study through Matlab/Simulink, carry on contrast with traditional PI controller.

2. Vector control system

2.1 Induction motor model

Dynamic model of induction motor is a high, nonlinear, close coupled and multivariable system. Take forward of voltage, current, flux linkage of each winding as motor routine and right-hand screw rule. At this time, mathematical model of induction motor is constitute by voltage equation, flux linkage equation, torque equation of two-phase arbitrary revolution coordinate as follows:

(1) voltage equation

$$\begin{bmatrix} u_{sd} \\ u_{sq} \\ u_{rd} \\ u_{rq} \end{bmatrix} = \begin{bmatrix} R_s + L_s p & -\omega_r L_s & L_m p & -\omega_r L_m \\ \omega_r L_s & R_s + L_s p & \omega_r L_m & L_m p \\ L_m p & -\omega_r L_m & R_r + L_r p & -\omega_r L_r \\ \omega_r L_m & L_m p & \omega_r L_r & R_r + L_r p \end{bmatrix} \begin{bmatrix} i_{sd} \\ i_{sq} \\ i_{rd} \\ i_{rq} \end{bmatrix} \quad (1)$$

(2) flux linkage equation

$$\begin{cases} \psi_{sd} = L_s i_{sd} + L_m i_{rd} \\ \psi_{sq} = L_s i_{sq} + L_m i_{rq} \\ \psi_{rd} = L_m i_{sd} + L_r i_{rd} \\ \psi_{rq} = L_m i_{sq} + L_r i_{rq} \end{cases} \quad (2)$$

(3) electromagnetic torque equation

$$T_e = n_p L_m (i_{sq} i_{rd} - i_{sd} i_{rq}) \tag{3}$$

2.2 Vector principle

The basic principle of vector control is to simulate torque control rule of direct current motor in general three-phase AC motor, stator current vector is decomposed to field current component that generate magnetic flux and torque current component that generate torque, make them orthogonal and arm s length sale, and adjust independent. So, torque control of AC motor is similar to DC motor in principle. The key of vector control is to control amplitude and spatial location (frequency and phase).

In antecedent dynamic model analysis, as to synchronous revolution coordinate, $\omega_{dqs} = \omega_1$, $\omega_{dqr} = \omega_1 - \omega = \omega_s$, the inner part of rat cage motor is short-circuit, $u_{rd} = u_{rq} = 0$ state equations is achieved:

$$\begin{aligned} \frac{d\omega}{dt} &= \frac{p_n^2 L_m}{J L_r} (i_{sq} \Psi_{rd} - i_{sd} \Psi_{rq}) - \frac{p_n}{J} T_L \\ \frac{d\Psi_{rd}}{dt} &= -\frac{1}{T_r} \Psi_{rd} + (\omega_1 - \omega) \Psi_{rq} + \frac{L_m}{T_r} i_{sd} \\ \frac{d\Psi_{rq}}{dt} &= -\frac{1}{T_r} \Psi_{rq} + (\omega_1 - \omega) \Psi_{rd} + \frac{L_m}{T_r} i_{sq} \\ \frac{di_{sd}}{dt} &= \frac{L_m}{\sigma L_s L_r T_r} \Psi_{rd} + \frac{L_m}{\sigma L_s L_r} \omega \Psi_{rq} - \frac{R_s L_s^2 + R_r L_m^2}{\sigma L_s L_r^2} i_{sd} + \omega_1 i_{sq} + \frac{u_{sd}}{\sigma L_s} \\ \frac{di_{sq}}{dt} &= \frac{L_m}{\sigma L_s L_r T_r} \Psi_{rq} - \frac{L_m}{\sigma L_s L_r} \omega \Psi_{rd} - \frac{R_s L_s^2 + R_r L_m^2}{\sigma L_s L_r^2} i_{sq} - \omega_1 i_{sd} + \frac{u_{sd}}{\sigma L_s} \end{aligned} \tag{4}$$

In the equation: σ -motor leakage coefficient, $\sigma = 1 - L_m^2 / L_s L_r$, T_r -rotor electromagnetic time constant. $T_r = L_r / R_r$

If daxis is taken as direction of whole flux linkage vector, anti-clockwise 90 is q axis, it against to vector, named T axis, this two phase synchronous revolution coordinate is based on field orientation coordinate. M axis is rotor field orientation, T axis is torque control component. Like DC motor, it control individual field current and torque current so that control torque. So, $\Psi_{rd} = \Psi_{rm} = \Psi_r$, $\Psi_{rq} = \Psi_{rt} = 0$, $\Psi_{rt} = 0$, state equations substituted is given:

$$\omega_{st} = L_m i_{st} / T_r \psi_r \tag{5}$$

$$i_{sm} = (T_r p + 1) \psi_r / L_m \tag{6}$$

It can be seen, rotor field is generated by state current having no relation to torque component, speak from this meaning, field excitation component and torque component of state current is decoupling.

The above formula still expresses that both are first-order inertia link, time constan is rotor flux field time constant, when field excitation i_{sm} happen to change suddenly, the change of Ψ_r is objected by field excitation inertia, seeing from this, inertial function of DC motor field-winding is same to the Ψ_r . Mathematical model is described as following structural style.

3. Fuzzy PI controller design

Under the circumstance of nonlinear and parameter time- varying object controlled, accurate model can not be given. Although traditional PID control is simple, controlling result better, it can not solve the circumstance that model parameter occur variety, moreover, in practical spot, because of being subjected to parameter setting, traditional PID parameter setted is not good, its performance is not quite good, be badly to the adaptability. So, according to complex circumstance appllied and the control request of high-performance, having an urgent request to PID parameter self-setted, fuzzy control to PID setted is a good solution.

3.1 Fuzzy PI principle

Fuzzy control is computer intelligent control based on fuzzy set theory, fuzzy language, fuzzy logical-inference, its basic idea is presented by famous professor named L.A.Zadeh in California university in America, who achieved the great success in fuzzy control theory and application study through development of many years.

3.2 Fuzzy PI parameter setted

Fuzzy self adapting controller has many kind of structural style at the present time, but their operating principle is same to each other. Fuzzy self adapting controller take error e and error alteration ec as an input, amend parameter at a real time using fuzzy control regulation, these constitute fuzzy self adapting controller.

PID parameter fuzzy self adapting is to find fuzzy relationship of three parameter, e and ec, check e and ec continuously in service, according to fuzzy control principle amending three parameter in real time, meeting the different need of controlled parameter in different time, making object controlled having good dynamic and static character.

The core of PID controller design that parameter fuzzy self-adapting is to create suitable fuzzy regulation, see figure 1,

figure 2, figure 3 individually. At the present, the building of fuzzy regulation is achieved by generalizing experience of operation crews, analysing closed loop response of system, and using method of trial and error through many simulation test.

Establish fuzzy controller inferenced by Mamdani of 1 two-input and three-output using figure windows editor, supposed that input and output is (-3,3),corresponding language value is negative big(NB),negative middle(NM), negative small(NS), zero(Z), positive small(PS), positive middle(PM), positive big (PB), all the degree of membership function of input and output variance are trimf, see figure 2.fuzzy regulation table of Kp see Table 1, fuzzy regulation table of Ki see Table 2,fuzzy regulation table of Kd see Table 3.

4. Simulation result

Simulation curve diagram is from figure 4 to figure 6. Figure 3 and figure 4 express individually that speed response curve of fuzzy PI and PI with a speed code valuation equal to 120rpm/min, rotational speed is zero at initial state, when time is equal to 0.5 second. Figure 5 and figure 6 express individually that torque response curve of fuzzy PI and PI with a torque code valuation equal to 150N.m, rotational speed is zero at initial state, when time is equal to 1 second.

See from simulation result, with initial code valuation, fuzzy PI controller is better than traditional PI controller in speed response and overshoot suppression. When there is some load torque, the former is very excellent in against-interference ability and robust is strong. Under the circumstance of adding code valuation, fuzzy PI controller is superior to traditional PI controller in speed response and steady-state error, which meet the design request.

5. Conclusion

Aiming at the characteristic of induction motor with higher order, nonlinear, closed linkage, adopt vector control system according to rotor field orientation control method, integrate fuzzy and PI these two algorithm, design a kind of self-adapting fuzzy controller, proceed simulation test using fuzzy tool in Matlab, compare to traditional PI controller, test express that fuzzy PI controller is superior to traditional PI controller in speed response, steady-state accuracy and against-inference.

References

A. Visioli. (2001). *Tuning of PI controllers with fuzzy logic*[J].IEEE Proc-Control Theory, 2001, 148(1): 69~81.
 Chen, boshi. (2005). *AC speed system*[M]. Beijing: Machinery Industry Press, 2005.
 Driankov, D.H.Hellendoorn, M.Reinfrank. (1993). *An Introduction to Fuzzy Control, Springervrelag*, Berlin.1993.
 Edson, Bim. (2001). *Fuzzy Optimization for Rotor Constant Identification of an Indirect FOC Induction Motor Drive*. [J]*IEEE Transactions on Industrial Electronics*, 2001, 48 (6): 1293~1295.
 Karr, C L, etal. (1993). Fuzzy control of PH using genetic algorithms.*IEEE Trans.on Fuzzy Systems*, 1993, 1. (1) 46~53.
 L. A. Zadeh. (1968). *Fuzzy Algorithms* [J].Information and Control, 1968 (12): 28~30.
 L.A. Zadeh. (1968). *Fuzzy Algorithms* [J]. Information and Control, 1968, 12.
 Lin, C. T. (1994). *Neural Fuzzy Control Systems with Structure and Parameter Learning*,*World Scientific*.Singapore, 1994.
 Wen, xin, Zhou, lu, (2001). *MATLAB toolbox Fuzzy Logic Analysis and Application*[M].beijing: Beijing Science Press, 2001.
 Yi, jigai, Hou, yuanbin. (2004). *Intelligent Control Technology(Fifth Edition)*[M].beijing: Beijing Industrial University Press, 2004.

Table 1. fuzzy regulation table of Kp

Δkp	ec	NB	NM	NS	Z	PS	PM	PB
e	NB	PB	PB	PM	PM	PS	Z	Z
NM	PB	PB	PM	PS	PS	Z	NS	NS
PS	PM	PM	PM	PS	Z	NS	NS	NS
Z	PM	PM	PS	Z	NS	NM	NM	NM
PS	PS	PS	Z	NS	NS	NM	NM	NM
PM	PS	Z	NS	NM	NM	NM	NM	NB
PB	Z	Z	NM	NM	NM	NM	NB	NB

Table 2. fuzzy regulation table of Ki

Δk_i ec	NB	NM	NS	Z	PS	PM	PB
NB	NB	NB	NM	NM	NS	Z	Z
NM	NB	NB	NM	NS	NS	Z	Z
PS	NB	NM	NS	NS	Z	PS	PS
Z	NM	NM	NS	Z	PS	PM	PM
PS	NM	NS	Z	PS	PS	PM	PB
PM	Z	Z	PS	PS	PM	PB	PB
PB	Z	Z	PS	PM	PM	PB	PB

Table 3. fuzzy regulation table of Kd

Δk_d ec	NB	NM	NS	Z	PS	PM	PB
NB	PS	NS	NB	NB	NB	NM	PS
NM	PS	NS	NB	NM	NM	NS	Z
PS	Z	NS	NM	NM	NS	NS	Z
Z	Z	NS	NS	NS	NS	NS	Z
PS	Z	Z	Z	Z	Z	Z	Z
PM	PB	PS	PS	PS	PS	PS	PB
PB	PB	PM	PM	PM	PS	PS	PB

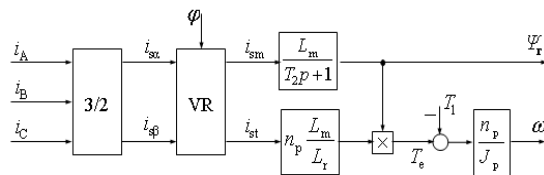


Figure 1. mathematical model of vector transformation and current decoupling of induction motor

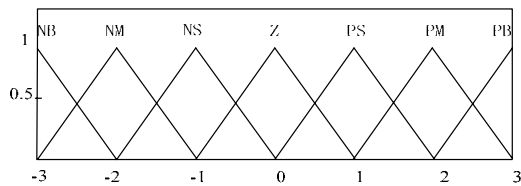


Figure 2. degree of membership function of e, ec, Kp, Ki, Kd

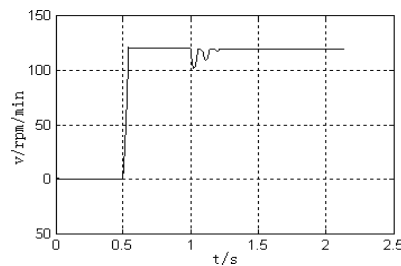


Figure 3. speed response curve of PI algorithm controller

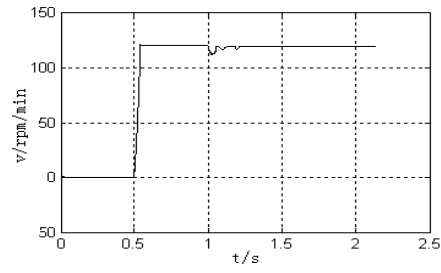


Figure 4. speed response curve of fuzzy PI algorithm controller

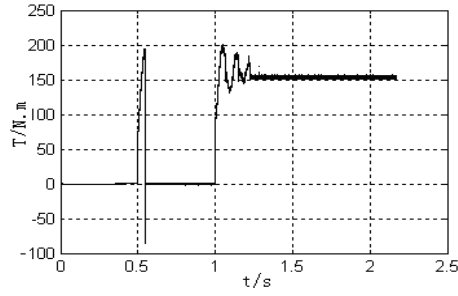


Figure 5. torque response curve of PI algorithm controller

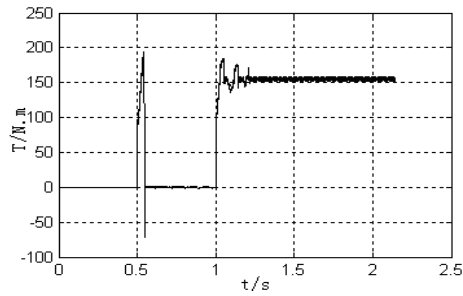


Figure 6. torque response curve of fuzzy PI algorithm controller



Investigation on Ethylenediaminetetra-Acetic Acid as Corrosion Inhibitor for Mild Steel in 1.0M Hydrochloric Acid

Ahmed Y. Musa (Corresponding author)

Department of Chemical and Process Engineering
Universiti Kebangsaan Malaysia, Bangi, 43600, Selangor, Malaysia
Tel: 60-17-308-6840 E-mail: ahmed.musa@ymail.com

Abdul Amir H. Kadhun

Department of Chemical and Process Engineering
Universiti Kebangsaan Malaysia, Bangi, 43600, Selangor, Malaysia
Tel: 60-3-8921-6411 E-mail: amir@eng.ukm.my

Mohd Sobri Takriff

Department of Chemical and Process Engineering
Universiti Kebangsaan Malaysia, Bangi, 43600, Selangor, Malaysia
Tel: 60-3-8921-6400 E-mail: sobri@eng.ukm.my

Abdul Razak Daud

School of Applied Physics
Universiti Kebangsaan Malaysia, Bangi, 43600, Selangor, Malaysia
Tel: 60-3-8921-3806 E-mail: kpfg@ukm.my

Siti Kartom Kamarudin

Department of Chemical and Process Engineering
Universiti Kebangsaan Malaysia, Bangi, 43600, Selangor, Malaysia
Tel: 60-3-8921-6422 E-mail: ctie@eng.ukm.my

The research is financed by National University of Malaysia. No.UKM GUP-BTT-07-25-170

Abstract

The influence of ethylenediaminetetra-acetic acid (EDTA) on the corrosion of mild steel in 1.0 M hydrochloric acid solution was investigated by means of potentiodynamic polarization and electrochemical impedance spectroscopy (EIS). The efficiency of EDTA was compared with thiourea. Primary results obtained revealed that EDTA performed as good corrosion inhibitor for mild steel in 1.0 M hydrochloric acid media comparing with thiourea. Polarization curves show that the behavior of EDTA and thiourea are mixed-type inhibitors. EIS shows that the control step for corrosion process is a charge transfer mechanism.

Keywords: Corrosion inhibitor, Ethylenediaminetetra-acetic acid, Thiourea, Mild steel, Electrochemical measurement

1. Introduction

Mild steel is widely used as a constitutional material in many industries due to its good mechanical properties and low cost. The corrosion of mild steel is of fundamental academic and industrial concern that has received a considerable amount of attention. Acid pickling baths are employed to remove undesirable scale from the surface of the metals. Once the scale is removed, the acid is then free for further attack on the metal surface. The use of inhibitor is one of the most practical methods for protection against corrosion, especially in acidic media.

A survey of literature reveals that the applicability of organic compounds as corrosion inhibitors for mild steel in acidic media has been recognized for a long time. Compounds studied as inhibitors include triazole derivatives (Bentiss et al 1999a, Bentiss et al 1999b), bipyrazolic derivatives (Touhami et al 2000), surfactants (Algaber et al 2004, Branzoi et al 2000) aromatic hydrazides (Quraishi et al 2001), organic dyes (Oguzie et al 2004a, Oguzie et al 2005b), Poly

(4-vinylpyridine) (Larabi et al 2004) and thiosemicarbazide-type organic compounds (Benali 2006). These compounds can adsorb on the mild steel surface and block the active sites decreasing the corrosion rate.

This paper describes the affect of ethylenediaminetetra-Acetic acid (EDTA), $C_{10}H_{16}N_2O_8Na_2$, on corrosion inhibition of mild steel in 1.0M hydrochloric acid solutions comparing with thiourea. Figure 1 shows the molecular structure of used inhibitors.

2. Experimental

Commercially mild steel metal was used. Sample was mechanically polished using SiC paper in successive grades from 200 to 1500 and was rinsed with methanol. The acid solutions were made from RA grade HCl. Appropriate concentration of acid was prepared by using distilled water. The measurements were carried out in a three electrodes electrochemical cell with a graphite counter electrode and saturated calomel electrode (SCE) as reference. Potentiodynamic polarization curves were obtained starting from E_{corr} with the potential scan rate of 125 μ V/s. EIS measurement was carried out on steady state open circuit potential (OCP) disturbed with amplitude of 10 mV A.C. sine wave at frequencies between 0.01 Hz and 100 KHz. Measurements were performed at room temperature using Potentiostat/Galvanostat/ZRA (Gamery instrument, Ref600 model, USA)

3. Results and Discussion

3.1 Polarization measurements

The effect of the concentration of EDTA and thiourea are shown in Figure 2 which presents the anodic and cathodic Tafel curves of mild steel in 1 M HCl. Values of anodic β_a and cathodic β_c Tafel constant and corrosion current density are listed in Table 1 and 2. These values were calculated from the intersection of the anodic and cathodic Tafel lines of the polarization curve at E_{corr} . The inhibition efficiencies are calculated by the following expression:

$$IE\% = \frac{i_{uninhibit} - i_{inhibit}}{i_{uninhibit}} \times 100 \quad (1)$$

where $i_{uninhibit}$ and $i_{inhibit}$ are respectively, the corrosion current density without and with EDTA or thiourea in 1.0 M HCl solution.

The anodic and cathodic Tafel lines for mild steel in presence of EDTA or thiourea were almost parallel upon increasing inhibitor concentrations. This suggests that the inhibitor act by simple blocking the mild steel surface (Manahan, 1996). In the other words, the inhibitor decreasing the exposed surface area for corrosion as well as it doesn't affect the mechanism of mild steel dissolution or hydrogen evolution reaction. Only when the change in E_{corr} value is no less than 85 mV, a compound can be recognized as an anodic or a cathodic type inhibitor (Ashassi-Sorkhabi et al 2004). The largest displacement of the corrosion potentials (E) were about 8 mV and 11 mV in presence of EDTA and thiourea, respectively. Therefore, EDTA and thiourea are acts as corrosion mixed-type inhibitors. Also the inhibition efficiencies increase with increasing inhibitors concentration as shown in Table 1 and 2.

3.2 EIS measurements

The results of EIS were figured by Nyquist plots, Figure 3. Double layer capacitance values (Cdl) and polarization resistance values (Rp) were obtained from impedance as described by Moretti (2004). The fitted values of Rp and Cdl are listed in Table 1 and 2. The inhibition efficiencies IE% is calculated by polarization resistance (Rp) as follows:

$$IE\% = \frac{R_{p(uninhibit)} - R_{p(inhibit)}}{R_{p(uninhibit)}} \times 100 \quad (2)$$

The Rp values increase with the increase in concentration of either EDTA or thiourea, indicating an insulated adsorption layer formation; the decrease in Cdl values suggested a decrease in local dielectric constant between the metal and electrolyte induced by the adsorption of EDTA or thiourea (Khaled and Hackerman 2003).

4. Conclusion

EDTA showed good inhibition performance comparing with thiourea. Polarization curves indicated that the EDTA and thiourea behave mainly as mixed-type inhibitors. EIS showed that the charge transfer controls the corrosion process in the uninhibited and inhibited solutions either for EDTA or thiourea.

Acknowledgment

This work was supported by National University of Malaysia (No. UKM GUP-BTT-07-25-170) which is gratefully acknowledged.

References

- Algaber AS, EM. El-Nemna, & Saleh MM. (2004). Effect of octylphenol polyethylene oxide on the corrosion inhibition of steel in 0.5 M H₂SO₄. *Journal of Materials Chemistry and Physics*, 86, 26-32.
- Ashassi-Sorkhabi H, MR. Majidi, & Seyyedi K. (2004). Investigation of inhibition effect of some amino acids against steel corrosion in HCl solution. *Journal of Applied Surface Science*, 225, 176-185.
- Benali O, L. Larabi, S.M Mekelleche, & Harek Y. (2006). Influence of substitution of phenyl group by naphthyl in a diphenylthiourea molecule on corrosion inhibition of cold-rolled steel in 0.5 M H₂SO₄. *Journal of Material Science*, 41, 7064-7073.
- Bentiss F, M. Traisnel, L. Gengembre and .Lagrene ' e. M. (1999a). A new triazole derivative as inhibitor of the acid corrosion of mild steel: electrochemical studies, weight loss determination, SEM and XPS. *Journal of Applied Surface Science*, 152, 237-249.
- Bentiss F, M. Lagrene ' e, M. Traisnel, & Gornez J. (1999b). The corrosion inhibition of mild steel in acidic media by a new triazole derivative. *Journal of Corrosion Science*, 41, 789-803.
- Branzoi V, F. Branzoi, & Baibarac M. (2000). The inhibition of the corrosion of armco iron in HCl solutions in the presence of surfactants of the type of n-alkyl quaternary ammonium salts. *Journal of Materials Chemistry and Physics*, 65, 288-297.
- Khaled KF, & Hackerman N. (2004). Investigation of the inhibitive effect of ortho-substituted anilines on corrosion of iron in 0.5 M H₂SO₄ solutions. *Journal of Materials Chemistry and Physics*, 82, 949-960.
- Larabi L, Y. Harek, M. Traisnel, & Mansri A. (2004). Synergistic influence of poly(4-vinylpyridine) and potassium iodide on inhibition of corrosion of mild steel in 1 M HCl. *Journal of Applied Electrochemistry*, 34,833-889.
- Manahan SE. (1996). Environmental Chemistry. sixth ed. Lewis Publishers, (Chapter 6).
- Moretti, G., Guidi, F., and Grion, G. (2004), Tryptamine as a green iron corrosion inhibitor in 0.5 M deaerated sulphuric acid, *Corrosion science*, 46, 387-403.
- Oguzie EE, C. Unaegbu, CBN. Okolue, & Onuchukwu AI. (2004a). Inhibition of mild steel corrosion in sulphuric acid using indigo dye and synergistic halide additives. *Journal of Materials Chemistry and Physics*, 84,363-368.
- Oguzie EE, GN. Onuoha, & Onuchukwu AI. (2005b). Inhibitory mechanism of mild steel corrosion in 2 M sulphuric acid solution by methylene blue dye. *Journal of Materials Chemistry and Physics*, 89, 305-311.
- Quraishi MA, R. Sardar, & Jamel D. (2001). Corrosion inhibition of mild steel in hydrochloric acid by some aromatic hydrazides. *Journal of Materials Chemistry and Physics*, 71, 309-313.
- Touhami T, A. Aounti, Y. Abed , B. Hammouti , S. Kertit , A. Ramdani, & K. Elkacemi. (2000). Corrosion Inhibition of Armco Iron In 1 M Hcl Media By New Bipyrzolic Derivatives. *Corrosion Science*, 42, 929-94.

Table 1. Polarization parameters and EIS parameters for mild steel in 1.0 M HCl with different concentrations of EDTA

Technique	Parameters	Inhibitor concentration (mg/l)					
		Blank	10	20	40	80	160
Polarization parameters	E _{corr} (mV)	493	497	500	499	503	495
	I _{corr} (μA/cm ²)	615	452	356	334	289	192
	β _a (mV/decade)	0.12	0.16	0.11	0.1	0.1	0.1
	β _c (mV/decade)	0.14	0.17	0.13	0.13	0.13	0.12
	IE%	0	26.50	42.11	45.69	53.01	68.78
EIS parameters	R _p (ohm. cm ²)	36.5	48.06	49.23	54.15	55.02	68
	C _{dl} (μF/cm ²)	173.9	137.6	127.7	113.1	111.9	89.5
	IE%	0	24.05	25.86	32.59	33.66	46.32

Table 2. Polarization parameters and EIS parameters for mild steel in 1.0 M HCl with different concentrations of thiourea

Technique	Parameters	Inhibitor concentration (mg/l)					
		Blank	10	20	40	80	160
Polarization parameters	E _{corr} (mV)	493	510	512	507	514	513
	I _{corr} (μA/cm ²)	615	504	431	371	298	234
	β _a (mV/decade)	0.12	0.11	0.10	0.11	0.10	0.12
	β _c (mV/decade)	0.14	0.13	0.13	0.13	0.12	0.13
	IE%	0.00	18.05	29.92	39.67	51.54	61.95
EIS parameters	R _p (ohm. cm ²)	36.5	68.27	73.64	84.64	86.59	95.55
	C _{dl} (μF/cm ²)	173.9	147.4	135,2	127.2	114.5	85.4
	IE%	0	46.53	50.43	56.87	57.84	61.8

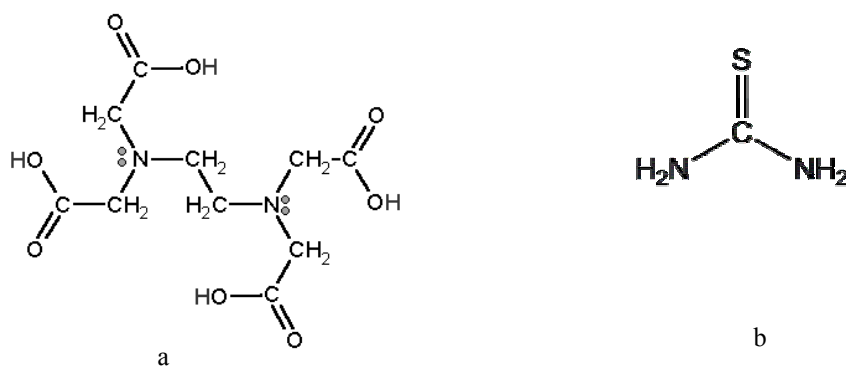
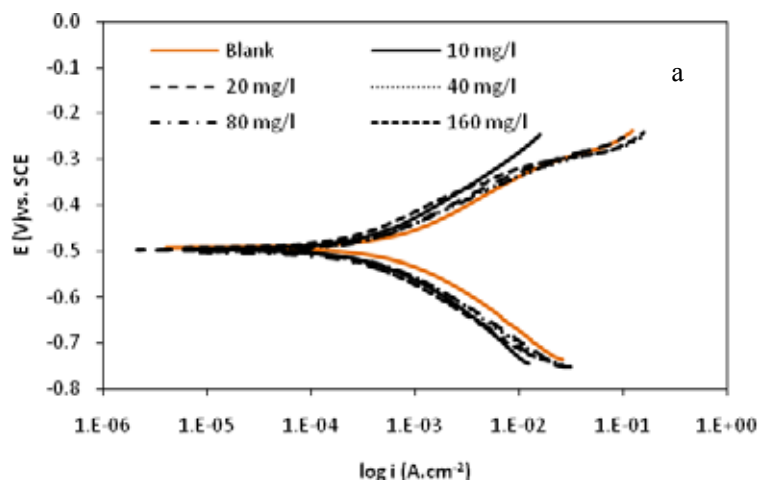


Figure 1. Molecular structures for EDTA (a) and thiourea (b)



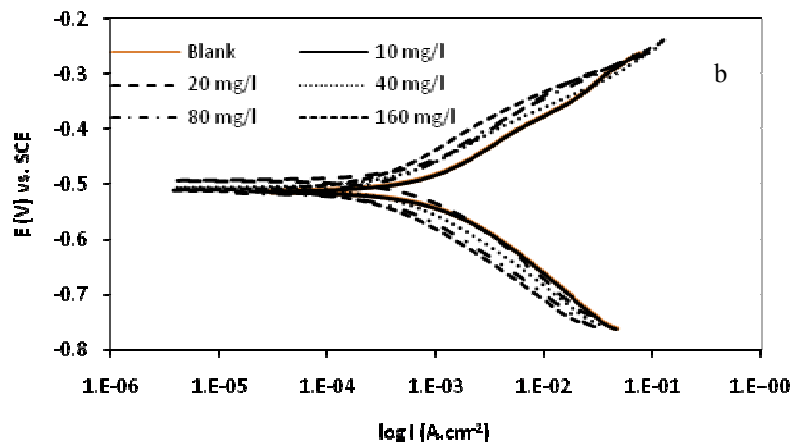


Figure 2. Polarization curves for mild steel in 1.0 M HCl with different concentrations of EDTA (a) and thiourea (b)

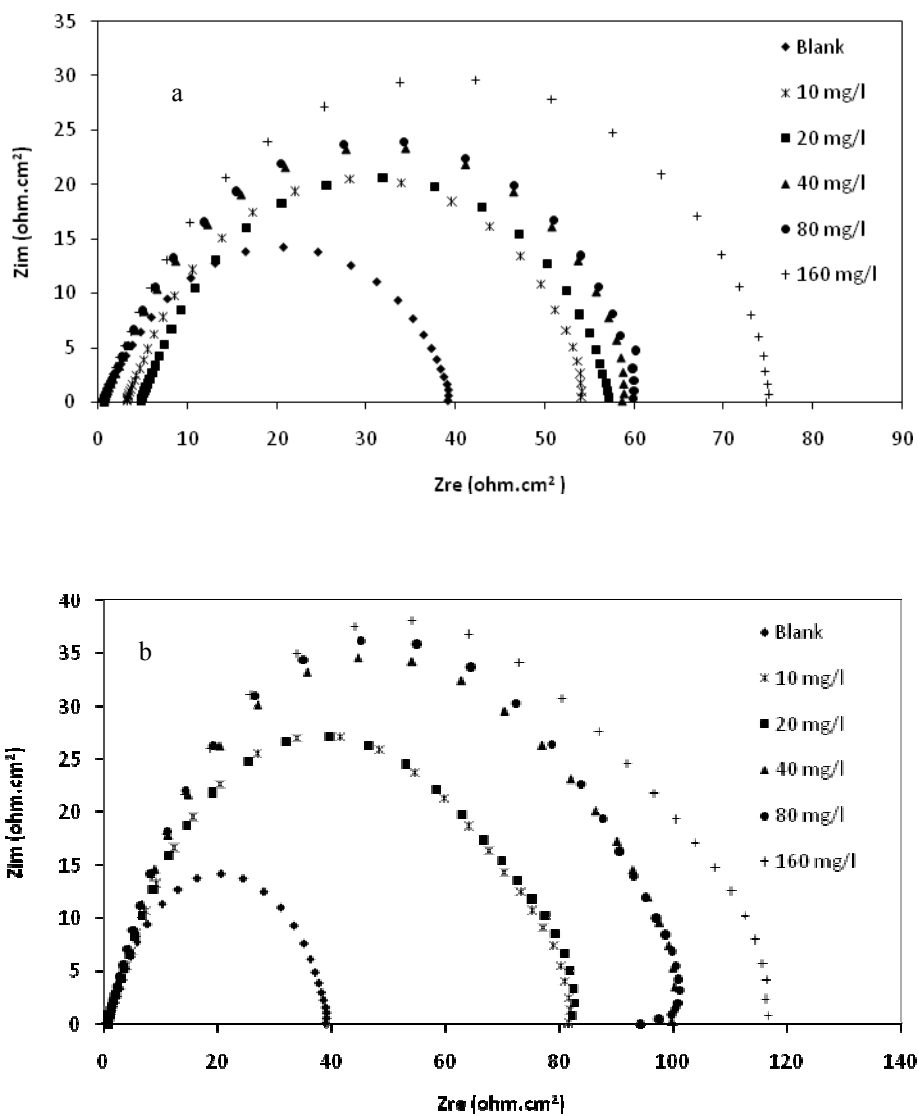


Figure 3. Nyquist plots for mild steel in 1.0M HCl with different concentrations of EDTA (a) and thiourea(b)



Study on the Intelligent Video Monitoring Technology and Its Applications

Yi Wang

China Criminal Police University, Shenyang 110035, China

Tel: 86-24-8678-8898 E-mail: wangyi1513@yahoo.com.cn

Abstract

The intelligence, the digitization and the networking are the necessary trend for the development of the video monitoring technology, and the occurrence of the intelligent video monitor is the direct embodiment of this trend. The intelligent video monitoring equipment possesses stronger image processing ability and more intelligent factors than common network video monitoring equipment, and it can provide more super video analysis functions for users, and it can largely enhance the ability of the video monitoring system and makes the video resources exert stronger functions.

Keywords: Video monitoring, Intelligent, Digitization, Networking

For about twenty years, the video monitoring system has experienced three stages from the first generated a hundred percent analog system, i.e. the video cassette recorder (VCR), to the second generated partial digital system, i.e. the digital video recording/ network video recorder (DVR/NVR), and to the third generated complete digital system, i.e. the network camera and the video server. In this evolution process, though the video monitoring system and equipments were largely enhanced for the functions and performances, but it is still limited by some intrinsic factors which includes onto only human physiological weakness, but the limitations of the functions and performances in the video monitoring system and equipment. These limited factors make various video monitoring systems have many deficiencies such as the bad alarming precision, the misinformation and report failure, long alarming response time and difficult video data analysis more or less, so the security and the practicability of the whole system will be reduced.

In recent years, with the quick enhancement of the network bandwidth, the computer processing ability and the memory capacity, the occurrence of various video information processing technologies, the advantages of the digital and networking video monitoring system are more and more obvious, and its highly opening, integration and flexibility create necessary conditions for the enhancement of the whole performance of the video monitoring system and equipment, and offer more abroad development space for the development of the whole security and protection industry. The new application mode and the market opportunities continually occur, and the intelligent video monitoring technology is one of the most popular applications modes in the networking video monitoring domain.

1. The concept of the intelligent video

The intelligent video (IV) is from the computer vision (CV) technology which is one of branch of the artificial intelligent (AI) research, and CV can establish the mapping relation between the image and the image description and make the computer to understand the contents in the video image through the digital image processing and analysis. The IV in the video monitoring technology mainly means “automatically analyzing and abstracting the key information in the video resources”. If the camera is taken as human eyes, the intelligent video system or equipment is human brain. In virtue of strong data processing function of the computer, the intelligent video technology analyzes the large numbers of data in the video pictures with high speed, filtrate the information which users don't care about, and only offer useful key information for the supervisor.

The intelligent video monitoring takes the digitization and networking video monitoring as the base, but it is different with general networking video monitoring, and it is a sort of more super video monitoring application. The intelligent video monitoring system can identify different objects, find the abnormal circumstances in the supervising pictures, and emit alarms and offer useful information by the quickest and optimal mode to assist security personnel to deal with the crisis more effectively and reduce the misinformation and report failures to the largest extents. In the day that the world anti-terrorist battle is more and more drastic, the intelligent video monitoring obviously can be the powerful assistant tool to reply the terrorist attack and deal with the emergencies. In addition, the intelligent video monitoring technology can also be applied in many non-security relative situations such as the traffic management, the client behavior analysis and the client service to enhance users' investment returns.

2. The advantages of the intelligent video

The intelligent video monitoring is based on the general networking video monitoring, and except for the advantages of the networking video monitoring, the intelligent video monitoring system can bring more benefits for users as follows.

(1) 24 x 7 hours reliable monitoring. The intelligent video monitoring will fully change the past mode that the monitoring pictures are supervised and analyzed by the security personnel, and it persistently analyze the monitored pictured through the intelligent video module embedded in the front end equipment (the networking camera or the video server).

(2) Largely enhancing the alarming precision. The front end equipment (the networking camera or the video server) can integrate powerful image processing ability, run the super intelligent algorithm, make users more exactly define the characters of the security threats, reduce the misinformation and the report failures effectively, and decrease the useless data.

(3) Largely enhancing the response speed. The intelligent video monitoring can identify suspicious activities (for example, someone leaves suspicious objects in public places, or someone stays too long in the sensitive region), and reminder security personnel to notice the relative supervision pictures to prepare before the security threat happens, and it can also make users more exactly define the special security threat and adopt proper actions, and ensure the crisis processing approaches could be exerted exactly accruing to the plan, and effectively prevent the delays induced by the man-made factors in the confusion.

(4) Effectively extending the purposes of the video resource. The intelligent video monitoring can apply the video resource into the non-security domains, for example, the monitoring system in the main foyer of the marketplace can be used to automatically identify VIP users' characters, and inform client service personnel to make services in time, and when it finds some one slips up, it will inform of relative personnel to offer helps. In addition, the intelligent video system can help the boss of the retail store to count the consumer quantity in the present day, which can be used to analyze the sales goods for the store.

3. The main potential applications of the intelligent video

The application of the intelligent video can be divided into two sorts, i.e. the security correlative application and the non-security correlative application. The correlative application of the security mainly means the intelligent video application in the present market, and especially after "Sep. 11" attack, Madrid explosion and London explosion, the demands about this sort continually increase. This sort of application is mainly used to enhance the security and protection of the public environment in the large outside region for the government or the security department in other institutions. And this sort of application mainly includes the advanced VMD, motion tracking, facial detection, vehicle identification and object persistence.

The memory structure to monitor the host computer applied in the financial monitoring industry all uses the IDE and PCI bus to complete the hard disk control and extension because of the costs whether for the embedded project or the industrial control project. According to the hard disk address order, the monitoring computer marks out the logic drive letter, and the image data are written into the hard disk accruing to the drive letter sequence. Because the video data are written in the whole day, so the higher data written in and index pressures exist in the certain period for each hard disk. At the same time, the DVR hard disk is installed densely, and the heat dispersion is difficult, so the failures of the hard disk and the data loss often happen. In addition, for the management of the memory data, there are two reasons which may induce the data loss, first, because the monitoring host computers are all in the bank branches, the failures of the equipment can not be found in time, and the data will be loss when inquiring, second, the data loss will occur because of the reasons in the management, for example, the data memory and the host computer are in the locale, the failure of the equipment can not be found in time and the data can not be found, or in the interior management, the system doesn't be exerted strictly, and outlaws find the opportunity given by to stop the system or randomly delete the data.

Aiming at above problems, the solution is to copy the video data off site. In the financial industry network system solution, Tianjin Tiandiweiye Co. Ltd put forward to utilize the bank network and the memory software to implement the data off-site memory in the management center with the professional network memory equipment, which can ensure the security of data, and ensure that the corresponding image can be found when problems occur. At present, there are two solutions for the center off-site data memory, and one solution is that because the network in the bank branch is very busy in the daytime, the data is stored in the locale, and copied to the center memory equipment by the network bandwidth in the night, and the second solution is to plan certain network bandwidth for the data transfer in the bank branch, and make the image could be copied to the superior data center timely. Because the networks of the bank branches have been updated to the E1 line or the network environment with wider bandwidth in recent years, the center off-site data memory project becomes possible, and the bank can select the solution to fulfill the monitoring demands according to the network environment and business characters.

Except for the security correlative application, the intelligent video is also applied in some non-security correlative

applications. These applications mainly face to the industrials such as retail and service, and the intelligent video is looked as the assistance tool for the management and service to enhance the service level and the turnover. These applications mainly include people counting, flow control, attention control and traffic flow control.

4. The survey of foreign and domestic intelligent video markets

Form the demands of the market, with the increasingly drastic anti-terrorist situation, the intelligent video monitoring system is more and more concerned by people, and its demands continually increase. As a whole, the foreign intelligent video application market is transforming from the “concept validation” to the “scale application”, and the intelligent video has been forming an industry.

Since the concept model of the intelligent video application occurred shortly, some foreign companies begun to research relative software and hardware products. For example, the global leading manufacture of the networking video market, Swedish Axis Network Communication Co. Ltd had pushed the intelligent video products including AXIS242SIV video server and AXIS IVM120 people counting intelligent video application module. AXIS242SIV integrates special DSP chip (TIDM642), and it possesses powerful image processing ability and it can support the running and the development of the third party application software module. The AXIS IVM120 people counting intelligent video application module can automatically count the amount of the people who enter in or go out the special region through analyzing the monitoring pictures by the video monitoring equipment, and the function can effectively help the managers in many industries such as the service and retail to analyze the operation or enhance the service quality. AXIS also planed to push more intelligent video application modules including the vehicle plate recognition and object persistence.

The domestic intelligent video market still has large difference comparing with foreign market, and it is still in the blank status at present. The “intelligent video monitoring” in the monitoring system is actually staying in the concept of the common network video monitoring (IP monitoring, digital monitoring). Along with the application demands of the intelligent video in the market like foreign market, some domestic manufactures have begun to introduce intelligent video software and hardware products and technologies made by foreign famous manufactures, and planed to push them by the form of OEM.

5. Conclusions

The intelligence, the digitization and the networking are the necessary trend for the development of the video monitoring technology, and the occurrence of the intelligent video monitor is the direct embodiment of this trend. The intelligent video monitoring equipment possesses stronger image processing ability and more intelligent factors than common network video monitoring equipment, and it can provide more super video analysis functions for users, and it can largely enhance the ability of the video monitoring system and makes the video resources exert stronger functions. To push the development of the intelligent video industry and achieve the multiple-win effect, all participators including the monitoring equipment hardware supplier, the intelligent video software supplier, the distributors, the dealers and the system integrators should be reasonably organized to make them fully exert their own advantages and create the comprehensive solution which can fulfill users’ final demands.

References

- Qi, Mo. (2005). *Digital Communication Base*. China Machine Press.
- Shen, Yuehong. (2004). *Communication Theory*. China Machine Press.
- The Bureau of Science and Technology of Chinese Ministry of Public Security. (2003). *Compilation of Social Public Security Standards*. China Standards Publishing House.
- The Compiling Committee of Chinese Ministry of Public Security. (2004). *Security and Protection Technology*. China People’s Public Security University.
- Wang, Qingyou. (2000). *CCD Application Technology*. Tianjin University Press.



Distribution System Restoration Using Genetic Algorithm with Distributed Generation

N.Shanmuga Vadivoo (Corresponding author)

Department of Electrical and Electronics Engineering

Tel:91-452-248-2240(210) E-mail: nsveee@tce.edu

S.Mary Raja Slochanal

Department of Electrical and Electronics Engineering

Thiagarajar College of Engineering

Madurai-625 015, Tamil Nadu, India

Tel:91-452-248-2240(201) E-mail: smrsee@tce.edu

Abstract

Distribution system automation is carried out to improve the reliability, stability, efficiency and service quality of a system. When a fault occurs in the system quick restoration is required in the faulted area, which needs dedicated software to assist the operator. In this paper, an algorithm is developed to find the radial configuration to restore the system after a fault using Genetic Algorithm (GA). The restoration is carried out with minimum system loss, voltage drop and number of switching operations with line current and bus voltage limits as constraints. The load flow is performed by forward/backward sweeping algorithm. Additional mesh checking of the network is avoided using Prufer number encoding of strings. The effect of DG in loss reduction during restoration is analyzed which is observed to be a high level from the results. The developed algorithm is tested on IEEE 16-Bus and 33-Bus radial distribution systems.

Keywords: Distribution system, Genetic Algorithm, Restoration, Prufer number encoding, Multiobjective performance index, Distributed Generation

1. Introduction

Distribution system is planned in such a way that it supplies the consumers without any longer interruption during the outage condition. When a fault occurs in the system, relays detect the faulted areas and disconnect the network by opening the circuit breakers. During the fault, power becomes unavailable to the loads in certain areas or to the particular customer loads and the power utilities should re-energize the loads as quickly as possible. The re-energizing procedure is called as service restoration. The operators in control centers detect the out-of-service areas and decide the switches to be opened and closed in order to restore the out-of-service areas via feeder reconfiguration.

Recently Distributed Generations play an important role in the minimization of loss of the system. DG is considered as "taking power to the load" by both conventional and renewable energy resources such as wind, solar, geothermal, biomass and ocean energy. DG generates electricity with high efficiency and low pollution. Thomas Ackermann et al. (Thomas Ackermann, Goran Andersson, and Lennart Soder., 2001) stated that DG can be installed at or near the load at different ratings varying from 1 W to 300 MW. The impacts of DG on voltage regulation, losses, voltage flicker and harmonics etc. were presented by Barker et al. (Barker Philip,P., and Mello Robert W.De., 2000). In order to minimize line losses of power systems, it is important to define the size and location of DG. An analytical approach to determine exclusively the optimal location to place a DG in radial systems to minimize the total loss of the system was presented by Wang and Nehrir (Wang,C., and Nehrir,M.H., 2004). A general approach and a set of indices to assess some of the technical and environmental benefits of DG in a quantitative manner were proposed by Pathomthat et al. (Pathomthat Chiradeja, and Ramakumar,R., 2004). Reduced line losses, voltage profile improvement, reduced emissions of pollutants, increased overall energy efficiency, enhanced system reliability and security, improved power quality and relieved transmission and distribution congestion, reduced operation and maintenance costs of some DG technologies, enhanced productivity, reduced health care costs due to improved environment and reduced fuel costs due to increased overall efficiency are some of the major benefits.

In this paper, an algorithm is developed to find the optimal radial network using Genetic Algorithm to restore the system after the occurrence of a fault. The restoration is carried out for minimum system loss, voltage drop and number of switching. Distribution networks are normally radial in nature. After the occurrence of a fault, it is essential to ensure

that the restored network is in radial. Generally an additional mesh checking is required after the restoration. Prufer number encoding explained by Ying and Saw (Ying-Yi Hong, and Saw-Yu Ho., 2005) is used for representing the strings to avoid this additional mesh checking. An IEEE 16-Bus applied by Ying and Saw (Ying-Yi Hong, and Saw-Yu Ho., 2005) and a 33-Bus radial distribution systems applied by Baran et al. (Baran.M.E., and Wu,F.F., 1989) are considered to validate the effectiveness of the developed algorithm. The restoration is also carried out with the inclusion of DG with a selected size and location. The effect of DG for the reduction of real power loss and total voltage drop is analyzed.

2. Problem Formulation

When a fault occurs in a system, it is essential to restore the system with minimum time. The minimization of the time is directly related with the minimization of the number of switching operations. The objective of this work is to find the optimal network for restoration with minimum system loss, voltage drop and number of switching operations. The problem is solved and analyzed into two cases.

- 1) Optimal network without DG
- 2) Optimal network with DG

The location and size of the DG are selected for minimum loss and voltage drop.

The objective function and the constraints of the service restoration problem are described below.

2.1 Objective and Constraints

The total real power loss, the voltage drop and the number of switching operations to be minimized are given in Eq. (1), (2) and (3) respectively.

$$f_1(x) = \sum_{j=1}^{nl} k_j |I_j|^2 R_j \tag{1}$$

$$f_2(x) = \sum_{j=2}^{NB} |V_{j+1}| - |V_j| \tag{2}$$

$$f_3(x) = \sum_{j=1}^s |sw_j - k_j| \quad j \in 1,2,3,\dots, s \tag{3}$$

The objective function is calculated using Eq. (4).

$$objective\ function = W_1 * f_1(x) + W_2 * f_2(x) + W_3 * f_3(x) \tag{4}$$

The weighting factors are selected such that $W_1 + W_2 + W_3 = 1$

The numbers of switching operations are calculated using the expression given by Yogendra et al. (Yogendra Kumar, Biswarup Das, and Jaydev Sharma., 2005) sw_j is the status of j^{th} switch just after the fault and k_j is the status of j^{th} switch in the restored network.

The constraints are as follows.

- Radial network should be maintained.
- Bus voltages should be within the acceptable range, which is given by Eq.(5).
- Line currents should be within the acceptable range, which is given by Eq.(6).

$$V_{min} < V_j < V_{max} \tag{5}$$

$$I_{min} < I_j < I_{max} \tag{6}$$

3. Steps for the Proposed Algorithm

The steps for solving the restoration problem are as follows:

Step 1: The bus data, line data, switch locations and concerned faults of the system for service restoration problem are read.

Step 2: The population size, crossover rate and mutation rate for GA are selected.

Step 3: Each chromosome is represented using prufer number encoding method.

Step 4: The total real power loss, voltage drop and the number of switching operations for each chromosome using forward/backward sweep method are determined.

Step 5: The fitness value and the penalty function for inequality violated constraints are calculated. This penalty function is augmented to the objective function.

Step 6: The elitist strategy and tournament selection method to select the better chromosomes with larger fitness values are used.

Step 7: Genetic operations: crossover and mutation are performed.

Step 8: If all chromosomes are identical, the iterations are convergent; otherwise, go to Step 4.

Steps for determining the optimal network by the proposed method is given in Fig.1. The same can be applied for the restoration with DG by modifying the bus and the line data.

4. Implementation of Genetic Algorithm

Genetic Algorithm (GA) is a search algorithm, based on the mechanics of natural selection and natural genetics. It combines survival of the fittest among string structures. Effective search is carried out using GA to find Pareto optimal solutions for the reconfiguration problems. The basic operators of GA applied in this work are explained as follows.

4.1 String encoding

Since the topology of a distribution network can be uniquely defined by the statuses of all available tie and sectionalizing switches, a solution to the restoration problem is encoded as a function of the controllable switch states of the network. The length of the binary string is equal to the number of switches in the network. Each switch state is represented by one bit with a value '1' or '0' corresponding to 'close' or 'open', respectively.

4.2 Initial Population of the String

The population of the strings is randomly generated such that the number of '1's is equal to the number of sectionalizing switches and the number of '0's is equal to the number of the tie switches. The length of the string is equal to the total number of available switches. All the strings are in radial since they are represented by the prufer number encoding algorithm as follows.

4.2.1 Prufer number encoding for 16-Bus system

Representation of a string [1 1 1 1 1 0 0 1 1 1 1 1 1 0] of the 16-Bus system as a Prufer number

"6-4-14-5-4-1-2-9-8-2-3-13-13-15" is explained as in Fig.2.

1) The end node which is called as leaf node, with the smallest number (ie) bus 7, in the system is located. The unique adjacent bus for bus 7 is bus 6, which is assigned as the most left number of the Prufer number.

2) Bus 7 and the branch between buses 6 and 7 are deleted.

3) Now the leaf node with the smallest number is bus 6. The unique adjacent bus for bus 6 is bus 4, and therefore 4 is the next number after 6 in the Prufer number. Delete bus 6 and branch between buses 6 and 4.

4) This process is repeated until one bus is left.

A Prufer number "6-4-14-5-4-1-2-9-8-2-3-13-13-15" is obtained. For the 16-Bus distribution configuration, the length of the prufer number is 14 (16-2) for radial configuration.

4.3 Fitness Evolution

An objective function can be modified to account for the constraints by penalizing any solution that violates a constraint. In this work a penalty term, which depends on the constraint and the extent of its violation, is subtracted from the calculated fitness value. This 'penalty function method' permits new constraint formulations to be added readily to a GA-based optimization method. The multiobjective function is given in Eq.(3). The problem is a minimization problem.

Therefore, the fitness is given by Eq.(7).

$$\text{Fitness} = 1/f(x) \quad (7)$$

4.4 Penalty Functions

For dealing with inequality constraints in GA more efficiently, penalty functions are employed. This function indicates that a violated inequality constraint will be punished and then augmented to the fitness function. The penalty function dealing with the $V(i)$ is represented in Eq.(8).

$$- PF^{N/AS} \{(V_i - V_{\min})\}^2 \quad (8)$$

where PF is called the penalty factor and N is the iteration number. Eq.(8) implies that the penalty weight (PF^N / NS) should be increased gradually and has less effect in the initial NS iterations. The penalty factors for the voltages should be smaller than that for the line flows because the numerical order for the line flows is larger than that for the voltages.

4.5 Tournament Selection

In tournament selection, two chromosomes are chosen randomly. Through comparing their fitness function values, the good candidate for the fitness function is survived and the chosen chromosome is copied to the next generation directly.

4.6 Single Point Cross Over and Uniform Mutation

In single-point crossover one crossover position is selected uniformly at random and the variables are exchanged between the individuals about this point, then two new offsprings are produced. The process is that certain bit or some bits of gene in the chromosome are transformed inversely, which means gene is changed from 1 to 0 or from 0 to 1.

4.7 Termination of GA

The conventional termination of the GA after a pre-specified number of generations is applied. After the completion of the number of generations, the quality of the best members of the population is tested against the problem definition. If no acceptable solutions are found, the GA may be restarted or a fresh search is initiated.

5. Load flow using backward sweeping method for radial distribution systems

Many of the distribution feeders do not converge while using conventional Newton-Raphson (NR) and Fast Decoupled Load Flow (FDLF) methods due to high R/X values. In backward sweeping method for load flow technique explained by Das et al. (Das,D., Nagi,H.S., and Kothari, D.P., 1994), unique lateral, node and branch numbering scheme are employed and hence the convergence is guaranteed for any radial distribution network with high R/X values. Therefore backward sweeping method is applied for obtaining the load flow results. The load flow is performed using Eq.(9) and Eq.(10).

The current through branch j is given as

$$I_j = \frac{|V_j| \angle \alpha_j - |V_{i+j}| \angle \alpha_{i+j}}{R_j + jX_j} \tag{9}$$

Voltage on the ‘ $i+1$ ’th node is given as

$$|V_{i+j}| = \sqrt{\frac{\{ (P_{i+j} R_j + Q_{i+j} X_j - 0.5|V_i|^2) \}^2 - \{ (R_j^2 + X_j^2) (P_{i+j}^2 + Q_{i+j}^2) \}^{\frac{1}{2}}}{\{ (P_{i+j} R_j + Q_{i+j} X_j - 0.5|V_i|^2) \}}} \tag{10}$$

Since the substation voltage magnitude V_i is known, it is possible to find out the voltage magnitudes of all other nodes. The real power loss of branch j , LP_j is calculated from Eq.(11).

$$LP_j = \frac{R_j * (P_{i+j}^2 + Q_{i+j}^2)}{|V_{i+j}|^2} \tag{11}$$

The real power on ‘ $i+1$ ’th node is given in Eq.(12).

$$P_{i+j} = \sum_{j=i+1}^{NB} PL_j + \sum_{j=i+1}^{NB-1} LP_j \quad \text{for } i=1,2,3,\dots,NB-2 \tag{12}$$

The total real power loss in all branches and the total voltage drop in all lines are calculated from Eq.(1) and Eq.(2) respectively.

6. Load flow with DG

The DG can be operated in three modes: lagging or leading or unity power factor. Under lagging power factor operation, DG produces reactive power for the system and Q is positive. Also Q is negative for leading power factor operation because DG absorbs reactive power from network. The real power at node i is decreased by adding DG at that node, which is given as $PL_i - P_{Gi}$. The reactive power in per unit for DG at node i is given in Eq.(13).

$$Q_{Gi} = \frac{\{ -1 \}^{NG} \gamma PL_i \sqrt{1 - (PF_G)^2}}{PF_G} \tag{13}$$

where, $nG = 1$ for leading power factor operation
 $= 2$ for lagging power factor operation

$$\gamma = \frac{P_{Gi}}{P_{Li}}$$

The reactive power at node i is $QL_i - Q_{Gi}$ and the load flow is done for the radial system using Eq.(9) and Eq.(10).

Fig.3. shows the flowchart for the selection of the location and size of the DG.

7. Results and Discussion

In this work, the IEEE 16-Bus and 33-Bus radial distribution systems considered for testing the developed algorithm. For the 16-Bus system, GA with pruffer number encoding requires 14 (NB-2) bits for a chromosome. The population size, maximum number of generations, crossover rate and mutation rate are 10, 50, 0.8, and 0.01 respectively. The minimum and maximum values of voltage are selected as 0.95p.u and 1.05p.u. The current limits are $\pm 3\%$ of the line current of the original configuration.

7.1 Results for the 16-Bus system

The real power loss for the original system is 510 kW and the total voltage drop in the system is 0.6501 kV.

7.1.1 Restoration without DG

If a fault occurs on the branch 2 (between buses 4 and 5), the bus 5 is in out of service. The objective is to restore the loads connected to the bus in the out of service area. There may be a number of possible ways to restore the system by reconfiguring the network. In this case, the load can be reenergized by closing the switches 14, 15 and 16 by opening the switches 2, 4 and 7. This configuration gives the minimum loss 660 kW, minimum voltage drop of 0.6512 kV and minimum number of switching operations of 6 out of all possible configurations to restore the system. If weighting factors are 0.7, 0.2 and 0.1 then the loss, voltage drop and switching operations are 670 kW, 0.6652 kV and 2 respectively. Therefore based on the application it is essential to select the weighting factors. Similarly the faults on other branches are considered one by one and the simulation results for the restoration are obtained using GA, which are given in Table 1. The convergence characteristic is shown in Fig.4. It is observed from the graph that all the chromosomes are different at the end of the first generation. At the 33rd generation, all the chromosomes are identical. These chromosomes give optimum configuration.

7.1.2 Restoration with DG

The ratings of DG units are varied from 0 to the total real power load at all the nodes. The DG ratings are varied one by one in steps from 2000 to 30000 kW with a power factor of 0.8 lagging. For all DG ratings, the loss and voltage drops are determined for the initial configuration. The multiobjective performance index is calculated using $W_1 + W_2 = 1$. Since it is the initial configuration $W_3 = 0$. In this case, various values for the weighting factors are assumed in the initial configuration with all DG ratings at all locations and their index values are determined for loss and voltage drop. It is observed that for most of the combinations of the weighting factors, their minimum index value is obtained when the DG of 20000 kW is located at Bus-9. The variation of loss and the variation of voltage drop for different DG ratings at Bus-9 are shown in Fig.5. The variation of the multiobjective performance index values for DGs at all buses is given in Fig.6. The corresponding loss and voltage drop values are given in Table 2. It is observed from the graph that the performance index value is minimum (0.3714) at bus-9 with 20000 kW. Some points are available with index values lower than 0.3714 but their respective voltage drop is in negative, therefore they are neglected.

When the DG is present in the system the restoration is carried out by considering the faults on the lines one by one. The results are given in Table 3. The network for restoration is determined for minimum loss, voltage drop and minimum switching operations. For a fault on line 2 the restoration is done by closing the switch in branch 14 and 16 and by opening the switches 2 and 4. It is observed from the results that the loss is reduced by 43.13% and voltage drop is reduced by 98.81% for this configuration during restoration. Moreover the number of switching operations is reduced to 4. The fault is considered in all the buses one by one and the networks for restoration are determined. In all the cases there is a lot of reduction in the loss, voltage drop and the number of switching operations. The simulation is done using MATLAB 7.1 programming language on a 2.79 GHz machine. The execution time for obtaining the network for restoration is 25.594 seconds.

7.2 Results for the 33-Bus system

The faults on all the branches are considered one by one and the simulation results for the restoration without DG are obtained using GA. The restoration results after the occurrence of faults on some of the lines are given in Table 4. The DG ratings are varied one by one in steps from 400 to 4000 kW. In this case, the minimum loss and minimum voltage

drops are obtained at Bus-30 with DG of 2000 kW for many of the weighting factors. The variation of the multiobjective performance index values for DGs at all buses is given in Fig.7. It is observed from the graph that the performance index value is minimum (0.1776) at bus-30 with 2800 kW. The corresponding loss and voltage drop values are given in Table 5. When the DG is present in the system the restoration is carried out by considering the faults on the lines one by one. The restoration results after the occurrence of faults on some of the lines are given in Table 6.

8. Conclusion

A Genetic Algorithm based approach to solve a multiobjective service restoration problem without and with Distributed Generation is analyzed. The multiobjective performance index used in this method with weighting factors is most suitable and valid for incorporating new objective functions and constraints arising from the introduction of DG in modern distribution systems. The introduction of DG of proper size and location reduces the system loss and voltage drop to a higher level. Due to the elimination of additional mesh check by Prufer number encoding, the execution time is reduced enormously. The convergence is guaranteed for any radial distribution network due to the application of backward sweeping method of load flow. The proposed method is capable of solving large scale systems.

Notations

nl - the number of lines

NB - the number of buses/nodes

s - number of switches

i - the node number

j - the branch number where $j=1, 2, \dots, NB-1$.

V_b - voltage of i^{th} node

I_j - current through branch j

R_j - resistance in per unit of branch j

X_j - reactance in per unit of branch j

$k_j = 1$, if the branch j is closed

$= 0$, if the branch j is opened.

W_1 , W_2 and W_3 - Weighting factors for total real power loss, total voltage drop and the number of switching operations respectively.

V_{min} and V_{max} - the minimum and maximum acceptable bus voltages

I_{min} and I_{max} - the minimum and maximum acceptable branch currents

PL_i - real power load of i^{th} node

QL_i - reactive power load of i^{th} node

δ_{i+1} - voltage angle at node $i+1$

P_{i+1} and Q_{i+1} - total real and reactive power loads fed through node $i+1$ respectively

P_{Gi} - real power of DG at node i

Q_{Gi} - reactive power of DG at node i

PF_G - the operating power factor of DG

Acknowledgement

The authors are grateful to the Management and the Principal of Thiagarajar College of Engineering, Madurai, Tamil Nadu, India for providing all the necessary facilities to carry out this research work successfully.

References

Baran.M.E.,& Wu,F.F. (1989). Network reconfiguration in distribution systems for loss reduction and load balancing. *IEEE Transaction on Power Delivery*, PWRD-4, 1401-1407.

Barker Philip,P., & Mello Robert W.De. (2000). Determining the Impact of Distributed Generation on Power Systems: Part 1 – Radial Distribution Systems. *Proceedings on IEEE Power Engg. Soc. Summer Meeting*, 1645–1656.

Das,D., Nagi,H.S., & Kothari, D.P. (1994). Novel method for solving radial distribution networks. *IEE Proceedings on Generation, Transmission and Distribution*, 1994, 141, (4), 291-298.

Pathomthat Chiradeja, & Ramakumar,R. (2004). An Approach to Quantify the Technical Benefits of Distributed Generation. *IEEE Transactions on energy conversion*, 19, (4), 764-773.

Thomas Ackermann, Goran Andersson, & Lennart Soder. (2001). Distributed generation: a definition. *Journal on Electric Power System Research*, 51,195-204.

Wang,C., & Nehrir,M.H. (2004). Analytical Approaches for Optimal Placement of DG Sources in Power Systems. *IEEE Transaction on Power Systems*, 19,(4), 2068–2076.

Ying-Yi Hong, & Saw-Yu Ho. (2005). Determination of Network configuration consideration Multiobjective in Distributive systems using Genetic Algorithm. *IEEE Transactions on Power systems*, 20, (2), 1062-1069.

Yogendra Kumar, Biswarup Das, & Jaydev Sharma. (2005). Service restoration in distribution system using non-nominated sorting genetic algorithm. *Journal on Electric Power System Research*, pp.1-10

Table 1. Results for the restoration without DG for 16-Bus system (Case: 1)

Fault on branch	Minimum voltage		Total real power loss		Total Voltage drop		Switching Operations		Number of switching operations
	p.u.	kV	p.u.	kW	p.u.	kV	Switches to be closed	Switches to be opened	
2	0.9613	10.57	0.0066	660	0.0592	0.6512	14,15,16	2,4,7	6
3	0.9587	10.54	0.0071	710	0.0457	0.5027	14,16	3,6	4
4	0.9575	10.53	0.0069	690	0.0453	0.4983	14,15,16	4,6,7	6
6	0.9575	10.53	0.0069	690	0.0453	0.4983	14,15,16	4,6,7	6
7	0.9556	10.51	0.0069	690	0.0485	0.5335	14,15,16	6,7,16	4
8	0.9721	10.69	0.0048	480	0.0548	0.6028	14,15,16	4,7,8	6
11	0.9587	10.54	0.0057	570	0.0556	0.6116	14,15,16	3,8,11	6
12	0.9523	10.47	0.008	800	0.0512	0.5632	14,15,16	6,7,12	6
13	0.9541	10.49	0.0075	750	0.0486	0.5346	14,15,16	6,7,13	6

Table 2. Loss and voltage drop for the initial network with and without DG for 16-Bus system

Configuration Type	Switches in open	DG condition	Location of DG	Rating of DG (kW)	Total real power loss (kW)	% of Loss reduction	Total Voltage drop (p.u.)	% of voltage drop reduction
Initial Configuration	14,15,16	Without DG	-	-	510	-	0.0591	-
		With DG for min. combined loss & Voltage drop	Bus 9	20000	355.8	30.23	0.0008	98.68

Table 3. Results for the restoration with DG for 16-Bus system (Case: 2)

Fault on branch	Minimum voltage		Total real power loss		Total Voltage drop		Switching Operations		Number of switching operations
	p.u.	kV	p.u.	kW	p.u.	kV	Switches to be closed	Switches to be opened	
2	0.9802	10.78	0.0029	260	0.0007	0.0418	14,16	2,4	4
3	0.9731	10.704	0.0043	430	-0.0027	-0.0297	14,16	3,8	4
4	0.9802	10.78	0.0029	370	-0.0023	-0.0253	16	4	2
6	0.978	10.87	0.0057	520	0.0148	0.1628	14,15,16	4,6,7	6
7	0.978	10.83	0.0041	390	0.0003	0.0033	15,16	3,7	4
8	0.9802	10.82	0.0038	370	0.0025	0.0275	14,16	4,8	4
11	0.9801	10.78	0.0037	350	0.0022	0.0242	14,15,16	4,8,11	6
12	0.9735	10.703	0.0045	420	0.0026	0.0286	15,16	7,12	4
13	0.9817	10.791	0.0038	380	0.0008	0.0088	16	13	2

Table 4. Results for the restoration without DG for 33-Bus system (Case: 1)

Fault on branch	Total real power loss		Total Voltage drop		Switching Operations		Number of switching operations
	p.u.	kW	p.u.	kV	Switches to be closed	Switches to be opened	
3	0.0033	330	0.0066	0.0858	35,36,37	3,27,30	6
9	0.0018	180	0.1211	1.5743	34,35	9,13	4
10	0.0018	180	0.1123	1.4599	34,35,37	10,12	6
14	0.0029	290	0.1606	2.087	34,36	14,29	4
15	0.0019	190	0.1274	1.656	35,36,37	21,26	6
17	0.0017	170	0.1056	1.3728	35,36	17,8	4

Table 5. Loss and voltage drop for the initial network with and without DG for 33-Bus system

Configuration Type	Switches in open	DG condition	Location of DG	Rating of DG (kW)	Total real power loss (kW)	% of Loss reduction	Total Voltage drop (p.u.)	% of voltage drop reduction
Initial Configuration	33,34, 35,36, 37	Without DG	-	-	197	-	0.1318	-
		With DG for min. combined loss & Voltage drop	Bus 30	2800	117.35	40.43	0.004	97.72

Table 6. Results for the restoration with DG for 33-Bus system (Case: 2)

Fault on branch	Total real power loss		Total Voltage drop		Switching Operations		Number of switching operations
	p.u.	kW	p.u.	kV	Switches to be closed	Switches to be opened	
3	0.0011	110	0.019	0.247	33,36	3,7	4
9	0.0014	140	0.1233	1.5899	35	9	2
10	0.0012	120	0.0015	0.0195	34	10	2
14	0.0011	110	0.0024	0.0312	34	14	2
15	0.001	100	0.0056	0.0728	33,36	15,19	4
17	0.0011	110	0.019	0.247	33,36	17,3	4

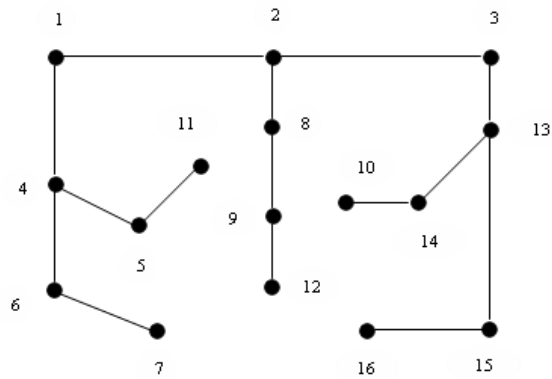


Figure 2. Representation of a string as a prufer number “6-4-14-5-4-1-2-9-8-2-3-13-13-15” for 16-Bus System

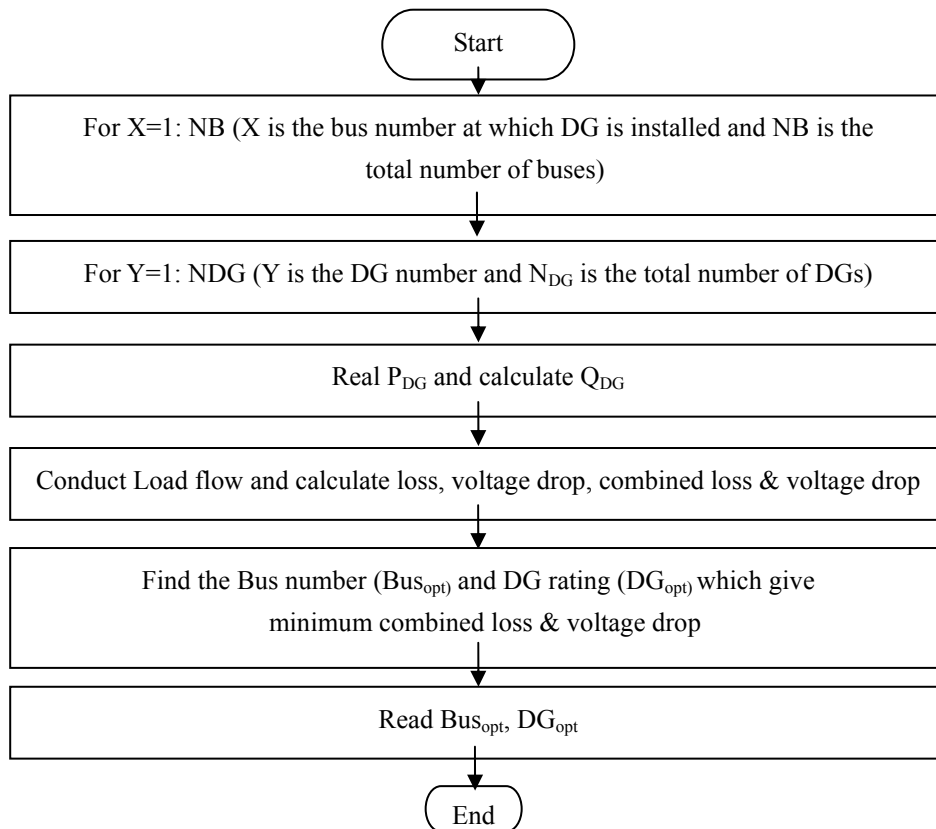


Figure 3. Flowchart to find the location and size of DG

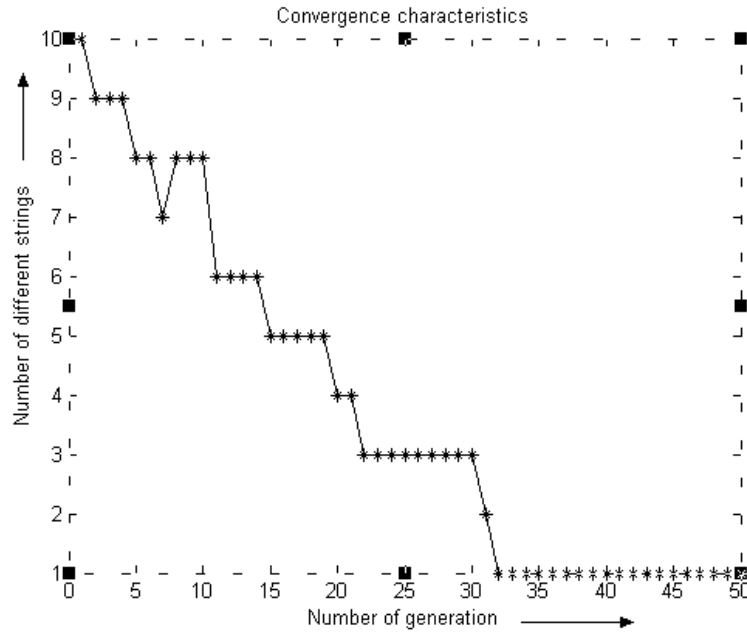


Figure 4. Convergence characteristic for restoration for 16-Bus system

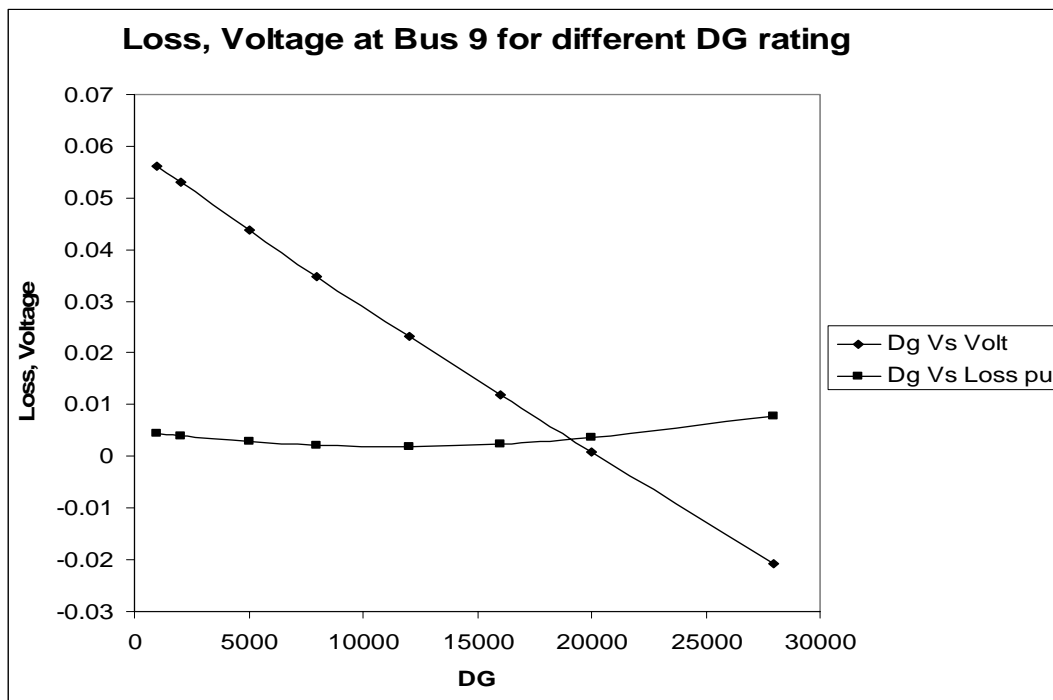


Figure 5. Variation of loss and voltage drop with different DG ratings at Bus-9 for 16-Bus system

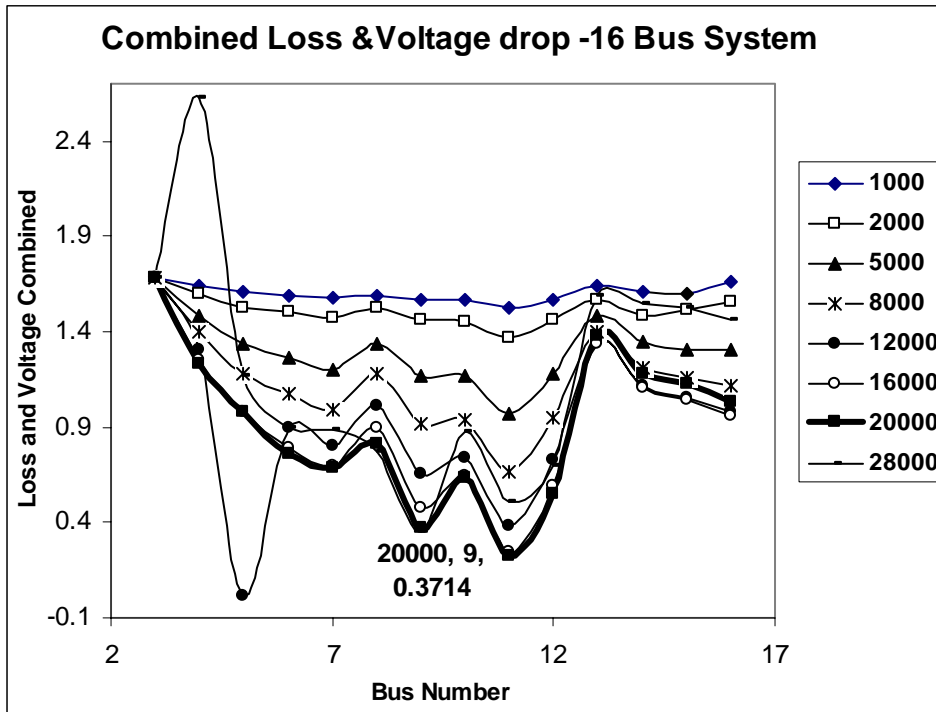


Figure 6. Loss and voltage drop (Multiobjective Index) with different DG at all buses in 16-Bus system

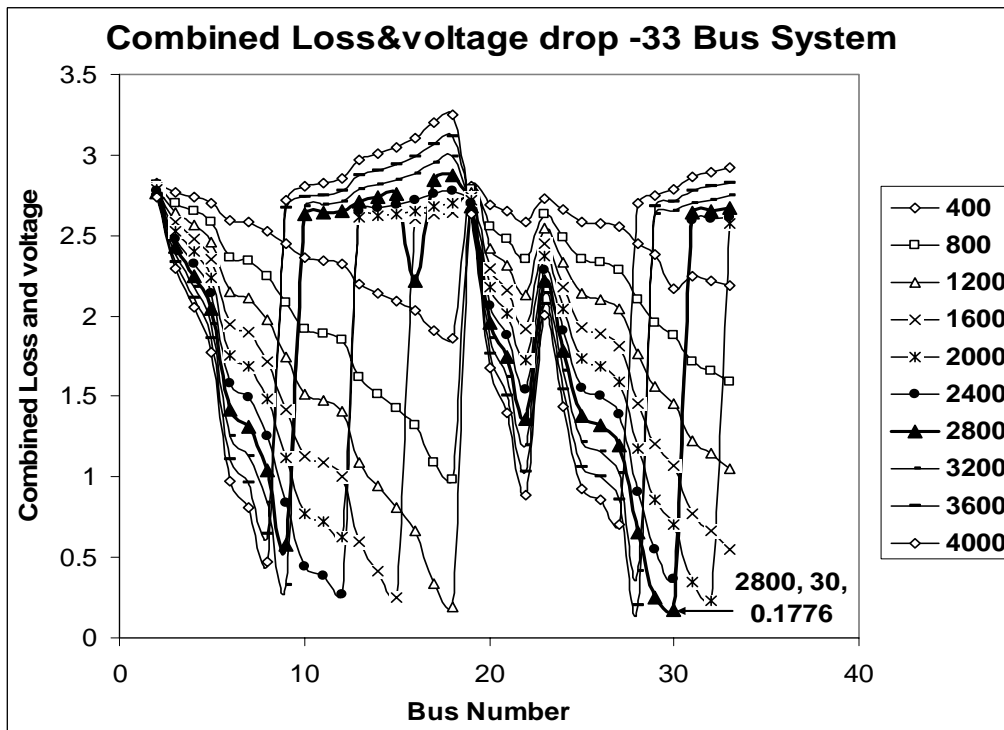


Figure 7. Loss and voltage drop (Multiobjective Index) with different DG at all buses in 33-Bus system



A Numerical Simulation of the Flow in a Diffusing S-Duct Inlet

Lifen Zhang & Zhenxia Liu

School of Power and Energy, Northwestern Polytechnical University

Xi'an 710072, China

Jian Jiang

Chinese Flight Test Establishment, Xi'an 710089, China

Abstract

A numerical simulation of the flow inside a diffusing S-duct inlet is conducted. The primary discussion herein focuses on flow analysis and development of secondary flow in the S-duct diffuser inlet. Full three-dimensional Navier-Stokes equations are solved and SST turbulence model is employed. Numerical results, including surface static pressure, total pressure recovery at exit, are compared with experiment. And fairly good agreement is apparent. Total performance, such as average total pressure recovery and distortion, is agreed well with the experiment. Shock waves in outer flow, pressure recovery and distortion at the exit are also discussed.

1. Introduction

S-duct inlet has been widely used for military and commercial aircraft, such as F-16, F-18 and Boeing 727. Inlet should decelerate the flow to the desired velocity while maintaining high total pressure recovery and flow uniformity. But in S-duct inlet two bends give rise to streamline curvature. The streamline curvature results in cross-stream pressure gradients which can produce significant secondary flows. Increasing cross-sectional area can lead to adverse pressure gradients. All of mentioned above increase risk of unacceptable inlet performance. So understanding flow in S-duct inlet is very important in inlet design process. (S.R. Wellborn, B.A. Reichert, T.H. Okiishi, 1992; B.A. Reichert, B.J. Wendt, 1993; G.J. Harloff, B.A. Reichert, S.R. Wellborn, 1992)

Usually, performance of S-duct inlet is determined by wind tunnel testing with expensive cost. But since the late 1960's, Computational Fluid Dynamics has been under continuous and wide-spread development. From 1990's, the CFD method has been developed to aid the design and analyze of aircraft propulsion component and system (G.J. Harloff, B.A. Reichert, S.R. Wellborn, 1992).

The purpose of the present study is to predict flow in a rectangular-to-circular S-duct inlet using a full Navier-Stokes equations and two-equation SST turbulence model, and analyze flow and development of secondary flow. Shock waves in outer flow, pressure recovery contour and distortion at exit are also discussed. A careful comparison of numerical predictions with experiment is necessary to establish and improve the numerical accuracy. In this paper, surface pressure, total pressure recovery and total performance are compared with experiment.

2. S-duct inlet and Numerical methods

The inlet configuration in this paper is a external compression, overhead three ramp and rectangular-to-circular designs, as shown in Fig.1. First ramp is fixed, second is removable, and the third is slaved. In order to eliminate boundary layer, there are thousands of small holes which diameter is just several millimeter in second and third ramp. The computed model is full scale, containing airframe and boundary layer diverter. Reported test is conducted with incoming Mach number of 1.2, flight altitude of 14km and zero degree angle of attack.

All solid surfaces are treated viscously and the entire flow is assumed fully turbulent. Freestream pressure is assumed at the external outflow boundary located approximately 3.5 vehicle lengths. The most difficult boundary condition is the exit of the diffuser. In this paper, static pressure at exit is estimated based on test data. In order to reduce the influence of the exit, diffuser is extended approximately 0.2 inlet lengths, pictured in Fig.2. Due to no accurate static pressure at the exit, some error is brought into the computational domain.

Full three-dimensional Reynolds-averaged Navier-Stokes equations in strong conservation form are used for computation. Two-equation SST turbulence model is employed. It has been found to be very robust and stable for a variety of flow conditions, and it solves equations for \mathcal{K} and ω in the inner region of the boundary layer and gradually changes to the high Reynolds number $\mathcal{K}-\varepsilon$ model away from the wall (F.R. Menter, 1993). Grid generation uses hybrid grid which includes tetrahedron and prism. Total number is approximately 0.5 million.

3. Results and discussion

Predicted surface static pressure and pressure recovery at exit are compared with experiment to insure accuracy of the computation. There are 15 pressure probes along the inlet surface. Surface static pressure is presented as pressure coefficients defined by Eq.1.

$$C_p = \frac{P - P_\infty}{q_\infty} \quad (1)$$

Where, P_∞ is the free stream static pressure, and q_∞ is the free stream dynamic pressure.

Numerical and experimental pressure coefficients are shown in Fig.3. Good agreement is apparent. From the picture, we can see along the inlet surface, pressure has a trend of increasing. That because velocity should be decelerated and pressure should be enhanced in diffuser.

Fig.4 displays comparison of numerical and experimental pressure recovery at exit. Probes of 21 to 24 have some disagreement between numerical and experimental. The agreement of other probes is fairly good.

Fig.5 displays Mach number along the S-duct centerline. From this picture two shock waves are observed in outer flow. The first is around airframe head, and flow is decelerated to sonic. The second is on the top lip, this shock wave is weaker than the first one. After the secondary shock wave, airflow is subsonic, and flow into S-duct inlet. Inside the inlet, the velocity is lower near the top of the surface, round the second bend, the mach number is 0.2. Near the bottom, the velocity is comparatively high. Before the second bend, the mach number reach 0.7, after the second bend, the mach number is 0.6. The high velocity at bottom mix low velocity at top along the inlet. When the flow reaches the exit, the mach number is about 0.4.

To better observe flow in the S-duct inlet, total pressure recovery in six cross-stream planes of the S-duct is presented in fig.6. In the first plane, the high total pressure is in the center and bottom, the highest value is 0.98, and the low total pressure is concentrated on the top, the lowest value is 0.79. As the flow progress downstream, the low total pressure flow develop from top to the center, and the high momentum flow is pushed to two sides. In this process, high and low momentum flow mix, and in the sixth plane, the high total pressure is around the center, and the highest value is 0.98. Area of the highest value becomes small. The low total pressure is in the center, and the lowest value is 0.89. The reason inducing the change of the total pressure is the development of secondary flow as shown in Fig.7. The curvature of the S-duct inlet's centerline gives rise to streamline curvature, which results in a cross-stream static pressure gradient initiating fluid motion within the boundary layer toward the inside of the inlet bend. In the first bend, due to the duct's curvature, a centrifugal force is produced. And pressure of outside bend is higher than inside bend, a pressure gradient is induced. In order to balance the centrifugal force, fluid has a trend to be pushed to the inside of the duct. Due to its slower velocity, the boundary layer is more sensitive to this pressure gradient. The balance of the forces on it will migrate it along the walls towards the inside of the bend more readily than the core flow. This accumulation of boundary layer fluid at the top of the bend would try to replace and push fluid already there away from the wall toward the center of the bend, thus producing lift-off effect (A.J. Anabtawi, R.F. Blackwelder, P.B.S. Lissaman, R.H. Liebeck,1999; S.E. Tournier, J.D. Paduano, D. pagan,2005). In the second bend, curvature opposite to the first one, and the direction of the secondary flow reverse. However, secondary flow caused by first bend is very strong and no cancellation effect take place (A.J. Anabtawi, R.F. Blackwelder, P.B.S. Lissaman, R.H. Liebeck,1999). Hence, the boundary layer fluid continues to accumulate near the top of the inlet. The top is low momentum flow, secondary flow reversal should firstly occur here, so a pair of vortices comes into being. The second bend also induces a pair of vortices, although it is weak and small, as pictured in Fig.8.

The numerical results of secondary flow at exit are shown in Fig.8. At the top of the exit, a pair of vortices is observed evidently. At the two sides below, a small pair of vortices is also observed but not very distinctly.

Total pressure recovery contour is displayed in Fig.9. High total pressure is around center, and low total pressure is in the center. That results from the naturally occurring vortices convecting low-momentum fluid away from walls to center. The largest value is 0.98, the average value is 0.932, and the experimental average value is 0.936. So the total performance is very good agreement with experiment.

Distortion descriptor of IDC_{max} is used to estimate the exit distortion. It defines as follows,

$$IDC_i = \frac{P_{i,avg} - P_{i,min}}{P_{face,avg}} \quad i=1to5;$$

$$\overline{IDC}_j = \frac{IDC_j + IDC_{j+1}}{2} \quad j=1to4;$$

$$IDC_{\max} = \text{Max}(\overline{IDC}_j) \quad j=1 \text{ to } 4;$$

The experimental value is 0.0570, and the numerical value is 0.0511. So the numerical result is agreed well with experimental.

4. Summary

There are two shock waves in outer flow. One is around airframe, the other is on the top lip. The shock waves decelerate velocity and increase pressure. In the S-duct inlet, pressure-driven secondary flow which is caused by curvature results in two pairs of vortices. One pair caused by first bend are large, the other caused by second bend are small and weak. These vortices convect the low momentum fluid of the boundary layer towards the center of the duct, degrading both the uniformity and total pressure recovery. Total performance, such as average total pressure recovery and distortion descriptor IDC, is agreed very well with experiment. And some details, including surface static pressure and total pressure recovery at exit, have fairly good agreement with experiment.

References

A.J. Anabtawi, R.F. Blackwelder, P.B.S. Lissaman, R.H. Liebeck, An experimental investigation of boundary layer ingestion in a diffusing S-duct with and without passive flow control. AIAA 99-2110.

B.A.Reichert, B.J.Wendt, An experimental investigation of S-duct flow control using arrays of low-profile vortex generators, AIAA 93-0018.

F.R. Menter, Zonal two equation $\kappa - \omega$ turbulence models for aerodynamic flows. AIAA 93-2906.

G.J. Harloff, B.A. Reichert, S.R. Wellborn, Navier-Stokes analysis and experimental data comparison of compressible flow in a diffusing S-duct. AIAA 92-2699.

S.E. Tournier, J.D. Paduano, D. Pagan, Flow analysis and control in a transonic inlet. AIAA 2005-4734.

S.R.Wellborn, B.A.Reichert, T.H.Okiishi, An experimental investigation of the flow in a diffusing S-duct, AIAA 92-3622.



Figure 1. Sketch of the S-duct inlet

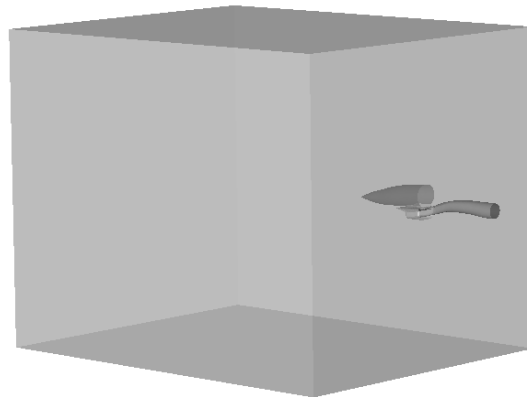


Figure 2. Computational domain

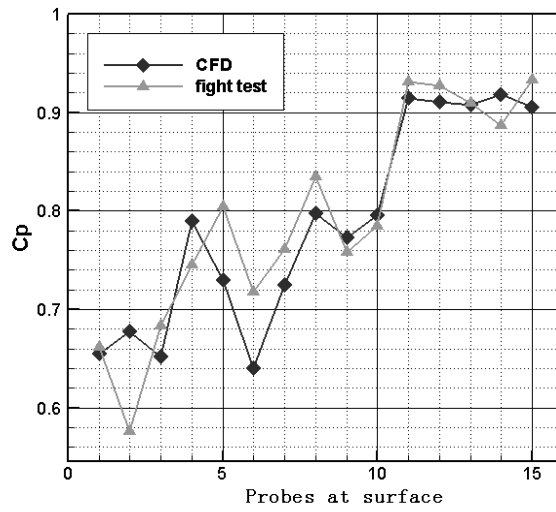


Figure 3. Surface static pressure coefficient

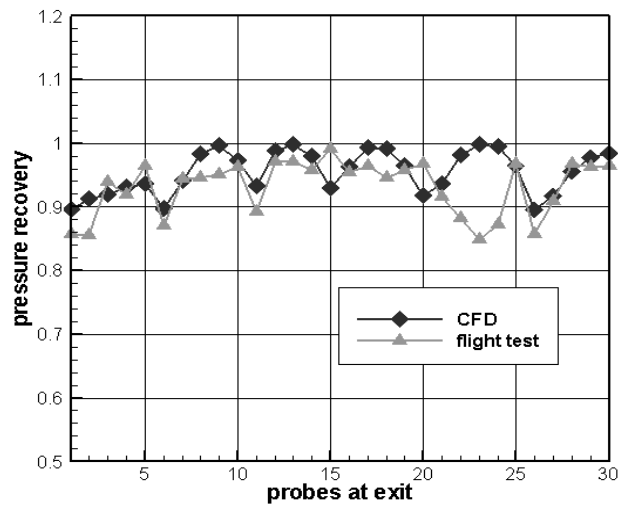


Figure 4. Total pressure recovery at exit

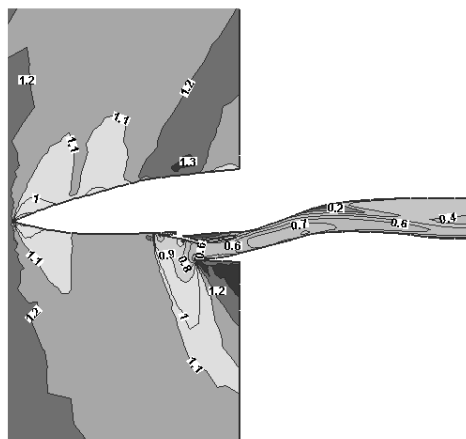


Figure 5. Mach number along the S-duct centerline

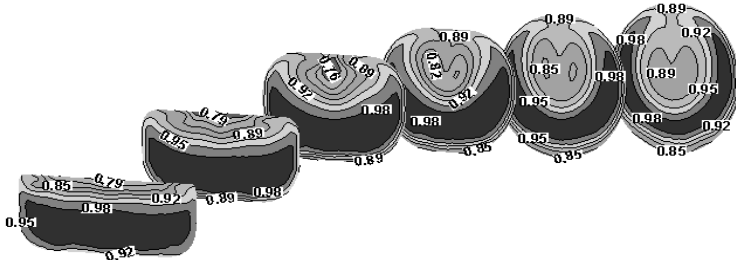


Figure 6. Total pressure recovery in six cross-stream planes

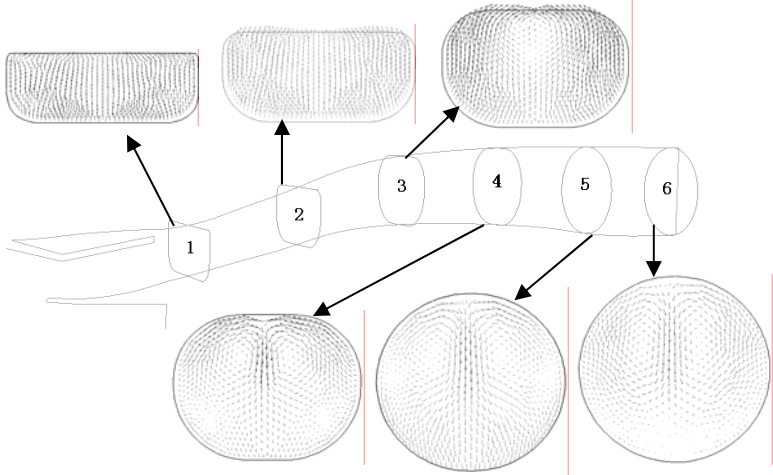


Figure 7. Secondary flow in six cross-stream planes

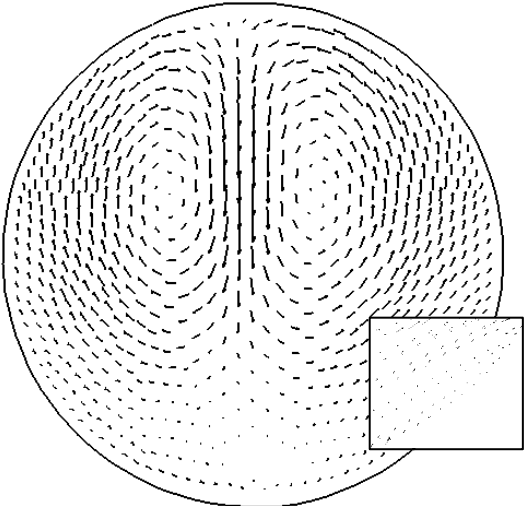


Figure 8. Secondary flow at exit

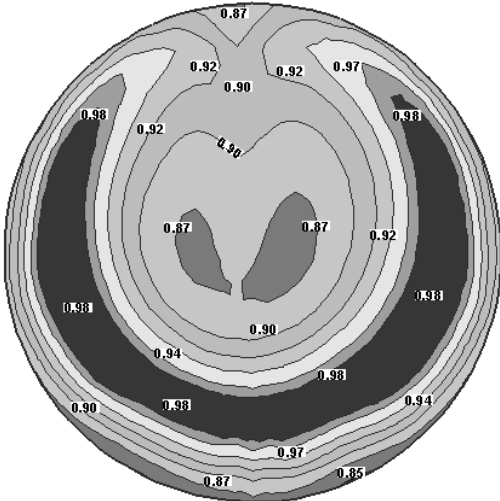


Figure 9. Total pressure recovery at exit



Hydrotropic Study on Furfural - Comprehensive Design Expert Plot

C.Jaya Kumar & N. Nagendra Gandhi

Department of Chemical Engineering, A.C. College of Technology, Anna University
Chennai – 600 025, India

Tel: 91-44-2220-3515 E-mail: n_nagendra2002@yahoo.com

Abstract

This work presents a comprehensive investigation on the solubility and mass transfer coefficient enhancement of furfural through Hydrotropy. The solubility and mass transfer coefficient studies were carried out using hydrotropes such as urea, tri-sodium citrate, sodium toluate and sodium benzoate under a wide range of hydrotrope concentrations (0 to 3.0 mol/L) and different system temperatures (303 to 333 K). The solubility of furfural increases with increase in hydrotrope concentration and also with system temperature. A Minimum Hydrotrope Concentration (MHC) in the aqueous phase was required to initiate significant solubilization of furfural. Consequent to the increase in solubilization of furfural, the mass transfer coefficient was also found to increase with increase in hydrotrope concentration. A threshold value of MHC is to be maintained to have an appreciable enhancement in the mass transfer coefficient. The maximum enhancement factor, which is the ratio of the value in the presence and absence of a hydrotrope, has been determined for all sets of experimentations. A comprehensive design expert plot for hydrotropic effect on furfural is also presented. The performance of hydrotropes was measured in terms of Setschnew constant K_s and reported for all hydrotropes used in this study.

Keywords: Hydrotropes, Solubilization, Mass transfer co-efficient, Separation, Solubilizers

1. Introduction

Hydrotropes are a class of chemical compounds which effect an increased aqueous solubility by several fold to certain solutes which are sparingly soluble in water under normal conditions. This phenomenon termed Hydrotropy can be considered to be a potentially and industrially attractive technique since the observed increase in solubility is much higher than that effected by other solubilization methods. Easy recovery of dissolved solute and possible re-use of hydrotrope solutions makes this method the most attractive one particularly at industrial levels.

Neuberg was the first to report hydrotropy when he dissolved a variety of organic substances, such as carbohydrates, esters, lipids, drugs, fats and oils in aqueous solutions containing hydrotropes. The advantage of certain properties, such as the solvent character being independent of pH, high selectivity, absence of emulsification, inexpensive aqueous phase makes this technique superior to other solubilization methods such as micellar solubilization, miscibility, co-solvency, salting-in, etc. Because of the solubilizing effect of these hydrotropes, the mass transfer coefficient of two-phase systems can considerably be enhanced.

It has been observed that in many two-phase reaction systems involving a sparingly soluble organic compound like furfural, the mass-transfer coefficient was found to be very low solely due to the poor solubility of furfural in the aqueous phase. Since furfural serves as a raw material/intermediate for a wide variety of chemicals and allied products and the separation of furfural from any liquid mixture seems to be difficult, this hydrotropic technique can be adapted to increase the solubility as well as to separate such mixtures effectively. The hydrotropes used in this work are freely soluble in water and practically insoluble in furfural. All are non- reactive and non- toxic and do not produce any temperature effect when dissolved in water. The easy availability and cheapness of hydrotropes are the other factors considered in the selection of hydrotropes. Data on various aspects of hydrotropic study on the solubility and mass-transfer coefficient for furfural -water system are reported for the first time.

2. Experimental

All the chemicals used in this work were manufactured by S.D.Finechemicals Pvt. Ltd., with a manufacturer's stated purity of 99%.

Thermostatic bath method was used to determine solubility values. For each solubility test, about 100 ml of furfural previously saturated with distilled water was taken in a separating funnel and 100 ml of a solution of the hydrotrope of known concentration was added. The separating funnel was sealed to avoid evaporation of mixtures at higher temperatures. The solution of different concentrations of the hydrotrope was prepared by dilution with distilled water. The separating funnel was immersed in a constant-temperature bath fitted with a temperature controller which could control the temperature within ± 0.1 °C. The setup was kept overnight for equilibration. After equilibrium was attained,

the aqueous layer was carefully separated from the ester layer and transferred into a beaker. The solute concentration was estimated by the addition of excess NaOH using a standardized HCl solution and phenolphthalein as an indicator. All the solubility experiments were conducted in duplicate to check the reproducibility. The observed error was <2%.

The experimental setup for the determination of the mass-transfer coefficient consisted of a vessel provided with baffles and a turbine impeller run by a motor to agitate the mixture. The speed of the impeller in rpm was selected in such a way to get effective mixing, which was maintained at the same value for all experiments.

The experimental procedure used for the determination of the transport coefficient is a well-adopted one. The vessel used for mass transfer studies is of height 40 cm and of inner diameter 15 cm. The turbine impeller diameter is 5 cm, the width is 1 cm, and the length is 1.2 cm. It has four blades. The baffle is 40 cm high with a diameter of 1.5 cm. There are about four baffles that rotate at a speed of 600 rpm. For each run to measure the mass-transfer coefficient; 250 ml of the furfural previously saturated with distilled water was added to the hydrotrope solution of known concentration. The sample was then agitated for a known time of 600, 1200, 1800, and 2400 seconds. After the end of fixed time t , the entire mixture was transferred to a separating funnel. After allowing to stand for some time, the aqueous layer was carefully separated from the furfural layer. The concentration of the solubilized furfural in aqueous hydrotrope solutions at time t was analyzed as done for solubility determinations. A plot of $-\log [1 - C_b/C^*]$ versus t is drawn, where C_b is the concentration of solute at time t and C^* is the equilibrium solubility of solute at the same hydrotrope concentration. The slope of the graph gives $k_L a/2.303$, from which $k_L a$, the mass-transfer coefficient was determined. Duplicate runs were made to check the reproducibility. The observed error was <2%.

3. Results and discussion

3.1 Solubility

The solubility of the furfural standard in water in the absence of any hydrotrope is 8.12×10^{-3} mol/L at 303 K (Table 1), compared to 8.32×10^{-3} mol/L as reported by Dean (1987). Thus, the solubility values in water are in excellent agreement with the earlier reported values.

Experimental data representing the average of duplicate determinations on the effect of hydrotropes, i.e., urea, tri-sodium citrate, sodium toluate and sodium benzoate on the solubility of furfural are presented in Tables 1-4 and are plotted in Figures 1-4. Urea is one of the hydrotropes used in this study. The solubility of furfural in water at 303 K in the absence of any hydrotrope is 8.12×10^{-3} mol/L. It has been observed that the solubility values increase significantly only after the addition of 0.40 mol/L of urea in the aqueous phase. This concentration is referred to as Minimum Hydrotrope Concentration (MHC).

Therefore, it is evident that hydrotropic solubilization is displayed only above the MHC, irrespective of system temperature. Hydrotrope does not seem to be operative below the MHC, which may be a characteristic of a particular hydrotrope with respect to each solute. This MHC value assumes greater significance in the context of recovery of hydrotrope solutions. Since hydrotrope appears to operate only at significant concentrations of hydrotrope in water, most hydrotropic solutions release the dissolved solute on dilution with distilled water below MHC. The knowledge of MHC values is necessary especially at industrial levels, as it ensures ready recovery of hydrotrope for reuse. MHC values remained unaltered even at increased system temperatures.

The solubilization effect varies with concentration of hydrotropes (Table 1). In the present case, a clear increasing trend in the solubility of furfural was observed above the MHC of urea. This increasing trend is maintained only up to a certain concentration of urea in the aqueous phase, beyond which there is no appreciable increase in the solubility of furfural. This concentration of citric acid (hydrotrope) in the aqueous phase is referred to as the maximum hydrotrope concentration (C_{\max}). From the analysis of the experimental data, it is observed that a further increase in hydrotrope concentration beyond C_{\max} does not bring any appreciable increase in the solubility of furfural even up to 3.00 mol/L of urea in the aqueous phase. Similar to the MHC values, the C_{\max} values of hydrotropes also remained unaltered with increase in system temperature.

The knowledge of MHC and C_{\max} values of each hydrotrope with respect to a particular solute assumes greater significance in this study since it indicates the beginning and saturation of the solubilization effect of hydrotropes. The values of MHC and C_{\max} of a hydrotrope with respect to furfural may be useful in determining the recovery of the solute even to an extent of the calculated amount from hydrotrope solutions at any concentration between MHC and C_{\max} by simple dilution with distilled water. This is the unique advantage of hydrotropic solubilization technique.

From the experimental data plotted in Figure 1, it can further be observed that, in order to achieve the particular solubility of to say 45×10^{-3} mol/L, the urea concentration should be 1.70 mol/L at 303 K, 1.30 mol/L at 313 K and 1.00 mol/L at 323 K in the aqueous phase. Thus it can be seen that as the system temperature increases, the concentration of urea required in the aqueous phase to achieve a particular solubility of furfural decreases. A similar trend has been observed for other systems also.

In the concentration range of urea between 0.00 and 3.00 mol/L, three different regions of urea as hydrotrope were observed. It was inactive below MHC value of 0.40 mol/L, above which an appreciable increase in the solubility of furfural was found up to 2.40 mol/L and beyond which there is no further increase in the solubility even upto 3.00 mol/L. Hence urea was found to be an effective hydrotrope in the concentration range between 0.40 and 2.40 mol/L towards furfural. It has also been observed that the solubilization effect of urea was not a linear function of the concentration of the urea solution. The solubilization effect of urea increases with increase in hydrotrope concentration and also with system temperature.

A similar trend has been observed in the solubilization effect of other hydrotropes namely tri-sodium citrate, sodium toluate and sodium benzoate. It has also been observed that the MHC values of hydrotrope used in this work range between 0.40 and 0.60 mol/L (Table 5), which seem to depend on the hydrophilicity of a hydrotrope. The C_{\max} values of hydrotropes range between 2.20 and 2.40 mol/L (Table 5) in most cases. The highest value of solubilization enhancement factors ϕ_s , which is the ratio of solubility values in the presence and absence of a hydrotrope has been observed in the case of urea as 8.05 at a system temperature of 333 K (Table 6).

3.2 Mass-Transfer Coefficient

The mass-transfer coefficient of furfural + water system in the absence of any hydrotrope was determined as $6.56 \times 10^{-5} \text{ s}^{-1}$ at 303K (Table 7). The effect of different hydrotropes on the mass-transfer coefficient of furfural at different hydrotrope concentrations is also given in the same table. It can be seen that a threshold value of 0.40 mol/L is required to effect significant enhancement in the mass transfer coefficient of furfural + water system, as was observed in the case of solubility determinations. The mass-transfer coefficient of furfural + water system increases with increase in urea concentration. The maximum enhancement factor for mass-transfer coefficient of furfural + water system in the presence of urea was found to be 7.83 (Table 7). A similar trend in the mass-transfer coefficient enhancement (ϕ_{mtc}) of furfural has been observed for other hydrotropes also namely tri-sodium citrate, sodium toluate and sodium benzoate. The highest value of ϕ_{mtc} (8.37) has been observed in the presence of urea as hydrotrope at C_{\max} of 3.00 mol/L.

Data on hydrotropic study for furfural has been provided using a comprehensive design expert plot for the first time in literature. (fig. 5)

3.3 Effectiveness of hydrotropes

The effectiveness factor of each hydrotrope with respect to furfural at different system temperatures has been determined by analyzing the experimental solubility data for each case applying the model suggested by Setschenow (1951) and later modified by Pathak and Gaikar (1992), as given by the equation

$$\log[S/S_m] = K_s[C_s - C_m] \quad (1)$$

Where S and S_m are the solubility of furfural at any hydrotrope concentration C_s and the minimum hydrotrope concentration C_m (same as MHC) respectively. The Setschenow constant K_s can be considered as a measure of the effectiveness of a hydrotrope at any given conditions of hydrotrope concentration and system temperature. The Setschenow constant values for hydrotropes namely urea, tri-sodium citrate, sodium toluate and sodium benzoate for furfural + water system at different system temperatures are listed in Table 8. The highest value has been observed as 0.452 in the case of urea as hydrotrope at 333K.

4. Conclusions

The solubility of furfural which is practically insoluble in water has been increased to a maximum value of 8.05 in the presence of urea as hydrotrope with a corresponding increase in the mass transfer coefficient. Hydrotropic study on furfural is given using a comprehensive design expert plot. This would be much useful in increasing the rate of output of the desired product made from furfural. The MHC and C_{\max} values of the hydrotrope with respect to furfural can be used for the recovery of the dissolved furfural and hydrotrope solutions at any hydrotrope concentration between MHC and C_{\max} by simple dilution with distilled water. This will eliminate the huge cost and energy normally involved in the separation of the solubilized solute from its solution. The unprecedented increase in the solubilizing effect of hydrotropes may be attributed to the formation of organized aggregates of hydrotrope molecules at a particular concentration.

References

- A. Pandit & M. M. Sharma. (1987). Intensification of heterogeneous reactions through hydrotropy. Alkaline hydrolysis of esters and oximation of cyclododecanone. *Chem. Eng. Sci.* 42, 2519-2523.
- A.A.Badwan, L.K. El-Khordagui & A.M. Saleh. (1983). The solubility of Benzodiazepines In Sodium Saicylate solutions and A Proposed mechanism for hydrotropic Solubilisation. *Int.J. Pharm.* 13, 67-74.
- Akhilesh Kumar Jain. (2008). reSolubilization of indomethacin using hydrotropes for aqueous injection European. *Journal of Pharmaceutics and Biopharmaceutics*, Volume 68, Issue 3, 701-714.

- B.Janakiraman & M.M. Sharma. (1985). Enhancing rates of multi phase reactions through hydrotropy. *Chem. Eng. Sci.* 40, 2156-2158.
- Badwan et al. (1982). The Solubility of Benzodiazepines in Sodium Salicylate Solutions and a Proposed Mechanism for Hydrotropic Solubilization. *Int. J. Pharm.* 13, 67-74.
- C. Neuberg. (1916). Hydrotropy. *Biochem. Z.* 76: 107-108.
- C.Isabel, Rigoli, C.Carla, Schmitt, & G. Miguel Neumann,(2007). The hydrotrope effect on the photopolymerization of styrenesulfonate initiated by Ru complexes. *Journal of Photochemistry and Photobiology A. Chemistry*, 188, Issues 2-3, 20. 329-333.
- Colonia et al. (1998). Phase Relations of *o* and *p* Chlorobenzoic Acids in Hydrotrope Solutions. *J. Chem. Eng. Data.* 43, 220-225.
- D. Balasubramanian, V. Srinivas, V. G. Gaikar, & M..M..Sharma. (1989). Aggregation Behavior of Hydrotropes in Aqueous Solutions, *J. Phys. Chem.*, 93, 3865-3870.
- Friberg et al. (1996). Reversible Extraction Process of Phenyl Ethyl Alcohol, a Fragrance. *Ind. Eng. Chem. Res.* 35, 2856-2859.
- K. Travis, Hodgdon, & Eric W. Kaler. (2007). Hydrotropic solutions, Current Opinion in *Colloid & Interface Science*, Volume 12, 3,121-128.
- M. Agarwal & V.G. Gaikar. (1992). Extractive Separation Using Hydrotropes. *Sep. Technol.* 2, 79-84.
- M. Laxman, M. M. Sharma. (1990). Reduction of Isophorone with Borohydride: Change in Regio Selectivity with Hydrotropes. *Synth. Commun.* 20, 111-117.
- Mahapatra et al.. (1988). New Strategies in Extractive Distillation; Use of Aqueous Solution of Hydrotropes and Organic Bases as Solvent for Organic Acids. *Sep. Sci. Technol.* 23, 429-436.
- N. Nagendra Gandhi & M. Dharmendra Kumar. (2000). Effect of Hydrotropes on Solubility and Mass Transfer Coefficient of Amyl Acetate. *Bioprocess Eng.* 449/0116.
- N. Nagendra Gandhi & N. Meyyappan. (2004). Solubility and Mass Transfer Coefficient Enhancement of Benzyl Acetate in Water through Hydrotropy. *J. Chem. Eng. Data*, 49, 1290-1294.
- N. Nagendra Gandhi & N. Meyyappan. (2004). Solubility and Mass Transfer Coefficient Enhancement of Benzyl Acetate in Water through Hydrotropy. *J. Chem. Eng. Data*, 49, 1290-1294.
- N. Nagendra Gandhi & N. Meyyappan. (2005). Solubility and Mass Transfer Coefficient Enhancement of Benzyl Benzoate in Water through Hydrotropy. *J. Chem. Eng. Data* 50, 796-800.
- N. Nagendra Gandhi & N. Meyyappan. (2005). Solubility and Mass Transfer Coefficient Enhancement of Benzyl Benzoate in Water through Hydrotropy. *J. Chem. Eng. Data.* 50, 796-800.
- N.Nagendra Gandhi & M. Dharmendra Kumar. (2000). Effect of Hydrotropes on Solubility and Mass Transfer Coefficient of Methyl Salicylate. *J. Chem. Eng. Data* 45, 419-423.
- Nagendra Gandhi et al. (1998). Solubility and Mass Transfer Coefficient Enhancement of Ethyl Benzoate through Hydrotropy. *Hungarian J. Ind. Chem.* 1998, 26, 63-68.
- Nagendra Gandhi et al.. (1998). Effect of Hydrotropes on Solubility and Mass-Transfer Coefficient of Butyl Acetate. *J. Chem. Eng.Data.* 43, 695-699.
- P. O Raynaud-Lacroze & N. S. Tavare. (1993). Separation of 2-naphthol: Hydrotropy and Precipitation. *Ind. Eng. Chem. Res.* 32, 685-691.
- S. Barbosa, P. Taboada, E. Castro & V. Mosquera. (2006). Influence of SDS and two anionic hydrotropes on the micellized state of the triblock copolymer E71G7E71, *J Colloid Interface Sci.* 296, 677-684.
- S.E. Friberg & C. Brancewicz. (1994). O/W Microemulsions and Hydrotropes: The Coupling Action of a Hydrotrope. *Langmuir.* 10, 2945-2949.
- Sara Nicoli, Franca Zani, Stefania Bilzi, Ruggero Bettini & Patrizia Santi. (2008). Association of nicotinamide with parabens: Effect on solubility, partition and transdermal permeation *European Journal of Pharmaceutics and Biopharmaceutics*, Volume 69, Issue 2, 613-621.
- V. Deepak, Dandekar, G.K. Jayaprakasha, Bhimanagouda S. Patil. (2008). Hydrotropic extraction of bioactive limonin from sour orange (*Citrus aurantium L.*) seeds *Food Chemistry*, Volume 109, Issue 3, 515-520.
- V.G. Gaikar. & P.V. Phatak. (1999). Selective Solubilisation of Isomers in Hydrotrope Solution *o*-/*p*-Chlorobenzoic acids and *o*-/*p*- Nitro anilines. *Sep. Sci. Technol.* 34, 439-459.

X. Chen & J.C. Micheu. (2002). Hydrotropes Induced Auto Catalysis in the Biphasic Alkaline Hydrolysis of Aromatic Esters. *J. Colloid Interface Sci.* 249, 172-179.

Table 1. Effect of urea concentration (C) on the solubility (S) of furfural in water

S.No.	C, mol/L	$10^3 S$, mol/L			
		T=303 K	T = 313 K	T = 323 K	T = 333 K
1	0.00	8.12	8.36	8.92	9.17
2	0.10	8.48	8.67	9.15	9.33
3	0.20	8.75	8.93	9.56	9.82
4	0.30	8.92	9.32	9.81	10.35
5	0.40(MHC)	9.97	10.45	10.98	11.38
6	0.50	12.43	13.24	16.35	25.31
7	0.60	14.65	18.46	23.98	33.87
8	0.70	17.34	22.67	30.19	41.96
9	0.80	20.86	25.39	36.71	47.38
10	0.90	22.43	30.83	41.58	53.42
11	1.00	25.75	34.49	46.25	58.97
12	1.10	28.92	38.51	50.49	63.43
13	1.20	31.35	42.78	54.45	68.19
14	1.30	34.16	46.12	58.64	72.62
15	1.40	37.45	50.34	62.36	75.24
16	1.50	40.78	53.98	65.58	78.63
17	1.60	43.53	56.72	69.72	81.32
18	1.70	46.14	59.58	72.64	83.49
19	1.80	50.38	62.36	74.92	85.17
20	1.90	52.64	64.15	75.35	86.32
21	2.00	54.73	66.78	77.49	88.61
22	2.20	57.12	68.26	79.29	90.28
23	2.40(C_{max})	58.25	69.32	80.41	91.63
24	2.60	58.26	69.33	80.42	91.64
25	2.80	58.27	69.34	80.43	91.65
26	3.00	58.28	69.35	80.44	91.66

Table 2. Effect of tri-sodium citrate concentration (C) on the solubility (S) of furfural in water

S.No.	C, mol/L	$10^3 S$, mol/L			
		T=303 K	T = 313 K	T = 323 K	T = 333 K
1	0.00	8.12	8.36	8.92	9.17
2	0.10	8.41	8.67	9.08	9.33
3	0.20	8.63	8.96	9.47	9.82
4	0.30	8.75	9.32	9.76	10.34
5	0.40(MHC)	9.82	10.31	10.84	11.23
6	0.50	11.36	13.24	16.69	25.61
7	0.60	13.49	18.46	23.18	31.64
8	0.70	15.69	22.53	30.79	37.32
9	0.80	18.74	25.62	35.34	42.47
10	0.90	21.62	28.29	39.12	48.64
11	1.00	23.15	31.73	44.68	53.39
12	1.10	25.38	34.86	47.46	56.28
13	1.20	28.65	38.93	50.39	60.85
14	1.30	30.81	41.59	54.86	64.69
15	1.40	32.25	45.78	56.45	68.15
16	1.50	35.53	48.54	59.74	71.62
17	1.60	37.66	51.83	61.78	73.53
18	1.70	39.29	52.38	63.91	75.42
19	1.80	41.58	54.52	65.39	76.86
20	1.90	42.67	55.26	65.87	77.41
21	2.00	43.25	55.84	66.25	77.65
22	2.20	45.12	56.21	67.04	78.28
23	2.40(C_{max})	46.73	57.28	68.19	79.34
24	2.60	46.74	57.29	68.21	79.35
25	2.80	46.75	57.31	68.22	79.36
26	3.00	46.76	57.32	68.23	79.37

Table 3. Effect of tri-sodium citrate concentration (C) on the solubility (S) of furfural in water

S.No.	C, mol/L	$10^3 S$, mol/L			
		T=303 K	T = 313 K	T = 323 K	T = 333 K
1	0.00	8.12	8.36	8.92	9.17
2	0.10	8.37	8.52	9.05	9.28
3	0.20	8.51	8.86	9.21	9.75
4	0.30	8.63	9.15	9.86	10.63
5	0.40(MHC)	8.74	9.24	10.22	11.12
6	0.50	8.82	9.45	11.04	12.48
7	0.60	9.71	10.82	12.05	13.57
8	0.70	11.34	13.23	16.37	21.36
9	0.80	13.52	16.76	20.46	26.45
10	0.90	15.41	19.58	23.17	31.38
11	1.00	17.63	21.92	27.57	36.87
12	1.10	18.29	24.59	30.37	40.39
13	1.20	20.47	26.31	33.48	44.88
14	1.30	22.68	29.44	36.77	48.84
15	1.40	23.79	32.52	40.94	50.91
16	1.50	25.48	34.64	43.23	53.23
17	1.60	27.51	35.36	45.49	55.24
18	1.70	28.84	37.43	47.36	57.79
19	1.80	29.38	38.24	49.83	59.73
20	1.90	30.24	39.73	50.63	61.46
21	2.00	31.09	40.15	51.26	62.25
22	2.20	32.12	41.23	52.44	63.48
23	2.40(C_{max})	32.13	41.24	52.45	63.49
24	2.60	32.14	41.25	52.46	63.51
25	2.80	32.15	41.26	52.47	63.52
26	3.00	32.16	41.27	52.48	63.53

Table 4. Effect of sodium benzoate concentration (C) on the solubility (S) of furfural in water

S.No.	C, mol/L	10^3 S, mol/L			
		T=303 K	T = 313 K	T = 323 K	T = 333 K
1	0.00	8.12	8.36	8.92	9.17
2	0.10	8.23	8.47	9.03	9.33
3	0.20	8.31	8.75	9.17	9.82
4	0.30	8.37	8.94	9.68	10.34
5	0.40	8.41	9.13	10.29	11.05
6	0.50	8.48	9.21	10.58	11.76
7	0.60 (MHC)	9.53	10.29	11.72	12.87
8	0.70	10.26	13.53	16.53	19.59
9	0.80	11.67	15.16	18.18	23.53
10	0.90	12.25	16.35	20.39	26.36
11	1.00	13.16	18.48	23.76	29.42
12	1.10	14.07	20.84	25.59	32.71
13	1.20	15.31	22.13	28.35	35.48
14	1.30	16.23	23.48	31.62	37.89
15	1.40	17.14	25.78	32.41	40.75
16	1.50	18.21	27.32	34.83	41.95
17	1.60	19.12	28.76	37.59	45.56
18	1.70	20.54	30.86	38.34	46.38
19	1.80	20.86	31.54	39.86	48.27
20	1.90	21.69	32.75	40.28	49.65
21	2.00	22.31	33.48	42.14	51.25
22	2.20(C_{max})	23.48	34.59	43.23	52.41
23	2.40	23.49	34.6	43.24	52.42
24	2.60	23.5	34.61	43.25	52.43
25	2.80	23.51	34.62	43.26	52.44
26	3.00	23.52	34.63	43.27	52.45

Table 5. MHC and C_{max} values of Hydrotropes

No.	Hydrotrope	MHC, mol/L	C_{max} , mol/L
1	Urea	0.40	2.40
2	Tri-Sodium Citrate	0.40	2.40
3	Sodium Toluate	0.60	2.20
4	Sodium Benzoate	0.60	2.20

Table 6. Maximum solubilisation enhancement factor of (ϕ_s) furfural

No.	Hydrotrope	Maximum enhancement factor for solubility (ϕ_s)			
		T = 303 K	T = 313 K	T = 323 K	T = 333 K
1	Urea	5.84	6.63	7.32	8.05
2	Tri-Sodium Citrate	4.75	5.55	6.38	7.06
3	Sodium Toluate	3.30	3.81	4.35	5.26
4	Sodium Benzoate	2.46	3.36	3.68	4.07

Table 7. Effect of hydrotrope concentration (C) on the mass transfer co-efficient (k_{La}) of furfural

No.	Hydrotrope	C, mol/L	k_{La} 10^5 s^{-1}	Enhancement factor for Mass Transfer Coefficient (Φ_{mtc})
1	Urea	0.00	6.56	-
		0.20	7.25	1.10
		0.40(MHC)	10.64	1.62
		0.60	15.28	2.32
		0.80	22.83	3.48
		1.00	28.46	4.33
		1.20	33.52	5.10
		1.40	39.34	5.99
		1.60	41.65	6.34
		1.80	46.95	7.15
		2.00	48.36	7.37
		2.20	50.59	7.71
		2.40(C_{max})	51.43	7.83
		2.60	52.38	7.98
2.80	53.81	8.20		
3.00	54.94	8.37		
2	Tri-Sodium Citrate	0.00	6.56	-
		0.20	7.15	1.08
		0.40(MHC)	9.32	1.42
		0.60	13.86	2.11
		0.80	19.54	2.97
		1.00	25.68	3.91
		1.20	30.42	4.63
		1.40	36.84	5.61
		1.60	38.57	5.87
		1.80	39.75	6.05
		2.00	40.34	6.14
		2.20	41.29	6.29
		2.40(C_{max})	42.64	6.50
		2.60	43.52	6.63
2.80	43.91	6.69		
3.00	44.28	6.75		

3	Sodium Toluate	0.00	6.56	-
		0.20	7.09	1.08
		0.40	8.54	1.30
		0.60(MHC)	10.67	1.62
		0.80	13.42	2.04
		1.00	15.48	2.35
		1.20	18.63	2.83
		1.40	20.27	3.08
		1.60	21.48	3.27
		1.80	23.56	3.59
		2.00	25.49	3.88
		2.20(C _{max})	27.64	4.21
		2.40	28.25	4.30
		2.60	29.53	4.51
		2.80	30.48	4.64
		3.00	31.69	4.83
4	Sodium Benzoate	0.00	6.56	-
		0.20	6.82	1.03
		0.40	7.69	1.17
		0.60(MHC)	8.43	1.28
		0.80	9.12	1.39
		1.00	9.85	1.50
		1.20	10.46	1.59
		1.40	11.29	1.72
		1.60	12.23	1.86
		1.80	13.49	2.05
		2.00	14.64	2.23
		2.20(C _{max})	15.58	2.37
		2.40	17.32	2.64
		2.60	18.49	2.81
		2.80	20.62	3.14
		3.00	21.58	3.28

Table 8. Setschenow constant values (ks) of hydrotropes with respect to furfural

No.	Hydrotrope	Setschenow Constant (K_s)			
		T = 303 K	T = 313 K	T = 323 K	T = 333 K
1	Urea	0.383	0.410	0.432	0.452
2	Tri-Sodium Citrate	0.338	0.372	0.402	0.424
3	Sodium Toluate	0.324	0.363	0.399	0.418
4	Sodium Benzoate	0.244	0.329	0.354	0.381

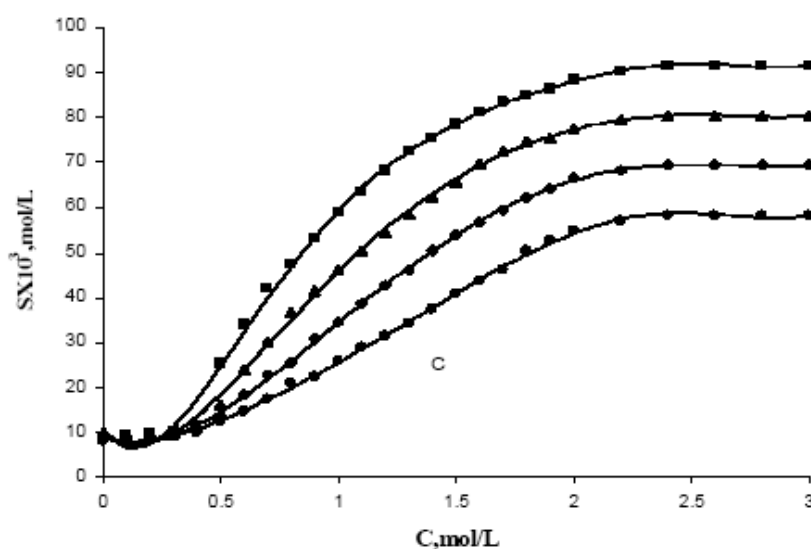


Figure 1. Effect of urea concentration (C) on the solubility (S) of furfural in water(at ● 303K ◆ 313K ▲ 323K ■ 333K)

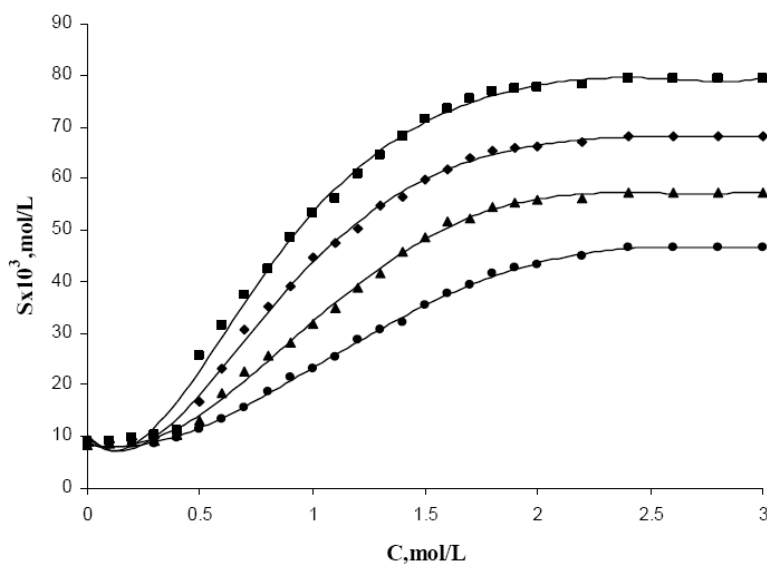


Figure 2. Effect of tri-sodium citrate concentration (C) on the solubility (S) of furfural in water (at ● 303K ▲ 313K ◆ 323K ■ 333K)

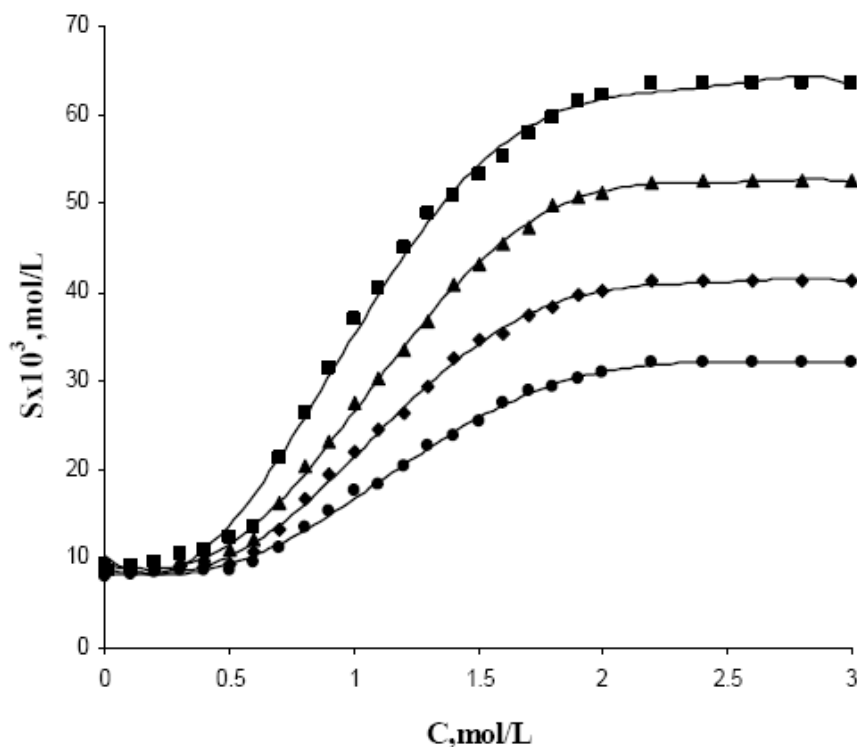


Figure 3. Effect of sodium toluate concentration (C) on the solubility (S) of furfural in water (at ● 303K ◆ 313K ▲ 323K ■ 333K)

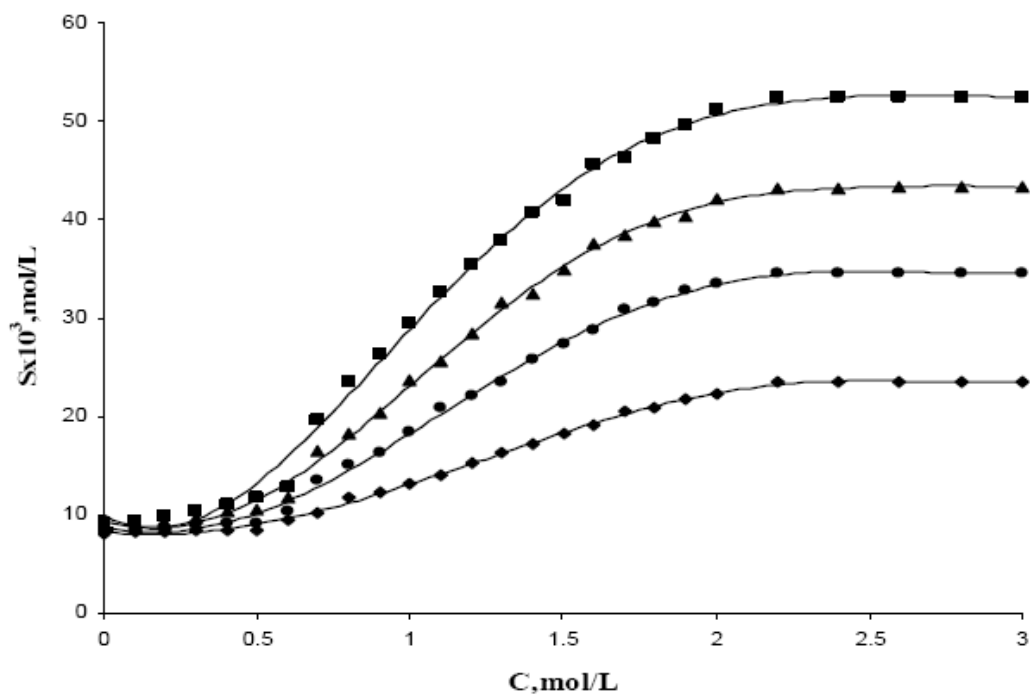


Figure 4. Effect of sodium benzoate concentration (C) on the solubility (S) of furfural in water (at ◆ 303K ● 313K ▲ 323K ■ 333K)

DESIGN-EXPERT Plot

StdErr of Design

X = A: urea concentration (C)

Y = B: Effect of urea concentration (C) on the solubility (S) of furfural in water

Actual Factors

C: tri-sodium citrate concentration (C) = 1.50

D: Effect of tri-sodium citrate concentration (C) on the solubility (S) of furfural in water

E: sodium toluate concentration (C) on the solubility (S) of furfural in water

F: Effect of sodium toluate concentration (C) on the solubility (S) of furfural in water

G: sodium benzoate concentration (C) on the solubility (S) of furfural in water

H: Effect of sodium benzoate concentration (C) on the solubility (S) of furfural in water

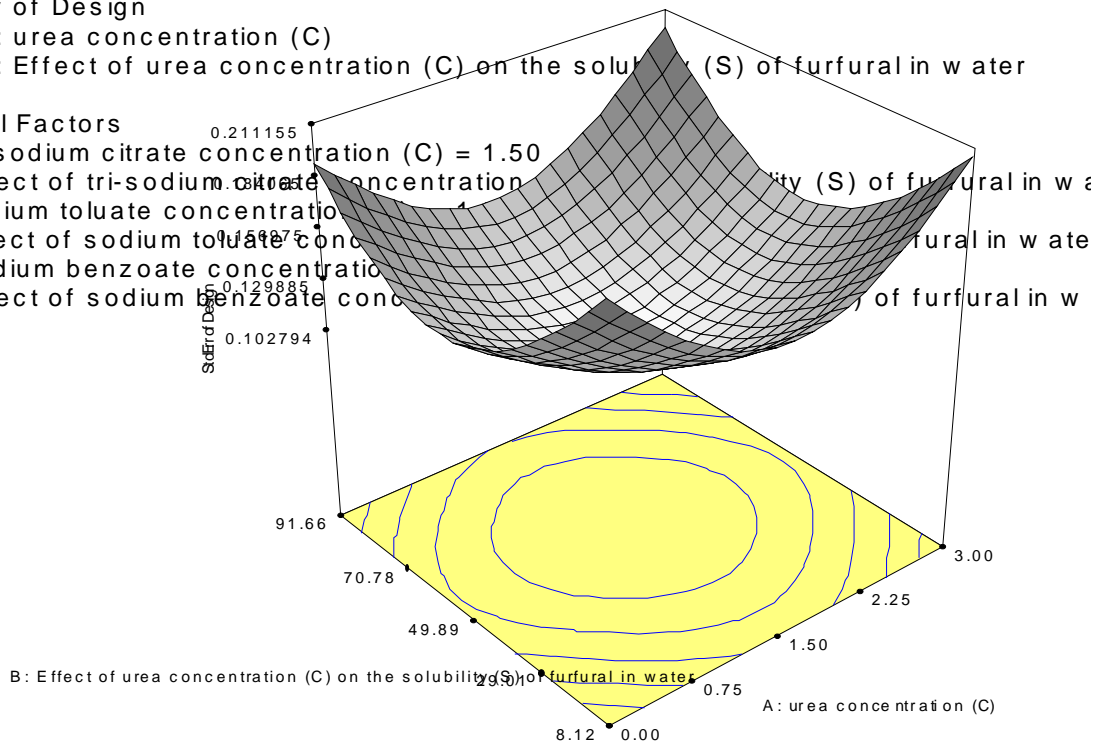


Figure 5. Effect of hydrotrope concentration (C) on the solubility (S), on the mass transfer co-efficient ($k_L a$), Enhancement factor for mass transfer coefficient(ϕ_{mtc}) of furfural in water.



Synthesis and Characterization of Novel Soluble Aromatic Polyesters with Pendant Cyano Groups

Yikai Yu, Mingzhong Cai & Tao Wang

College of Chemistry and Chemical Engineering, Jiangxi Normal University

Nanchang 330022, China

E-mail: yuyikai1980@163.com

Abstract

2, 6-Bis (4-carboxyphenoxy) benzonitrile was first synthesized by condensation of 2, 6-difluorobenzonitrile with *p*-Hydroxybenzoic acid in the presence of KOH and DMSO. And then the reaction of 2, 6-bis (4-carboxyphenoxy) benzonitrile with sulfur oxychloride yielded 2, 6-bis (4-chloroformylphenoxy) benzonitrile (BCIPOBN). A series of novel soluble aromatic polyesters with pendant cyano groups were prepared by polycondensation of different aromatic diphenols and 2,6-bis (4-chloroformylphenoxy) benzonitrile (BCIPOBN) using 1,2-dichloroethane (DCE) as solvent and pyridine as the absorbent of HCl. The resulting polymers were characterized by different physico-chemical techniques, such as FT-IR, Thermogravimetric analysis (TGA), Wide angle X-ray diffraction (WAXD), and so on. All the polymers had the proposed structure and were amorphous. Thermogravimetric studies showed that the thermal decomposition temperatures (T_{d5}) at 5% weight loss of polymers were 391~406 °C in N_2 atmosphere, indicating they had good thermal stabilities. The prepared polyesters exhibited good solubility in some common solvents, such as $CHCl_3$, ethylene dichloride (DCE), CH_2Cl_2 , tetrahydrofuran (THF) as well as aprotic polar organic solvents such as *N*-methyl pyrrolidone (NMP), *N,N*-dimethylacetamide (DMAC) and *N,N*-dimethylformamide (DMF), and so on.

Keywords: Novel soluble aromatic polyesters with pendant cyano groups, Polycondensation, Solubility

1. Introduction

Aromatic polyesters are a type of high-performance polymers with excellent thermal, physical and mechanical properties. But their poor solubility in organic solvents often restricts the use for many applications (Su JQ, 1994) (Nye S. A., Swint S. A. 1994). Thus, it appears very important that various structure changes are introduced in the polyesters' chain to obtain better solubility for processing (Wang C. S., Yang R. W., Gravalos K. G. 1998) (Kallitais J. K., Kakali F., Gravalos K. G. 1994) (Chern Y. T., Huang C. M. 2000) (Mikroyannidis J. A. 2000). Previously it has been found that introduction of groups with sp^3 -hybridized atoms ($-CR_2-$), ether linkage, and pendant phenyl groups can improve the solubility of polyesters (Brochini S., James K., Tangpasuthadol V., Kohn J. 1997) (Liaw D. J., Liaw B. J., Hsu J. J., Liaw B. Y., Cheng Y. C. 2000) (Liaw D. J., Hsu J. J., Liaw B. Y. 2001). Due to strong polarity and easy reactivity of cyano group, better heat-resistant properties of the polymers would be received and many functional polymers could be prepared by the several reactions of cyano group if cyano group was incorporated into polymers' main chain as side groups. Moreover, these aromatic polymers containing pendant cyano groups would undergo crosslinking on being heated to elevated temperatures (Hergenrother P.M. 1974) (Cao G. P., Chen W. J., and Liu X. B. 2008). As a result of crosslinking, the glass transition temperatures (T_g s) of these polymers would increase and solvent-resistant films could be yielded. However, it appears that soluble aromatic polyesters with pendant cyano groups have not been reported in detail in the open literatures. In this article, we designed a series of novel soluble aromatic polyesters with pendant cyano groups as the following route: a new monomer 2, 6-bis (4-chloroformylphenoxy) benzonitrile (BCIPOBN) was first prepared. Then a series of novel soluble aromatic polyesters with pendant cyano groups were synthesized by polycondensation of 2, 6-bis (4-chloroformylphenoxy) benzonitrile (BCIPOBN) and different aromatic diphenols.

2. Experimental

2.1 Materials

p-Hydroxybenzoic acid (Aldrich, Shanghai Wulian Chemical Factory, China), 2, 6-difluorobenzonitrile (Aldrich), *N*-methyl pyrrolidone (NMP, Aldrich), dimethyl sulphoxide (DMSO, Aldrich), *N,N*-dimethylacetamide (DMAC, Aldrich, Tianjin Damao Chemical Reagent Factory, China) and *N,N*-dimethylformamide (DMF, Aldrich, The First

Chemical Reagent Factory of Tianjin, China) were used as received. 1, 2-Dichloroethane (DCE, Aldrich) and pyridine were dried with molecular sieves (type 4Å). The other fractions were collected and stored over sieves.

2.2 Synthesis of new Monomer: 2, 6-bis (4-chloroformylphenoxy) benzonitrile (BCIPOBN)

To a 250ml, round-bottomed flask equipped with a mechanical stirrer, a thermometer, nitrogen inlet and out tubes, and a Dean-Stark trap, 72 mmol of p-Hydroxybenzoic acid, 144mmol of KOH, 70 ml of dimethyl sulphoxide (DMSO) and 55 ml of toluene were added. The reaction mixture was heated to 140~150 °C until no further water was azeotropically distilled from the reaction mixture, and then temperature was raised to 170 °C to remove toluene. After being cooled to 40 °C, 30mmol of 2, 6-difluorobenzonitrile was added and the reaction mixture was heated to 185~195 °C and stirred at this temperature for 8h. After cooling to room temperature, the reaction mixture was dissolved in water and hydrochloric acid was added, and then the product was precipitated. The solid product was washed with water and recrystallized from the mixture of ethyl alcohol and water three times to give 2, 6-bis (4-carboxyphenoxy) benzonitrile. Yield 85%; Purity 96%; m.p.311~312 °C; IR(KBr): 3429(OH),2235(CN),1695(C=O),1605,1578,1506(C=C), 1245(—O—). Elemental Analysis calculated for C₂₁H₁₃NO₆; C, 67.2; H, 3.47; O, 25.6. Found: C, 67.3; H, 3.54; O, 25.7.

The reaction of 2, 6-bis (4-carboxyphenoxy) benzonitrile with sulfur oxychloride yielded 2, 6-bis (4-chloroformylphenoxy) benzonitrile (BCIPOBN). The product was recrystallized from anhydrous hexane. Yield 96%; Purity 97%; m.p.140~142 °C; IR(KBr): 2232(CN),1774(C=O),1602,1574,1497(C=C); 1245(—O—). Elemental Analysis calculated for C₂₁H₁₁NCl₂O₄; C, 61.65; H, 2.70; O, 15.53; Cl, 17.23. Found: C, 61.59; H, 2.67; O, 15.46; Cl, 17.36.

2, 6-Bis (4-chloroformylphenoxy) benzonitrile (BCIPOBN) was synthesized as shown in scheme 1.

2.3 Polymer synthesis

To a 100ml, round-bottomed flask equipped with a mechanical stirrer, a thermometer, nitrogen inlet and out tubes. 0.01mol diphenols, 25ml of 1, 2-dichloroethane (DCE), and 1ml pyridine as the absorbent of HCl were added. Into the resulting suspension were added 0.01mol 2, 6-bis (4-chloroformylphenoxy) benzonitrile (BCIPOBN). The reaction mixture was stirred at room temperature for 8 h and then warmed to 80 °C over 2h. After the reaction is over, the products were precipitated from hexane, washed with water, and dried under vacuum to give the novel aromatic soluble polyesters with pendant cyano groups.

The novel soluble aromatic polyesters with pendant cyano groups were synthesized by polycondensation of 2, 6-bis (4-chloroformylphenoxy) benzonitrile (BCIPOBN) and different aromatic diphenols as shown in scheme 2.

2.4 Characterization

Elemental analysis was performed with Perkin-Elmer Model 2400 CHN analyzer. The inherent viscosities (η_{inh}) of polymers were measured in a 0.1wt% NMP solution at 30 °C. The FT-IR spectra of the polymers in KBr pellets (2%) were recorded using a Nicolet FT-IR (510P) spectrophotometer. Thermogravimetric analysis (TGA) was carried out on a Perkin-Elmer 7 Series thermal analysis system with an increasing rate of 10 °C/min, N₂ atmosphere at the flow rate of 40ml/min, scanning scope ranging from 50 to 750 °C, and sample weight of 5.0~7.0mg. Wide angle X-ray diffraction (WAXD) was measured with a Rigaku D/MAX- A X-ray diffractometer, using CuK α radiation, at 30KV and 20mA. The diffractograms were recorded at room temperature over the range of $2\theta=10\sim40^\circ$.

3. Results and discussion

3.1 New monomer synthesis

2, 6-Bis (4-chloroformylphenoxy) benzonitrile (BCIPOBN) was synthesized as shown in scheme 1. 2, 6-bis (4-carboxyphenoxy) benzonitrile was first synthesized by condensation of 2, 6-difluorobenzonitrile with p-Hydroxybenzoic acid in the presence of KOH and DMSO, and toluene was used for the azeotropic removal of water. Then the reaction of 2, 6-bis (4-carboxyphenoxy) benzonitrile with sulfur oxychloride yielded 2, 6-bis (4-chloroformylphenoxy) benzonitrile (BCIPOBN), and a little DMF was added to improve the rate of production. The chemical structure of BCIPBN was confirmed by FT-IR and elemental analysis.

3.2 Novel polyester synthesis

Scheme 2 outlines the synthesis of novel soluble aromatic polyesters with pendant cyano groups by polycondensation. Firstly, Inherent viscosities (η_{inh}) of polymers are affected by the purity of monomers. Thus, the monomers (BCIPOBN and diphenols) must be purified by recrystallizing many times before polycondensation. Secondly, the molar ratios of monomers (BCIPOBN and diphenols) affect also the inherent viscosities (η_{inh}) of polymers. According to the modified Carothers equation (Cao J.k.; Su W. C.; Piao M. J., et al. 1992), i.e., $X_n = (1+r)/(1-r)$, where X_n is the number-average degree of polymerization and r is the molar ratio of BCIPBN to diphenols, the η_{inh} values of polymers are highest when the molar ratio of BCIPBN to diphenols is near to 1:1. In addition, pyridine which is added to the reaction

mixture as the absorbent of HCl is benefit to obtain higher-weight-molecular polymers.

3.3 The FT-IR and elemental analysis

The chemical structures of the prepared polyesters were confirmed by FT-IR and elemental analysis. The results are as follows:

Polymer I: IR (cm^{-1}): 2231(CN); 1739(C=O, ester); 1261(C-O-C, ester); 1242(Ar-O-Ar). Calculated(found)elemental Analysis for $(\text{C}_{27}\text{H}_{15}\text{NO}_6)_n$, %: C, 72.16(72.14); H, 3.34(3.33); N, 3.12(3.10).

Polymer II: IR (cm^{-1}): 2232(CN); 1738(C=O, ester); 12621(C-O-C, ester); 1241(Ar-O-Ar). Calculated(found)elemental Analysis for $(\text{C}_{34}\text{H}_{21}\text{NO}_6)_n$, %: C, 75.70(75.66); H, 3.90(3.89); N, 2.60(2.58).

Polymer III: IR (cm^{-1}): 2231(CN); 1740(C=O, ester); 1259(C-O-C, ester); 1243(Ar-O-Ar); 2971(-CH₃). Calculated(found) elemental Analysis for $(\text{C}_{36}\text{H}_{25}\text{NO}_6)_n$, %: C, 76.19(76.16); H, 4.41(4.39); N, 2.50(2.48).

Polymer IV: IR (cm^{-1}): 2233(CN); 1737(C=O, ester); 1774(C=O); 1259(C-O-C, ester); 1241(Ar-O-Ar). Calculated(found)elemental Analysis for $(\text{C}_{41}\text{H}_{23}\text{NO}_7)_n$, %: C, 76.76(76.71); H, 3.59(3.56); N, 2.18(2.17).

The elemental analysis values, i.e., C, H, and N content of polymers I-IV are in close agreement with theoretical values confirming the proposed structure. The FT-IR spectra of polymers show that All the spectra have a stretching vibration for the C=O group in the ester linkage, a stretching vibration for CN group, a stretching vibration for ester C-O-C, and a stretching vibration for the ether group asymmetrical vibration of Ar—O—Ar, indicating that the prepared polyesters have the proposed structure. Figure 1 shows the FT-IR spectra of polymer II.

3.4 The WAXD analysis

The analysis of WAXD shows, all the polymers are amorphous. This might be attributed to the flexible units (meta-phenylene units, etc) and cyano pendant groups which can't make the polymers match the crystalline structure. The curves of polymer I, II, III and IV is shown in Figure 2.

3.5 Thermogravimetric analysis (TGA) of polymers

The thermal stabilities of the polymers were investigated by TGA. Thermogravimetric analysis (TGA) was carried out on a Perkin-Elmer 7 Series thermal analysis system with an increasing rate of 10 °C/min, N₂ atmosphere at the flow rate of 40ml/min, scanning scope ranging from 50 to 750 °C. The thermal decomposition temperatures (T_{d5}) at 5% weight loss of the polymers are also listed in Table 1. The thermal decomposition temperatures (T_{d5}) of the polymers show the polymers prepared are thermally stable from 391 °C to 406 °C, indicating that the novel polymers have good thermal stabilities used as novel polyester materials. The TGA curve of polymer II is shown in Figure 3.

3.6 The solubility and inherent viscosities (η_{inh}) of polymers

The solubility behavior of the polymers prepared in this study was determined for powdery samples in excess solvents at room temperature for 24 h and the results are listed in Table 2. It is shown that all the polymers are soluble in some common solvents, such as CHCl₃, ethylene dichloride (DCE), CH₂Cl₂, tetrahydrofuran (THF) as well as aprotic polar organic solvents such as N-methyl pyrrolidone (NMP), N, N-dimethylacetamide (DMAC) and N, N-dimethylformamide (DMF), and so on, the good solubility of polymers might be attributed to flexible units (meta-phenylene units, etc) and cyano pendant groups. In addition, the good solubility of polymers indicates they have much potential for solvent processing and application. Inherent viscosities of the polymers are also given in Table 2. Inherent viscosities (η_{inh}) (0.61~0.68 dl/g) reveal that high molecular weight polymers are obtained in the given reaction medium. Thus, the polycondensation route is appropriate.

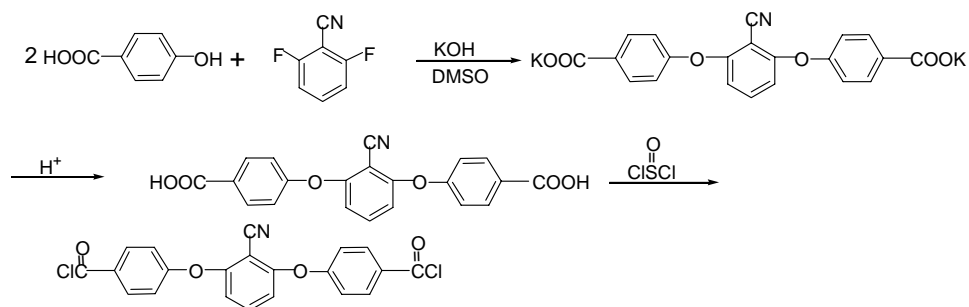
4. Conclusions

The conclusions that can be drawn from the present study are as follows:

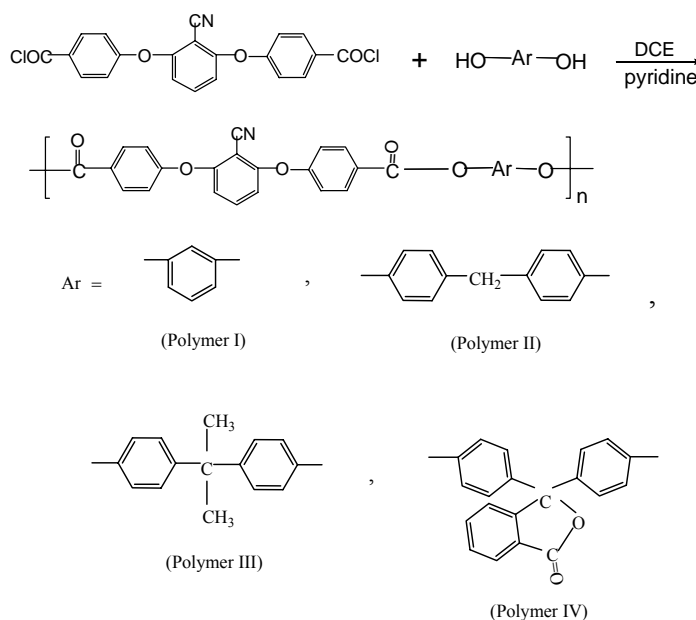
- (1) A new monomer 2, 6-bis (4-chloroformylphenoxy) benzonitrile (BCIPOBN) was first prepared. Then a series of novel soluble aromatic polyesters with pendant cyano groups were synthesized by polycondensation of 2, 6-bis (4-chloroformylphenoxy) benzonitrile (BCIPOBN) and different aromatic diphenols.
- (2) Thermogravimetric studies showed that the thermal decomposition temperatures (T_{d5}) at 5% weight loss of polymers were 391~406 °C in N₂ atmosphere, indicating they had good thermal stabilities used as novel polyester materials.
- (3) The prepared polyesters exhibited good solubility in some common solvents, such as CHCl₃, ethylene dichloride (DCE), CH₂Cl₂, tetrahydrofuran (THF) as well as aprotic polar organic solvents such as N-methyl pyrrolidone (NMP), N, N-dimethylacetamide (DMAC) and N, N-dimethylformamide (DMF), and so on, indicating they have much potential for solvent processing and application. Inherent viscosities (η_{inh}) (0.61~0.68 dl/g) reveal that high molecular weight polymers are obtained in the given reaction medium. Thus, the polycondensation route is appropriate.

References

- Brochini S., James K., Tangpasuthadol V., Kohn J.. (1997). A combinatorial approach for polymer design. *J. Am. Chem. Soc.*, 119 (19): 4553~4554.
- Cao G. P., Chen W. J., and Liu X. B.. (2008). Synthesis and thermal properties of the thermosetting resin based on yano functionalized benzoxazine. *Polymer Degradation and Stability*, 93: 739~734.
- Cao J.k.; Su W. C.; Piao M. J., et al. (1992). Studies on the rigid-rigid block copolymer(I)-The structure and properties of PEEK-PES block copolymers. *Chem J Chin Univ.*, 13(10): 1327.
- Chern Y. T., Huang C. M.. (2000). Synthesis and characterization of new polyesters derived from 1, 6- or 4, 9-diamantenedicarboxylic acyl chlorides with aryl ether diols. *Polymer*, 39 (11):2325~2329.
- Hergenrother P.M. (1974). Poly (phenyl-as-triazines) and poly(phenylquinoxalines). New and cross-linked polymers. *Macromolecules*, 7:575~582.
- Kallitais J. K., Kakali F., Gravalos K. G. (1994). Synthesis and characterization of soluble aromatic polyesters containing oligophenyl moieties in the main chain. *Macromolecules*, 27(16): 4509~4515.
- Liaw D. J., Hsu J. J., Liaw B. Y.. (2001). Synthesis and characterization of new soluble cardo polyesters derived from 1, 1-bis [4-(4-chlorocarboxyphenoxy) phenyl]-4-tet-butylcyclohexane with various bisphenols by solution polycondensation. *J. Polym. Sci. Part A: Polym. Chem.*, 39(17):2951~2956.
- Liaw D. J., Liaw B.J., Hsu J. J., Liaw B. Y., Cheng Y. C.. (2000). Synthesis and characterization of new soluble polyesters derived from various cardo bisphenols by solution polycondensation. *J. Polym. Sci. Part A: Polym. Chem.*, 38(24):4451~4456.
- Mikroyannidis J. A.. (2000). Synthesis and characterization of soluble ,photoluminescent polyamides, polyesters, polyesters containing 9,10-di(4-biphenyl)anthracene segments in the main chain. *Polymer*, 41 (23): 8193~8204.
- Nye S. A., Swint S. A.. (1994). Synthesis and characterization of polyarylates derived from 4,4'-dihydroxy-meta-terphenyl and aromatic diacid chlorides. *J. Polym. Sci. Part A: Polym. Chem.*, 32: 721~727.
- Su JQ. (1994). Thermal transparent plastic—polyarylesters. *New Chemical Materials*, 10: 20~23.
- Wang C. S., Yang R. W., Gravalos K. G. (1998). Synthesis and properties of a novel perfluorononyloxy group containing polyarylates. *J. Polym. Sci. Part A: Polym. Chem.*, 36 (4): 645~653.



Scheme 1. Synthesis of BCIPBN



Scheme 2. Synthesis of novel aromatic polyesters

Table 1. the TGA of polymers

Polymer	I	II	III	IV
T _d ()	391	397	406	403

T_d (): Temperatures at 5% weight loss

Table 2. the η_{inh} and solubility of polymers

Polymer	NMP	DMAC	DMF	CHCl ₃	DCE	THF	C ₂ H ₅ OH	η_{inh} (dl/g)
Polymer I	+	+	+	+	+	+	-	0.63
Polymer II	+	+	+	+	+	+	-	0.68
Polymer III	+	+	+	+	+	+	-	0.67
Polymer IV	+	+	+	+	+	+	-	0.61

+: soluble; -: insoluble

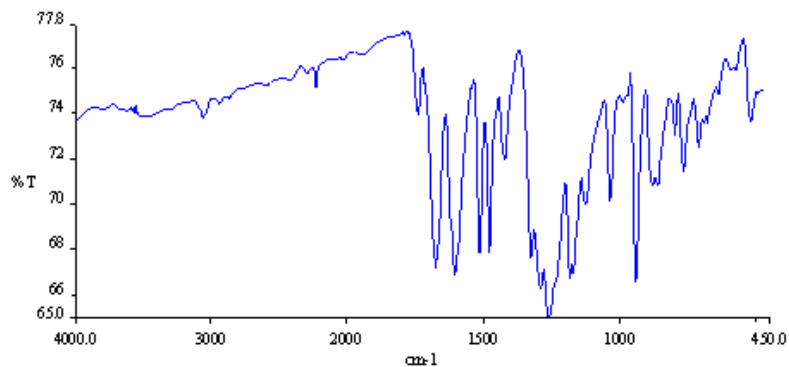


Figure 1. the FT-IR spectra of polymer II

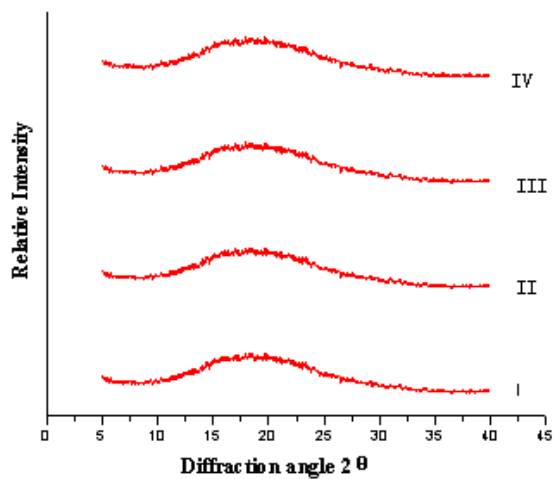


Figure 2. the WAXD curves of polymer I, II, III and IV

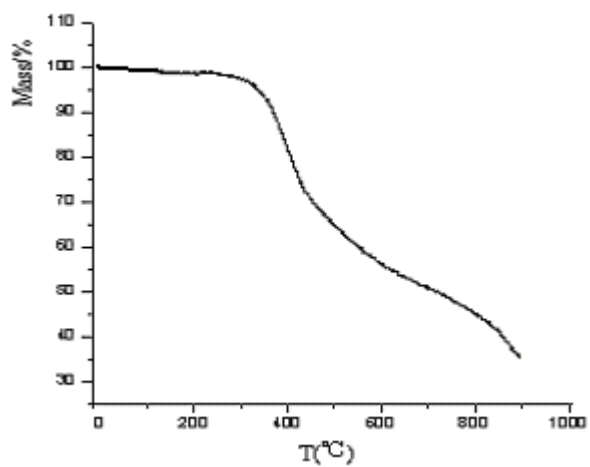


Figure 3. the TGA curve of polymer II



Experimental Investigation on the Effects of Audible Sound to the Growth of *Aspergillus* Spp

Poopathy Muthu Karippen

School of Science and Technology, Universiti Malaysia Sabah

Lock Bag 2073, 88999 Kota Kinabalu, Sabah, Malaysia

E-mail: pups_leo@yahoo.com

Jedol Dayou

Vibration and Sound Research Group (VIBS), Universiti Malaysia Sabah

Lock Bag 2073, 88999 Kota Kinabalu, Sabah, Malaysia

Tel: 60-88-320-302 Fax: 60-88-435-324 E-mail: jed@ums.edu.my

Chong Khim Phin (Corresponding author)

School of Sustainable Agriculture, Universiti Malaysia Sabah

Lock Bag 2073, 88999 Kota Kinabalu, Sabah, Malaysia

Tel: 60-88-320-000 x5655 E-mail: chongkp@ums.edu.my

Abstract

This paper discusses the effect of sound on the growth of fungus, *Aspergillus* spp. *Aspergillus* was cultured on Potato Dextrose Agar (PDA) and Potato Dextrose Broth (PDB) and exposed to sound waves for five hours per day for three days. This experiment was observed for three days and data were recorded everyday after the exposure. Four parameters were used to measure the growth of fungus which were colony forming units per ml, optical density, length of germ tube and the diameter of the colony. The results showed that sound waves have effects on the growth of *Aspergillus*. When *Aspergillus* was exposed to sound waves with frequencies of 5 kHz, 10 kHz and 15 kHz, the growth was affected by the different frequency. The higher the frequency, the higher the growth inhibition found on *Aspergillus*. All the three frequencies inhibited the growth of *Aspergillus* compared to the control (No exposure to sound) and the maximum inhibition occurred at the frequency of 15 kHz.

Keywords: *Aspergillus*, Inhibition, 5 kHz, 10 kHz, 15 kHz, Sound frequency

1. Introduction

Waves are a common phenomenon in our environment. We are surrounded by sound waves, light waves, water waves and other kinds of waves, which we can control and use to convey information or transport energy from one location to another (Young and Freedman, 1996). Mechanical waves have been shown to have effect on microbes. Ultrasound for example, has been used for sterilizing and killing unwanted bacteria due to thinning of cell membranes, localized heating and production of free radicals (Piyasena et al., 2003). Ultrasound is able to inactivate bacteria and deagglomerate bacterial clusters or flocks through a number of physical, mechanical and chemical effects arising from acoustic cavitations (Joyce et al., 2003).

Sound waves have been used for different types of experiments not only on bacteria but also certain parts of plants that react to the sound waves. Some researchers reported that optimization of *Chrysanthemum* callus growth can be altered with different sound wave frequencies, strength and loading time. In their study, they have concluded that sound wave stimulation significantly affects the production of *Chrysanthemum* callus. The optimum formulation for the relation of the sound wave stimulus and callus growth could be predicted (Jiping, et al., 2003). In another experiment conducted by Bochu et al. (2004) using chrysanthemum callus treated by optimal sound waves (1.4 kHz or 0.095 kdb) they found that callus of chrysanthemum has significantly higher IAA but lower ABA levels than the untreated samples. The effect of

sound stimulation on the metabolism of chrysanthemum roots was also studied and it was found that the growth of roots was not inhibited but accelerated under suitable sound stimulation (Yi et al., 2003).

In another experiment to study the germination index, stem height, relative increase rate of fresh weight, rooting ability, root system activity and the penetrability of cell membrane in paddy found it was found that 400 Hz and 106 dB are the 'best frequency and intensity' for the best stimulation. However when the sound wave stimulation exceeds 4 kHz or 111 dB, it is harmful to the seeds. Considering the advantages that can be altered either to promote or retard the growth of bacteria or certain parts or compounds in plants, we hypothesized that the application of this concept may be appropriate for controlling the growth of fungus especially *Aspergillus* spp, in food storage. In this study, the effect of audible sound of certain frequencies to *Aspergillus* was investigated. The effect was assessed based of the comparison on their, turbidity by turbidimetric method, colony forming unit, germ tube elongation and diameter of colony with their respective control samples.

2. Materials and methods

2.1 *Aspergillus* spp

Aspergillus spp was originally isolated from one week old bread kept under high humidity in a natural environment. The confirmation of the isolated fungus was done based on their classical morphology. The culture was maintained at 25°C inside an incubator until needed.

2.2 Dilution Plating Using Spread Plate Technique

Aspergillus spp. was scraped once from the cultivated media and dispersed into 9 ml of sterile water. 1ml of this solution was transferred to a second tube containing 9 ml of sterile water, resulting in a 0.01 dilution of the spore mass in the original material. A 1-ml portion from the dilution was pipette to a separate Petri dish containing cooled agar medium and spread evenly throughout using a spreader. After a day of incubation, colonies appeared in varying densities, depending upon the amount of dilution from the original material. The number of spores present in the original sample was calculated by selecting the plates showing 40-100 colonies. With this information the following calculation was performed:

$$\text{Colonies per gram of original sample} = \frac{\text{Colony count}}{\text{Dilution factor}}$$

For Potato Dextrose Broth (PDB), *Aspergillus* spp was scraped once from the cultivated media and dispersed into 9 ml of sterile water. One ml of this solution was transferred directly into the bottles containing PDB which was prepared earlier. The cultured media was incubated for a day and the growth of fungus was measured using a spectrophotometer, haemocytometer and micrometer.

2.3 Sound Wave Device

An air-tight experimental sound wave chamber (MarJedLV) with the speaker in the middle to provide sound waves was used in this study (Figure 1). A generator was used to generate a different range of frequencies to the treatment. The treated groups were loaded and placed in the device with optimal sound waves conditions within three different ranges. The control treatment was placed without exposure to sound waves. The growth of fungus was observed and data recorded daily.

2.4 Optical Density

A Cary 50 UV/Vis Spectrophotometer was used for comparing the growth of *Aspergillus* spp after the treatments. The PDB was set as blank, and the turbidity among the samples were expressed as Optical Density (OD). The turbidity measurement was correlated with the growth of microbial population (Tortora, et al., 2001).

2.5 Colony Forming Unit (CFU/ml or CFU/g)

The plate count technique was performed to determine the number of cells or cells clumps that are capable of forming colonies on agar plates after exposure to sound waves. These treatments were prepared using the spread plate technique. Knowing the dilution factor, volume plated, and number of colonies on the plate (or average from the duplicate plates), count of microorganisms in the treatment was calculated using the following equation (Ahmed and Carlstrom, 2003):

$$\text{Count (CFU/ml or CFU/g)} = \frac{\text{Average number of colonies from duplicate plates}}{\text{Dilution factor} \times \text{volume plated}}$$

2.6 Measurement of Germ tube using Micrometer

The elongations of the germ tube after exposed to the different treatments compared to control were measured using a micrometer attached to a Zeiss Axioplan Microscope.

2.7 Diameter of Colony

For each treatment that was prepared using the spread plate technique, and the diameter of 10 colonies for each replicate was taken. The average diameter of colony was recorded. The same method was followed for the other two replicates and data was recorded continuously for five days.

3. Results and discussion

3.1 Optical Density

Mean values of the optical density showed an increase from the start to day three for all four frequencies tested. The mean values of other frequencies showed a lower value compared to the control treatment. Figure 2 clearly shows that the control treatment had the highest growth rate compared to other treatments. There were significant differences between the OD from day one to day three for the different frequencies (except between day one and two for control, frequency 5kHz and 15kHz). There was no significant difference between the OD from the onset of the experiment to day one.

3.2 Colony Forming Units (CFU/ml or CFU/g)

The ability of the treated *Aspergillus* spp. to survive was tested based on the colony forming units per mL (CFU/mL). The control treatment showed the highest growth rate, followed by 5 kHz, 10 kHz and 15 kHz (Figure 3). The growth of fungus was inhibited when higher frequencies were used. Thus, the growth of *Aspergillus* was restricted by the sound effect. But surprisingly, there was no significant difference between the onset of the experiment and day one for both control and 10 kHz. From day two to day three, there was no significant difference between exposure to frequency of 10 kHz and the control. For other recorded data there were significant differences among the control, 5 kHz, 10 kHz and 15 kHz.

3.3 Measurement of Germ Tube Elongation

The mean *Aspergillus* spp. germ tube elongation was observed and measured using a micrometer. The mean values for sound treatments were lower when compared to control (Figure 4). The same increase in the mean values from start to day one was observed for all the frequencies. The slower growths of germ tube were only found after day one for 5 kHz, 10 kHz and 15 kHz (Figure 4). In contrast, the control treatment showed a constant increase in the mean value and had the highest mean value from day one to day three. There was no significant difference between day one and two among the control, 10 kHz and 15 kHz compared to the control. There was also no significant difference between days two and three, for the 5 kHz treatment as compared to control. For other recorded data there were significant differences among the control, 5 kHz, 10 kHz and 15 kHz.

3.4 Diameter of colony

The control treatment showed the highest increase in the mean diameter of colonies when compared to other sound treatments (Figure 5). But surprisingly, there was no significant difference in the growth among the different frequencies in comparison with the control.

4. Conclusion

In general, the findings suggest that sound wave have effects on the growth of *Aspergillus* spp. The higher the frequency used, the higher the chance to inhibit the growth of this fungus. The frequencies of 5 kHz, 10 kHz and 15 kHz showed inhibition on the growth of *Aspergillus*. The maximum inhibition was found at 15 kHz. It is recommended that future research consider using higher frequencies to verify the possibility for a faster inhibition on the growth of fungus. The findings may benefit the food industry whereby food expiry can be slowed down. Future research should also consider some other internal factors that may contribute to inhibiting the growth of fungus.

References

- Ahmed E. Yousef and Carlstrom, C. (2003). *Food Microbiology: A Laboratory Manual*. John Wiley & Sons, Inc. Hoboken, New Jersey.
- Bochu, W., Jiping, S., Biao, L., Jie, L. and Chuanren, D. (2004). Sound wave stimulation triggers the content change of the endogenous hormone of the Chrysanthemum mature callus. *Colloids and Surfaces B: Biointerface*, 37 (3-4): 107-112.
- Jiping, S., Bochu, W., Meisheng, L., Hongyang, Z., Xin, C. and Chuanren, D. (2003). Optimal designs for sound wave stimulation on the growth conditions of Chrysanthemum callus. *Colloids and Surfaces B: Biointerfaces*, 30(1-2): 93-98.
- Joyce, E., Phull, S.S., Lorimer, J.P. & Mason, T.J. (2003). The development and evaluation of ultrasound for the treatment of bacterial suspensions. A study of frequency, power and sonification time on cultured bacillus species. *Ultrasonics Sonochemistry*, 10(6): 315-318.
- Piyasena, P., Mohareb, E. & McKellar, R.C. (2003). Inactivation of microbes using ultrasound: A review. *International Journal of Food Microbiology*, 87(3): 207-216.

Tortora, G. J., Funke, B. R. and Case, C. L. (2001). *Microbiology: An introduction*. 7th edition. Addison Wesley Longman, Inc. United States.

Yi, J., Bochu, W., Xiujuan, W., Daohong, W., Chuanren, D., Toyama, Y. and Sakanishi, A. (2003). Effect of sound wave on the metabolism of chrysanthemum roots. *Colloids and Surfaces B: Biointerface*, 29 (2-3): 115-118.

Young, H. D. and Freedman, A. (1996). *Extended Version with Modern Physics: University Physics*. 9th Edition. Addison-Wesley Publishing Company, Inc., United States.



Figure 1. The sound wave chamber (MarJedLV)

Optical Density

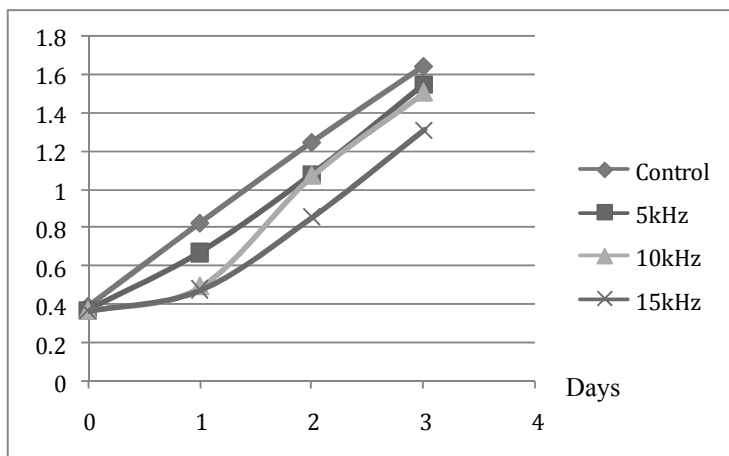


Figure 2. Effect of the different frequencies on the optical density of *Aspergillus* spp

CFU/ml

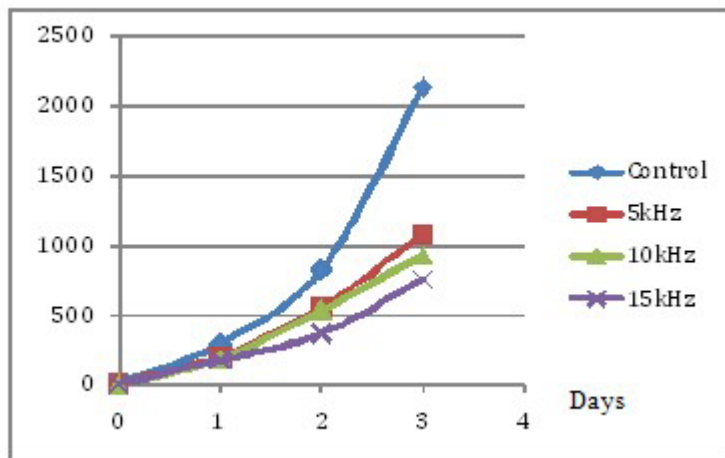


Figure 3. The effect of different frequencies on the colony forming units of *Aspergillus* spp

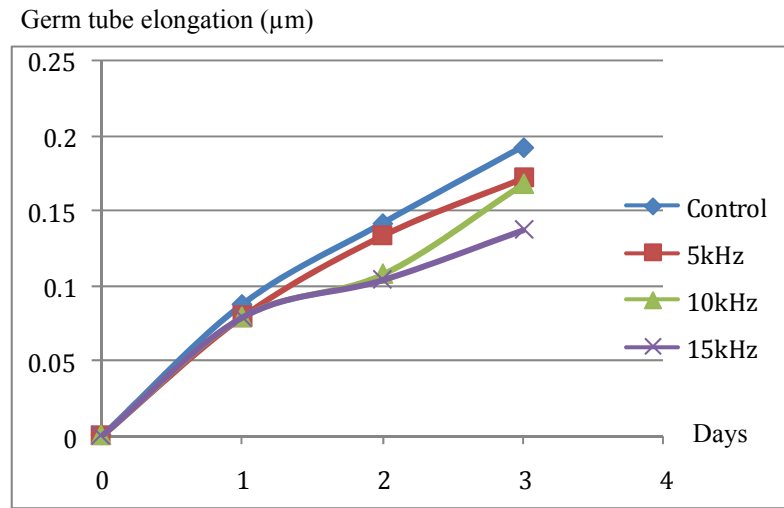


Figure 4. The effect of the different frequencies on germ tube elongation of *Aspergillus* spp

Diameter of colony (cm)

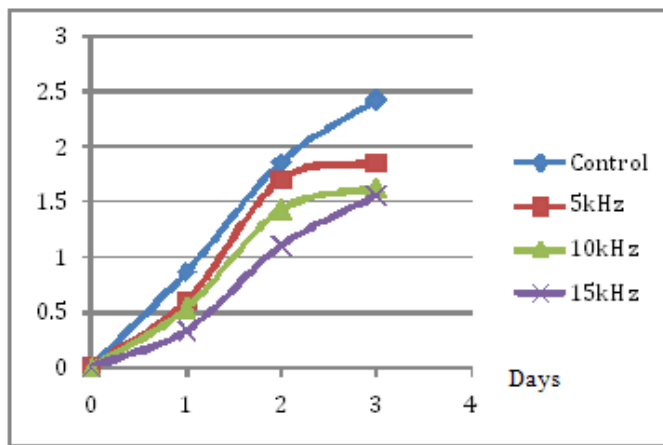


Figure 5. The effect of different frequencies on the mean diameter of colonies of *Aspergillus* spp



Extended Cesaro Operator from A_ϕ^∞ to Bloch Space

Mingzhu Yang

School of Tianjin University of Finance and Economics

25 Zhu Jiang Street, Tianjin 300222, China

E-mail: mzhyang@mail.nankai.edu.cn

Abstract

Let g be a holomorphic function of the unit ball B in several complex variables, and denote by T_g the induced extended Cesaro operator. This paper discussed the boundedness and compactness of T_g acting from A_ϕ^∞ to Bloch space in the unit ball.

Keywords: Cesaro operator, Unit ball, Bounded, Compact, Bloch space

1. Introduction

Let B be the unit ball of C^n , and $H(B)$ denotes the class of analytic functions in B . Let H^p be the standard Hardy space on the unit disc D . For $f(z) = \sum_{j=0}^{\infty} a_j z^j$ in H^p , the classical Cesaro operator acting on f is given by the formula

$$C[f](z) = \sum_{j=0}^{\infty} \left(\frac{1}{j+1} \sum_{k=0}^j a_k \right) z^j.$$

The study of Cesaro operator has become a major driving force in the development of modern complex analysis. The recent papers are good sources for information on much of the developments in the theory of Cesaro operators up to the middle of last decade. In the recent years, boundedness and compactness of extended Cesaro operator between several spaces of holomorphic functions have been studied by many mathematicians. It is well known that the operator C is bounded on the usual Hardy spaces H^p and Bergman space, as well as the Dirichlet space. Basic results facts on Hardy spaces can be found in Durn(1970). For $0 < p < \infty$, Siskakis (1987) studied the spectrum of C , as a by-product he obtained that C is bounded on $H^p(D)$. For $p = 1$, the boundedness of C was given also by Siskakis (1990) by a particularly elegant method, independent of spectrum theory, a different proof of the result can be found in Giang and Morricz(1995)}. After that, for $0 < p < 1$, Miao(1992) proved C is also bounded. For $p = \infty$, the boundedness of C was given by Danikas and Sisakis(1993).

A little calculation shows $C[f](z) = \frac{1}{z} \int_0^z f(t) (\ln \frac{1}{1-t})' dt$. From this point of view, if $g \in H(B)$, it is natural to consider the extended Cesaro operator defined by

$$T_g(f)(z) = \int_0^1 f(tz) Rg(tz) \frac{dt}{t} \quad \text{Where} \quad Rg(z) = \sum_{j=0}^n z_j \frac{\partial g}{\partial z_j}(z).$$

It is easy to see that T_g take $H(B)$ into itself. In general, there is no easy way to determine when an extended Cesaro operator is bounded or compact.

The boundedness and compactness of this operator on weighted Bergman, mixed norm, Bloch, and Dirichlet spaces in the unit ball have been studied by Xiao and Hu. In this paper, we continue this line of research.

Now we introduce some spaces first. We define Bloch space Bloch as the space of holomorphic functions $f \in H(B)$ such that $\|f\|_{Bloch} = |f(0)| + \sup_{z \in B} (1 - |z|^2) |Rf(z)|$.

Let ϕ denote a strictly decreasing continuous function $\phi: [0,1] \rightarrow R$, with $\phi(0) = 1$. For $z \in B$, $\phi(z)$ will denote $\phi(|z|)$. The Banach space of all analytic functions $f \in H(B)$ which satisfy $\|f\|_\phi = \sup_{z \in B} \phi(z) |f(z)|$ will be denoted by A_ϕ^∞ . For example, $\phi(r) = (1 - r^2)^\alpha$ with $\alpha > 0$. When $\phi = 1$, it becomes the classical bounded function space.

2. Some Lemmas

In the following, we will use the symbol C or M to denote a finite positive number which does not depend on variable z and may depend on some norms and parameters f , not necessarily the same at each occurrence.

By Montel theorem and the definition of compact operator, the following lemma follows.

2.1 Assume that $g \in H(B)$. Then $T_g : A_\phi^\infty \rightarrow Bloch$ is compact if and only if T_g is bounded and for any bounded sequence $f_k (k \in N)$ in A_ϕ^∞ which converges to zero uniformly on compact subsets of B as $k \rightarrow \infty$, $\|T_g f_k\|_{Bloch} \rightarrow 0$ as $k \rightarrow \infty$.

Proof. Assume that T_g is compact and suppose $f_k (k \in N)$ is a sequence in A_ϕ^∞ with $\sup_{n \in N} \|f\|_\phi < \infty$ and $f_k \rightarrow 0$ uniformly on compact subsets of B . By the compactness of T_g we have that $T_g f_k$ has a subsequence $T_g f_{k_m}$ which converges in A_ϕ^∞ , say, to h . We have that for any compact set $K \subset B$, there is a positive constant C_K independent of f such that $|T_g f_k(z) - h(z)| \leq C_K \|T_g f_k - h\|_{Bloch}$ for all $z \in K$. This implies that $T_g f_k(z) - h(z) \rightarrow 0$ uniformly on compact sets of B . Since K is a compact subset of B , by the hypothesis and the definition of T_g , $T_g f_k(z)$ converges to zero uniformly on K . It follows from the arbitrary of K that the limit function h is equal to 0 . Since it's true for arbitrary subsequence of f_k , we see that $T_g f_k$ converges to 0 in $Bloch$.

Conversely, $\{f_k\} \in K_r = B_{A_\phi^\infty}(0, r)$, where $B_{A_\phi^\infty}(0, r)$ is a ball in A_ϕ^∞ , then by Montel's Lemma, f_k is a normal family, therefore there is a subsequence f_{k_m} which converges uniformly to $f \in H(B)$ on compact subsets of B .

Denote $B_k = B(0, 1 - \frac{1}{k}) \subset C^n$, and since $\{f_k\} \in K_r = B_{A_\phi^\infty}(0, r)$ then

$$\phi(z) |f(z)| = \lim_{m \rightarrow \infty} \phi(z) |f_{k_m}(z)| < r. \text{ Hence the sequence } \{f_{k_m} - f\} \text{ is such that}$$

$\|f_{k_m} - f\|_\phi \leq 2r < \infty$ and converges to 0 on compact subsets of B , by the hypothesis of this lemma, we have that $T_g f_{k_m} \rightarrow T_g f$ in $Bloch$. Thus the set $T_g(K_r)$ is relatively compact, so T_g is compact, finishing the proof.

2.2 Let $g \in H(B)$, then $RT_g f(z) = f(z)Rg(z)$ for any $f \in H(B)$ and $z \in B$.

Proof: Suppose the holomorphic function fRg has the Taylor expansion

$$(fRg)(z) = \sum_{|\alpha| \geq 1} a_\alpha z^\alpha.$$

Then we have

$$\begin{aligned} R(T_g f)(z) &= R \int_0^1 f(tz)Rg(tz) \frac{dt}{t} = R \int_0^1 \sum_{|\alpha| \geq 1} a_\alpha (tz)^\alpha \frac{dt}{t} \\ &= R \left[\sum_{|\alpha| \geq 1} \frac{a_\alpha z^\alpha}{|\alpha|} \right] = \sum_{|\alpha| \geq 1} a_\alpha z^\alpha = (fRg)(z). \end{aligned}$$

3. Main Theorem

3.1 Suppose $g \in H(B)$, then $T_g : A_\phi^\infty \rightarrow Bloch$ is bounded if and only if

$$\sup_{z \in B} \frac{(1 - |z|^2)}{\phi(z)} |Rg(z)| < +\infty.$$

Proof: We proof the sufficiency frist. Since $T_g f(0) = 0$ and

$$\sup_{z \in B} (1 - |z|^2) |RT_g f(z)| = \sup_{z \in B} (1 - |z|^2) |f(z)| |Rg(z)| \leq \|f\|_\phi \left[\sup_{z \in B} \frac{(1 - |z|^2)}{\phi(z)} |Rg(z)| \right]$$

Therefore, $\sup_{z \in B} \frac{(1 - |z|^2)}{\phi(z)} |Rg(z)| < +\infty$ implies that T_g is bounded.

Now we turn to the necessity. Setting the test function , for any $w \in B$, let $f_w(z) = \frac{1}{\phi(w)} \frac{1-|w|}{1-\langle z, w \rangle}$, Then it is easy to see that $\sup_{w \in B} \|f_w\|_{\phi} = M < \infty$.

$$\begin{aligned} \text{Then } M \|T_g\| &\geq \|T_g f_w\|_{Bloch} = \sup_{z \in B} (1-|z|^2) |RT_g f_w(z)| \\ &\geq (1-|w|^2) |f_w(w)| \cdot |Rg(w)| \geq \frac{1}{2} \frac{(1-|w|^2)}{\phi(w)} |Rg(w)| \end{aligned}$$

Since $w \in B$ is arbitrary, we get the necessity.

Remark: note that by take the test function $f = 1$, we can get $g \in Bloch$.

3.2 Suppose $g \in H(B)$, and $\phi(z) = 1-|z|^2$, then $T_g : A_{\phi}^{\infty} \rightarrow Bloch$ is bounded if and only if $\sup_{z \in B} |Rg(z)| < \infty$, that is Rg belongs to the class of bounded holomorphic functions.

Proof: It is obvious from the 3.1.

3.3 Suppose $g \in H(B)$, then $T_g : A_{\phi}^{\infty} \rightarrow Bloch$ is compact if and only if

$$\lim_{|z| \rightarrow 1} \frac{(1-|z|^2)}{\phi(z)} |Rg(z)| = 0 .$$

Proof: We consider the sufficiency first. Assume the condition holds, then for any given $\varepsilon > 0$, there exists a $\delta (0 < \delta < 1)$, such that $\frac{(1-|z|^2)}{\phi(z)} |Rg(z)| < \varepsilon$ when $|z| > \delta$. Let $K = \{z \in B : |z| \leq \delta\}$, and for any sequence f_k with

$\|f_k\|_{\phi} \leq C$ and f_k converges to 0 uniformly on compact subsets of B . Notice that $T_g f(0) = 0$, then

$$\|T_g f_k\|_{Bloch} = \sup_{z \in B} (1-|z|^2) |f_k(z)| |Rg(z)| \leq \sup_{z \in K} (1-|z|^2) |f_k(z)| |Rg(z)| + \sup_{z \in B-K} (1-|z|^2) |f_k(z)| |Rg(z)|$$

$$\leq \|g\|_{Bloch} \bullet \sup_{z \in K} |f_k(z)| + \sup_{z \in B-K} \frac{1-|z|^2}{\phi(z)} |Rg(z)| \bullet \|f_k\|_{\phi}$$

With the uniform convergence of f_k we get $\|T_g f_k\| \rightarrow 0$ as $k \rightarrow \infty$. Owing to Lemma 1, T_g is compact.

Now we turn to the necessity. For the necessity ,we choose the test functions as follows. For any sequence $\{z_j\}$ with

$|z_j| \rightarrow 1$ as $j \rightarrow \infty$. We set $h_j(z) = \frac{1}{\phi(z_j)} \frac{1-|z_j|}{1-\langle z, z_j \rangle}$. It is easy to check that $\sup_{j \in \mathbb{N}} \|h_j\|_{\phi} < \infty$ and h_j uniformly

converges to 0 in any compact subset of B . That is to say h_j satisfy the condition of lemma 2.1, then we have

$$\|T_g h_j\|_{Bloch} \rightarrow 0 \text{ as } j \rightarrow \infty .$$

$$\text{Therefore, } 0 \leftarrow \|T_g h_j\|_{Bloch} = \sup_{z \in B} (1-|z|^2) |RT_g h_j(z)| = \sup_{z \in B} (1-|z|^2) |h_j(z)| \cdot |Rg(z)|$$

$$\geq (1-|z_j|^2) |h_j(z_j)| \cdot |Rg(z_j)| \geq \frac{1}{2} \frac{1-|z_j|^2}{\phi(z_j)} \cdot |Rg(z_j)| .$$

The conclusion follows by the arbitrary of the sequence $\{z_j\}$.

3.4 Suppose $g \in H(B)$, and $\phi(z) = 1-|z|^2$, then $T_g : A_{\phi}^{\infty} \rightarrow Bloch$ is compact if and only if g is a constant.

Proof: By 3.3 we can obtain that $\lim_{|z| \rightarrow 1} |Rg(z)| = 0$, by the maximum module of principle we have $Rg \equiv 0$, and by the

formula that $f(z) - f(0) = \int_0^1 \frac{Rf(tz)}{t} dt$, we must have g is a constant.

References

A. Siskakis(1990).The cesaro operator is bounded on H^1 , Proc. Amer. Math. Soc., 110(1990):461-462.
 A. Siskakis. (1987). Composition semigroups and the cesaro operator on $H^p(D)$, J. London Math. Soc. 36(1987): 153-164.

- A. Siskakis. (1987). Semigroups of composition operators in Bergman spaces, *Bull. Austral. th. Soc.* 35 (1987): 397-406.
- C.C.Cowen and B.D.MacCluer. (1995). Composition operators on spaces of analytic functions, CRC Press, Boca Raton, FL, 1995.
- D. V. Giang and F. Morricz. (1995). The cesaro operator on Dirichlet is bounded on the Hardy space H^1 , *Acta Sci. Math.* 61 (1995): 535-544.
- J. Miao. (1992). The cesaro operator is bounded on H^p for $0 < p < 1$, *Proc. Amer. Math. Soc.*, 116, 1077-1079.
- J. Xiao. (2004). Riemann-Stieltjes operators on weighted Bloch and Bergman spaces of the unit ball, *J.London Math.Soc.*(2)70(2004) 199-214.
- K. H. Zhu. (2004). Spaces of Holomorphic functions in the Unit Ball, Springer-Verlag (GTM 226), 2004.
- N. Danikas and A. Siskakis. (1993). The cesaro operator on bounded analytic functions, *Analysis*, 13, 195-199.
- P. Durn(1970). *Theory of H^p space*, Academic Press, New York, 1970.
- P.Galanopoulos. (2001). The cesaro operator on Dirichlet spaces, *Acta Sci. Math.* 67 (2001), 441-420.
- W.Rudin. (1980). Function theory in the unit ball of C^n , Springer-Verlag, New York, 1980.
- Z. J. Hu. (2003). Extended cesaro operators on mixed norm space, *Proc. Amer. Math. Soc.*, 131, 2171-2179.
- Z. J. Hu. (2003). Extended cesaro operators on the Bloch spaces in the unit ball of C^n , *Acta Math. Sci.*, 23, (2003), 561-566.
- Zhong-Shan Fang and Ze-Hua Zhou. (2009). Extended Cesaro operators on Zygmund spaces in the unit ball, *Journal of Computational Analysis and Applications*, preprint.



Recycling of Woven Fabric Dyeing Wastewater Practiced in Perundurai Common Effluent Treatment Plant

M. Ramesh Kumar (Corresponding author)

Department of Textile Technology, SSM College of Engineering

Komarapalayam, Namakkal - 638183, Tamilnadu, India

Tel: 91- 098-9431-0132 E-mail: rk_textile@yahoo.co.in

K. Saravanan

Department of Chemical Engineering, Kongu Engineering College

Perundurai, Erode - 638052, Tamilnadu, India

Tel: 91-098-4270-5656 E-mail: rumisivaesh@yahoo.com

R. Shanmugam

Perundurai Common Effluent Treatment Plant

Perundurai, Erode - 638052, Tamilnadu, India

Tel: 91- 098-4324-1123

Abstract

Textile dyeing industries in Erode and Tirupur district of Tamilnadu (India) discharge effluents ranging between 100 and 200m³/t of production. Dyeing is performed by Jigger or advanced Soft Flow reactor process. Coloring of hosiery fabric takes place in the presence of high concentration of sodium sulphate or sodium chloride (30 – 75 kg/m³) in dye solutions. Wash water and dye bath waste water are the process effluents of dyeing industry which are collected separately and follow the advanced treatment for maximum recycling of recovered waters.

Wash water is treated using a sequence of physicochemical and biological unit process, the waste water is passed into ultrafiltration (UF), two stages reverse osmosis (RO) membrane system where the permeate is reused for processes. The rejects about 10 – 12 % of the inlet volume is subject to reverse osmosis for sent to evaporators. Dye bath water after treating, the permeate is used in process for dye bath preparation and the reject of about 20 – 25% is sent to multi effect evaporator / solar evaporation pond (SEP). The final rejects from reverse osmosis system is directed to multi effect evaporator system where condensed waters are recovered. The removal of Total Dissolved Solids (TDS), Chemical Oxygen Demand (COD) and Chloride are in the range of 82 – 97%, 90 – 97% and 78 – 97% respectively. This study was carrier out Common Effluent Treatment Plant (CETP), Perundurai, SIPCOT, Erode district.

Keywords: Textile effluent, Recycling wastewater, Reverse osmosis, PH, COD

1. Introduction

The second basic needs of man 'cloth' are supplied by processing of natural and man-made fibres in the textile industries. Increasing population and modernized civilization trend gave rise to booming of textile sectors in India. An estimate shows that textiles account for 14% of India's industrial production and around 27% of its export earnings.

India is the second largest export of cotton yarn. There are about 10,000 garment manufacturers and 2200 bleaching and dyeing industries in India. Majority are concentrated at Erode and Tirupur district of Tamil Nadu, Surat in Gujarat and Ludiyana in Punjab. Erode and Tirupur district atleast having 50% of dyeing and bleaching industries where in 30% industries are attached to CETP. Dyeing is a combined process of bleaching and coloring, which generates voluminous quantities of wastewaters and in turn causes environmental degradation. These effluents consist of high TDS, chloride, sulphate, hardness and carcinogenic dye ingredients (1).

2. Overview of Common Effluent Treatment Plant (CETP, SIPCOT - Perundurai)

Textile is a major source of income and of great importance for India's economy. At the same time textile processing has major environmental impact. A large proportion of the environmental issues are related to the use and discharge of water. Textile manufacturing is among the major industrial water users. To produce one kg of textile fabrication about 200 liters of water is used.

A lot of chemicals are added to the process for cleaning and dyeing purposes. Obviously the wastewater effluent from this unit contains considerable amounts of hazardous pollutants, and where heavy metals are very common. In India most of the effluent from the textile industry is discharged untreated into rivers. Today 70% of available water in India is polluted and two thirds of illness in India is related to water-borne diseases.

Water treatment is a very important step to change these conditions and to achieve a sustainable situation. India's government has an awareness of this and limits for water effluent quality exist. Unfortunately, this regulation is not closely supervised and a lot of places do not follow the regulation. In newly developed industrial areas advanced wastewater treatment is used for textile effluent, as the one such place is SIPCOT in Perundurai (2).

2.1 SIPCOT

The government is promoting industrial growth in backward and hitherto underdeveloped areas that have potential to grow. SIPCOT is an organization arranging this in the state of Tamil Nadu. Companies, willing to start up industries 'in that area, lease the land for 99 years and are guaranteed good infrastructure, electricity, sewage and water supply 24 hours a day.

2.1.1 SIPCOT Perundurai

SIPCOT Perundurai was started in the year 2000 and it is divided into two parts, the east and the west part, totally 1240 ha. SIPCOT only leases 732 ha of the total area and today 288 ha of the area is licensed. Currently 210 industries are located in the area within the fields of chemicals, textiles industries, food manufacturing, tanning and engineering products. SIPCOT has a common sewage plant, where black water from all industries is treated. The water comes by gravity in stone-laid drainage pipes and is then taken care of by oxidization ponds.

SIPCOT Perundurai industrial plan is an area designed for 54 different units within textile processing. The processes run at the textile industries are dyeing, bleaching and yarning. The industries in SIPCOT are mainly working with cotton. The cotton contributes with much organic matter in the water effluent. Each of the industries has two different pipe systems for wastewater. One system is taking care of the water from the first washing after dyeing, called the dye bath effluent. This water has always very high TDS, over 2100 mg/l and is therefore not measured. The other system is for the remaining effluents from acid wash, water washing, soap washing and softening water are called wash water. The industries have a sensor that measures the TDS value from the wash water, ensuring that it does not exceed 2100 mg/l. If the value is higher a valve will close and direct the water back to the receiving tank to dilute with the other wash water. The textile has two different effluent wastewater streams. The dye bath has a high TDS, above 2100 mg/l, and the wash water has a lower TDS, below 2100 mg/l. Each industry will also measure the flow in both effluent pipes. All effluent from the industries is sent to Perundurai Common Effluent Treatment Plant, PCETP.

2.1.2 Perundurai Common Effluent Treatment Plant

Each industry bears the responsibility for dealing with the effluent water from their processing. Therefore the 14 textile units together formed PCETP. Each of the units has different shares in the treatment plant and consequently they are allowed different maximum flows that they can discharge to the treatment plant. The treatment plant only handles industrial effluent from those 14 textile industries. PCETP can operate 3600 m³/d wash water and 450 m³/d dye bath.

2.1.2.1 Dye bath treatment plant

The dye bath treatment uses an evaporator for cleaning the water. Before the evaporator the water is pre-treated in the form of sedimentation and fine screening. The evaporation unit is a high technology system that vaporizes the water in five different evaporation tanks, three falling and two forced circulation (vacuum) tanks. They reduce the power input by using two heat exchangers and by doing so recover heat from the outgoing water to the incoming water. The outcomes from the evaporation tanks are two different waters, distilled water that goes back to the industries and the second water that goes to solar dryer ponds. The water in the solar dryer ponds evaporates to the atmosphere in 10 days. The rest consists to 95% of sodium chloride (Na Cl). The salt is collected from the bottom of the ponds and stored in sacks under roof. They produce 3.6 tons of salt every day and the space for storage is limited so this soon becomes a big and critical issue. Purify the salt where it can be reused in the textile industries.

2.1.2.2 Wash water treatment plant

The wash water treatment plant was opened in July 2002 which reduces COD and BOD by 40-60%. They regularly measure pH, TSS, BOD, COD and TDS. The plant has no seasonal variation as the textile industry produces the same

quantity throughout the year. However, the hourly inflow varies widely in both quality and quantity. The receiving tank and the bar screens are designed for the peak flow, but the units downstream. If the equalization tank are designed for an average flow and an average quality. The energy consumption is approximately 0.9 kWh/m³ water treated and the cost is Rs.12-20 m³ treated water.

2.1.2.2.1 Flowchart for PCETP

The flowchart for Wash water treatment plant in PCETP is shown in the Figure 1. A number is connected to every unit. The bar screen (1) is where the wastewater first passes through and is situated in the influent of the receiving sump (2). It is used to take care of rags and large objects in the wastewater, so that these objects do not destroy the forthcoming units, for example pumps. PCETP has two screens that are located inside the receiving sump. The shapes are rectangular, size 1.5 x 2.5 m². The clear openings (spaces between bars) of the first screen are 10-15 mm and clear openings of the second screen are 20 mm. The screen is hand-cleaned once in a day and this is sufficient because the character of the water is good.

The purpose of the receiving sump is to attain the same flow into the treatment plant. The diameter of the receiving sump is 8.0 meters and it has a depth of 2.3 meters. The flow into the treatment plant is about 132-150 m³/h and TDS is less than 2100 mg/l. In general, TDS is around 1800 mg/l, pH is about 8-9 and the retention time in the tank is approximately 45 minutes.

Afterwards the water is pumped to the equalization tank (3). The water is spread over three floating aerators, which distribute the water on to the surface of the equalization tank. The water is mixed with air so that an anaerobic process does not occur and settling of suspended solids is avoided. The equalization tank is there to equalize the temperature, quality and flow rate of the water. In other words, minimizing the fluctuation in those parameters for the downstream units. The equalization tank in PCETP has a diameter of 32 meters and a depth of 4 meters. The retention time in the tank is about 24 hours with a flow of 150 m³/h.

The water is then again pumped to the flash mixing tank (4). The first goal for the mixing tank is to raise the wastewater pH to form metal hydroxide particles, by the addition of lime. The next step is to add iron sulphate and polyelectrolyte into the wastewater. Iron sulphate destabilizes the colloids so they are able to flocculate. The polyelectrolyte attaches to the metal solid particles and small metal hydroxide particles become entangled in the polyelectrolyte. This increases the particle size, which promotes settling. The mixing tank has a volume of 1.5 x 1.5 x 1.8 m³ and the mixer is mechanical. In PCETP they add lime to raise the pH to 11. Water samples are collected about every two hours from the equalization tank so the dose of the chemicals can be regulated to the quality of the water. On average, the chemicals added in 1 liter wash water are 80-90 ml Lime, Ca(OH)₂ 5% and 20 ml iron sulphate, FeSO₄ 5%. The water retention time in the flash mixing tank is about two minutes.

After that the water goes into the clariflocculator (5), where the particles coagulate and sink to the bottom as sludge. The deposited sludge is scratched off from the bottom of the tank and pumped into the sludge sump. The cleaner water reaches the top; it flows out through the outfall, which extends all around the settling tank. The outlet water from the clariflocculator goes to the clarified effluent sump (6). The sump is used to provide a constant flow into the next unit, the Auto Valveless Gravity Filter (AVGF) (7). The clarified effluent sump in PCETP has a retention time of 30 minutes. The dimension of the tank is 10.0 x 6.0 x 2.5 m³. The water is pumped by means of the Autovalves gravity filter feed pump to the Automatic Valves Gravity Filter (AVGF). The purpose of the filtering is to remove suspended solids, which did not settle in the sedimentation basin. The reason the particles do not settle could be that they are too small and do not have sufficient time to settle. The particles instead follow the water out. The wastewater passes through the filter bed composed of granular material. The removed particles are accumulated in the voids in the sand therefore the head increases. When the pressure gets too high, automatic backwashing starts to remove the suspended solids. In PCETP, the sand filter is used because it is effective and made of cheap material. They have three different sand stones of a different density to increase the flow. The coarse material is on the bottom and the fine material on the top. The driving force in the sand filter is the capillary drainage system in the bottom. The flow in the filters is 7 m³/h. This gives a retention time of approximately 10 minutes. The filter is backwashed for about 15 minutes with a flow of 50 m³/h, in general twice a day. The backwash water from the sand filter goes back to the receiving sump.

After the AVGF, HCl is added and mixed into the water with a static mixer (8) to reduce the pH to 7.5 - 7.8. A static mixer is placed on the pipe to the stability tank and is designed with baffles. This mixes the water hydraulically with HCl. The water then goes to the stabilization sump (9), where the pH in the water stabilizes, resulting in fixed pH at 7.5 - 7.8 before the water goes to the carbon filter.

The water is pumped into an Automatic Carbon Filter (ACF) (10). The most effective method to take away unwanted materials such as odour, heavy metals organic and inorganic pollutants is to use an ACF. Activated carbon can be prepared from anything consisting of carbon, for example hardwood or nut shell. The materials are heated to 200-1000°C without oxygen and are activated by reheating to a high temperature whilst providing steam. This will give a

fine capillary structure with a surface area of 1000-2000m²/g. The carbon will adsorb the pollution and in that way remove the substance. PCETP has two granular carbon filters, one in each system. The volume of the tanks is 10 m³ and each tank is under a pressure of 2.5 - 3.5 kPa. The retention time in ACF is eight minutes. The thickness of the carbon bed is 0.5-0.75 meter and it is made of coconut shells. The coconut shells are used for two years before they are replaced. The filter is backwashed every eight hours for 15 minutes. The back washing and the first filtrate go to the receiving sump.

After the ACF, the clean water goes through a magnetic flow meter (II), which registers TDS and pH. This unit forms the last control of the water before it goes to the field for irrigation. The effluent water has a flow of about 139m³/h, pH around 7.5 and a TDS of 1700mg/l. Finally the water is pumped with a booster pump out to the field for irrigation. The sludge from the bottom of the clariflocculator goes to the sludge sump (12) and then further to the sludge thickener (13). The sludge sump is a tank where the sludge is collected before it goes to the sludge thickener. This tank is essential to achieve a constant flow into the next unit. The sludge sump in the treatment plant has a diameter of 1.5 meters and a depth of 3.0 meters.

The purpose of the thickener (15) is to increase the solids content of the sludge by removing a portion of the liquid fraction. The thickener has a slow speed mixer. The mixer has the function of making air channels in the sludge, which makes it easy for the water to escape. Another function of the mixer is to scratch the sludge into the middle of the tank where the sludge is taken out. In PCETP the sludge thickener has a diameter of 6.0 meters and a depth of 2.0 meters.

After the sludge thickener the sludge can go two different ways. The centrifugation (14) separates liquids from solids by considerably increasing the gravity power. Due to different density between the solids and the liquid the solids go immediately to the periphery and the water stays closer to the centre and can then be separated. PCETP has two centrifuges but only uses one at a time. The centrifuge extracts the water so the outlet DS is 25%. Each day 10-15 tons of sludge is produced. The rest of the sludge goes to the drying beds (16). Sludge-drying beds are used to dewater digested sludge. The bed is similar to slow filtration through sand. The bed is filled up with one meter of sludge and it stays untouched for 20 days. Under the sand layer there are drainpipes to collect the separated water. After drying, the sludge is removed and packed into bags and stored under a roof. The sand has three different fractions to increase the flow speed through the bed. The five drying beds are a complement to the centrifuge. They are used instead of the centrifuge when capacity is not sufficient. The dimensions of each bed are 11 x 5.0 x 1.0 m³.

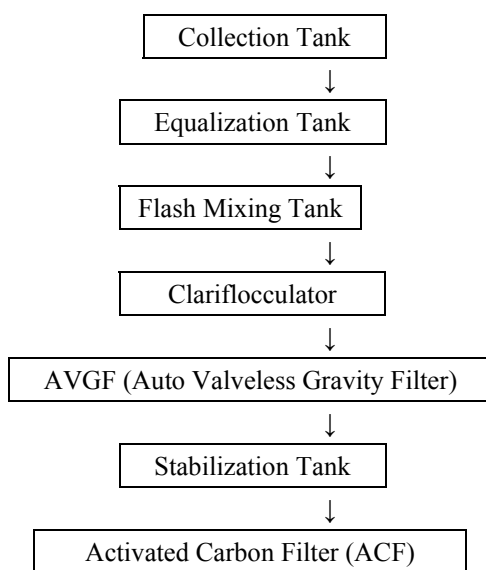
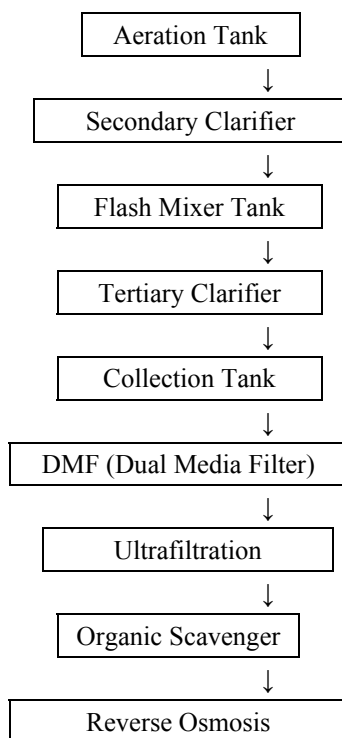
As a final point the sludge is packed in sacks and stored under a roof until further notice. PCETP has made an investigation regarding the use of sludge for brick production. The result was very positive (Charlotta Leissner, 2005).

3. Materials and methods

One of the leading woven fabric dyeing unit, SIPCOT, Perunduarai, Erode, visited and information on manufacturing process and waste water quantity were collected. Waste water samples from the wash water collection tanks and dye bath collection tanks, intermediate points and at the outlets effluent plants were collected and analysed laboratory using standard methods.

Following samples were collected and tested:

- a) Wash water untreated effluent
- b) Dye bath plant feed parameters
- c) Wash water treated effluent (Biological – inlet Parameters)
- d) Biological treatment – secondary clarifier
- e) Tertiary clarifier – DMF (Dual Media Filter) out put
- f) Ultrafiltration feed parameters
- g) Ultrafiltration Permeate parameters
- h) Ultrafiltration reject parameters
- i) Feed parameters of Reverse Osmosis
- j) Permeate parameters of Reverse Osmosis
- k) Reject parameters of Reverse Osmosis

PCETP – Pretreatment I (Washwater Plant):**Pretreatment II (Biological & Tertiary Treatment):****4. Result and Discussion**

This study was carried out at one of knitted fabric dyeing industry located at SIPCOT, Perundurai, Erode. Seven numbers of soft flow with different capacities are used for dyeing including wetting, bleaching, neutralizing, washing, coloring, washing, etc. Dye bath solution requires dyes alkali and sodium salt in the process quantity of salt (sodium chloride) used usually depends on the requirement of color shade. Effluents are segregated in to dye bath waste water and wash water and treatment is effected accordingly.

Wash water equalized in a holding tank is subjected to primary treatment by flash mixing with lime and ferrous sulfate and are allowed for settling. Primary treatment is followed by the secondary treatment such as biological oxidation through tertiary clarifier, activated carbon bed, Dual media filter, ultrafiltration and reverse osmosis (RO) system. Double stage RO is followed with a feed water flow rate of 50m³/h. High pressure pumps used to feed the filters water

to the first array of the RO and reject of the first RO to second RO and final reject (5m³/h) in sent for multi effect evaporator. Permeate is used in the recycling process.

Whereas dye bath water is collected in a separate tank and allowed for lime and ferrous sulfate flocculation to remove the color. These light color effluents mixed with the rejects of RO are sent to Multi effect evaporation system. The permeate is used for preparation of dye bath solution. The characteristics of the raw effluents, intermediate effluents and permeate are presented in the (table-1 to table-11) the low hardness of permeate is an added advantages in the process, which was observed in the span of fifteen day.

5. Conclusion

Perundurai Common Effluent Treatment Plant, PCETP implement and recent technology to simplify operation. The plant is well operated and maintains constant effluent as per pollution control board (PCB) norms in water quality.

The study shows the recycling of treated wastewater and zero wastewater discharge concept are found technically feasible and economically viable in the textile dyeing industries located in the area of Erode and Tirupur in Tamil Nadu. By implementing novel technology PCETP, the average of BOD, COD, TDS and Chloride can reduced in the range of 88 – 98%, 91 – 97%, 80 – 97% and 76 – 97% respectively.

Nomenclature

pH	– Percentage of Hydrogen
TDS	– Total Dissolved Solids
COD	– Chemical Oxygen Demand
RO	– Reverse Osmosis
BOD	– Biological Oxygen Demand
TSS	– Total Suspended Solids
TH	– Total Hardness
Cl ⁻	– Chloride
So ₃	– Sulphide
So ₄	– Sulphate
Si	– Silica
Cl ₂	– Chlorine
Fe	– Iron
CETP	– Common Effluent Treatment Plant
PCETP	– Perundurai Common Effluent Treatment Plant
PCB	– Pollution Control Board
PPM	– Parts Per Millian
NTU	– Nepelometric Turbidity Unit

References

- Azbar. N, Yonar. T and Kestioglu. K., (2004). Comparison of various advanced oxidation process and chemical treatment method for COD and color removal from a polyester and acetate fibre dyeing effluent; *Chemosphere* 55, 35 – 43.
- Charlotta Leissner, Elisebeth Wegen (2005). Industrial wastewater treatment at PCETP, INDIA A Primary investigation of heavy metal content. Master's Thesis 2005, Department of Civil and Environmental Engineering, Water Environment Technology, Chalmers University of Technology, 20-26.
- Emerson Process Management, Basics of pH control, (August, 2004) [www.emersonprocess.com/rainhome/documents / Liq_AppData_43](http://www.emersonprocess.com/rainhome/documents/Liq_AppData_43)
- Shankar. U., (2003). Common effluent treatment plant: An institutional arrangement for pollution control for small scale tanneries in India. [online] [http:// www. elaw.org/assets/pdf/India2000.pdf](http://www.elaw.org/assets/pdf/India2000.pdf).

Table 1. Wash water (untreated effluent)

Day	pH	TDS ppm	TSS ppm	COD ppm	BOD ppm	Cl ⁻ ppm	Total Alkalinity ppm	Total Hardness ppm
1	10.11	3180	720	830	230	1205	1250	122
2	9.88	1730	830	720	260	854	1300	90
3	8.34	1690	300	750	180	527	1080	140
4	9.45	3340	700	810	405	425	1200	100
5	9.53	2300	700	740	225	947	1060	210
6	9.58	1190	720	730	200	420	1110	160
7	9.10	1580	900	672	279	632	980	180
8	9.20	2310	800	816	315	716	810	170
9	9.10	2210	830	824	280	752	1240	160
10	9.16	2230	710	808	285	815	1040	152
11	8.88	2410	740	820	240	1060	1450	160
12	8.92	2120	880	824	260	996	1320	135
13	9.01	2100	860	816	280	1120	1120	145
14	8.86	2300	710	752	260	1000	1020	140
15	9.10	1950	740	832	275	957	1300	128

Table 2. Dye bath plant feed parameters

Day	pH	TDS ppm	TSS ppm
1	10.47	24000	2950
2	10.39	25900	3400
3	9.97	26800	9950
4	10.50	27600	9900
5	10.42	27800	9000
6	10.44	33900	9900
7	10.40	20100	4600
8	9.92	24200	8800
9	10.26	23600	7600
10	10.40	25100	8200
11	10.38	25800	6900
12	9.93	24300	7350
13	10.18	22900	8200
14	10.02	27100	8450
15	9.96	25300	7690

Table 3. Wash water treated effluent (Biological inlet parameters)

Day	pH	TDS ppm	TSS ppm	COD ppm	BOD ppm	Cl ⁻ ppm	Total Alkalinity ppm	Total Hardness ppm	Turability NTU
1	7.45	2710	520	330	182	1262	250	120	14.4
2	8.09	2480	540	452	190	1056	550	100	16.2
3	7.10	2680	440	420	164	1134	230	116	13.4
4	6.99	2730	330	448	102	1098	460	128	11.0
5	6.78	2430	300	420	140	1106	320	112	13.1
6	6.70	2560	320	344	160	1040	340	138	12.9
7	7.04	2290	310	384	125	1140	360	116	13.2
8	7.10	2380	390	480	188	1210	300	108	11.3
9	7.15	2280	420	384	164	1050	400	96	13.6
10	7.90	2140	380	392	168	1070	420	70	12.5
11	8.02	2120	330	408	192	910	510	82	10.2
12	7.38	2150	320	410	188	751	420	98	11.4
13	7.80	2200	380	400	178	892	490	102	14.8
14	7.88	2120	340	420	186	890	400	112	12.2
15	7.90	2030	380	414	180	920	450	120	10.8

Table 4. Biological treatment (Secondary clarifier)

Day	pH	TDS ppm	TSS ppm	COD ppm	BOD ppm	Cl ⁻ ppm	Total Hardness ppm
1	7.36	2300	50	56	17	990	100
2	7.35	2510	50	88	24	1130	92
3	7.34	2500	60	84	15	1162	94
4	7.34	2510	70	72	32	1066	88
5	7.24	2480	60	76	20	1100	90
6	7.14	2520	46	84	24	1120	92
7	7.25	2500	50	86	26	1120	96
8	7.35	2380	54	74	30	1040	80
9	7.35	2460	48	100	32	1056	82
10	7.30	2400	50	86	24	1116	84
11	7.27	2500	60	70	30	990	88
12	7.30	2420	80	82	26	1020	68
13	7.40	2380	80	84	26	920	72
14	7.30	2390	70	76	32	964	80
15	7.34	2380	60	74	30	980	68

Table 5. Tertiary classifier DMF (Dual Media Filter) output

Day	pH	TDS ppm	TSS ppm	COD ppm	BOD ppm	Cl ⁻ ppm	Total Hardness ppm	Total Alkalinity ppm	Turability NTU
1	6.70	2280	50	48	30	990	125	210	1.0
2	6.96	2520	50	64	26	1130	110	250	0.9
3	7.20	2580	60	60	28	1160	115	200	1.0
4	7.16	2550	70	48	26	1063	104	240	1.0
5	7.20	2570	60	64	26	1098	116	220	1.2
6	7.00	2560	46	60	25	1120	108	260	1.1
7	7.02	2500	50	56	28	1012	120	250	1.0
8	7.04	2420	54	56	30	1230	108	225	0.8
9	7.02	2530	48	64	32	1156	108	200	.07
10	6.90	2470	50	56	26	1116	120	210	1.0
11	6.85	2600	60	48	24	987	80	310	0.9
12	6.90	2500	80	72	28	1028	94	340	0.7
13	7.05	2480	80	64	30	921	92	280	0.6
14	6.92	2400	70	60	32	980	94	270	0.6
15	7.06	2370	60	48	30	974	90	290	0.8

Table 6. Ultrafiltration feed parameters

Day	pH	TDS ppm	Cl ⁻ ppm	Total Hardness ppm	Total Alkalinity ppm	Turability NTU	Free Cl ₂ ppm
1	6.74	2450	1100	120	130	0.3	0.380
2	7.30	2500	1200	124	120	0.2	0.392
3	7.18	2400	1220	124	140	0.3	0.390
4	7.13	2450	1210	126	120	0.2	0.398
5	7.33	2540	1191	130	130	0.6	0.370
6	7.22	2600	1210	132	170	0.6	0.778
7	7.30	2460	1200	120	140	0.1	0.340
8	7.40	2510	1190	122	150	0.4	0.360
9	7.11	2540	1210	124	145	0.3	0.380
10	7.25	2460	1220	130	155	0.4	0.398
11	6.91	2620	1220	132	145	0.2	0.480
12	7.16	2510	1190	100	125	0.2	0.220
13	7.38	2440	1210	92	135	0.3	0.325
14	7.40	2420	1240	110	125	0.2	0.330
15	7.32	2400	1250	116	125	0.4	0.200

Table 7. Ultrafiltration permeate parameters

Day	pH	TDS ppm	Cl ⁻ ppm	Total Hardness ppm
1	7.40	2300	1000	120
2	7.43	2450	1010	126
3	7.37	2500	1040	130
4	7.36	2510	1020	132
5	7.30	2550	1070	128
6	7.35	2400	1010	122
7	7.38	2350	980	130
8	7.26	2330	990	100
9	7.30	2540	1010	102
10	7.20	2650	1010	106
11	7.26	2300	1020	110
12	7.24	2500	1000	100
13	7.19	2250	940	88
14	7.20	2310	960	96
15	7.30	2300	1000	98

Table 8. Ultrafiltration reject parameters

Day	pH	TDS ppm
1	7.10	2350
2	7.03	2450
3	7.43	2550
4	7.39	2540
5	7.44	2500
6	7.30	2350
7	7.40	2390
8	7.32	2410
9	7.20	2550
10	7.30	2660
11	7.32	2400
12	7.40	2570
13	7.20	2290
14	7.22	2360
15	7.33	2400

Table 9. Reverse Osmosis feed parameters

Day	pH	TDS ppm	COD ppm	Cl ⁻ ppm	Total Hardness ppm	Total Alkalinity ppm	SO ₄ ppm	SO ₃ ppm	Free Cl ₂ ppm	Si ppm	Fe ppm
1	6.92	2260	48	1127	112	150	228	5.4	Nil	12.2	0.06
2	7.00	2500	52	1170	112	180	224	4.6	Nil	32	0.04
3	6.97	2540	48	1169	136	170	256	6.4	0.025	20	0.05
4	6.99	2550	50	1191	128	210	264	5.6	0.086	10.5	0.06
5	7.00	2520	54	1077	130	200	236	8.1	Nil	9.0	0.05
6	6.87	2580	48	1180	150	200	278	7.4	Nil	10.22	0.06
7	6.80	2490	38	1200	130	160	240	7.0	Nil	12.10	0.06
8	6.80	2490	64	1319	108	150	285	5.4	Nil	9.0	0.08
9	6.91	2540	56	1230	150	120	278	3.3	Nil	8.25	0.11
10	6.69	2580	38	1354	100	150	254	5.0	Nil	11.15	0.06
11	7.25	2560	56	1063	110	150	278	6.2	Nil	22.7	0.07
12	6.88	2500	50	1098	100	140	280	7.8	Nil	10.40	0.08
13	7.04	2500	48	922	88	160	248	7.0	Nil	12.20	0.07
14	7.05	2460	52	1100	84	150	260	6.8	Nil	9.75	0.08
15	6.85	2390	50	1098	86	140	288	2.9	Nil	20.87	0.07

Table 10. Reverse Osmosis Permeate parameters

Day	pH	TDS ppm	Cl ⁻ ppm	Total Hardness ppm
1	6.13	190	85.0	3.0
2	6.12	160	78.6	2.5
3	6.12	130	79.4	3.0
4	6.09	130	81.5	3.0
5	6.23	110	92.0	1.5
6	6.03	110	58.0	1.5
7	5.90	105	64.0	2.5
8	6.00	90	55.0	1.5
9	5.95	90	61.0	2.0
10	6.91	140	71.0	2.0
11	5.94	120	56.0	3.0
12	6.23	100	57.0	6.0
13	6.18	120	50.0	4.0
14	6.20	115	52.0	3.5
15	6.07	110	54.0	3.0

Table 11. Reverse Osmosis Reject parameters

Day	pH	TDS ppm	Cl⁻ ppm	Total Hardness ppm
1	7.14	20200	9997	965
2	7.20	21800	9394	910
3	7.20	18400	9040	940
4	7.14	18600	8508	1120
5	7.36	21400	9010	800
6	7.20	19000	9020	920
7	7.15	19300	9910	890
8	7.02	19300	9075	850
9	7.09	21400	11340	795
10	7.26	23600	10565	790
11	7.07	22100	9640	810
12	7.02	17100	9580	624
13	7.19	19300	9290	780
14	7.10	20100	9380	790
15	7.09	21400	9480	696

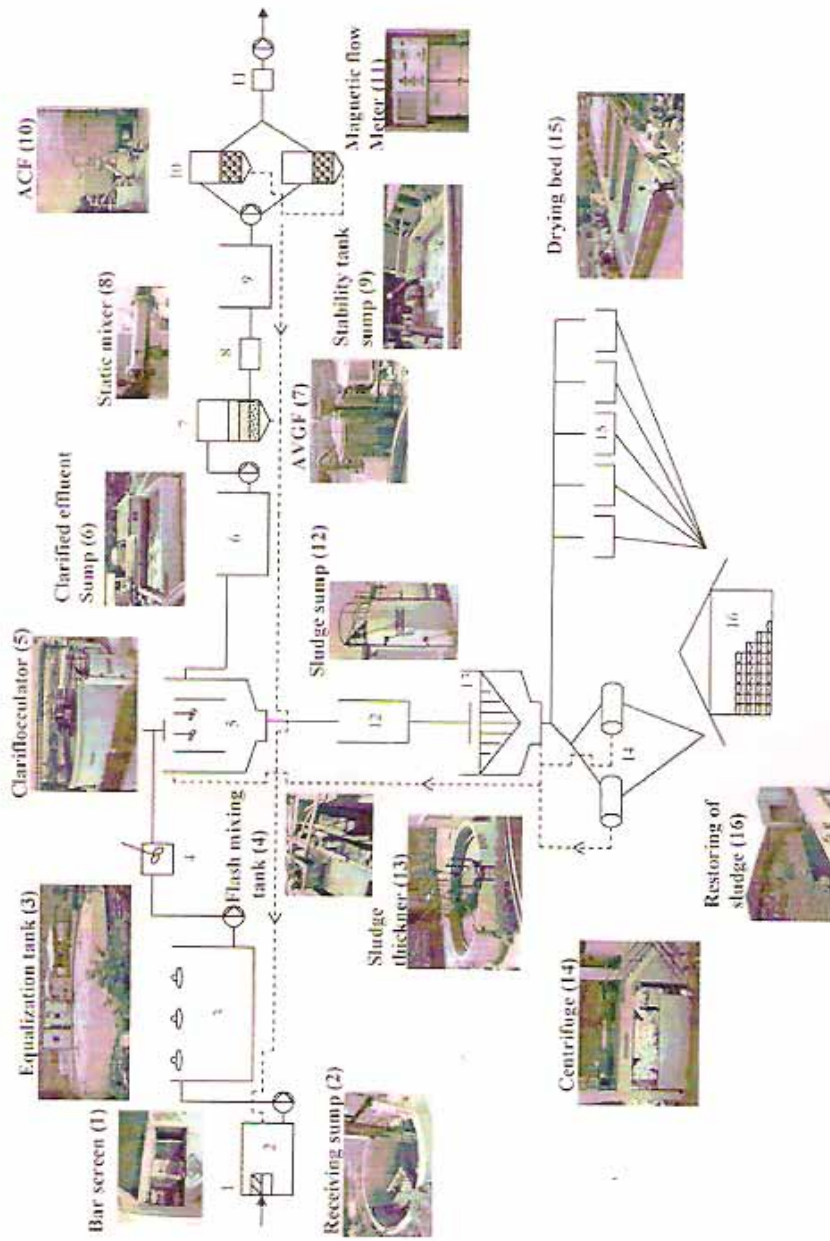


Figure 1. Flowchart of PCETP

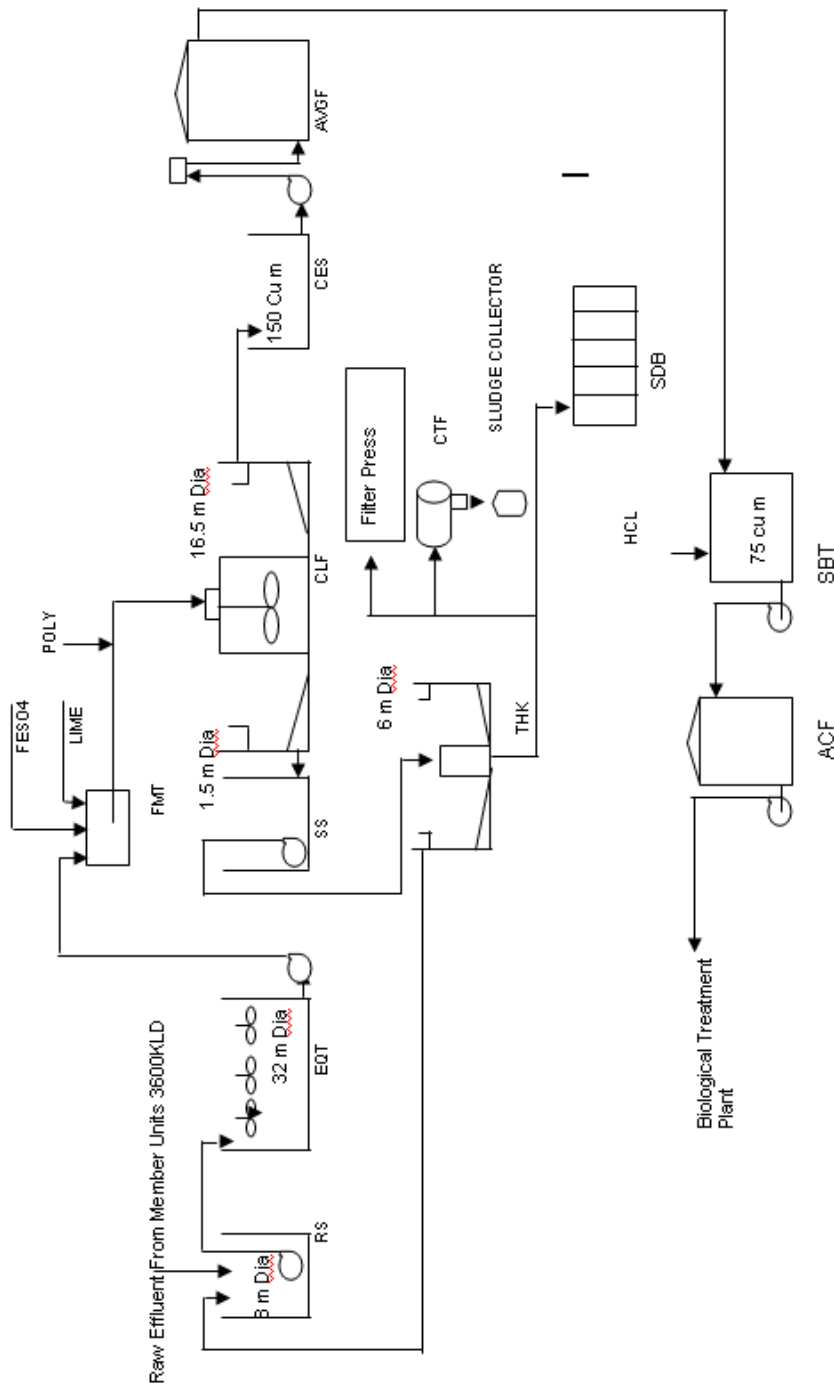


Figure 2, Pre treatment – I (Wash water Plant)

RS	RECEIVING SUMP			
EQT	EQUALISATION TANK			
FMT	FLASH MIXING TANK			
CLF	CLARIFLOCCULATOR			
		CES	CLARIFIED EFFLUENT SUMP	
		AVGF	AUTO VALVELESS GRAVITY FILTER	
		SBT	STABILISATION TANK	
		ACF	ACTIVATED CARBON FILTER	
		SS	SLUDGE SUMP	
		THK	THICKENER	
		CTF	CENTRIFUGE	
		SDB	SLUDGE DRYING BED	



Chance-constrained Portfolio Selection with Birandom Returns

Limei Yan

Department of Mathematics, Dezhou University

Dezhou 253023, China

E-mail: yanlimei9898@163.com

Abstract

The aim of this paper is to solve the portfolio problem when security returns are birandom variables. Two types of portfolio selection based on chance measure are provided according to birandom theory. Since the proposed optimization problems are difficult to solve by traditional methods, a hybrid intelligent algorithm by integrating birandom simulation and genetic algorithm is designed. Finally, two numerical experiments are provided to illustrate the effectiveness of the algorithm.

Keywords: Portfolio selection, Birandom variable, Birandom simulation, Genetic algorithm

1. Introduction

The theory of portfolio selection was initially provided by Markowitz (1952, p.77) and has been greatly developed since then. It is concerned with selecting a combination of securities among portfolios containing large number of securities to reach the goal of obtaining satisfactory investment return. In his path-break work, Markowitz proposed a principle that when making investment decision, an investor should always strike a balance between maximizing the return and minimizing the risk, i.e., the investor maximize return for a given level of risk, or one should minimize risk for a predetermined return level. More importantly, Markowitz initially quantified investment return as the expected value of returns of securities, and risk as variance from the expected value. After Markowitz's work, scholars have been showing great enthusiasm in portfolio management, trying different mathematical approaches to develop the theory of portfolio selection. Traditionally, returns of individual securities are assumed to be stochastic variables, and many researchers were focused on extending Markowitz's mean-variance models and on developing new mathematical approaches to solve the problems of computation. Peng (2007, p. 433) proposed concept of birandom variable and the framework of birandom programming. However, investors may come across birandom returns in portfolio selection situations. For example, security returns are usually regarded to be normally distributed random variables, but the expected value may be still random variable, thus investors have to face random returns with random parameters, to deal with this type of uncertainty, we propose the security returns could be regarded as birandom variables. As a general mathematical description for this kind of stochastic phenomenon with incomplete statistical information, birandom variable is defined as a mapping with some kind of measurability from a probability space to a collection of random variables.

In general, there are three types of stochastic programming models for optimization problems in uncertain environment. The first is expected value model (EVM), which optimizes the expected objective function subject to some expected constraints. The second chance-constrained programming (CCP) was proposed by Charnes and Cooper (1965, p.73) and developed by many scholars as means of dealing with uncertainty by specifying a confidence level at which the uncertain constraints hold. We try to do something in this area. In this paper, returns of securities are assumed to be birandom parameters instead of stochastic ones. The portfolio will be selected according to the second type of programming models for optimization problems.

The rest of this paper is arranged as follows. After reviewing some necessary knowledge about birandom variable in section 2, in section 3, one type of single-objective birandom chance measure model and one type of birandom CCP model are proposed. To provide a general method for solving the new models, in section 4, a hybrid intelligent algorithm integrating genetic algorithm and birandom simulation is designed. To better illustrate the modeling idea of the paper and demonstrate the effectiveness of the proposed algorithm, two numerical examples are provided in section 5.

2. Preliminaries

Birandom variable theory was introduced by Peng in 2007. To better understand the chance measure and the CCP model for portfolio selection, let us briefly review some necessary knowledge about birandom variable.

Definition 1 A birandom variable ξ is a mapping from a probability space (Ω, A, Pr) to a collection of random

variables such that for any Borel subset B of the real line R , the induced function $\Pr\{\xi(\omega) \in B\}$ is a measurable function with respect to ω .

Example 1 Let $\Omega = \{\omega_1, \omega_2\}$, and $\Pr\{\omega_1\} = \Pr\{\omega_2\} = 1/2$. Assume that ξ is a function on (Ω, A, \Pr) as follows.

$$\xi(\omega) = \begin{cases} \xi_1, & \omega = \omega_1 \\ \xi_2, & \omega = \omega_2 \end{cases}$$

where ξ_1 is a uniformly distributed random variable on $[0,1]$ and ξ_2 is a normally distributed random variable with mean 0 and variance 1, i.e., $\xi_1 \sim U[0,1]$ and $\xi_2 \sim N(0,1)$. Then ξ is a birandom variable according to the definition.

The definition of the primitive chance of birandom event as follows.

Definition 2 Let $\xi = (\xi_1, \xi_2, \dots, \xi_n)$ be a birandom vector on (Ω, A, \Pr) , and $f: R^n \rightarrow R^m$ be a vector-valued Borel measurable function. Then the primitive chance of birandom event characterized by $f(\xi) \leq 0$ is a function from $(0,1]$ to $[0,1]$, defined as

$$\text{ch}\{f(\xi) \leq 0\}(\alpha) = \sup\{\beta \mid \Pr\{\omega \in \Omega \mid \Pr\{f(\xi(\omega)) \leq 0\} \geq \beta\} \geq \alpha\}.$$

The following are the definitions of optimistic value and pessimistic value of birandom variable ξ .

Definition 3 Let ξ be a birandom variable, and $\gamma, \delta \in (0,1]$, then

$$\xi_{\text{sup}}(\gamma, \delta) = \sup\{x \mid \text{ch}\{\xi \geq x\}(\gamma) \geq \delta\}$$

is called the (γ, δ) -optimistic value to ξ , and

$$\xi_{\text{inf}}(\gamma, \delta) = \inf\{x \mid \text{ch}\{\xi \leq x\}(\gamma) \geq \delta\}$$

is called the (γ, δ) -pessimistic value to ξ .

3. Birandom chance-constrained portfolio selection

Let x_i denote the investment proportions in security i , ξ_i the birandom return for the i th security, $i=1,2,\dots,n$, respectively, if the investor wants to maximize the chance of the total investment return no less than R at the confidence level α , where R is the predetermined total return and α is the predetermined confidence level, then the model is

$$\begin{aligned} \max_x \quad & \text{Ch}\left\{\sum_{i=1}^n x_i \xi_i \geq R\right\}(\alpha) \\ \text{s. t.} \quad & \sum_{i=1}^n x_i = 1 \\ & x_i \geq 0, \quad i=1,2,\dots,n \end{aligned} \quad (1)$$

In the following, we provide a spectrum of birandom chance-constrained programming (CCP) of portfolio selection.

$$\begin{aligned} \max \quad & \bar{f} \\ \text{s.t.} \quad & \text{Ch}\{x_1 \xi_1 + x_2 \xi_2 + \dots + x_n \xi_n \geq \bar{f}\}(\gamma) \geq \delta \\ & x_1 + x_2 + \dots + x_n = 1 \\ & x_i \geq 0, \quad i=1,2,\dots,n \end{aligned} \quad (2)$$

where γ and δ are the predetermined investment levels that the investor feels satisfactory, and $\max \bar{f}$ is the (γ, δ) -optimistic value to the security return with respect to primitive chance.

4. Hybrid intelligent algorithm

Since the two-fold uncertainty of birandom variable, it is difficult to analytically solve the models (1) and (2). To provide a general solution to the models, we design a hybrid intelligent algorithm integrating genetic algorithm (GA) and birandom simulation. Roughly speaking, in the proposed hybrid intelligent algorithm, the technique of birandom simulation is applied to compute the chance measure and (γ, δ) -optimistic value of the return function, then birandom simulation and GA are integrated for solving the birandom models.

4.1 Birandom simulation

In this section, we mainly discuss the calculation of the chance measure of birandom variables and (r, δ) -optimistic value of birandom variables.

Let ξ_i be birandom variables and x_i decision variables, $i = 1, 2, \dots, n$, respectively. Write

$$f(x, \xi) = \sum_{i=1}^n x_i \xi_i,$$

where $x = (x_1, x_2, \dots, x_n)$, $\xi = (\xi_1, \xi_2, \dots, \xi_n)$. In order to solve the proposed models, we must handle the following two types of uncertain function.

$$U_1 : x \rightarrow \text{Ch}\{f(x, \xi) \geq R\}(\alpha)$$

$$U_2 : x \rightarrow \text{Ch}\{f(x, \xi) \geq \bar{f}\}(\gamma) \geq \delta$$

$U_1(x)$ may be estimated by the following procedure.

Algorithm 1 (birandom simulation for $U_1(x)$)

Step 1 Generate $\omega_1, \omega_2, \dots, \omega_N$ from Ω according to the probability measure Pr.

Step 2 Compute the probability $\beta_n = \text{Pr}\{f(x, \xi(\omega_n)) \geq R\}$ for $n = 1, 2, \dots, N$, respectively, by stochastic simulation.

Step 3 Set N' as the integer part of αN .

Step 4 Return the N' th largest element $\bar{\beta}$ in $\{\beta_1, \beta_2, \dots, \beta_N\}$.

Algorithm 2 (birandom simulation for $U_2(x)$)

Step 1 Generate $\omega_1, \omega_2, \dots, \omega_N$ from Ω according to the probability measure Pr.

Step 2 Find the largest value \bar{f}_n such that

$$\text{Pr}\{f(x, \xi(\omega)) \geq \bar{f}_n\} \geq \delta$$

for $n = 1, 2, \dots, N$, respectively, by stochastic simulation.

Step 3 Set N' as the integer part of γN .

Step 4 Return the N' th largest element in $\{\bar{f}_1, \bar{f}_2, \dots, \bar{f}_N\}$.

4.2 Genetic algorithm

Representation structure: A solution $x = (x_1, x_2, \dots, x_n)$ is represented by the chromosome $V = (v_1, v_2, \dots, v_n)$, where the genes v_1, v_2, \dots, v_n are randomly generated in the interval $[0, 1]$, and the relation between x and V are formulated as follows:

$$x_i = v_i / (v_1 + v_2 + \dots + v_n), i = 1, 2, \dots, n,$$

which ensures that

$$x_1 + x_2 + \dots + x_n = 1, x_i \geq 0, i = 1, 2, \dots, n \text{ always holds.}$$

Initialization process: pop_size number of chromosomes are initialized randomly by generating points (v_1, v_2, \dots, v_n) from the hypercube $[0, 1]^n$ pop_size times. Since the constraint required that $x = (x_1, x_2, \dots, x_n)$ satisfy $x_1 + x_2 + \dots + x_n = 1$, based on the relation between x and V , the feasibility of the randomly generated chromosomes is obvious.

Evaluation function: Evaluation function, denoted by $Eva(V)$, is to assign a probability of reproduction to each chromosome V so that its likelihood of being selected is proportional to its fitness relative to the other chromosomes in the population. That is, the chromosomes with higher fitness will have more chance to produce offspring by using roulette wheel selection.

One well-known evaluation function is based on allocation of reproductive trial according to rank rather than actual objective values. We can rearrange the pop_size chromosomes according to their objective values to make better chromosome take smaller ordinal number. That is, after rearrange, among pop_size chromosomes $V_1, V_2, \dots, V_{pop_size}$,

V_1 is the best chromosome, and V_{pop_size} the worst one, then a parameter $a \in (0,1)$ in the genetic system is given. We can define the rank-based evaluation function as follows:

$$\text{Eva}(V_i) = a(1-a)^i, \quad i = 1, 2, \dots, pop_size.$$

Note that $i=1$ means the best individual, $i = pop_size$ the worst one.

Selection process: Firstly, calculate the cumulative probability q_i for each chromosome V_i ,

$$q_0 = 0, \quad q_i = \sum_{j=i}^{pop_size} \text{Eva}(V_j), \quad i = 1, 2, \dots, pop_size$$

Secondly, generate a random number r in $(0, q_{pop_size}]$, and select the chromosome V_i if r satisfies $q_{i-1} < r \leq q_i$.

Repeat the second and third steps pop_size times and obtain pop_size copies of chromosome.

Crossover operation: A parameter p_c of a genetic system as the probability of crossover is defined first. The parents for crossover operation are selected by doing the following process repeatedly from $i=1$ to pop_size : Generating a random number r from the interval $[0,1]$, the chromosome V_i is selected as a parent if $r < p_c$, the selected parents are denoted by V'_1, V'_2, V'_3, \dots and divided into the pairs: $(V'_1, V'_2), (V'_3, V'_4), (V'_5, V'_6), \dots$. The crossover operation on each pair is illustrated by (V'_1, V'_2) . At first, we generate a random number c from the open interval $(0,1)$, then the operator on V'_1 and V'_2 will product two children X and Y as follows:

$$X = cV'_1 + (1-c)V'_2, \quad Y = (1-c)V'_1 + cV'_2.$$

If both children are feasible, then we replace the parents with them. If not, we keep the feasible one if it exists, and then redo the crossover operator by regenerating a random number c until two feasible children are obtained or a given number of cycles is finished. In this case, we only replace the parents with the feasible child.

Mutation operation: A parameter p_m of a genetic system as the probability of mutation is defined first. This probability gives us the expected number of $p_m \cdot pop_size$ of chromosomes undergoing the mutation operations. We repeat the following steps from $i=1$ to pop_size : Generating a random number r from the interval $[0,1]$, the chromosome V_i is selected as a parent if $r < p_m$. For each selected parent V_i , we mutate it in the following way. Let M be an appropriate large positive number. We choose a mutation direction d in R^n randomly. If $V + M \cdot d$ is not feasible, then we set M as a random number between 0 and M until it is feasible. If the above process cannot find a feasible solution in a predetermined number of iterations, then we set $M = 0$. Anyway, we replace the parent V_i with its feasible child $V + M \cdot d$.

The following is the hybrid intelligent algorithm integrating birandom simulation and genetic algorithm.

Algorithm 3 (hybrid intelligent algorithm)

Step 1 Initialize pop_size chromosomes.

Step 2 Calculate the objective values for all chromosomes by birandom simulation.

Step 3 Given the rank order of the chromosomes according to the objective values, and the values of the rank-based evaluation function of the chromosomes.

Step 4 Compute the fitness of each chromosome according to the rank-based evaluation function.

Step 5 Select the chromosomes by spinning the roulette wheel.

Step 6 Update the chromosomes by crossover and mutation operations.

Step 7 Repeat the second step to the sixth step for a given number of cycles.

Step 8 Take the best chromosomes as the solution of portfolio selection.

5. Numerical examples

To illustrate the modeling idea and to test the effectiveness of the designed hybrid intelligent algorithm, let us consider two numerical examples. The two examples are both performed on a personal computer by using C++ programming language. The parameters in the HIA are set as follows: the probability of crossover $p_c = 0.3$, the probability of mutation $p_m = 0.2$, the parameter $a = 0.05$ in the rank-based evaluation function.

Example 2 Assume that there are 5 securities, the returns of securities are all birandom variables.

$$\max_x \text{Ch}\{\sum_{i=1}^5 x_i \xi_i \geq R\}(\alpha)$$

subject to

$$\sum_{i=1}^5 x_i = 1$$

$$x_i \geq 0, \quad i = 1, 2, 3, 4, 5$$

Where

$$\xi_1 \sim N(\mu_1, 1) \text{ with } \mu_1 \sim N(1, 1), \xi_2 \sim N(\mu_2, 1) \text{ with } \mu_2 \sim N(2, 2), \xi_3 \sim N(\mu_3, 1) \text{ with } \mu_3 \sim N(3, 2^2), \\ \xi_4 \sim N(\mu_4, 2) \text{ with } \mu_4 \sim N(4, 3^2), \xi_5 \sim N(\mu_5, 1) \text{ with } \mu_5 \sim N(5, 3^2) \text{ and } R = 2.321, \alpha = 0.9.$$

Here, $N(\mu, \sigma^2)$ represents the normally distributed random variable with mean μ and standard variance σ . A run of the hybrid intelligent algorithm with 3000 generations shows that among 5 securities, in order to gain maximum chance measure of the total securities return no less than the predetermined total return R at the confidence level α , the investor should assign his money according to the optimal solution:

$$x_1^* = 0, \quad x_2^* = 0.2125, \quad x_3^* = 0.2456, \quad x_4^* = 0.1672, \quad x_5^* = 0.3747.$$

Example 3 Consider the following CCP birandom portfolio selection,

$$\max \bar{f}$$

subject to

$$\text{Ch}\{x_1 \xi_1 + x_2 \xi_2 + x_3 \xi_3 + x_4 \xi_4 \geq \bar{f}\}(0.95) \geq 0.95$$

$$x_1 + x_2 + x_3 + x_4 = 1$$

$$x_i \geq 0, \quad i = 1, 2, 3, 4.$$

where $\xi_1, \xi_2, \xi_3, \xi_4$ are birandom variables representing the securities returns defined as follows,

$$\xi_1 \sim N(\mu_1, 1) \text{ with } \mu_1 \sim U(0, 1), \quad \xi_2 \sim N(\mu_2, 1) \text{ with } \mu_2 \sim U(1, 2), \quad \xi_3 \sim N(\mu_3, 1) \text{ with } \mu_3 \sim U(2, 3) \\ \xi_4 \sim N(\mu_4, 2) \text{ with } \mu_4 \sim N(0, 1).$$

A run of the HIA 5000 cycles shows that the optimal solution is

$$x_1^* = 0.1365, \quad x_2^* = 0.3217, \quad x_3^* = 0.4561, \quad x_4^* = 0.0857$$

The corresponding (0.95, 0.95) optimistic value is

$$\bar{f}^* = 1.9782.$$

References

- A. Charnes & W. W. Cooper. (1965). Chance-constrained programming. *Management Science*, 6, 73-79.
- B. Liu. Uncertainty theory, 3rd edition. [Online] Available: <http://orsc.edu.cn/liu/ut.pdf>.
- H. Markowitz. (1952). Portfolio selection. *Journal of Finance*. 7, 77-91.
- Peng, jin. (2007). Birandom variables and birandom programming. *Computer & Industrial Engineering*, 53, 433-453.
- Huang, Xiaoxia. (2006). Fuzzy chance-constrained portfolio selection. *Applied mathematics and computation*, 177, 500-507.
- Huang, Xiaoxia. (2007). A new perspective for optimal portfolio selection with random fuzzy returns. *Information science*, 177, 5404-5414.



Neural Based pH System in Effluent Treatment Process

B. Meenakhsipriya (Corresponding author)

Department of Mechatronics Engineering, Kongu Engineering College

Perundurai, Erode – 638052, Tamilnadu, India

Tel: 91-098-4279-9990 E-mail: devameena@rediffmail.com

Dr.K.Saravanan

Department of Chemical Engineering, Kongu Engineering College

Perundurai, Erode – 638052, Tamilnadu, India

Tel: 91-098-4270-5656 E-mail: rumisivaesh@yahoo.com

S.Sathiyavathi

Department of Mechatronics Engineering, Kongu Engineering College

Perundurai, Erode – 638052, Tamilnadu, India

Tel: 91-098-4339-9667 E-mail: sathi.ed@gmail.com

Abstract

This investigation considers the application of Artificial Neural Network (ANN) techniques to estimate the pH value for effluent treatment process. ANN has the ability to identify the non-linear dynamical systems from the input-output data. An important requirement of the application is robustness of the system against erroneous sensor measurements. The simulation model of the pH system for common effluent treatment plant (CETP) is developed using MATLAB 7.5, GUI tool box. A novel off-line and on-line training scheme for the neural network is developed by error back propagation training algorithm to model the pH system for CETP, accurately. For this purpose, a simple feed forward, back propagation neural network, with only one hidden layer, and sigmoidal activation functions is used. The training of such network is based on Input-Output data which is collected from Perundurai common effluent treatment plant (PCETP). Experimentation and simulation results on this neuro identifier of pH system for common effluent treatment plant are shown.

Keywords: pH system, CETP, PCETP, ANN, Alkali wastes

1. Introduction

The textile industry occupies an important place in the economy of India and other developing countries. The low efficiency of chemical operations and spillage of chemical, cause a significant pollution hazard and make the treatment of discharged wastewater a complex problem. Group of textile industries are joined together to form common effluent treatment plant to economize the process. The industrial pollution control regime in India is based on the standards and regulation approach. Source specific concentration based standard have been laid down for polluting units and penalties for non compliance, disconnection of electricity/water supply and closure of the units. The standards are same for large and medium units as well as for small units. While most of the large and medium polluting units have been able to erect and operate effluent treatment plants, this option does not appear to be viable for many small units because of their small size, and technical, financial and managerial constraints. Common effluent treatment plants are being suggested as a cost-effective option for compliance with the standards for small polluting units in industrial clusters (Shankar, U., 2003).

Most process plants generate a wastewater effluent that must be neutralized prior to discharge or reuse. Consequently, pH control is needed in just about every process plant, and yet a large percentage of pH loops perform poorly. Results are inferior product quality, environmental pollution, and material waste. However, implementing a pH system is like putting a puzzle together. It will only work when all the components are in place. While various pH probes and actuators for pH control are available, commercial adaptive pH controllers are still in demand. The challenge is to provide a controller that is able to deal with large nonlinear gain changes in the pH loop. It will be useful for not only wastewater neutralization, but also chemical concentration control, since concentration is a key quality variable. It is impossible for a fixed controller like PID to effectively control this process (OMEGA Engineering, 2006).

In 1999, Hunt, K., J. et al said that the internal model control is used to directly incorporate networks modeling the plant and its inverse within the control strategy. Rejecting disturbances caused by coupling effects have shown a significant improvement over that achieved by fixed parameter PID control designed using a conventional method. In 2003, Yu, D., L. et al said that the Implementation of a neural network model based predictive control scheme to a laboratory sealed multivariable chemical reactor, three variables are controlled in the reactor- temperature, PH and dissolved oxygen. The optical control performance in tracking set-points and rejecting disturbances caused by coupling effects have significant improvement over that achieved by fixed parameter PID control designed using a conventional method.

In 1998, Lin-En Kuo et al said that the Neural Network based Model Predictive Controller (NNMPC) is applied to the control of coagulant dosing in a drinking water treatment plant. The hybrid system developed includes raw data validation and reconstruction based on a Kohonen self-organizing feature map, and prediction of coagulant dosage using multilayer perceptrons. The performance of the network is obviously dependent on the quality and completeness of data provided for system training. Continuous updating of training data during operational use will improve the performance of the system.

In 1996, Junhong Nie et al said that the modeling and identification of pH-processes via fuzzy neural approaches is done. Extensive simulations including on-line modeling have shown that these nonlinear pH-processes can be modeled reasonably well by the present schemes which are simple but efficient. Compared with the backpropagation neural network (BNN) modeling approach, this method is particularly suitable for real-time applications. The identification of a fuzzy model via a CPN neural network can be completed very quickly by presenting the training examples once only. This feature of fast response to new situations has been demonstrated in modeling.

In 2005, Bernt M. Akesson et al said that the process is modeled by a set of linear models constructed by velocity-based linearization in order to reduce the computational requirements associated with the solution of the continuous-time nonlinear system equations. The resulting quasi-linear models also simplify the estimation of the system state from the measured outputs. The accuracy of the neural network controller approximation which is required to ensure stability and performance is shown to be related to the fragility of the model predictive controller. The proposed approach is applied to a simulated nonlinear pH neutralization process. The study shows that it is possible to achieve good control performance with this approach, reducing the required on-line computations significantly.

Lamanna, R. et al said that the tuning procedure of a PID is very tedious and time consuming, and the controller produces responses of a quality comparable to that of the neural controller within very narrow operating limits. The weights are adjusted, depending on the task at hand, to improve performance. The ability to learn is one of the main advantages that make the neural network so attractive. Neural networks can also provide significant fault tolerance. Since damage to a few links need not significantly impair the overall performance.

Based on the literature survey, it is seen that a good amount of work has been done using ANN to control the pH value for drinking water treatment and waste water treatment process. Literature has suggested few mathematical models; few case studies on neural network approach have been attempted, how ever without a real time or simulation study. There is no research work was carried out to control the pH value in effluent treatment process. Hence the problem of pH control for effluent treatment process using neural network is pursued.

2. Effluent Treatment Plant

This section describes the wash water treatment process of Perundurai Common Effluent Treatment Plant (PCETP). The wash water treatment plant was opened in July 2002 and reduces COD and BOD by 40-60%. They regularly measure pH, TSS, TS BOD, COD and TDS. The receiving tank and the bar screens are designed for the peak flow, but the units down stream of the equalization tank are designed for an average flow and an average quality.

The wash water plant is designed to treat 3600 m³ per day of wash water effluent received from 14 member units and the plant consists of the following

2.1 Screening

The raw effluent from the plant is first passed through a bar screen of 20mm and 15 mm size removes the floating matters in the receiving sump. In the receiving sump, the variation of pH value at various intervals of time is shown in Figure 1.

2.2 Equalization

The screened effluent is collected in the equalization tank. The function of equalization tank is to homogenize the flow and characteristic of the effluent. The equalization tank is designed for a hydraulic retention time of 24 hrs. The equalization tank is provided with floating surface aerators to ensure proper mixing and to avoid settling of suspended solids. The variation of pH value at various intervals of time is shown in Figure 2.

2.3 Colour Removal

The equalized effluent is pumped to flash mixer, where lime, ferrous sulphate and poly electrolyte is dozed for precipitation of colour and coagulation of the solids formed. The dosing arrangement has been provided to adjust the dosage based on the incoming effluent's pH.

2.4 Clarification

The coagulated suspended solids and precipitate formed due to colour removal will then be let to clariflocculator for settling and removal of suspended solids. Settled sludge will be moved continuously along the floor towards center of unit by means of slowly rotating scrapper which covers the entire floor area. The accumulated sludge will be transferred to sludge pocket of the clarifier for sludge drawn off. The excess sludge will be removed from time to time to avoid the build up of the same. The variation of pH value at various intervals of time is shown in Figure 3.

2.5 Filtration

The clarified effluent from clariflocculator is taken to Auto Valve less Gravity Filter (AVGF) for filtration. The filter operated automatically on the loss of head principle. This is generally accepted as being the most accurate control besides the constant analysis of the filtered water turbidity which is seldom practical on a continuous basis. The head loss at which AVGF initiates backwashing is determined by the height of the inverted U-turn at the top of the backwash pipe. The level of water in this pipe is proportional to the head loss across the filtered bed. The AVGF filtered effluent is neutralized in the static mixer with HCl acid and pumped to the Activated Carbon Filter to remove odor in the effluent. Then, it is pumped to farm land for irrigation.

2.6 Sludge Treatment

The underflow from the clariflocculator, are pumped to the sludge thickener. The thickened sludge with 6% consistency will then pumped to the centrifuge. Polymer is dosed to enhance the efficiency of thickening and dewatering. The filtrate from the centrifuge is taken back to the clariflocculator while dewatered sludge is collected in bags and stacked in the roofed shed (Meenakshipriya, B. et al, 2008).

3. SIMULINK Block Diagram

The SIMULINK block diagram of pH identifier using MATLAB 7.5, GUI- Neural Network toolbox is shown in Figure 4. The following parameters are considered to develop the SIMULINK model of pH identifier.

```
net = newff([-1 1;-1 1],[2,1],{'purelin' 'tansig'},'trainscg');
net.layers{1}.initFcn='initwb';
net.inputweights{1,1}.initFcn='rands';
net.biases{1,1}.initFcn='rands';
net.biases{2,1}.initFcn='rands';
net.layers{2}.initFcn='initwb';
net.layerweights{2,1}.initFcn='rands';
net.biases{1}.initFcn='rands';
net=init(net);
net.trainparam.show=139;
net.trainparam.epochs=100;
net.trainparam.goal=0;
net=train(net,Inputs',Target');
A=sim(net,inputs');
gensim(net);
```

3.1 Generation of data

The values of pH before treatment, HCl dosing and pH after treatment are measured at various intervals of time. The sampled data of all these parameters are used as training and testing input pairs to model the pH identifier as shown in Table 1.

3.2 Neural Network Training

A feed forward neural architecture is selected and the training is done using TRAINLM Levenberg-Marquardt back propagation algorithm. The selected number of input variables is 2 which are pH before treatment, HCl dosing and output variable is 1 i.e., pH after treatment. The number of epochs are fixed at 100 and learning rate parameter is

selected as 0.001. The initial weights are set randomly (very close to zero) and training is carried out for the given number of epochs.

The neural network is trained with various values of hidden nodes, learning rate and number of epochs. Neural network with too many hidden nodes may over fit the network and cause unrealistic oscillation between the training samples. On the other hand network with small number of hidden nodes may fail to approximate/generalize the complex underlying relationship in the data with fine fidelity. When the number of training epochs is increased during the training process, the training error approaches to zero, but the problem of excessive training occurs and the network converges to memorization of the training data. The training error indicates the average deviation from the actual values used for training. The activation function used between the input and hidden layer is sigmoid and the one between hidden and output layer is linear.

4. Simulation Results

The simulation results are shown in Table 1 and the response of measured pH value Vs neural predicted pH value is shown in Figure 5. The value of measured pH is shown as solid lines and the neural predicted pH value is shown as dotted lines. Figure 6 shows the error analysis of pH identifier for training, validation and testing. From the error analysis, the accuracy of neural identifier is 0.004% in terms of error.

5. Conclusion

In this paper, a new method of pH identifier using neural network is proposed to increase the performance of pH control system. Neural network with linear filter architecture and back propagation through time learning algorithm is used to design the pH control system. The neural network learning process has been performed in both on-line and off-line. Model by means of data collection over a wide range of pH improves the accuracy, reduces the complexity, increases the immunity to the noise and fewer controllers are needed. In many applications, the network has to emulate nonlinear and time varying functions where the functions might change depending on the plant operating condition and parameter variation. In such cases the network requires continuous training on-line so that it correctly emulates the model. From the presented results it can be noted that the neural systems offer an attractive solution for pH control system. The neural approach show good simulated response and suggest that further research in this area would be worthwhile. Future work could include:

- An investigation of the implications of a practical implementation.
- An evaluation of learning algorithms which offer superior performance to the error back propagation algorithm.

Nomenclature

CETP	-	Common Effluent Treatment Plant
PCETP	-	Perundurai Common Effluent Treatment Plant
ANN	-	Artificial Neural Network
BNN	-	Backpropagation Neural Network
PID	-	Proportional Integral Derivative
AVGF	-	Automatic Valves Gravity Filter
ACF	-	Automatic Carbon Filter
TDS	-	Total Dissolved Solids
TSS	-	Total Suspended Solids
COD	-	Chemical Oxygen Demand
BOD	-	Biological Oxygen Demand
HCl	-	Hydro Chloride

References

- Bernt M. Akesson, Hannu T. Toivonen, Jonas B. Waller and Rasmus H. Nystrom. (2005). Neural network approximation of a nonlinear model predictive controller applied to a pH neutralization process. *Journal of Computers and chemical engineering*, 29, 323-335.
- Hunt, K., J. and Sbarbaro, D. (1999). Neural networks for nonlinear internal model control. *IEEE Transactions*, 138, 431-438.
- Junhong Nie, Loh, A., P. and Hang, C., C. (1996). Modelling pH neutralization processes using fuzzy-neural approaches. *Journal of Fuzzy sets and systems*, 78, 5-22.

Lamanna, R., Uria, M., Kelly, J., A., and Pinto, E. (1996). Neural Network Based Control of PH in a Laboratory – Scale Plant. Proceedings of International Workshop on Neural Networks for Identification, Control, Robotics, and Signal/Image Processing, 314 – 320.

Lin-En Kuo and Stephen S. Melsheimer. (1998). Wastewater Neutralization control using a Neural Network Based Model Predictive Controller. Proceedings of the American Control Conference, 3896 – 3899.

Meenakshipriya, B., Dr. Saravanan, K., Shanmugam, R. and Sathiyavathi, S. (2008). Study of pH system in common effluent treatment plant. *Journal of Modern Applied Science*, 2, 113-120.

OMEGA Engineering. (2006). Introduction to pH, [Online] Available: <http://www.omega.com/techref/ph.html>.

Shankar, U. (2003). Common effluent treatment plants: An institutional arrangement for pollution control for small scale tanneries in India. [Online] Available: <http://www.elaw.org/assets/pdf/India2000.pdf>.

Yu, D., L. and Gomm, J., B. (2003). Implementation of neural network predictive controller to a multi variable chemical reactor. *Journal of Control engineering practice*, 11, 1315-1323.

Table 1. Comparison of Measured pH value and Neural predicted pH value

DATE	TIME	pH before treatment	HCl dosing (ml)	pH after treatment	Neural Predicted pH value	Error value
27.02.08	12.15	8.29	0.7	7.8	7.7524	0.0476
	1.15	8.32	0.6	7.5	7.5185	-0.0185
	2.15	8.42	0.6	7.59	7.5689	0.0211
	3.15	8.51	0.6	7.61	7.5984	0.0116
	4.15	8.56	0.6	7.54	7.5938	-0.0538
	5.15	8.62	0.6	7.62	7.5828	0.0372
29.02.08	2.15	7.89	0.6	7.64	7.6403	-0.0003
	3.15	7.71	0.7	7.79	7.7859	0.0041
	4.15	7.73	0.7	7.6	7.6055	-0.0055
15.03.08	10.15	8.71	0.8	7.46	7.5124	-0.0524
	11.15	8.61	0.5	7.71	7.6135	0.0965
	12.15	8.72	0.6	7.61	7.5663	0.0437
	1.15	8.76	0.9	7.52	7.5203	-0.0003
	2.15	8.77	0.8	7.51	7.5296	-0.0196
	3.15	8.78	0.6	7.52	7.5778	-0.0578
	4.15	8.85	1.0	7.55	7.5499	1E-04
16.03.08	10.15	9.0	0.7	7.6	7.5503	0.0497
	11.15	8.7	0.5	7.7	7.6203	0.0797
	12.15	8.9	0.6	7.6	7.6281	-0.0281
	1.15	8.8	0.5	7.7	7.6084	0.0916
	2.15	8.6	0.6	7.8	7.5882	0.2118
	3.15	8.5	0.7	7.8	7.6712	0.1288
	4.15	8.6	0.6	7.5	7.5882	-0.0882
17.03.08	10.15	8.42	0.6	7.6	7.5689	0.0311
	11.15	8.52	0.6	7.61	7.5991	0.0109
	12.15	8.41	0.7	7.7	7.7445	-0.0445

	1.15	8.61	0.5	7.65	7.6135	0.0365
	2.15	8.62	0.7	7.51	7.5533	-0.0433
	3.15	8.73	0.8	7.62	7.5114	0.1086
	4.15	8.76	0.7	7.5	7.5661	-0.0661
18.03.08	10.15	8.72	0.6	7.61	7.5663	0.0437
	11.15	8.77	0.8	7.51	7.5296	-0.0196
	12.15	7.69	0.6	7.64	7.5663	0.0737
	1.15	8.32	0.6	7.5	7.5296	-0.0296
	2.15	8.61	0.7	7.63	7.64	-0.01
	3.15	8.74	0.6	7.52	7.5185	0.0015
	4.15	8.91	0.7	7.63	7.5604	0.0696
19.03.08	1.15	8.81	0.6	7.6	7.568	0.032
	2.15	8.8	0.5	7.7	7.6541	0.0459
	3.15	8.8	0.7	7.6	7.5896	0.0104
	4.15	8.96	0.7	7.5	7.6084	-0.1084
20.03.08	11	6.7	-	6.7	6.699	0.001
	12	6.3	-	6.3	6.3	0
	2	6.4	-	6.4	6.4009	-0.0009
	3	6.3	-	6.3	6.3	0
	4	6.3	-	6.3	6.3	0
	5	6.3	-	6.3	6.3	0
21.03.08	11	7.9	0.5	7.5	7.5002	-0.0002
	12	7.9	0.4	7.6	7.6	0
	2	8.1	0.7	7.7	7.6648	0.0352
	3	8.0	0.7	7.6	7.5849	0.0151
	4	8.2	0.6	7.6	7.5455	0.0545
	5	8.1	0.7	7.6	7.6648	-0.0648
22.03.08	9.35	7.0	-	7.0	7.0004	-0.0004
	10.35	7.0	-	7.0	7.0004	-0.0004
	11.35	7.1	-	7.1	7.1006	-0.0006
	12.35	7.1	-	7.1	7.1006	-0.0006
	2.35	7.2	-	7.2	7.1992	0.0008
	3.35	7.3	-	7.3	7.2996	0.0004
	4.35	7.4	-	7.4	7.4011	-0.0011
	5.35	7.5	-	7.5	7.4988	0.0012
23.03.08	9.15	7.2	-	7.2	7.1992	0.0008
	10.15	7.4	-	7.4	7.4011	-0.0011
	11.15	7.4	-	7.4	7.4011	-0.0011
	12.15	7.2	-	7.2	7.1992	0.0008
	2.15	7.4	-	7.4	7.4011	-0.0011
	3.15	7.6	-	7.6	7.6012	-0.0012

	4.15	7.5	-	7.5	7.4988	0.0012
	5.15	7.5	-	7.5	7.4988	0.0012
24.03.08	11.15	8.7	0.3	7.6	7.6029	-0.0029
	12.15	8.6	0.3	7.5	7.4999	1E-04
	2.15	8.9	0.5	7.5	7.5772	-0.0772
	3.15	9.0	0.5	7.6	7.6629	-0.0629
	4.15	9.0	0.4	7.8	7.7008	0.0992
	5.15	8.9	0.3	7.5	7.4987	0.0013
	6.15	9.0	0.4	7.7	7.7008	-0.0008
25.03.08	11.15	9.1	0.7	7.5	7.501	-0.001
	12.15	9.0	0.7	7.5	7.5503	-0.0503
	2.15	8.8	0.6	7.6	7.5854	0.0146
	3.15	8.6	0.4	7.5	7.4865	0.0135
	4.15	8.5	0.3	7.7	7.6982	0.0018
	5.15	8.7	0.5	7.6	7.6203	-0.0203
	6.15	8.8	0.6	7.5	7.5854	-0.0854
26.03.08	11.35	8.9	0.7	7.6	7.6563	-0.0563
	12.35	8.2	0.6	7.5	7.5455	-0.0455
	1.35	8.8	0.5	7.6	7.6084	-0.0084
	2.35	8.9	0.6	7.5	7.6281	-0.1281
	3.35	8.7	0.6	7.5	7.5667	-0.0667
	4.35	8.9	0.6	7.6	7.6281	-0.0281
	5.35	8.9	0.7	7.7	7.6563	0.0437
27.03.08	11.15	8.9	0.6	7.8	7.6281	0.1719
	12.15	8.9	0.6	7.8	7.6281	0.1719
	1.15	8.8	0.7	7.6	7.6009	-0.0009
	2.15	8.7	0.7	7.5	7.5342	-0.0342
	3.15	8.7	0.7	7.5	7.5342	-0.0342
	4.15	8.7	0.6	7.7	7.5667	0.1333
	5.15	8.8	0.7	7.5	7.6009	-0.1009
28.03.08	11.15	9.0	0.7	7.5	7.5503	-0.0503
	12.15	9.1	0.6	7.7	7.6981	0.0019
	1.15	9.0	0.7	7.6	7.5503	0.0497
	2.15	9.0	0.7	7.6	7.5503	0.0497
	3.15	9.0	0.6	7.6	7.6277	-0.0277
	4.15	8.9	0.6	7.5	7.6281	-0.1281
	5.15	8.9	0.5	7.6	7.5772	0.0228
30.03.08	9.15	8.8	0.5	7.5	7.6084	-0.1084
	10.15	8.7	0.6	7.7	7.5667	0.1333
	11.15	8.9	0.5	7.6	7.5772	0.0228
	12.15	8.9	0.6	7.8	7.6281	0.1719

	2.15	8.5	0.7	7.6	7.6712	-0.0712
	3.15	8.6	0.6	7.5	7.5882	-0.0882
	4.15	8.7	0.5	7.6	7.6203	-0.0203
31.03.08	11.35	8.8	0.6	7.5	7.5854	-0.0854
	12.35	8.7	0.7	7.6	7.5342	0.0658
	1.35	8.5	0.7	7.6	7.6712	-0.0712
	2.35	8.6	0.5	7.5	7.614	-0.114
	3.35	8.6	0.6	7.6	7.5882	0.0118
	4.35	8.5	0.4	7.6	7.6128	-0.0128
	5.35	8.7	0.5	7.5	7.6203	-0.1203
01.04.08	11.35	6.7	-	6.7	6.699	0.001
	12.35	6.6	-	6.6	6.6011	-0.0011
	1.35	6.6	-	6.6	6.6011	-0.0011
	2.35	6.5	-	6.5	6.4989	0.0011
	3.35	6.5	-	6.5	6.4989	0.0011
	4.35	6.6	-	6.6	6.6011	-0.0011
	5.35	6.3	-	6.3	6.3	0
02.04.08	11.35	8.6	0.6	7.5	7.5882	-0.0882
	12.35	8.5	0.5	7.7	7.6811	0.0189
	1.35	8.9	0.6	7.7	7.6281	0.0719
	2.35	8.6	0.7	7.6	7.5683	0.0317
	3.35	8.7	0.8	7.5	7.5167	-0.0167
	4.35	8.9	0.6	7.6	7.6281	-0.0281
	5.35	8.8	0.7	7.7	7.6009	0.0991
03.04.08	11.15	9.0	0.5	7.6	7.6629	-0.0629
	12.15	8.9	0.7	7.8	7.6563	0.1437
	1.15	8.9	0.6	7.5	7.6281	-0.1281
	2.15	9.0	0.4	7.6	7.7008	-0.1008
	3.15	9.0	0.5	7.8	7.6629	0.1371
	4.15	8.9	0.6	7.6	7.6281	-0.0281
	5.15	8.6	0.6	7.5	7.5882	-0.0882

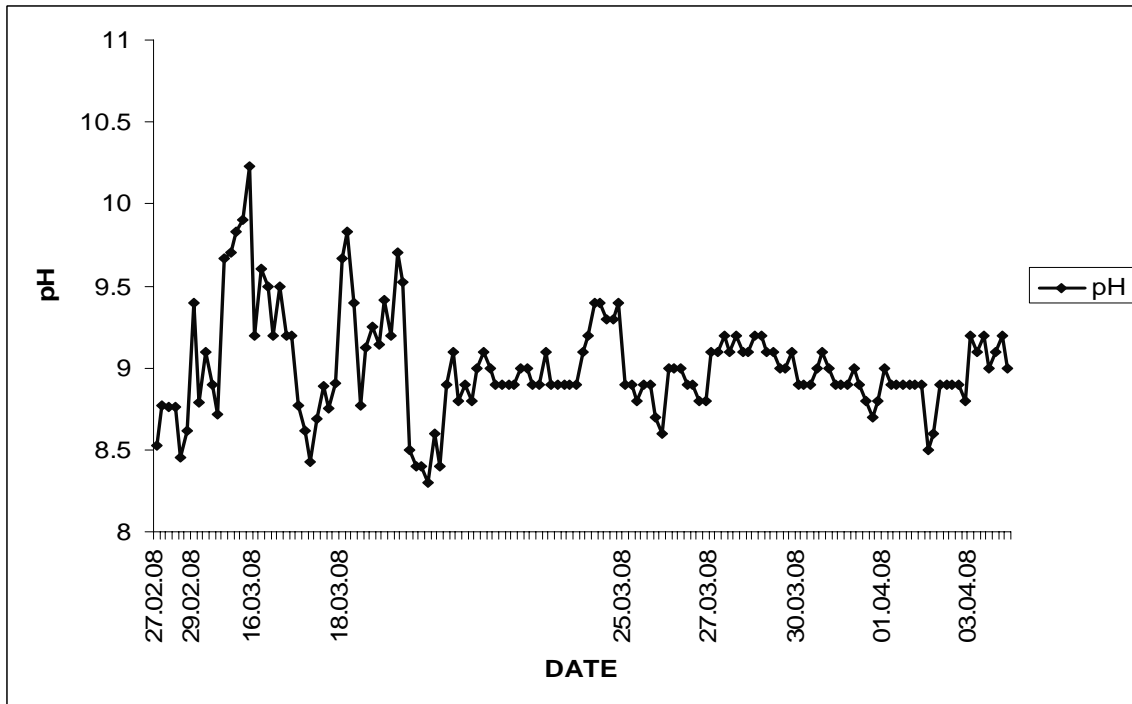


Figure 1. pH variation in Receiving Sump

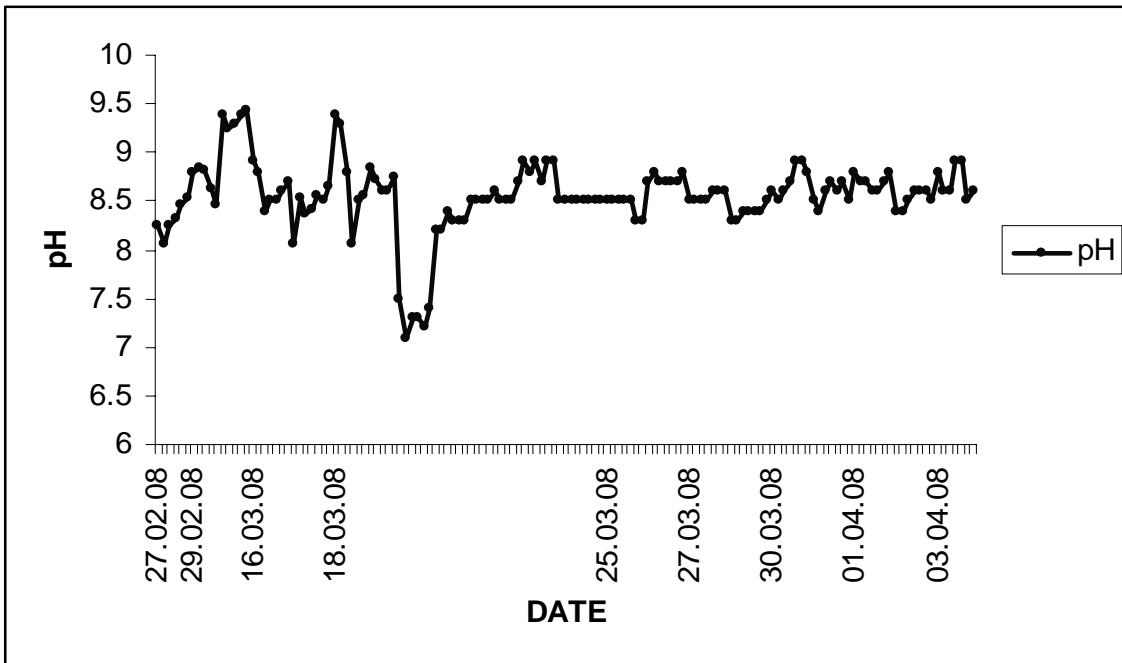


Figure 2. pH variation in Equalization Tank

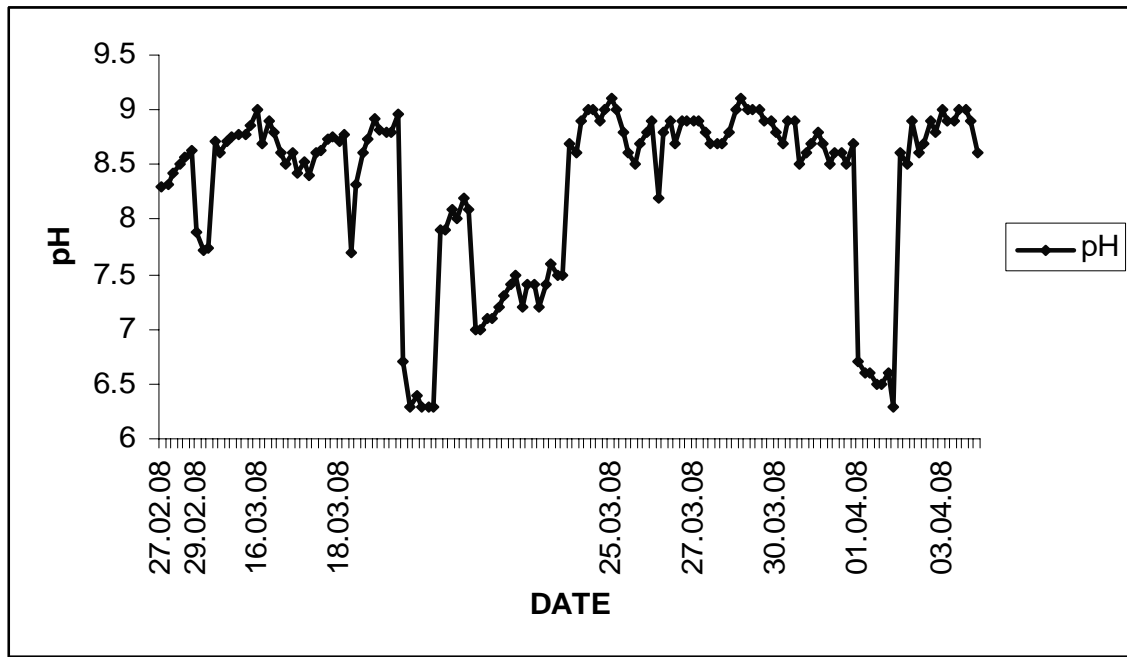


Figure 3. pH variation in Clariflocculator Overflow

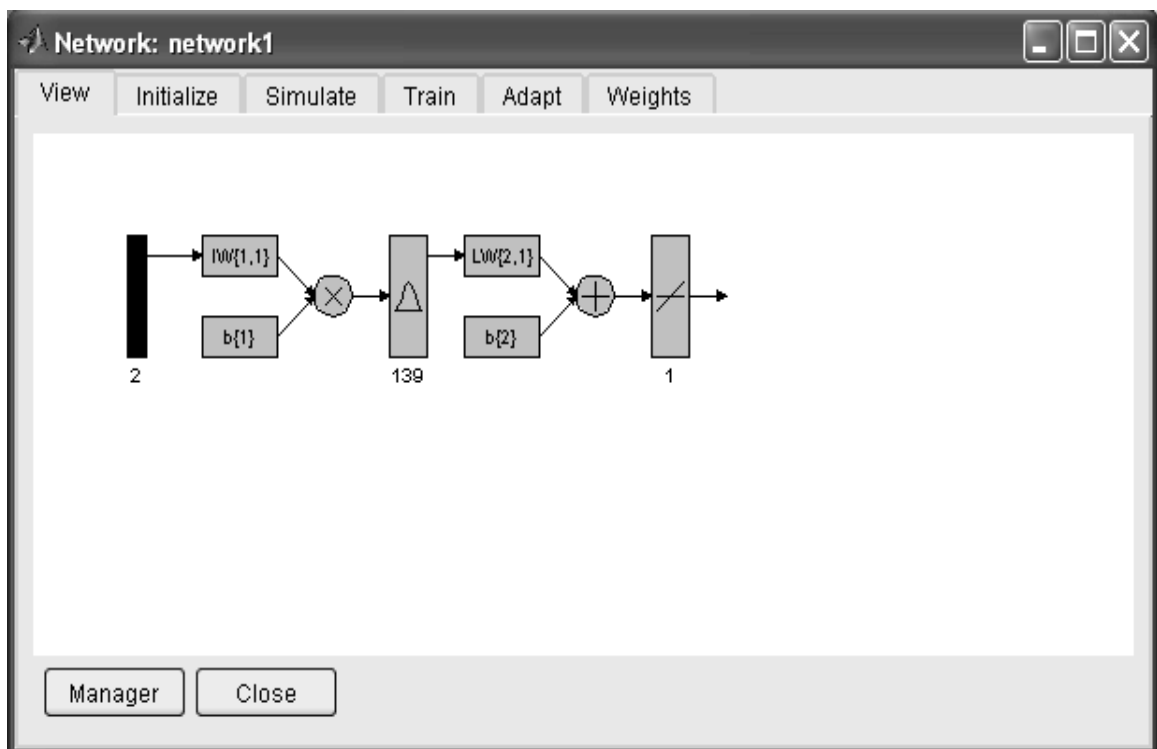


Figure 4. SIMULINK Block Diagram for pH Identifier

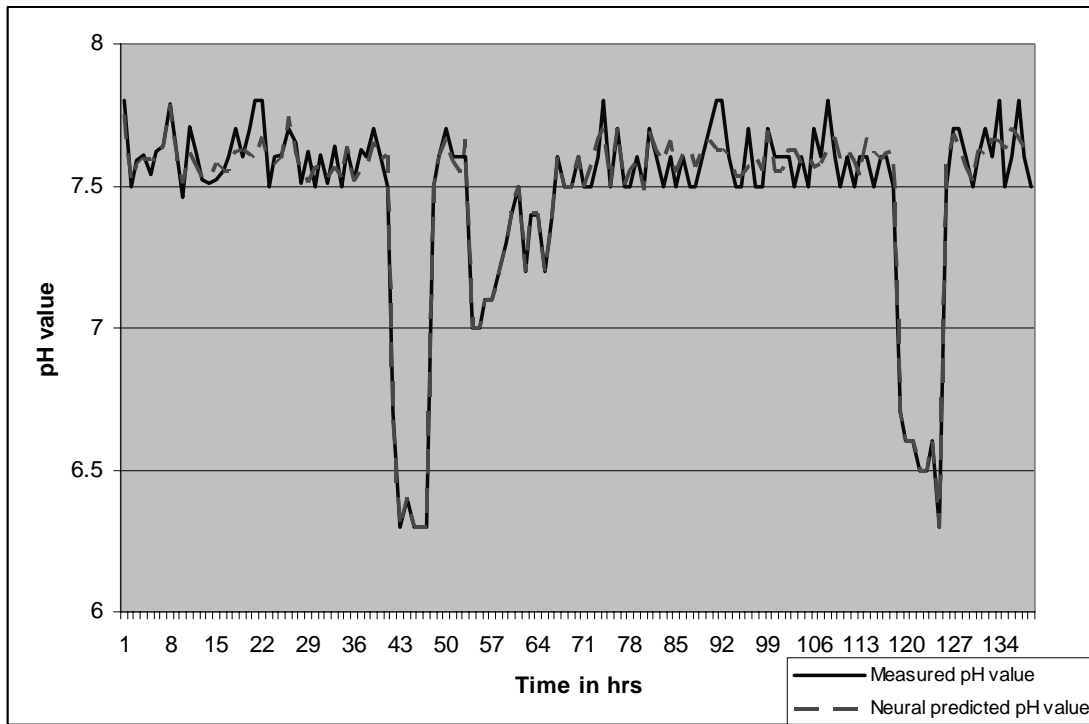


Figure 5. Measured pH value Vs Neural predicted pH value

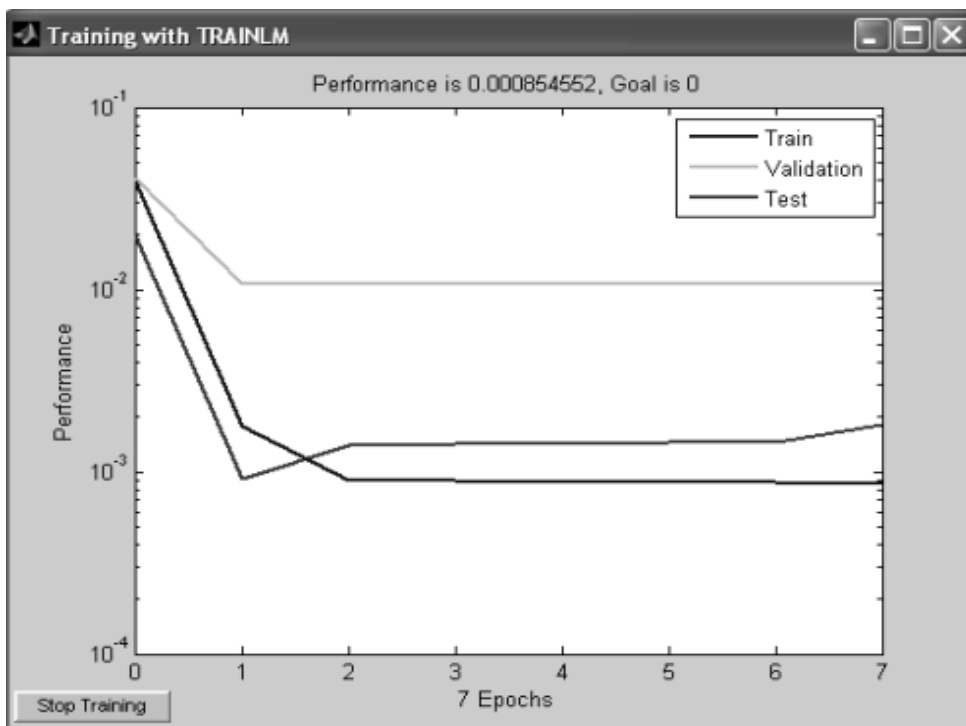


Figure 6. Error response



Catalytic Decomposition of Formaldehyde on Nanometer Manganese Dioxide

Xiujuan Chu & Hua Zhang (Corresponding author)

Tianjin Municipal Key Lab of Fibres Modification and Functional Fibres Institute of Functional Fibres

Tianjin Polytechnic University

Tianjin 300160, China

Tel: 86-22-2452-8453 E-mail: eva@tjpu.edu.cn

This research was funded by Tianjin nature science Found (No. 07JCYBJC02400).

Abstract

In this paper, nanostructure MnO_2 was synthesized in aqueous solution, without using any templates, catalysts, and organic reagents. The as-prepared nano- MnO_2 was systematically characterized by X-ray diffraction (XRD), and transmission electron microscopy (TEM) Fourier transform infrared (FT-IR) spectroscopy analysis. The catalytic decompositions of HCHO were studied at different conditions using the nano- MnO_2 as catalyst. The resulting nano- MnO_2 particles were found to exhibit remarkable environmental catalytic performance in catalytic decomposition of formaldehyde in aqueous solution.

Keywords: Chemical coprecipitation, Nano- MnO_2 , HCHO, Catalytic decomposition

1. Introduction

Manganese oxides (MnO_2) are of considerable interest since these materials can be used in adsorption, catalysis, and other applications. Nano- MnO_2 has a great potentially application in environment protection field as a new generation of environmental friendly catalyst. Cai et al. (2006, p.1971-1976) investigated the removal of a cationic dye, methylene blue, from aqueous solutions by adsorption onto manganese dioxide and found that δ manganese dioxide had the strongest ability for removal among the materials. Gaseous toluene can be oxidated into CO_2 by nano- MnO_2 at ambient temperature (Liu. et al. 2005, p.276-283). Formaldehyde (HCHO) is one of the main pollutants in indoor air. The best way to remove HCHO is to turn it into CO_2 and H_2O . Yoshika et al. (2002, p.5543-5547) have found that manganese oxide could react with HCHO and release carbon dioxide even at room temperature.

MnO_2 with different physical and chemical properties, such as crystallinity, amount of combined water, specific surface areas, and electrochemical performance, can be yielded under different synthesis conditions. Up to now, many routes for the preparation of MnO_2 have been developed including thermal oxidation of Mn (II) nitrates, chemical coprecipitation route (Cai et al., 2006, 1971-1976), electrolysis of Mn (II) salts, and sol-gel method. The chemical coprecipitation process was simple and the reaction conditions were easy to control, so it has been widely applied.

In the paper, the chemical coprecipitation process was used to prepare nano- MnO_2 powders. The catalytic decomposition of HCHO was also studied using as-prepared MnO_2 powders as catalyst at different conditions.

2. Experiments

2.1. Chemicals

Potassium permanganate was obtained from Tianjin Standard Science And Technology Co., Ltd. (Tianjin, China). Manganic sulfate was purchased from Tianjin Kermel Chemical Reagent Co.,Ltd. Carmellose Sodium was obtained from Tianjin Bodi Chemical Co., Ltd. All other chemicals were of analytical grade and used without further purification.

2.2. Preparation of the MnO_2 samples

A chemical coprecipitation route was used to prepare MnO_2 catalyst. The detailed process was as follows: Manganic sulfate were dissolved in distilled water, potassium permanganate aqueous solution was added slowly with magnetic stirring at a molar ratio of $\text{KMnO}_4/\text{MnSO}_4 = 2/3$ at room temperature. The resulting black solution was kept at room temperature in air for 24 h, then filtered and washed with double deionized water for several times to remove any

soluble products. After that, the deposition was dried at 80 °C in air for about 12 h.

2.3. Characterization of the as-prepared MnO₂ particles

Structures of the MnO₂ were characterized using X-ray diffraction (XRD). XRD data were collected using a Rigaku D/MAX 2500 diffractometer with Cu K α radiation ($\lambda=0.15418\text{nm}$). The diffractograms were recorded in the range of 10–80°. Transmission electron microscope (TEM; Hitachi 7650, Japan) was used to observe the morphology of the MnO₂. FT-IR analysis was carried out on a Nicolet 510P FT-IR spectrophotometer.

2.4 Decomposition experiments of HCHO

Under atmospheric pressure, MnO₂ particles were placed in 100mL of glass vessels. And 50mL of HCHO solution with different concentration was introduced into the vessels and the vessels were closed with rubber stopper. The concentrations of HCHO were measured every 12 h. Formaldehyde was spectrophotometrically determined by the acetylacetone method at 412 nm, following Chinese Standards GB18580-2001.

3. Results and discussions

3.1 Characterization of the as-prepared MnO₂ nanoparticles

Fig.1 shows the XRD recorded for the chemical coprecipitation MnO₂ nanostructures. It can be seen from the figure that the peak profile is broad and most of the peaks ($2\theta = 23.5^\circ, 37.14^\circ, 42.48^\circ, 56.30^\circ$) are indexable to γ -MnO₂ phase with a peak ($2\theta = 66.84^\circ$) of δ -MnO₂ phase. The broadness of the peaks indicates that the formed compound has predominantly nanophase.

Fig.2 shows the TEM micrograph MnO₂ particles. The results show distinctly that a nanorod structure with diameter about 5-10nm can be fabricated with this method. Here, we can observe the highly agglomerated nanorods of MnO₂ as shown in the inset of Fig.2.

The FT-IR spectra for MnO₂ before and after catalytic decomposition are shown in Fig.3. Broad absorption peaks centered at around 3421cm^{-1} and 1635cm^{-1} are caused by the absorbed water molecules and carbon dioxide because the nanocrystalline materials exhibit a high surface-to-volume ratio (Zhang Y.C. et al, 2005, p. 652-657). A peak due to Mn–O vibrations was observed at 578cm^{-1} in the spectra of MnO₂. The band at 1109cm^{-1} is absorption peak of the Mn-OH functional group, and band at 1400cm^{-1} are associated with the hydration water of MnO₂. The FT-IR spectra were no obvious difference between before and after catalytic decomposition.

3.2 Catalytic decomposition of HCHO using nano-MnO₂ particles

3.2.1 Effect of initial HCHO concentration

Fig.3 and fig.4 represent the experimental results for the decompositions of HCHO at different initial concentrations using 0.5g nano-MnO₂ powers at 30°C. It is clear that the decomposition of HCHO is relatively high in the region of high HCHO concentration, but it is quickly slowed down in the region of low HCHO concentration (fig.3). The amount HCHO decomposed takes a maximum at the initial concentration of 0.44mg/m^3 (fig.4).

3.2.2 Effect of decomposition temperature

Fig.5 represents the effect of temperature on the decomposition of HCHO at an initial concentration of 40mg/m^3 using 0.5g nano-MnO₂ powers, where the temperature was maintained at 30, 45 and 60 °C. The rate of decomposition of HCHO takes a maximum at 45°C and tends to decrease with the increase or decrease in the temperature, indicating that the catalytic decomposition of HCHO should be carried out at an appropriate temperature.

3.2.3 Effect of amount of nano-MnO₂ particles

Fig.6 shows the effect of applied amount of nano-MnO₂ particles on the removal efficiencies of HCHO at an initial concentration of 44mg/m^3 at 30°C. The removal efficiencies measured after 12 h increased with the amount of nano-MnO₂ particles and reached 87.2% (fig.7) using 0.5 g nano-MnO₂ particles.

4. Conclusions

In summary, the nanostructure MnO₂ particles have been prepared using chemical coprecipitation route. We investigated the catalytic decompositions of HCHO at different conditions using the nanostructures MnO₂. IR spectra indicate that structures of the nano-MnO₂ were no obvious difference between before and after catalytic decomposition. The experimental results show that the catalytic decompositions can be influenced by initial concentration of HCHO, catalytic temperature and amount of nano-MnO₂.

References

- Cai D M & Ren N Q. (2006). Removal of methylene blue from aqueous solution onto manganese oxide with various crystal structures [J]. *Acta Scientiarum Circumstantiae*, 2006, 26(12), 1971-1976.
- F. Shiraishi et al. (2005). Decomposition of gaseous formaldehyde in a photocatalytic reactor with a parallel array of

light sources: 1. Fundamental experiment for reactor design. *Chemical Engineering Journal*, 114, 153–159.

Li L. et al. (2007). Synthesis and shape evolution of novel cuniform-like MnO_2 in aqueous solution. *Materials Letters*, 61, 1609–1613.

Li Y D, Li C W & Qian Y T, et al. (1997). Preparation of superfine $\gamma\text{-MnO}_2$ of different shape [J]. *Chinese Journal of Applied Chemistry*, 14(2), 93-95.

Liu R P, Yang Y L & Xia S J, et al. (2005). Surface chemistry of hydrous manganese dioxide characterization and its effectiveness of removing pollutants [J]. *Environmental Chemistry*, 24(3), 338-341.

Liu Yangsheng & Yi Sha. (2005). Study on oxidation of gaseous toluene by MnO_2 supported on activated carbon filters. *Journal of Basic Science and Engineering*, 13(3), 276-283.

Yoshika Sekin. (2002). Oxidative decomposition of formaldehyde by metal oxides at room temperature. *Atmospheric Environment*, 36, 5543-5547.

Zhang Y.C., Qiao T., Hu. X.Y & Zhou W.D.. (2005). Simple hydrothermal preparation of $\gamma\text{-MnOOH}$ nanowires and their low-temperature thermal conversion to $\beta\text{-MnO}_2$ nanowires [J]. *Journal of Crystal Growth*, 280, 652-657.

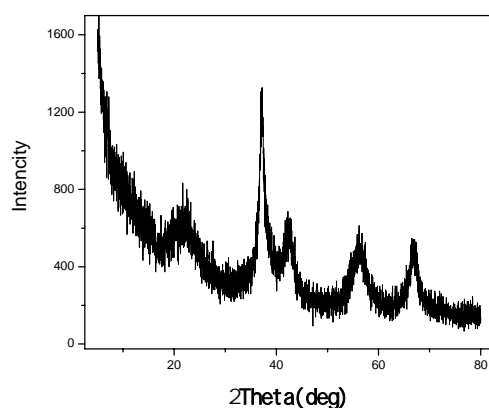


Figure 1. X-ray diffraction patterns of MnO_2 particles

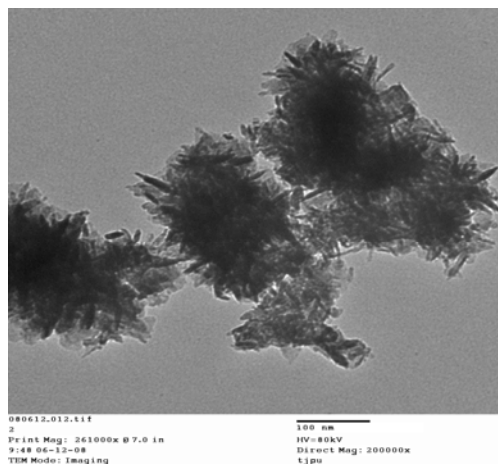


Figure 2. TEM micrograph MnO_2 particles

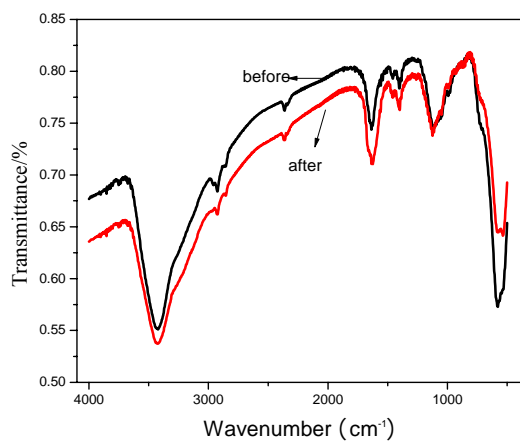


Figure 3. FT-IR spectra for MnO₂

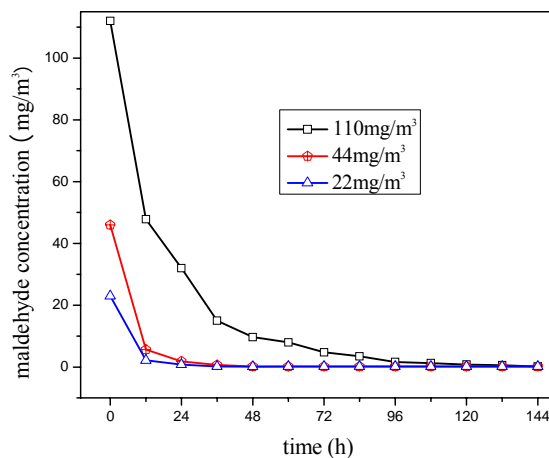


Figure 4. Time courses of concentrations of HCHO at different initial concentration using 0.5g nano-MnO₂ particles at 30°C

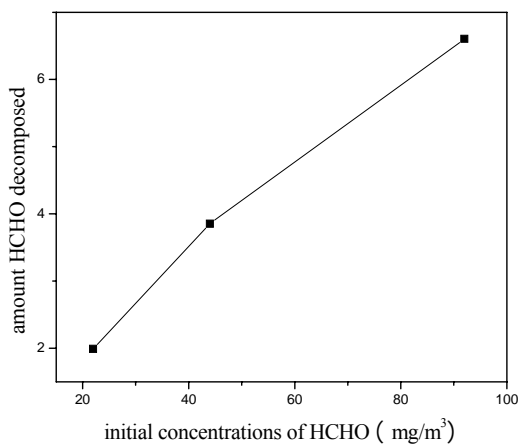


Figure 5. The amount HCHO decomposed at different initial concentration of HCHO using 0.5g nano-MnO₂ particles at 30°C after 12h

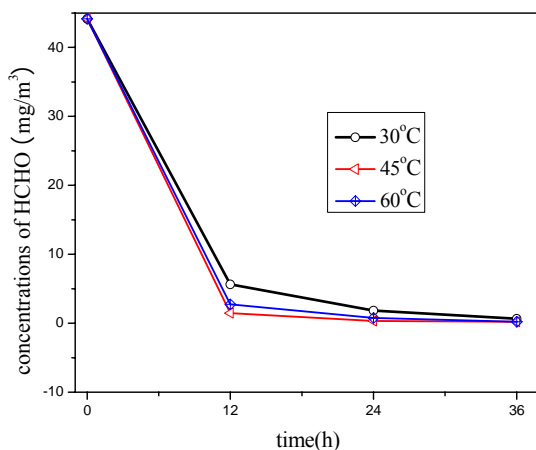


Figure 6. Time courses of concentrations of HCHO at different temperature using 0.5g nano-MnO₂ particles at an initial concentration of 44mg/m³

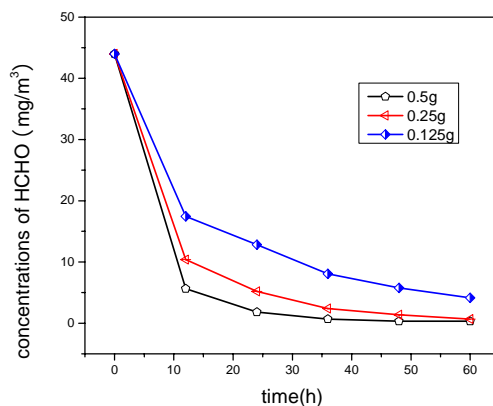


Figure 7. Time courses of concentrations of HCHO at an initial concentration of 44mg/m³ at 30°C using different amount of nano-MnO₂ particles

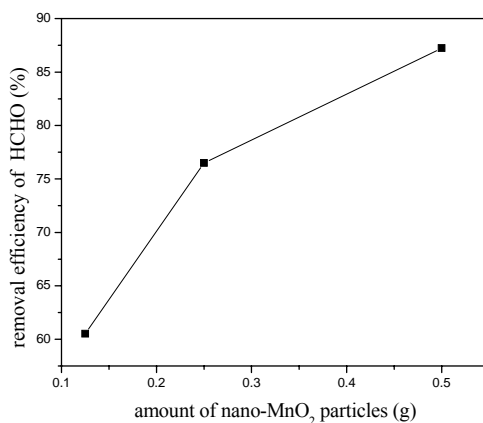


Figure 8. Decomposition rate of HCHO at an initial concentration of 44mg/m³ at 30°C using different amount of nano-MnO₂ particles after 12h



Model Development on Disposal of Municipal Solid Waste through Experimental Studies

Dr.Kaliannan Saravanan

Department of Chemical Engineering, Kongu Engineering College

Erode-638052, India

E-mail: rumisivaesh@yahoo.com

Arumugam Velumani(Corresponding author)

Department of Civil Engineering, Avinashilingam University for Women

Coimbatore-641108, India

E-mail: ganesanvels@yahoo.co.in

Kaliappan Ganesan

Department of Mechanical Engineering, Amritha School of Engineering

Coimbatore-641105, India

E-mail: k_ganesan63@yahoo.com

Abstract

The aim of this paper is to assess emissions associated with collection and transportation of Municipal Solid Waste (MSW) for Coimbatore City located in southern India. Despite the fact that the major environmental impact is linked to the emissions of landfill gases, the study shows that vehicles carrying MSW also make a substantial contribution to the impact. A model was developed to predict and quantify the emissions released into the atmosphere. An analysis was carried out to calculate the emissions generated by the diesel vehicles carrying MSW, focussing upon different modes of speed and time interval of collection and transportation in different routes of the city. Two different vehicles were suggested to collect and transport degradable and recyclable waste to the respective treatment yard such as composting and recyclable yard for Coimbatore city. The amount of CO, CO₂, HC, and NO_x emissions generated by the MSW vehicles during the collection and transportation of the degradable and recyclable waste to the proposed treatment yard were quantified. The emissions were predicted by forecasting the generation of MSW based on the population growth up to the year 2020 for Coimbatore city

Keywords: Gas emissions, MSW Collection, MSW Transport, MSW, Environmental impact, Degradable waste, Recyclable waste, Diesel Vehicles

1. Introduction

Among the various threats and challenges facing mankind today, perhaps the most formidable and menacing one, is air pollution. A World Bank report released recently (2005) states that more than 40,000 people die prematurely every year in India because of health problems related to air pollution. Air pollution is an additional risk factor that increases the statistical probability of death and other adverse health effects caused primarily by cardio-vascular and respiratory diseases (European commission, 2005). New Delhi has the dubious distinction of being the fourth most polluted city in the world [Satyaramchander.A, 1997]. In recent years due to the health and environmental concerns many municipalities particularly in industrialized nations have been forced to assess their Solid Waste Management programs and examine its cost effectiveness in terms of collection, transportation, processing and landfill [Koushki.P, Hulsey.J, Bashaw.E, 1996]. Vehicular emissions are influenced by the combinations of parameters like vehicle technology, fuel quality, vehicle maintenance, driving patterns and traffic controls [Santosh A Jalihal and T. S. Reddy., 2006].

The MSW vehicles substantially add atmospheric pollution in addition to the solid waste generated from the city. As there are only limited studies on the emission loading of MSW vehicles, there is a need to study and quantify the emission on the environment generated by these diesel vehicles. The present work focuses on the emission of various gases into environment due to the collection and transportation of MSW carrying vehicles in the area of Coimbatore City situated in the state of Tamil Nadu, southern part of India. In this paper a model has been developed to quantify the

emission generated by these vehicles. This model was applied for disposal of wastes to the proposed composting and recyclable yard in Coimbatore city. The emissions generated by these MSW vehicles were predicted by forecasting the population upto the year 2020.

2. Disposal of Solid Waste - A Scenario

The Coimbatore city has a population of 10,93,888 with an aerial extent of 105.6 Sq km, produce MSW of 564 tons per day as per the census 2004 (Commissioner of Municipal Administration, India, 2000). This excludes the construction debris and industrial waste. It has very poor solid waste management practices. The entire city with 72 wards is divided into four zones namely North, South, East and West. It is estimated that per capita solid waste generation by Coimbatore dwellers is about 515 gms per day. The unsegregated MSW collected in the different zones of the city is being dumped on open places. In most of the places the wastes are thrown in and around the bins. At present unrecognized rag pickers are involved in the collection of recyclable fractions from the different parts of the city and also from the unsanitary landfills.

At present, the entire hygiene of the city relies on the efficiency of the collection system and conversion techniques used. The number of dumping sites in the city is four, but only one site is in operation at Vellalur that covers an area of 604 acres. Other sites are currently not in use. The wastes are collected through open body trucks and are dumped on the recognized open dumping sites, i.e. unsanitary landfills. Table 1 refers to the total number of owned and hired vehicles for the purpose of collection and transportation of MSW to the dumping yard of Coimbatore [Commissioner of Municipal Administration, India, 2000]. It is inferred from the Table 1 that more number of diesel vehicles are utilized for carrying MSW. In the state of Kuwait seven private companies are incharge of collection, transportation, disposal of household wastes and its cost accounts to \$24.00 per ton of waste. Public complaints regarding this service are non-existent or rare [Koushki.P.A, U.Al.Durajj , W.Al-Ghimlas, 2004]. The quantity of zone wise wastes generation of MSW and the corresponding population statistics are given in Table 2 (Commissioner of Municipal Administration, India, 2000).

The waste prognosis is mainly based on the income level, life style, population growth, life expectancy rate, mortality rate of the people in the city etc.,. But no studies were conducted for the prognosis of waste in Indian cities. Hence in this paper the waste is predicted based on the per capita solid waste and population growth of the city. Figures 1and 2 shows the total quantity of waste generated by the Coimbatore dwellers for degradable and recyclable waste respectively upto the year 2020.

3. Methods adopted in Developing Models

3.1 Traffic studies

To estimate the load of pollutants, it is necessary to estimate the speed of the vehicle travelled with time interval on Coimbatore roads during collection and transportation of MSW. In order to accomplish these estimates, extensive traffic studies were carried out on the road network of Coimbatore city. The traffic studies were designed and conducted to quantify the emission load on atmosphere particularly by these diesel vehicles. An analysis was carried out to calculate the emissions generated by diesel vehicles carrying MSW to obtain the different modes of speed and time interval during different hours of the day. Twelve different samples were randomly chosen for different time intervals of the day.

Employing these data, weighing factor for the different speeds of the vehicle was calculated. The speed of the vehicle was converted into engine rpm by choosing the respective gear ratios.

3.2 Model Development

Based on the experimental interpretations, the following model has been developed by the author to calculate the emissions generated by diesel vehicles during the collection and transportation of MSW. The weighing factor for the different speeds of the vehicle was calculated using the following equation

$$W_{ij} = \frac{t_{ij}}{T} \tag{1}$$

so that $W_{ij} = 1$ for

$i=10, 20, \dots, 60$

$j=10, 20, \dots, 60$

Where

- W_{ij} = Weighing factor for the i^{th} to j^{th} speed step of the vehicle.
- t_{ij} = Duration in which the vehicles travel from i^{th} to j^{th} speed step in seconds
- T = Total time travelled by the vehicle in seconds.

Measuring direct vehicle emissions for different road speeds is a difficult task. Hence the speed of the vehicle is transformed to engine rpm using the relation

$$N = \frac{S(2.65 \times G)}{R} \quad (2)$$

Where

N = Number of revolutions per minute

S = Speed of the vehicle in km/hr

G = Gear ratio for different speeds of the vehicle

R = Radius of the vehicle tyre in metre.

For the corresponding engine speed and load condition, the emission exhausted by the engine was measured using the engine test beds and gas analysers, which in turn weighed as follows,

$$(\text{CO})_T = \sum_{i=0}^{60} W_{ij} (\text{CO})_i \quad (3)$$

$$(\text{CO}_2)_T = \sum_{i=0}^{60} W_{ij} (\text{CO}_2)_i \quad (4)$$

$$(\text{HC})_T = \sum_{i=0}^{60} W_{ij} (\text{HC})_i \quad (5)$$

$$(\text{NO}_x)_T = \sum_{i=0}^{60} W_{ij} (\text{NO}_x)_i \quad (6)$$

Where,

$(\text{CO})_i$, $(\text{CO}_2)_i$, $(\text{HC})_i$, and $(\text{NO}_x)_i$ are the emissions in gm/cycle and

$(\text{CO})_T$, $(\text{CO}_2)_T$, $(\text{HC})_T$ and $(\text{NO}_x)_T$ are the total emissions in gm/cycle respectively during the generating cycle.

4. Model application for Coimbatore City

Emission load on disposal of waste are analysed for the city of Coimbatore. The source-segregated waste is recommended to collect separately by placing two bins for two different waste such as degradable and recyclable. In this case two separate vehicles are considered for collection and transportation of these wastes to the respective treatment yards. In the first case, emission load of pollutants into the atmosphere for the degradable wastes to the proposed Vellalur Composting yard is analysed. In the second case, it is analysed when the recyclable waste are disposed separately to the Ukkadam recyclable treatment yards.

4.1 Collection and Transportation of MSW

Collection and Transportation of MSW include the

- Collection of segregated wastes such as degradable and recyclable fractions in an urban area
- Transportation of the collected waste to the respective processing facilities

4.1.1 Collection of MSW

The collection time in the city takes nearly two hours for each trip. It involves frequent stopping and starting of vehicles and running the vehicle at non-optimal speeds. This leads to more fuel consumption of the vehicle. The expenditure on collection of waste alone amounts to 45-75% of total solid waste management system, in manual intensive system, which is being adopted in India and other developing countries. It is necessary to pay attention to this aspect in order to improve and provide services at a lesser cost. [Kapil.P.Devang, 2006]. Thirty to forty percent of the waste is left uncollected in streets. This is due to the non-availability of sufficient transportation of fleet, frequent breakdown of vehicles and absenteeism of the crew. Part of the waste is being disposed by open burning. The emission load of pollutants due to open burning of MSW for Tamilnadu is growing at the rate of 3 tons/year [Chnahi Sinha, 1997]. Figure.3 shows the average vehicular speed for the collection of MSW.

From the observed data, only 10% of the time, engine of the vehicle was not in running conditions. Also from the graph it was predicted that collection vehicle travels at an average speed of 14.5 km/hr. Thus total distance covered by the vehicle during collection in km per year D_{ct} was calculated using the following equation

$$D_{ct} = N \times D_c \quad (7)$$

$$D_c = 0.9 \times \sum_{i=0}^{60} [t_i \times S_c]$$

where,

D_c = Total distance covered in Km per trip.

N = Total number of trips per year.

t_i = Total collection time per trip and

S_c = Speed of MSW vehicles in km per hr during collection of wastes.

4.1.2 Transportation of MSW

Coimbatore Corporation is planning to supply 100 tons of biodegradable waste and 30 tons of recyclable waste per day to the private entrepreneurs for the composting and recycling respectively. This proposal is under process. Figure 4 shows the average vehicular for the transport of MSW.

The total fleet of vehicles used in a day depends on the total MSW generated in a city and the vehicles hauling capacity, number of bins and collection frequency. Trucks are designed to carry 5-7 tons of building material of large density, but the MSW is lighter and hence the truck actually carries only 3 tons of MSW. Total distance travelled, during transportation in km/year, expressed as D_t , could be worked from the following relationships

$$D_t = \sum_{i=1}^4 [MSW_g \div C] \times [T_i] \quad (8)$$

Where,

MSW_g = Total municipal solid waste generated in tons for four zones of the city

C = Hauling capacity of the vehicles in tons per trip.

T_i = Travelling distance of vehicle during transportation in km per trip for four zones of the city.

The total distance travelled by the vehicle was calculated to estimate the emission loading into the environment. The total distance travelled by the vehicle for disposal of the waste is calculated using the equations (7) and (8). Figure 5 predicts the emission of various pollutants such as CO, CO₂, HC and NO_x for different rpm of engines. From these figures, emissions are interpolated for different average engine rpm of MSW carrying vehicles. Thus the total emission load was estimated using the equations 3-6.

5. Results and Discussion

The suggested model in this paper can be applied to urban and rural areas to quantify the emissions generated by MSW carrying vehicles. It also helps the decision makers in waste management system to understand the Greenhouse gases released due to vehicle pollution in MSW management sector. The risk of global warming is intensified by the CO₂ emissions of increasing activities of the transport sector.

The amount of CO, CO₂, HC, and NO_x emissions generated during the collection and transportation of the disposal of wastes for the existing situation and the proposed composting yard for the degradable fractions are same. This is due to the lesser quantity of the generation of the recyclable fractions. The total distance travelled by the vehicle to dispose the degradable fraction to the composting yard is 24.84 times higher than recyclable fractions to the recycling yard. This is mainly due to more generation of the degradable fractions than the recyclable fractions by the residents. It is found that generation of the degradable and recyclable fractions are 94% and 6% respectively by the Coimbatore dwellers. All the emissions generated during the collection of the degradable fraction are 3.06 times lesser than collection of recyclables. Also CO, CO₂, HC, and NO_x emissions during collection of degradable wastes are 1.77, 2.29, 2.95 and 3.00 times higher than transportation of the same to the compost yard.

Figure 6-9 shows the emissions generated exclusively by the MSW vehicles up to the year 2020. This shows that the emissions are increasing every year due to the generation of more quantity of waste. The waste management sector emphasis 3R policies i.e., Reduction, Reuse and Recycling of the waste. This reduces transportation used for disposal of MSW and thereby reducing CO₂ emissions.

6. Conclusion

From the experimental studies and with the help of the model predictions, the following observation has been suggested to reduce the emission of Greenhouse gases.

- 1) The total distance travelled by the vehicle during collection can be reduced by the optimisation of collection routes and also implementation of 3 R policies, thus releasing lesser emission load.
- 2) The body of the MSW vehicle can be modified based on the bulk density of the waste.
- 3) Source sorted wastes from the households can be collected through pushcarts to reach the community bin and
- 4) Vehicles with two separate compartments to collect degradable and recyclable waste fractions can be considered to reduce the total distance travelled by the vehicle.

References

- A.Satyaramchander. (Feb 1997). "Vehicular pollution in Urban areas –Causes, Effects and Remedies, Indian journal of transport management, 122-130.
- Chnahi Sinha, (1997). Open burning of urban municipal solid waste; *State level analysis Teri- Information monitor on Environmental Science* (2), No 2, 71-77.
- Commissioner of Municipal Administration, (2000)., *Action Plan for Implementation of Municipal Solid Waste Management and Handling Rules 2000*. Prepared as per the Guidelines Issued by the Commissioner of Municipal Administration, India.
- European commission. (2005). *The fifth framework programme, On Integrated systems for forecasting urban meteorology, Air pollution and population exposure, Deliverables 7.3*.
- Kapil.P.Devang. (2006). *Application of LCA approach to Evaluate Municipal Solid Wastemanagement options*, Unpublished M.E. thesis, National Institute of Technology, Nagpur, India.
- Koushki.P,U.Al-Duaij. W-Al .Ghmlas. (2004). *Collection and transportation cost of household solid waste in Kuwait. Waste Management*, (24) , 957-964.
- Koushki.P.A. Hulsey.J.Bashaw.E. (1996) *Household solid waste: trait and disposal site selection*. ASCE, Journal of urban planning and development, USA:123(1), 9.
- Santosh A Jalihal and T. S. Reddy. (June 2006). *Assessment of the impact of improvement measures on air quality: Case of Delhi*. Journal of transportation engineering ASCE 482-488.

Table 1. Vehicles used for collection and transportation of MSW

S.No	Type of vehicles	Total number of vehicles
Corporation vehicles		
1	Lorries with tipper	9
2	Lorries with non tipper	3
3	Dumper placers	17
4	Bulk Refuse carrier	2
Private vehicles		
5	Hired private lorries	49

Table 2. Zone wise of Generation of Solid Waste

Sl.No	Zone	No. of Houses	Population	Garbage Generated in MT/ Day			
				Degradable	Recyclable	Inert	Total
1	East	63,355	2,87,553	102	7.2	22.4	13.6
2	West	59,838	2,66,717	114.4	7.9	21.4	143.7
3	South	46,509	2,38,571	120.4	8.1	19.1	147.6
4	North	59,007	3,01,047	109.4	7.8	23.9	141.1
TOTAL		2,28,709	10,93,888	446.2	31	86.8	564

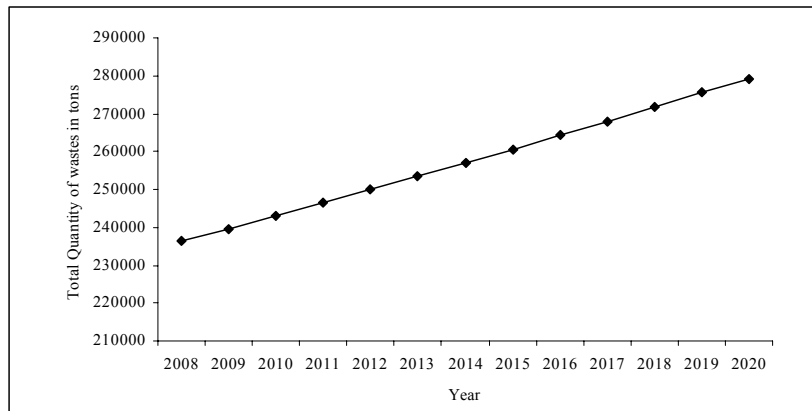


Figure 1. Generation of Total Quantity of Degradable waste

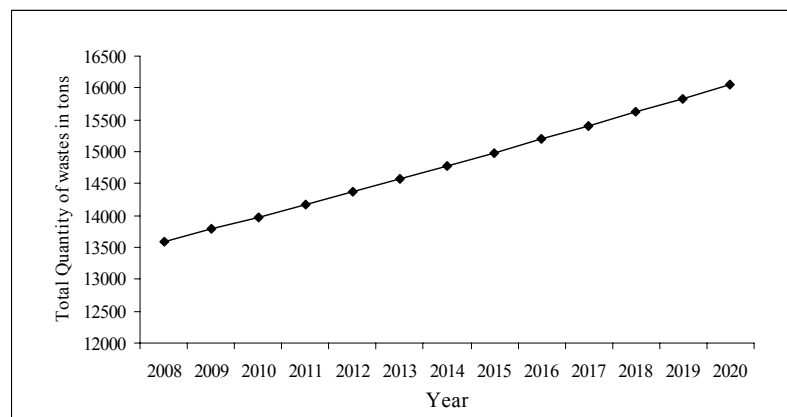


Figure 2. Generation of Total Quantity of Recyclable waste

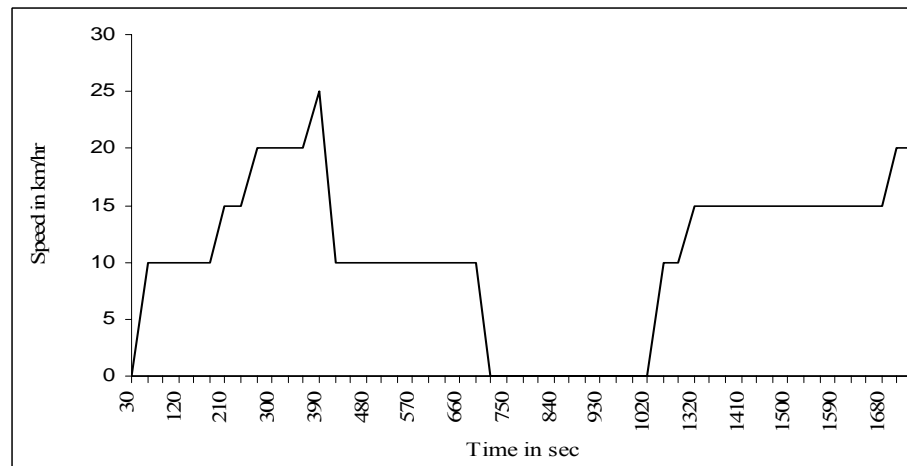


Figure 3. Average vehicular speed for the transport of MSW

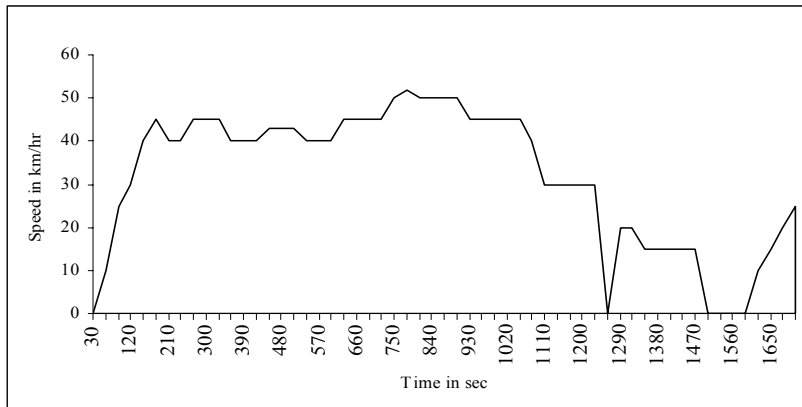
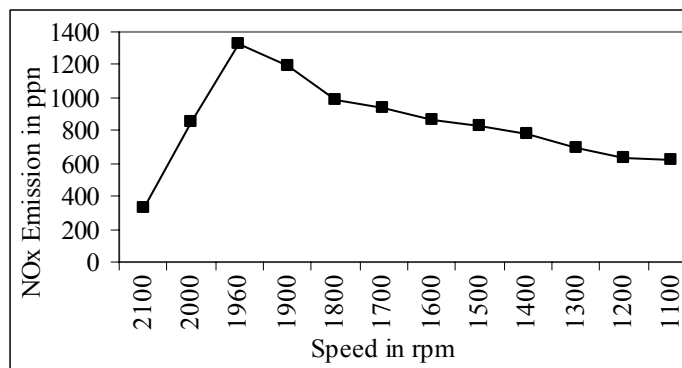
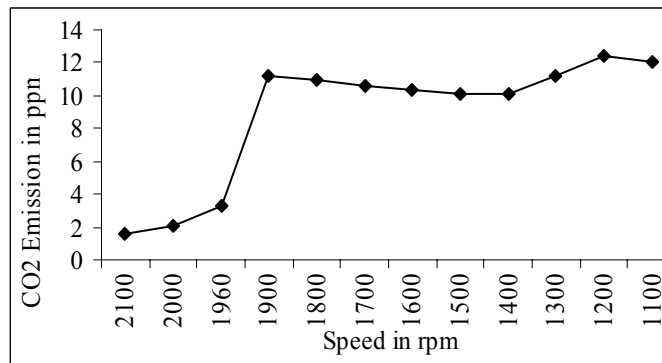
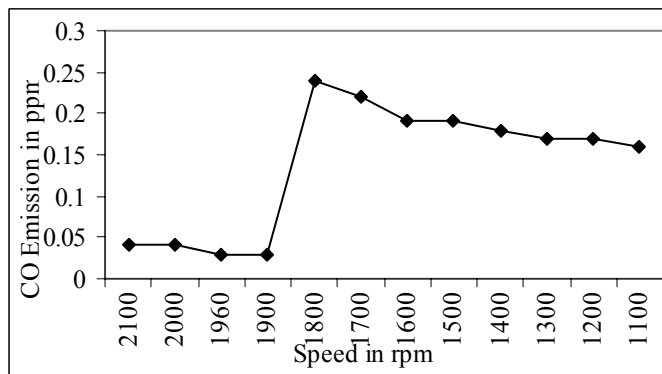


Figure 4. Average vehicular speed for the transport of MSW



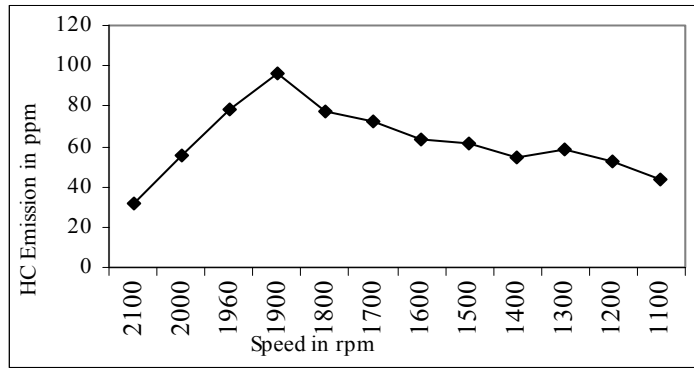


Figure 5. Emission of various pollutants for different rpm of the engine

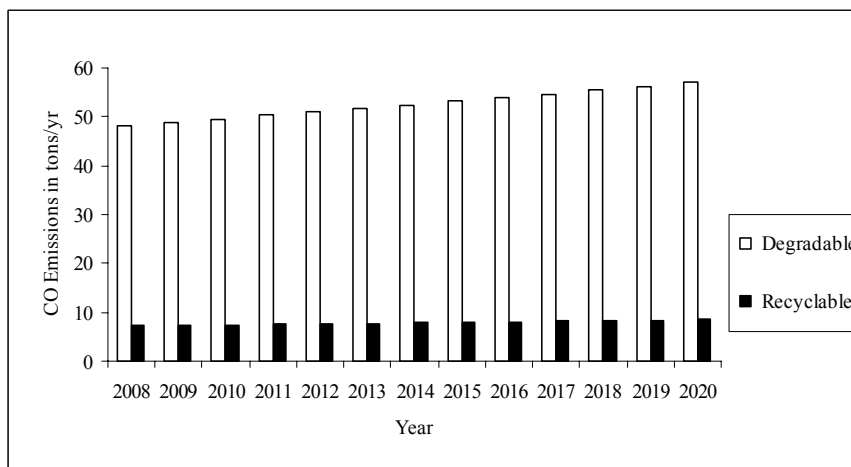


Figure 6. CO Emissions for disposal of Degradable and Recyclable waste

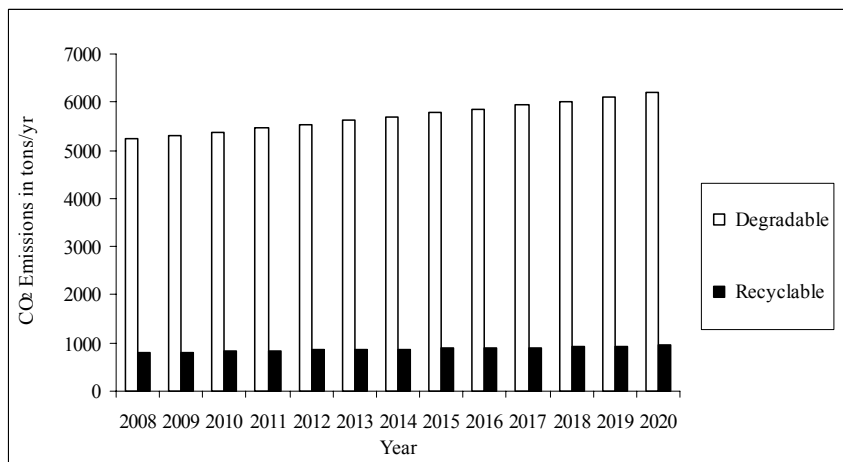


Figure 7. CO₂ Emissions for disposal of Degradable and Recyclable waste

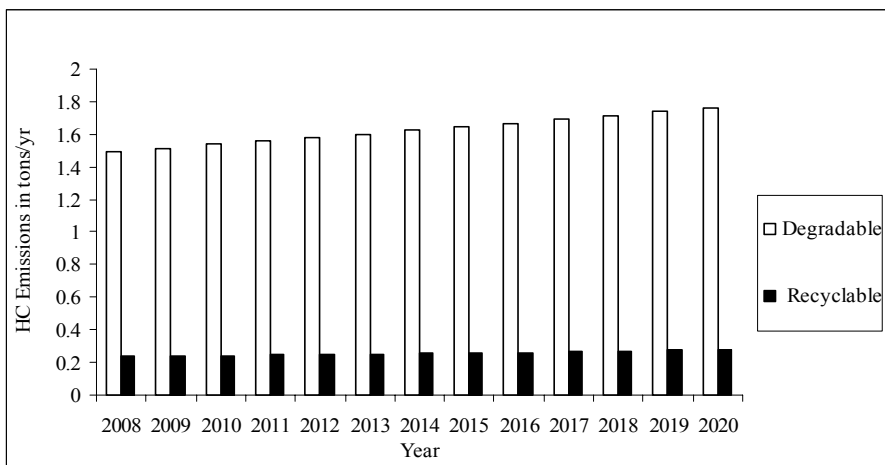


Figure 8. HC Emissions for disposal of Degradable and Recyclable waste

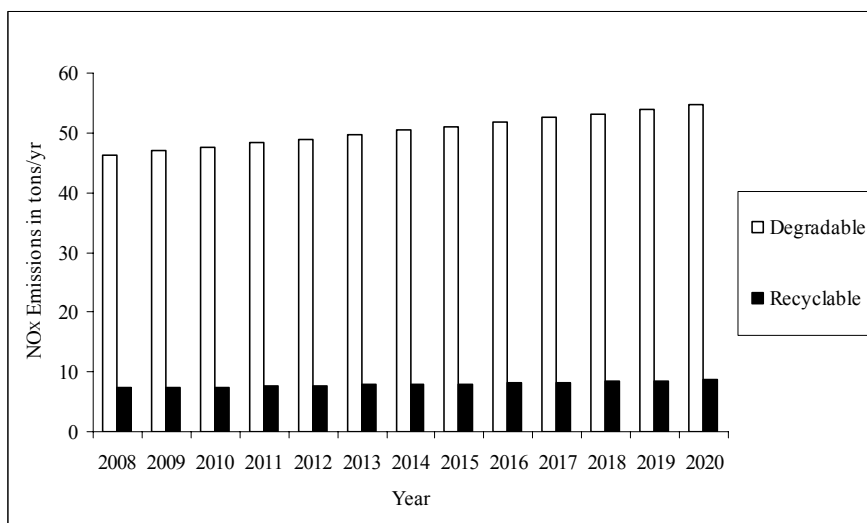


Figure 9. NO_x Emissions for disposal of Degradable and Recyclable waste



Analysis of Instantaneous Center of Zero Acceleration of Rigid Body in Planar Motion

Haibin Sun (Corresponding author) & Tingting Liu

Department of Physics and Electronics

Taishan University

Shandong 271021, China

E-mail: sunhbphy@hotmail.com

Abstract

When the angular velocity vector of rigid body in the plane motion unequal to zero, we can certainly find a point which instantaneous acceleration equal to zero at that particular instant. The point is named instantaneous center of zero acceleration. We proved the existence of the point and obtained the location of the point. We could solve mechanical problem quickly using instantaneous center of acceleration as base point.

Keywords: Instantaneous center of zero acceleration, Rigid body, Planar motion

1. Introduction

Let us analyze a rigid body which is in planar motion. It is clear that if we could find a point, C , in the rigid body for which the instantaneous velocity is zero, then the velocity of the body at that particular instant would consist only of a pure rotation of the body about that point (no translation)(Fredy R. Zypman,2005) . If we choose the point C which is momentarily stationary at the instant considered as a base point, the velocity equation for an arbitrary point A in the body simplifies to

$$v_A = \omega \times r_A, \tag{1}$$

where ω is the body angular velocity (J. F. LI,2001). If we know the angular velocity, and the radius vector of point A with respect to C , then we could determine the velocity of point A . Point C can be taken as the center of rotation only at the given instant, and is therefore known as the instantaneous center of zero velocity. If we can determine the instantaneous center of zero acceleration, we can solve some mechanical problems efficiently.

2. Deduction of instantaneous center of zero acceleration

The acceleration of an arbitrary point P in the rigid body is (SH M CH, 2001)

$$a = a_A + \frac{d\omega}{dt} \times (r - r_0) - \omega^2 (r - r_0). \tag{2}$$

Here, A is a base point, r is the radius vector of the point considered with respect to the fixed point O , r_0 is the radius vector of the point A with respect to the point O , r' is the radius vector of the point with respect to the point A , and $r' = r - r_0$; ω is the angular velocity, $\alpha = \frac{d\omega}{dt}$ is the angular acceleration. The directions of the angular velocity and angular acceleration indicate the axis of rotation. Consider the base point A and the point P having coordinates (ξ_0, η_0) and (ξ, η) in a fixed Cartesian coordinate system, $o-\xi\eta$. In Cartesian coordinate system, $A-xy$, which is a body fixed reference system, the point P having coordinates (x, y) . Take Z axis to be the fixed direction perpendicular to the planar motion. The position of point A and P are illustrated in Fig. 1.

2.1 Existence proof

When the rigid body moves in plane with angular velocity, ω , which is unequal to zero, we choose a point, C , in the body for which the instantaneous acceleration is zero. We define this point as the instantaneous center of zero acceleration. From Eq. (2), we have

$$0 = a_A + \frac{d\omega}{dt} \times (r_c - r_0) - \omega^2 (r_c - r_0), \tag{3}$$

where, $\mathbf{r}_c = \xi_c \mathbf{i} + \eta_c \mathbf{j}$ is the radius vector of the instantaneous center of zero acceleration with respect to the origin O .

Taking the scalar product of Eq. (2) with $\boldsymbol{\omega}$, we obtain

$$0 = \boldsymbol{\omega} \cdot \mathbf{a}_A + \boldsymbol{\omega} \cdot \left[\frac{d\boldsymbol{\omega}}{dt} \times (\mathbf{r}_c - \mathbf{r}_0) \right] - \boldsymbol{\omega} \cdot [\boldsymbol{\omega}^2 (\mathbf{r}_c - \mathbf{r}_0)]. \quad (4)$$

The direction of angular velocity vector, $\boldsymbol{\omega}$, is parallel to the direction of angular acceleration vector, $\boldsymbol{\alpha} = \frac{d\boldsymbol{\omega}}{dt}$. So $\boldsymbol{\omega}$ is orthogonal to $\frac{d\boldsymbol{\omega}}{dt} \times (\mathbf{r}_c - \mathbf{r}_0)$. Hence,

$$\boldsymbol{\omega} \cdot \left[\frac{d\boldsymbol{\omega}}{dt} \times (\mathbf{r}_c - \mathbf{r}_0) \right] = 0. \quad (5)$$

In fact, the angular velocity, $\boldsymbol{\omega}$, is perpendicular to the plane that the body is moving, and the relative radius vector, $\mathbf{r}_c - \mathbf{r}_0$, also lies in this plane. So the vector angular velocity, $\boldsymbol{\omega}$, is perpendicular to the vector $\mathbf{r}_c - \mathbf{r}_0$. Therefore, we have

$$\boldsymbol{\omega} \cdot [\boldsymbol{\omega}^2 (\mathbf{r}_c - \mathbf{r}_0)] = 0. \quad (6)$$

Substituting Eqs. (5) and (6) into Eq. (4), we obtain

$$\boldsymbol{\omega} \cdot \mathbf{a}_A = 0. \quad (7)$$

In the case, the acceleration of any point in the rigid body, \mathbf{a}_A , must be orthogonal to the angular velocity, $\boldsymbol{\omega}$. Surely Eq. (7) is an identity.

In conclusion, when the rigid body moves in plane with angular velocity, $\boldsymbol{\omega}$, that is unequal to zero, we can certainly find the point, C , in the body for which the instantaneous acceleration is zero, i.e., the instantaneous center of zero acceleration must exist.

2.2 Position of the instantaneous center of zero acceleration

Taking the vector product of Eq. (2) with $\boldsymbol{\omega}$, we obtain

$$0 = \boldsymbol{\omega} \times \mathbf{a}_A + \boldsymbol{\omega} \times \left[\frac{d\boldsymbol{\omega}}{dt} \times (\mathbf{r}_c - \mathbf{r}_0) \right] - \boldsymbol{\omega} \times [\boldsymbol{\omega}^2 (\mathbf{r}_c - \mathbf{r}_0)]. \quad (8)$$

Additionally,

$$\boldsymbol{\omega} \times \left[\frac{d\boldsymbol{\omega}}{dt} \times (\mathbf{r}_c - \mathbf{r}_0) \right] = \boldsymbol{\alpha} [(\mathbf{r}_c - \mathbf{r}_0) \cdot \boldsymbol{\omega}] - (\mathbf{r}_c - \mathbf{r}_0)(\boldsymbol{\omega} \cdot \boldsymbol{\alpha}) = -(\mathbf{r}_c - \mathbf{r}_0)(\boldsymbol{\omega} \cdot \boldsymbol{\alpha}). \quad (9)$$

Here, we have used the vector identity: $\mathbf{A} \times (\mathbf{B} \times \mathbf{C}) = (\mathbf{A} \cdot \mathbf{C})\mathbf{B} - (\mathbf{A} \cdot \mathbf{B})\mathbf{C}$ (K. F. Riley, 2002).

Substituting Eq. (9) into Eq. (8), we have

$$0 = \boldsymbol{\omega} \times \mathbf{a}_A - (\mathbf{r}_c - \mathbf{r}_0)(\boldsymbol{\omega} \cdot \boldsymbol{\alpha}) - (\mathbf{r}_c - \mathbf{r}_0)(\boldsymbol{\omega} \cdot \boldsymbol{\alpha}). \quad (10)$$

From Eq. (10), we can obtain the radius vector of the instantaneous center of zero acceleration. The calculation of \mathbf{r}_c , in this case, requires knowing \mathbf{r}_0 , \mathbf{a}_A , $\boldsymbol{\omega}$ and $\boldsymbol{\alpha}$. In general, the angular acceleration vector, $\boldsymbol{\alpha}$, is unknown to us. Therefore, the location of the instantaneous center of zero acceleration is difficult to locate.

In the fixed Cartesian coordinate system $o-\xi\eta$, Eq. (10) can be written as

$$\begin{cases} \xi_c = \xi_0 + \frac{\omega^2 a_{A\xi} - \alpha a_{A\eta}}{\alpha^2 + \omega^4} \\ \eta_c = \eta_0 + \frac{\alpha a_{A\xi} + \omega^2 a_{A\eta}}{\alpha^2 + \omega^4} \end{cases}, \quad (11)$$

In the moving Cartesian coordinate system $A-xy$, Eq. (10) can be written as

$$\begin{cases} x_c = \frac{\omega^2 a_{Ax} - \alpha a_{Ay}}{\alpha^2 + \omega^4} \\ y_c = \frac{\alpha a_{Ax} + \omega^2 a_{Ay}}{\alpha^2 + \omega^4} \end{cases}, \tag{12}$$

It should be noted that the location of the instantaneous center of zero acceleration will change in time. The path described by the instantaneous center is called the space centrode, and the locus of the positions of the instantaneous centers on the body is called the body centrode.

3. Application of the instantaneous center of zero acceleration

3.1 Acceleration of any point in the rigid body

If we define the instantaneous center of zero acceleration, C , as the base point, the acceleration of any point, D , in the body can be obtained from Eq. (2),

$$\mathbf{a}_D = \frac{d\boldsymbol{\omega}}{dt} \times (\mathbf{r} - \mathbf{r}_c) - \omega^2 (\mathbf{r} - \mathbf{r}_c) = \frac{d[\boldsymbol{\omega} \times (\mathbf{r} - \mathbf{r}_c)]}{dt}. \tag{13}$$

Here, $\frac{d\boldsymbol{\omega}}{dt} \times (\mathbf{r} - \mathbf{r}_c)$, is the tangential component of the acceleration with respect to the instantaneous center, and, $-\omega^2 (\mathbf{r} - \mathbf{r}_c)$, is the normal component of the acceleration with respect to the instantaneous center. The above equation is analogous to the equation expressing the acceleration to fixed axis rotation. So we can say that the acceleration of the body at that particular instant would consist only of a pure rotation of the body about the instantaneous center of acceleration.

We choose the instantaneous center of acceleration as the origin of the Cartesian coordinate, in this coordinate system, Eq. (13) has the form

$$\mathbf{a}_D = \frac{d\boldsymbol{\omega}}{dt} \times \mathbf{r} - \omega^2 \mathbf{r} = \frac{d(\boldsymbol{\omega} \times \mathbf{r})}{dt}, \tag{14}$$

where $\mathbf{r} = \overline{CD} = xi+yj$ is the radius vector of point D with respect to the instantaneous center, C (cf. Fig. 2).

Assume that the angular velocity, $\boldsymbol{\omega}$, and the angular acceleration, $\boldsymbol{\alpha} = \frac{d\boldsymbol{\omega}}{dt}$, have the same direction. In component form, Eq. (14) can be written as

$$\begin{cases} a_{Dx} = -\omega^2 x - \alpha y \\ a_{Dy} = \alpha x - \omega^2 y \end{cases}, \tag{15}$$

3.2 Location of the instantaneous center of acceleration

At a particular instant, the angular velocity, $\boldsymbol{\omega}$, the angular acceleration, $\boldsymbol{\alpha} = \frac{d\boldsymbol{\omega}}{dt}$, and the acceleration of point D , $\mathbf{a}_D = a_{Dx}\mathbf{i} + a_{Dy}\mathbf{j}$, all have certain values. Solving Eqs. (15), we have

$$\begin{cases} x = -\frac{\omega^2 a_{Dx} - \alpha a_{Dy}}{\alpha^2 + \omega^4} \\ y = -\frac{\alpha a_{Dx} + \omega^2 a_{Dy}}{\alpha^2 + \omega^4} \end{cases}, \tag{16}$$

From Eqs. (16), we can obtain the distance between point D and instant center C :

$$|\mathbf{r}| = \overline{CD} = \sqrt{x^2 + y^2} = \frac{a_D}{\sqrt{\alpha^2 + \omega^4}}. \tag{17}$$

Here, $a_D = \sqrt{a_{Dx}^2 + a_{Dy}^2}$, is the magnitude of acceleration \mathbf{a}_D .

The angle, φ , between the direction of acceleration vector \mathbf{a}_D and the direction of radius vector \mathbf{r} is

$$\varphi = \arctan \frac{\alpha}{\omega^2}. \quad (18)$$

Here, if $\alpha > 0$, φ is a positive acute angle, i.e., counterclockwise to point D ; otherwise, φ clockwise to point D .

According to Eqs. (17) and (18), if we know the values of ω , α and \mathbf{a}_D , we can calculate the angle, φ , and the magnitude of \overline{CD} . Then we can draw the location of the instantaneous center of zero acceleration, C (Ch H Ch, 1999). See Fig. 3.

3.3 Theorem of relative angular momentum about the instantaneous center

The equation of relative angular momentum of a rigid body which is in planar motion is (H. E. Williams, 2000)

$$\mathbf{M}_A = \frac{d\mathbf{L}_A}{dt} + m\mathbf{r}_{CA} \times \mathbf{a}_A. \quad (19)$$

Here, \mathbf{M}_A is the net moment about A , \mathbf{L}_A is the relative angular momentum about A , \mathbf{r}_{CA} is the radius vector of point C about A and \mathbf{a}_A is the acceleration of point A .

When we define the instantaneous center of zero acceleration, C , as the base point, the theorem of relative angular momentum with respect to the instantaneous center can be expressed as

$$\mathbf{M}_c = \frac{d\mathbf{L}}{dt} = I\boldsymbol{\alpha} \quad (20)$$

Here, \mathbf{M}_c is the net moment about point C of all external forces acting on the body, \mathbf{L} is the relative angular momentum about C of the body, I is the moment of inertia about C , $\boldsymbol{\alpha}$ is the angular acceleration of the body.

4. Conclusion

On the basis of vector algebra, we have proved the existence of the instantaneous center of zero acceleration, and calculated the location of the instantaneous center of acceleration. The instantaneous center of zero acceleration plays an important role in solving mechanical problems.

References

- Ch H Ch. (1999). Analyses on Instantaneous Acceleration Center of Rigid Bodies Planner Motion. *Journal of Ji'mei University(natural Science)*, Vol. 4, No. 1:19-22.
- Fredy R. Zypman. (2005). Instantaneous center of rotation and centrodes: background and new examples. *Int. J. Mech. Enging. Educ.*, 35 (1):79–90.
- H. E. Williams. (2000). A note on the use of the instant center as a reference point for angular momentum theorems. *Int. J. Mech. Enging. Educ.*, 28 (2):185–186.
- J. F. LI, X. Zhang. (2001). *Classical Mechanics*. Tsinghua University Press, Beijing, 30.
- K. F. Riley, M. P. Hobson and S. J. Bence. (2002). *Mathematical Methods for Physics and Engineering* (second edition). Cambridge University Press, Cambridge, 230.
- SH M CH. (2001). *Theoretical Mechanics*. Higher Education Press, Beijing, 117.

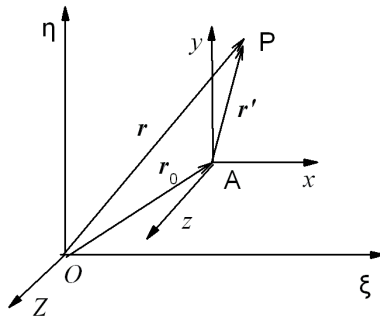


Fig. 1. The position of any point P in a rigid body which is in planar motion.

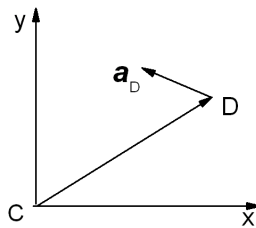


Fig. 2. Acceleration of any point D with respect to the instantaneous center of zero acceleration C.

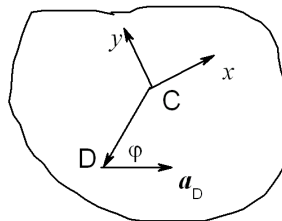


Fig. 3. Location of the instantaneous center of zero acceleration given the direction and magnitude of acceleration of any point.



A New Hybrid Optimization Method for Optimum Distribution Capacitor Planning

Ali Reza Seifi (Corresponding author)

Department of Electrical & Electronic Eng

School of Engineering, Shiraz University, Shiraz, I.R. of Iran

Tel: 98-711-230-3081 E-mail: seifi@shirazu.ac.ir

Abstract

This work presents a new algorithm based on a combination of fuzzy (FUZ), Dynamic Programming (DP), and Genetic Algorithm (GA) approach for capacitor allocation in distribution feeders. The problem formulation considers two distinct objectives related to total cost of power loss and total cost of capacitors including the purchase and installation costs. The novel formulation is a multi-objective and non-differentiable optimization problem. The proposed method of this article uses fuzzy reasoning for siting of capacitors in radial distribution feeders, DP for sizing and finally GA for finding the optimum shape of membership functions which are used in fuzzy reasoning stage. The proposed method has been implemented in a software package and its effectiveness has been verified through a 9-bus radial distribution feeder for the sake of conclusions supports. A comparison has been done among the proposed method of this paper and similar methods in other research works that shows the effectiveness of the proposed method of this paper for solving optimum capacitor planning problem.

Keywords: Capacitor planning, Fuzzy logic method, Genetic Algorithm, Dynamic programming, Radial Distribution feeder

1. INTRODUCTION

The installation of shunt capacitors on radial distribution feeders is essential for many reasons. Some of these reasons are power flow control, improving system stability, power factor correction, voltage profile management, and losses minimization.

Capacitor planning must determine the optimal site and size of capacitors to be installed on the buses of a radial distribution system. Many approaches have been proposed to solve the capacitor planning problem. For instance, (M.E. Baran, and F.F. Wu, 1989) formulated the problem as a mixed integer programming problem that incorporated power flows and voltage constraints. The problem was decomposed into a master problem and a slave problem to determine the siting of the capacitors (finding suitable buses for installing capacitor banks), and the types as well as size of the capacitors placed on the system. References 0 (M. Chis, M.M.A. Salama, and S. Jayaran, 1997) proposed heuristic approaches to identify the sensitive nodes by the levels of effect on the system losses. Reference (M.Y. Cho, and Y.W.1997) adopted an equivalent circuit of a lateral branch to simplify the distribution loss analysis, which obtained the capacitor operational strategies according to the reactive load duration curve and sensitivity index. Moreover, optimal capacitor planning based on the fuzzy logic algorithm was implemented to present the imprecise nature of its parameters or solutions in practical distribution systems 0(H. N. Ng, and M.M.A), 0(C.T. Su, and C.C. Tsai, 1996),(K.H. Abdul-Rahman, and S.M. Shahidepour, 1993). Several investigations have recently applied artificial intelligence (AI) techniques to resolve the optimal capacitor planning problem due to the growing popularity of AI. Reference (H. D. Chiang, J. C. Wang, and O. Cockings, 1990) presented a solution methodology based on a simulated annealing (SA) technique, then implemented the solution methodology in a software package and tested it on a real distribution system with 69 buses. Reference 0(H. D. Chiang, J. C. Wang, and O. Cockings, 1990) applied the tabu search technique to determine the optimal capacitor planning in Chiang et al's (H. D. Chiang, J. C. Wang, and O. Cockings, 1990) distribution system, and compared the results of the TS with the SA. In (V. Ajjarapu, and Z. Albanna, 1991) and (S. Sundharajan, and A. Pahwa, 1994), genetic algorithms (GA) were implemented to obtain the optimal selection of capacitors, but the objective function only considered the capacitor cost and power losses without involving operation constraints.

The capacitor planning problem is formulated as a multiple objective problem. The formulation proposed herein considers two distinct objectives related to (1) total cost of active power loss; (2) total cost of capacitors including the purchase and installation costs; and also considers (1) load flow restrictions; (2) security and operational constraints

such as loading of feeders and voltage profile; (3) maximum reactive compensation as practical constraints of the problem.

Moreover, a combination of FUZ–DP approaches along with GA solves the constrained and multiple objective problems.

The rest of this article is organized as follows: Section II describes a novel formulation of the capacitor planning problem. A solution algorithm based on the combination FUZ-DP-GA method for the multi-objective problems is developed in section III. Section IV demonstrates the effectiveness of the solution algorithm on a distribution case study. Conclusions are finally made in section V.

2. MATHEMATICAL MODEL OF THE PROBLEM

The capacitor planning problem for radial distribution feeders can be formulated as follows:

$$\text{Minimise } \{ (K_p \times (\sum_{i=0}^{N-1} P_{loss(i,i+1)}) + (\sum_{i=1}^{N_c} (C^{Q_{inst}} + C^{Q_{pwc}}))) \} \tag{1}$$

Such that:

$$P_{gi} - P_{di} - V_i \sum_{j=1}^N V_j Y_{ij} \cos(\delta_i - \delta_j - \theta_{ij}) = 0 \tag{2}$$

$$Q_{gi} - Q_{di} - V_i \sum_{j=1}^N V_j Y_{ij} \sin(\delta_i - \delta_j - \theta_{ij}) = 0 \tag{3}$$

$$V_i^{\min} \leq V_i \leq V_i^{\max} \tag{4}$$

$$P_{ij}^{\min} \leq P_{ij} \leq P_{ij}^{\max} \tag{5}$$

$$Q_C^{Total} \leq Q_L^{Total} \tag{6}$$

Where:

K_p , Cost per power loss, \$/kW/year

N , Total Number of buses in radial distribution network

$P_{loss(i,i+1)}$, Active power loss of (i,i+1) branch

N_c , Total number of capacitors

$C^{Q_{inst}}$, The cost of installation of a capacitor bank of Q (Var) on bus i

$C^{Q_{pwc}}$, The cost of purchasing of a capacitor bank of Q (Var) for bus i

P_{gi}, Q_{gi} , Active and reactive power generations at bus i.

P_{di}, Q_{di} , Active and reactive power load at bus i.

V 's, δ 's, System bus voltages magnitudes and phase angles.

Y_{ij}, θ_{ij} , Bus admittance matrix elements

Q_C^{Total} , Total connected Var by capacitor banks to radial distribution network

Q_L^{Total} , Total Var of connected loads in radial distribution network

The objective function considered herein, equation 1, consists of two terms. The first term, i.e. $(K_p \times (\sum_{i=0}^{N-1} P_{loss(i,i+1)})$, denotes the cost of power loss obtained by summing up the power losses of different branches, the second term, includes the total cost of capacitors, i.e. the purchase and installation costs.

Regarding the constraints, equations (2) and (3) point to well-known load flow restrictions, while security and operational constraints such as voltage profile and loading of feeders have been formulated in inequalities of (4) and (5). As a general rule, for reactive-power compensation, the maximum capacitor size should not exceed the connected reactive load. This results in a limited number of available capacitor sizes for installing on radial distribution networks. This concept has been formulated by equation (6) in the set of constraints of introduced objective function.

- Fuzzy Logic Modeling

The fuzzy set, which is a generalization of the conventional crisp set, extends the values of set membership from values in {0, 1} to the unit interval [0, 1]. A fuzzy set can be defined mathematically by assigning a value to each possible element of membership in the set. The application of fuzzy set theory in power system engineering has been

investigated by many researchers (H. Chin, and W. Lin, 1994)(C. Su and C. Tsai, 1996)(H. N. Ng, M. M. A. Salama, and A. Y. Chikhani, 1996)(H. N. Ng and M. M. A. Salama, 1995)(M. E. El-Hawary, 1998)(H. N. Ng, M. M. A. Salama, and A.Y. Chikhani, 2000)(R. E. Bellman and L. A. Zadeh, 1970)(H.-J. Zimmermann, 1990). Generally, sitting of capacitor banks (finding suitable buses for installing capacitor banks) is one of the problems in distribution capacitor planning due to a large number of customers available in distribution networks. This paper proposes a new fuzzy logic reasoning method for sitting. The paper assigns membership functions of equation 7 to bus voltages and membership functions in equation 8 to line losses.

$$\mu_v(i) = e^{-w_v \left[\frac{V(i)-1}{V_{\max}-V_{\min}} \right]^2} \quad (7)$$

$$\mu_p(i) = e^{-\frac{w_p \cdot L(i)}{P_{T, Loss}}} \quad (8)$$

Where:

- $\mu_v(i)$: Exponential membership functions of voltage for bus i
- W_v : Weighting factor of voltage membership function
- $V(i)$: Voltage of bus i
- V_{\max} : Maximum permitted voltage
- V_{\min} : Minimum permitted voltage
- $\mu_p(i)$: Exponential membership functions of real losses
- W_p : Weighting factor of real loss membership function
- $L(i)$: Real loss for line between i. and i+1 buses
- $P_{T, loss}$: Total power loss.

The fuzzy decision membership function is the intersection, thus

$$\mu_s(i) = \min\{\mu_p(i), \mu_v(i)\} \quad (9)$$

The solution algorithm can be summarized as follows.

By solving load flow equations, one can find the membership functions of voltage and losses, decide for the fuzzy sets of voltage and power loss, and determine the if-then rules and the fuzzy inference scheme. In this stage, we should identify the bus with the lowest membership function μ_s as the candidate node for installing the capacitor bank.

In section III, the proposed method has been explained and, subsequently, the paper has applied the proposed method to a case study as the proof of effectiveness of the methodology.

3. PROPOSED HYBRID OPTIMIZATION METHOD FOR CAPACITOR PLANNING OF A RADIAL DISTRIBUTION NETWORK (FUZ-DP-GA)

According to the principle of optimality that was introduced by Bellman and Dreyfus (R. E. Bellman, S. E. Dreyfus, 1962), a policy is optimal if, at a stated stage, whatever the preceding decisions may have been, the decisions still to be taken constitute an optimal policy when the result of the previous decisions is included. Using DP, this paper finds the optimal size of capacitors on each bus in radial distribution networks.

The solution algorithm for optimal distribution capacitor planning considering constant load condition, using a combined FUZ-DP approach is summarized as follows,

Step1. Enter network data

Step2. Determine the membership functions by setting w_v and w_p

Step3. Run the power flow equations and finding each bus voltage and each line loss.

Step4. Identify bus with the lowest membership function μ_s as the candidate node for installing the capacitor bank (sitting)

Step5. Finding the optimum size of capacitor in the candidate place determined in step4 according to the objective function and DP approach (sizing)

Step6. Check the stop criterion. If all bus voltages and line currents are in the range, go to the next step. Otherwise, go to the step 3

Step7. Find the objective function of the whole distribution network with installed capacitors for the w_v and w_p parameters

By running steps 1 through 7 in a radial distribution network, the objective value (optimal site and size of capacitors) can be found for specific weighting factors of voltage and real loss exponential membership function (wv and wp).

On the other hand, by running a sensitivity analysis between the membership function parameters, wv and wp, and the value of objective function, it becomes clear that the shape of membership functions (wv and wp) have a direct effect on the objective value. So finding the best values of wv and wp for having the minimum value of the objective function is of great interest.

The Genetic Algorithm (GA), as a meta heuristic optimization methodology, is proposed to find the optimal membership functions. The main idea of GA is that “the best member of a population has the highest probability for survival and reproduction” (A. S. Chung, and F. Wu, 2000)(J. H. Holland, 1992). Tools applying GA are reported in the literature to be capable of finding a global optimum for mathematical problems having a multiplicity of local optimum and hard non-convexities. GA has also proved powerful in the optimization process in various power engineering applications e.g., (D. E. Goldberg, 1989)(A S. Chung, and F. Wu, 2000)(T. Yokota, M. Gen, and Y. X. Li, 1996). The genetic optimization algorithm, as applied to find optimal membership functions, observes the following steps:

Decision variables are two variables namely wv and wp. A typical chromosome is shown in Figure 1.

The GA needs the definition of an initial population. The well known operators for genetic algorithm, namely, crossover and mutation, as explained in the literature on genetic algorithm theory (J. H. Holland, 1992), (D. E. Goldberg, 1989)(A S. Chung, and F. Wu, 2000) and (T. Yokota, M. Gen, and Y. X. Li, 1996) are used in this paper, too.

In this step, the original population grows through the addition of new members, which are obtained from the crossover and mutation steps. This enlarged population is ranked with a fitness function defined as follows:

$$Fitness(w_i) = \begin{cases} ObjVal(w_i) & \text{If } w_i \text{ meets all constraints} \\ B & \text{If } w_i \text{ doesnot meet all constraints} \end{cases} \quad (10)$$

w_i: A sample chromosome

B: A large number

Obj Val (w_i): Object value for chromosome w_i

The proposed hybrid optimization method of this paper for optimum distribution capacitor planning is depicted in figure 2. As it is clear from figure 2, the objective function of distribution capacitor planning problem is minimized in two steps ,namely, by FUZ-DP approach in installing capacitor banks and by GA method in finding wv and wp parameters. This feature is one of the unique powerful aspects of the proposed method for radial distribution network planning which leads to very promising results.

In the next section, we apply the hybrid optimization method to a 9-bus radial distribution networks as a proof for the proposed methodology.

4. CASE STUDY

The 9-bus radial distribution feeder of (J. J. Grainger and S. H. Lee, 1981) is taken as the test feeder. The rated voltage is 23 kV. The system is shown in Figure 3.

For the test feeder, yearly cost of losses is selected to be U.S.\$ 168/kW, and the voltage limits are 0.9 p.u and 1.1 p.u. The total reactive load of the system is 4186kVar that leads to 27 practical combinations of standard capacitor banks available in (S. F. Mekhamer, S. A. Soliman, M. A. Moustafa, and M. E. El-Hawary, 2003).

Applying the load flow program on this feeder before compensation, the cost function and the total power losses are U.S.\$ 131 675 and 783.8 kW, respectively. The maximum and minimum bus voltage magnitudes were 0.9929 and 0.8375 p.u., respectively, where the voltage of the substation (bus number 0) is assumed to be 1 p.u. The results of capacitor planning after applying the hybrid optimization method are collected in Table 1. The hybrid optimization technique (our method in Table 1), which is a new idea and powerful methodology, gives the best cost and loss reductions with a promising voltage profile among all other methodologies proposed by (S. F. Mekhamer, S. A. Soliman, M. A. Moustafa, and M. E. El-Hawary, 2003), (J. J. Grainger and S. H. Lee, 1981),(M. Chis, M. M. A. Salama, and S. Jayaram, 1997)(T. S. A.Salama, A. Y. Chikhani, and R.Hackam, 1994)(C. Su and C. Tsai, 1996)(H. C. Chin and W. M. Lin, 1994). Also, the results of loss reduction of our method are better than those of the heuristic methods of (M. Chis, M. M. A. Salama, and S. Jayaram, 1997) and (T. S. A.Salama, A. Y. Chikhani, and R.Hackam, 1994), and the analytical method of (M. M. A. Salama and A. Y. Chikhani, 1993), and even better than that of the fuzzy expert system (FES) presented in 0, with the same advantage of compromising between the voltage and losses importance.

5. CONCLUSION

This article presents a new combined optimization method for optimum capacitor planning problem. The proposed method uses fuzzy approach for siting of capacitors, DP for sizing and, finally GA for finding the optimum shape of membership functions of bus voltages and line losses.

The method developed herein is tested on 9-bus distribution system and the results have been compared with similar research works. The comparison shows the effectiveness of the proposed method, considering both the investment and the performance improvement of the distribution network

References

- A. S. Chung, and F. Wu, (2000). "An Extensile Genetic Algorithm Framework for Problem Solving in a Common Environment," *IEEE Trans. On power systems*, vol.15, no.1, Feb.2000.
- A. S. Chung, and F. Wu, (2000). "An extensile genetic algorithm framework for problem solving in a common environment," *IEEE Trans. On power systems*, vol.15, no.1, Feb.2000.
- C. Su and C. Tsai, (1996). "A new fuzzy-reasoning approach to optimum capacitor allocation for primary distribution systems," in *Proc. IEEE Int. Conf. Ind. Technol.*, pp. 237–241, 1996.
- C. Su and C. Tsai, (1996). "A New Fuzzy-reasoning Approach to Optimum Capacitor Allocation for Primary Distribution Systems." in *Proc. IEEE Int. Conf. Ind. Technol.*, pp.237-241, 1996.
- C.T. Su, and C.C. Tsai, (1996). "A new fuzzy-reasoning approach to optimum capacitor allocation for primary distribution systems," in *Proceedings of the IEEE international conference on industrial technology*, pp. 237-41, 1996.
- D. E. Goldberg, (1989). *Genetic Algorithms in Search, Optimization, and Machine Learning*, Addison Wesley, 1989.
- H. C. Chin and W. M. Lin, (1994). "Capacitor Placements for Distribution Systems with Fuzzy Algorithm", in *Proceedings of 1994 IEEE Region 10's Ninth Annual International Conference*, 94CH3417-3, Vol.2, pp.1025- 1029.
- H. Chin, and W. Lin, (1994). "Capacitor placement for distribution systems with fuzzy algorithm," in *Proc. 1994 IEEE Region 10's Ninth Annu. Int. Conf.*, vol. 2, pp. 1025–1029.
- H. D. Chiang, J. C. Wang, and O. Cockings, (1990). "Optimal capacitor placements in distribution systems: part 1: a new formulation and the overall problem," *IEEE Trans. Power Delivery*, Vol. 5(2), pp. 634-42,1990.
- H. N. Ng and M. M. A. Salama, (1995). "Fuzzy optimal capacitor sizing and placement," in *Proc. Canadian Conf. Elect. Comput. Eng.*, vol. 2, pp. 680–683, 1995.
- H. N. Ng, and M.M.A, "Salama. Fuzzy optimal capacitor sizing and placement," in *Proceedings of the Canadian conference on electrical and computer engineering*; pp. 684-687
- H. N. Ng, M. M. A. Salama, and A. Y. Chikhani, (1996). "Capacitor placement in distribution systems using fuzzy technique," in *Proc. Canadian Conf. Elect. Comput. Eng.*, vol. 2, pp. 790–793, 1996.
- H. N. Ng, M. M. A. Salama, and A.Y. Chikhani, (2000). "Capacitor allocation by approximate reasoning: Fuzzy capacitor placement," *IEEE Trans. Power Delivery*, vol. 15, pp. 393–398, Jan. 2000.
- H. N. Ng, M. M. A. Salama, and A.Y. (2000). Chikhani, "Capacitor allocation by approximate reasoning: Fuzzy capacitor placement," *IEEE Trans. Power Delivery*, vol. 15, pp. 393–398, Jan. 2000.
- H.-J. Zimmermann, (1990). *Fuzzy Set Theory and its Application*, 2nd ed. Norwell, MA: Kluwer, ch. 12, pp. 241–272, 1990.
- H.T. Yang, Y.C. Huang, C.L. Huang, (1995). "Solution to capacitor placement problem in radial distribution system using tabu search method," in *Proceedings of the international conference on energy management and power delivery*; pp. 388-93, 1995.
- J. H. Holland, (1992). "Genetic Algorithm," *Scientific American*, Vol. 267, No. 1, , pp.66-73, July 1992.
- J. J. Grainger and S. H. Lee, (1981). "Optimal size and location of shunt capacitor for reduction of losses in distribution feeders," *IEEE Trans. Power App. Syst.*, vol. PAS-100, pp. 1105–1118, Mar. 1981.
- K.H. Abdul-Rahman, and S.M. Shahidepour, (1993). "A fuzzy-based optimal reactive power control," *IEEE Trans. Power System*, Vol. 8(2): pp. 662-70, 1993.
- M. Chis , M.M.A. Salama, and S. Jayaran, (1997). " capacitor placement in distribution systems using heuristic search strategies," in *Proc. 1997 IEE Generation, Transmission and Distribution Conf.*, pp. 225-230.
- M. Chis, M. M. A. Salama, and S. Jayaram, (1997). "Capacitor Placement in Distribution Systems using Heuristic Search Strategies," in *Proc. Inst. Elect.Eng.*, vol.144, No.3, pp.225-230, 1997.
- M. E. El-Hawary, (1998). *Electric Power Applications of Fuzzy Systems*. Piscataway, NJ: IEEE Press, 1998.

M. M. A. Salama and A. Y. Chikhani, (1993). "A simplified network approach to the VAr control problem for radial distribution systems," *IEEE Trans. Power Delivery*, vol. 8, pp. 1529–1535, July 1993.

M.E. Baran, and F.F. Wu, (1989). "optimal capacitor placement in distribution systems," *IEEE Trans. Power Delivery*, vol. 4(1), pp. 725-734, 1989.

M.Y. Cho, and Y.W., (1997). "Chen Fixed/switched type shunt capacitor planning of distribution systems by considering customer load patterns and simplified feeder model," in *Proc. 1997 IEE Generation, Transmission and Distribution Conf.*, pp. 533-540.

R. E. Bellman and L. A. Zadeh, (1970). "Decision-making in a fuzzy environment," *Manage. Sci.*, vol. 17, no. 4, pp. 141–164, Dec. 1970.

R. E. Bellmen, S. E. Dreyfus, (1962). *applied Dynamic programming*, Princeton University press, Princeton, N.J., 1962.

S. F. Mekhamer, S. A. Soliman, M. A. Moustafa, and M. E. El-Hawary, (2003). "Application of Fuzzy Logic for Reactive-Power Compensation of Radial Distribution Feeders", *IEEE Transaction on Power Systems*, Vol.18, No.1, February 2003.

S. Sundharajan, and A. Pahwa, (1994). "optimal selection of capacitors for radial distribution systems using a genetic algorithm," *IEEE Trans. Power System*, Vol. 9(3), pp. 1499-507.1994.

T. S. A.Salama, A. Y. Chikhani, and R.Hackam, (1994). "A new technique for loss reduction using compensating capacitors applied to distribution systems with varying load condition," *IEEE Trans. On Power Delivery*, vol.9, pp.819-827, Apr.1994.

T. Yokota, M. Gen, and Y. X. Li, (1996). "Genetic Algorithm for Non-linear Mixed Integer Programming Problems and its Applications," *computers ind. Eng.*, Vol.30, No.4 ,pp.905-917, 1996.

T.S. Abdel-Salam, A. Y. Chikhani, and R. Hackam, (1994). "A new technique for loss reducing using compensating capacitors applied to distribution systems with varying load condition," *IEEE Trans. Power Delivery*, Vol.9(2), pp. 819-827, 1994

V. Ajarapu, and Z. Albanna, (1991). "Application of genetic based algorithms to optimal capacitor placement," in *Proceedings of the first international forum on applications of neural networks to power systems*; pp. 251-5,1991.

Table 1. Results for All Methods Applied to the 9-Bus Feeder Including Original Data and Our Solution Results

Bus No.	No Q _C (kVar) Placed	Q _C Using Method 1 of [26]	Q _C Using Method 2 of [26]	Q _C Using Modified Method 1 of [26]	Q _C Using Modified Method 2 of [26]	Q _C Using Method 4 of [26]	Q _C Using Method 5 of [26]	Q _C Using Method 3 of [26]	Q _C Using Method [26]	Q _C Using Our Method
1										
2								3300	3600	3600
3			1050	2400	3600	3300	2850	3900		4050
4		2100	1050	900		1800	2100		4050	450
5		2500	1950	2100	2100	1050	1050	1200	1650	1200
6										
7										
8									600	150
9		900	900	900	900	900	900	900		600
Real Loss (kW)	783.8	707	705	697	699	692	691.6	689	686	681.28
\$ Cost	131675	119736	119420	118296	118562	117571	117479	117330	117095	116320
Min V (p.u.)	0.8375	0.9000	0.9029	0.9005	0.9007	0.90004	0.9000	0.9006	0.9003	0.90014
Max V (p.u.)	1.0000	1.0000	1.0000	1.000	1.004	1.0012	1.001	1.006	1.007	1.007



Figure1. Sample chromosome

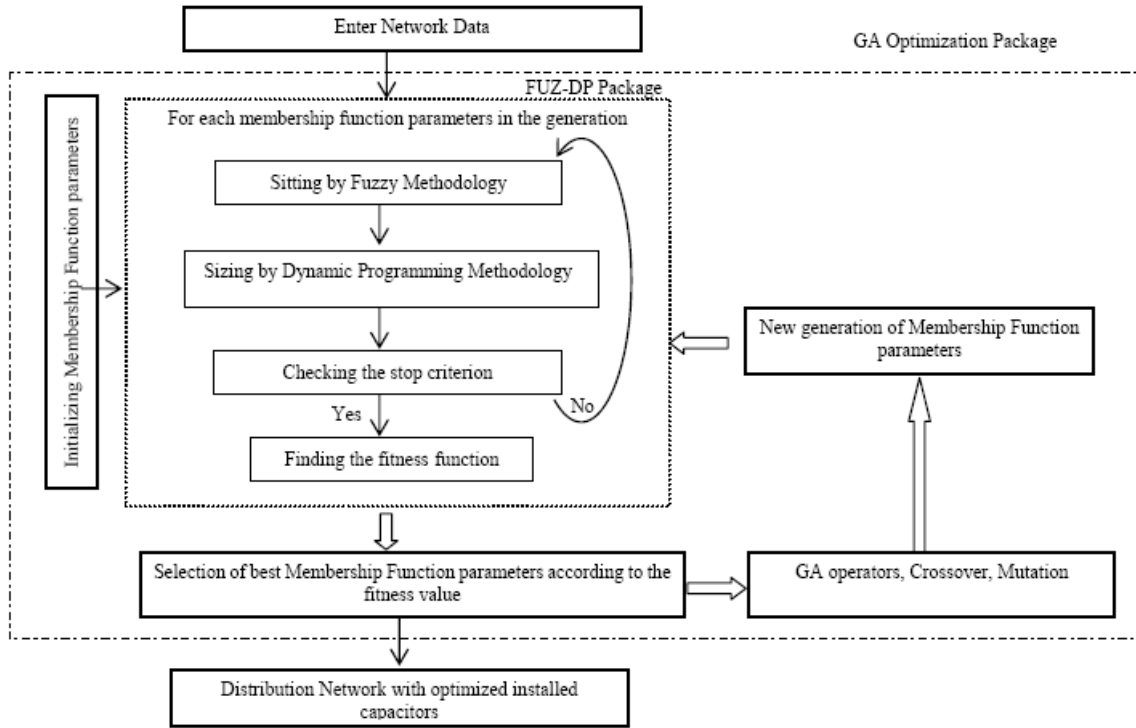


Figure 2. Proposed Hybrid Optimization Method

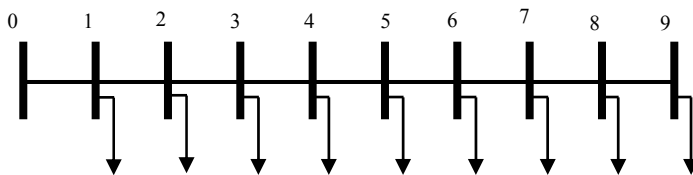


Figure 3. Nine-bus test feeders



Development of TEC System for Commercial Cooling Applications

Wael Salah, Soib Taib & Anwar Al-Mofleh

School of Electrical and Electronic Engineering

Universiti Sains Malaysia, Engineering Campus

14300 Nibong Tebal, Seberang Perai Selatan, Pulau Pinang, Malaysia

Tel: 60-4-5995-999 ext. 6073, Fax: 60-4-594-1023 E-mail: wael_sal@eng.usm.my

Abstract

This paper represents the possibility of using the TEC-Thermo Electric Coolers in cooling applications. Such application with small area away connected is possible with the use solar energy as power source. Factors affecting the performance of TE will be discussed also. The effect of Heat Sink Extender (HSE) for TEC assembling will be considered. TEC performance is tested for different modules. The assembling for best performance of TEC and the supply requirements using PV as a power source is presented for potential commercialization.

Keywords: TEC, Cooling, TE performance, Heat Sink Extender, Photovoltaic

1. Introduction

A thermoelectric (TE) cooler, is a semiconductor-based electronic component that functions as a small heat pump. By applying a low-voltage DC power source to a TE module, heat will be moved through the module from one side to the other. One module face will be cooled while the opposite face simultaneously is heated. Thermoelectric modules as shown in Figure 1 are solid-state heat pumps that operate on the Peltier effect.

The widely availability of Thermoelectric cooling (TEC) modules, making them a potential equipments to be apply for the thermal run away in electronics circuits. The TEC modules, which have a maximum rated operating temperature of 200 °C makes thermoelectric cooling a possible option in the thermal management of high temperature electronic packaging.

1.1 Advantages of a thermoelectric unit over a compressor

Thermoelectric modules have no moving parts and do not require the use of chlorofluorocarbons. Therefore they are inherently reliable and are virtually maintenance free. They can be operated in any orientation and are ideal for cooling devices that may be sensitive to mechanical vibration. Their compact size also makes them ideal for applications that are size or weight limited where even the smallest compressor would have excess capacity. Their ability to heat and cool lends them to applications where both heating and cooling is necessary or where precise temperature control is critical.

1.2 TEC Operation

Electrons can travel freely in the copper conductors but not so freely in the semiconductor. As the electrons leave the copper and enter the hot-side of the p-type, they must fill a "hole" in order to move through the p-type. When the electrons fill a hole, they drop down to a lower energy level and release heat in the process. Essentially the holes in the p-type are moving from the cold side to the hot side. Then, as the electrons move from the p-type into the copper conductor on the cold side, the electrons are bumped back to a higher energy level and absorb heat in the process. Next, the electrons move freely through the copper until they reach the cold side of the n-type semiconductor. The electrons bump up an energy level when they move into the n-type in order to move through the semiconductor then heat is absorbed, then the electrons leave the hot-side of the n-type and move freely in the copper and drop down to a lower energy level and release heat in the process.

1.3 TEC reliability

Thermoelectric systems are highly reliable provided they are installed and used in an appropriate manner. The specific reliability of thermoelectric coolers tends to be difficult to define because failure rates are highly dependent upon the particular application. Thermoelectric modules that are at steady state (constant power, heat load, temperature, etc.) can have mean time between failures (MTBFs) in excess of 200,000 hours.

1.4 Cool by nature

Environmental friendly cooling could be obtained by the use of TEC because there is no chlorofluorocarbons (CFCs) and also no need for refills. Once the thermoelectric cooling is implemented then there will be no worries that the cooling system has a negative impact on the environment as compared to the traditional cooling system.

1.5 TEC Installation

The two wires attached at the side of TEC is known as hot side if the red/black wire is connected to positive voltage/ground respectively. Usually, the red wire is positive and the black wire is ground. The hot side and cold side of TEC can be swapped if the red/black wire polarity is swapped.

2. TEC Cooling Design

2.1 TEC Proper fit consideration

The proper fit between the heat side of TEC and the heat sink affect the performance of TEC, good thermal conduction will lead to better performance, although good thermal isolation between heat and cold side will give better performance. Figure 2 shows a single TEC module with the heat side attached to a heat sink and the cool side is free to air. Figure 3 shows the temperature measured direct form TEC cold side. This shows two states of measurements i.e. the data measured good thermal conduction of heat sink and hot side of TEC and the other one with bad thermal conduction. The proper fit of TEC will improve its performance, especially when heat sink compound is added.

2.2 Thermal isolation

Selecting a proper heat sink is very important when a thermoelectric cooling system is designed. Usually, temperature of a heat sink rises 10°C above the ambient temperature after TEC is applied with a proper voltage and the cold side of TEC is without any heat load. The different TEC has a different operating voltage. Heat pump power is proportional to voltage power. The bigger the heat sink on hot side of TEC the better the performance of TEC.

For the best performance to be achieved for the TEC module, a good thermal isolation between hot and cold side is important since the distance between the two sides is so critical. To overcome such problem the extension of heat sink could be used for several purposes. One is to increase the distance from the heat sink plate to the cold sink plate. This allows for thicker insulation and longer assembly bolts. As a result, heat conducting from the heat sink plate back to the cold sink plate is reduced. Another purpose involves temperature control. In certain control schemes, the TE system operates until a thermostat trips off.

With a Heat Sink Extender in use, there will be a larger thermal resistance exist between the heated and cold sink. As a result, the cold space does not heat back up as quickly as compared with a systems that do not employ HSEs. Figure 4 shows the TEC module attached to a heat sink with extender. Probably the most important use of an extender is when the extender serves as a thermal junction. In many applications, a TE system is used to cool an insulated box. The cold sink and heat sink are separated by the thickness of the box's insulation. The extender, therefore, is used to thermally join the TE module to either the cold sink or the heat sink.

Table 1 shows the data taken using single module with HSE. A comparison with the above test without HSE shows that the temperature at cold side it higher; i.e. less cool but still convenient. On the other hand less heat at the hot side of the TEC module that attached to HSE. As shown in Table 1 the temperature at cold side is higher compared to without HSE. But the temperature at the cooled side also is lower referring to tests without HSE.

3. Cooling Applications

The precious section shows that the effect of good heat isolation is quite sensitive to the TEC performance. The small size and simplicity make TE the best choice to be applied for cooling application. One of the main application that can be considered is the cooling of away connected electronics, such as in the telecommunication cabinets. This cooling arrangement can be easily supplied from a PV panel with a DC-DC converter. The input power to the DC-DC converter will be supplied from an input solar panel of 72W power rating. The use of PV as a power source for the converter make it reliable for outdoor cooling applications.

Figure 5 shows a developed prototype for TEC cooling. This prototype uses 4 TECs of 15x15x3 mm size that attached to the four sides of the cooling box. This prototype is tested using the developed converter and draw a current of 2 to 5 amps. And the measured outlet temperature is 17 to 15 °C referring to ambient temperature of around 23 to 21 °C.

Figure 6 shows the TEC modules attached to heat sink (30x17x4 cm), then the spaces have to be filled by Teflon thin sheets. The cold side of TEC modules are attached to an aluminum sheet. Then the sheet is attached to testing a cabinet. The experiment is conducted to test the TEC function as shown in Figure 7. The TEC was connected in parallel combination and it's required about 12A current , which provided by a DC converter.

A sample of solar fridge prototype unit is developed using four TEC as shown in Figure 8. The prototype with a 12 in x 8 in x 6 dimension capable to function in both cooling and heating operation. The unit takes about 30 minutes to reach

the minimum temperature of 18 °C within the compartment. This invention uses sunlight which is captured by an array of solar panel of 70W. The coling is being preseved by a quality insulation, thus food and drinks cooled quickly even at high outside temperature.

The operation is controlled manually by switch which is located at the back of the unit.

Conclusion

The TEC cooling technique is found to be free of some problems attached to traditional cooling techniques such as noise, size and vibration. In addition it has no side effect on the environment with zero emission of CO₂ gas. The paper had discussed the use of the TEC-Thermo Electric Coolers in the off-grid mode where solar energy is used as power source. The TE performance found to be affected by many factors such as the usage of HSE and TEC proper fit assembling. The prototype TEC fridge has the potential for commercialization.

References

- C. Lertsatitthanakorn (2003), Cooling Performance of Thermoelectric Water Cooler, *Naresuan University Journal*: 11(2), pp: 1-9.
- Jianzhong, Z., Tiemin, W., Xueming, L., Guanghui, T. (1998), Application of the thermoelectric cooler in the seventeenth Chinese retrievable satellite, *Proceedings of the 5th International Conference on Solid-State and Integrated Circuit Technology*, pp: 865 - 868.
- MAGALAND TECHNOLOGY, INC., (2007). Thermoelectric Cooling Modules Application Note. Available: www.magaland.com (August, 2007).
- Moores, K.A., Joshi, Y.K., Miller, G. (1999). Performance assessment of thermoelectric coolers for use in high temperature electronics applications, *Eighteenth International Conference on Thermoelectrics*, pp:31 – 34.
- Optimizing TEC Drive Current Application Note (2006). Available: www.ilxlightwave.com.
- Optimizing TEC Drive Current Application Note (2006). Available: www.ilxlightwave.com.
- Paul G. Lau, Todd M. Ritzer and Richard J. Buist, (2005). Thermodynamic Optimization of Heat/Cold Sink Extenders in Thermoelectric Cooling Assemblies. TE Technology, Inc., Michigan 49686 USA.
- Supercool AB (2005). Available: www.supercool.com.
- Supercool AB. (2007). Available: www.supercool.com (Nov., 2007).
- TE Technology Inc, (2007). Available: www.tetech.com/techinfo (June, 2007).
- Thermoelectric Handbook (2006). Available: www.melcor.com (May, 2006).

Table 1. TEC with HSE

Amps	Cold side	Hot side (HSE)
0	23	23
0.5	20	24
1	18	25
1.5	15	25
2	12	26
2.5	6	27
3	1	28
3.5	-3	30

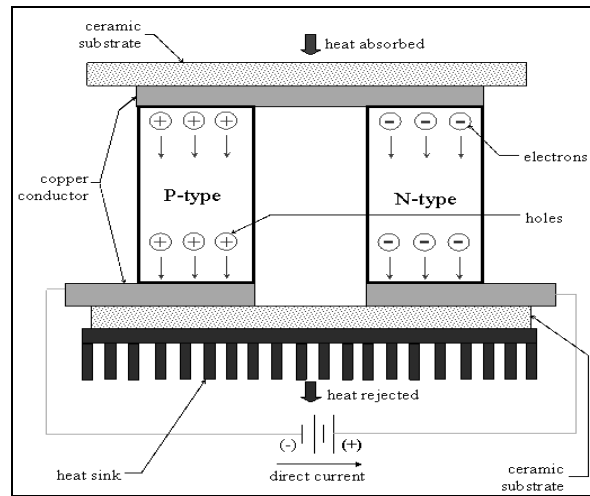


Figure 1. TEC Module

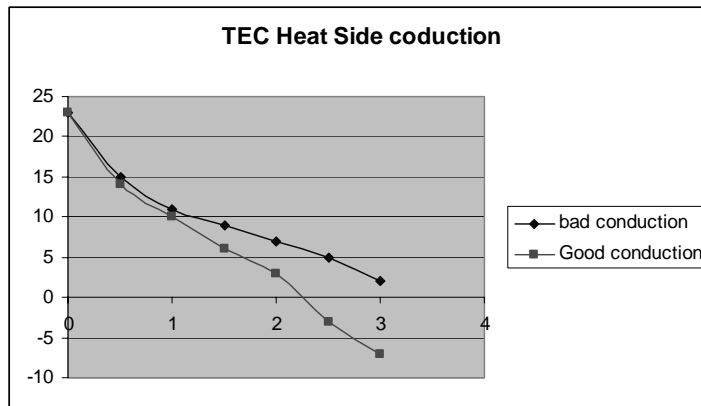


Figure 2. TEC direct measured temperature at cold side



Figure 3. TEC module with the heat sink

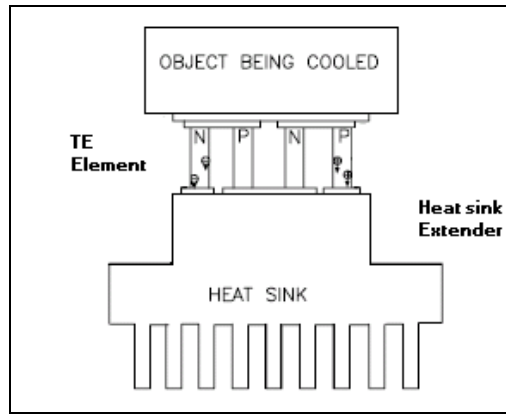


Figure 4. Heat sink with extender

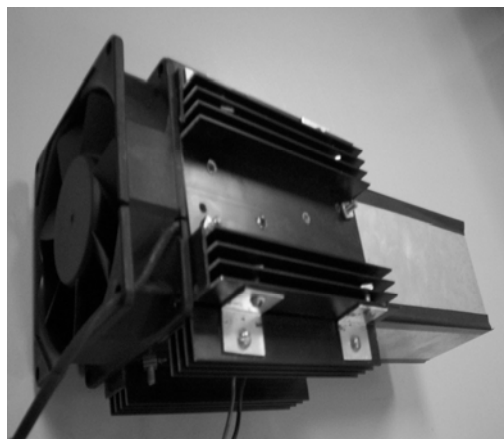


Figure 5. A developed TEC cooling prototype

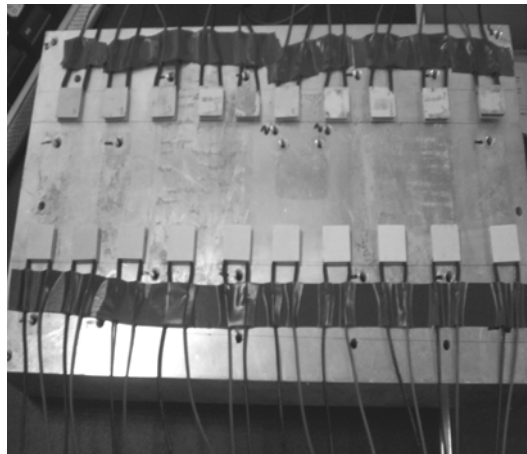


Figure 6. TEC modules attached to heat sink

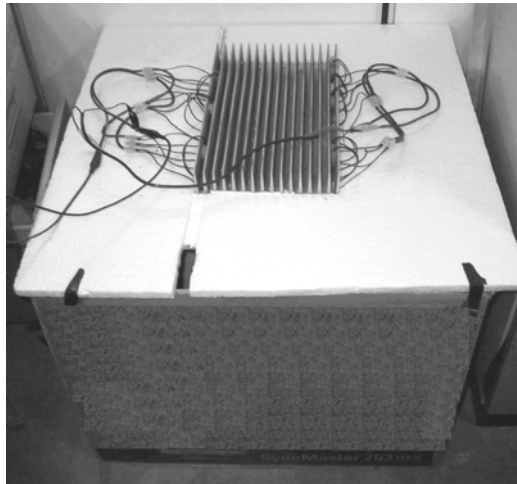


Figure 7. TEC modules attached to test cabinet



Figure 8. Mini solar and heater



The Research of Inverter Welding Power Source Based on DSP for Self-shielded Flux-cored Wire

Xiao Li, Liangyu Li, Tianqi Wang & Xu Yang

Tianjin Key Laboratory of Advanced Mechatronics Equipment Technology

Tianjin Polytechnic University

Tianjin, 300160, China

E-mail: lixiao0412@hotmail.com

Abstract

Based on DSP (Digital Signal Process), a inverter welding power source has been introduced. By designing of the software of system and circuitry of wire feeder, constant-voltage external characteristic for self-shielded flux-core wire and stable wire feed speed are acquired. To optimize the parameter, lots of tests had been done. To apply to pipe welding, the weld process is stable and credible. The facility is easy to use and multifunctional.

Keywords: Pipeline welding, DSP, Self-shielded flux-core wire welding

1. Introduction

As a special logistic facility, pipeline has extended every aspects of our life. In large-scale pipeline construction, the traditional electrode welding technology could not match the process of project, which has been replaced by semiautomatic self-shielded flux-cored welding. The process used to effectively reduce the cost and time limit for a project, raising productivity. So the prospect to apply is wide. This problem has been studied previously (Liu, 2006, p.34-35). The semiautomatic self-shielded flux-cored wire for filler and cosmetic welding is one of the common methods in pipeline project. The welding equipment is universal which is used in both semiautomatic welding and shielded metal arc welding. Thus the project needs fewer welding machines and techniques outfits, which reduce the total equipment cost. As a result, by way of a advanced construct technology, the semiautomatic self-shielded flux-cored wire welding is widely popularized in long pipe welding especially in big caliber long tube. This problem has been studied previously (Wang, 2007, p.23-24). Therefore a inverter welding power source based on DSP for self-shielded flux-cored wire has been devised, which can match the Self-shielded Flux-cored welding technology.

2. Design of Integrated Structural

The integrated structural design is shown in figure 1. First, the 380V three-phase alternating current is alternated by commutating and filtering into 540V direct current. Then in the control of the control circuit, to use IGBT DC transition (the inversion) 20 KHz exchange of high frequency power. The transformer and 2nd rectification is available for welding of low voltage DC.

In designing of the integrated structural of inverter welding power source system controlled by DSP for Self-shielded Flux-cored Wire, We should first consider software and hardware of rational resource allocation in order to achieve speed and flexibility of balanced. The hardware is highly responsive and reliable. And the characteristic of the software is flexible and adaptable. In this specific design, taking into account the main system circuit working at several 100 amperes, the control circuit of main circuit is constituted by the operational amplifier and PWM chip. Then it can improve the security and reliability of system.

3. Design of Control System

To adapt to the complexity of inverter welding power source, the control circuit taking PWM circuit as the core, adopt current and voltage negative feedback closed-loop control. The output current and voltage regulation is realized. And we can obtain external characteristic, the dynamic characteristic as well as the welding sequential control that meet the requirements adoption of the control circuit.

The main process is to let the feedback current and voltage signal go into DSP by signal processing circuit using a Hall sensor. Through analysis of feedback voltage and current by software, according to the system of different external characteristic, we can determine at this point the system carries on the control to the electric current or the voltage. The current and the voltage closed loop adjustment realized through PI circuit on control panel. That control the SG3526

chips to produce two groups of PWM signal that differs 180 °phase with the dead area. IGBT's turn—off time is determined by EXB841 which is a part of driving circuit. Thus it may control and regulate the output voltage and current.

We choose the TI Corporation's LF2407A DSP chip as the core chip. A/D, D/A transformation circuit, outside expand memory, SPI vision module, 3.3V-5V voltage transformation circuit and JTAG simulation port have been designed. The program could be debugging online in the computer through simulator with JTAG port. In simulation process, the outside expand ROM has high running speed and easy erased. When debugging program completely, the program should solidify in-chip FLASH. When running pattern has been set to micro-controller, the welding source power will run by itself separated from computer.

4. Design of Wire Feeding System Hardware

Negative feedback voltage and positive feedback current has been adopted in this control configuration of timing system. Armature voltage of wire-feed motor is regulated by the way of pulse width modulation (PWM). By introducing negative feedback voltage into the control system, the motor's speed could stabilize at set value. Positive feedback current is used to compensate voltage drop for armature resistance, which causes the rotational speed to be stable. The frame of feeding system is shown in figure 2.

In this system, the difference of set value and voltage feedback value with the addition of current feedback value is regarded as control signal, which were operated by operational amplifier. Control voltage signal to corresponding dutyfactor PWM signal transformation is completed by SG3525. After enhanced by driver circuit, PWM signal actuates the wire feeding machine's movements.

5. Design of Software

The static characteristic of self-shielded welding with flux-cored wire belongs to rising characteristic. Adopting constant wire-feed system, constant-voltage arc welding is selected from external characteristic, which causes arc self-regulation to be strong. And the welding parameter stability is best. Arc self-regulation means that the welding power source would reduce or increase the current when the arc is lengthened or shortened because of disturbing. Application of this static characteristic, arc restores the original arc length automatically. The sensitivity of arc self-regulation determined by $\Delta v_m / \Delta l_a$ (Δv_m --variable of melt speed, Δl_a --variable of arc length), the specific formulation is

$$\frac{\Delta v_m}{\Delta l_a} = -\frac{\alpha_m * E_c}{d^2 K_s} \quad (1)$$

Where, α_m --melting coefficient of wire, d --diameter of wire, E_c --electric field intensity, K_s --stability coefficient of external characteristic, a minus sign-- The arc length change and the melting speed's change is opposite.

Regarding constant-voltage and slowly dropping characteristic arc welding power source, the sensitivity of self-regulation arc will meet the requirement when declining slope of $\Delta v_m / \Delta l_a$ is less than 4V/100A.

5.1 Design of Constant-Voltage Characteristic

Program expressed in c language, is composed of main, initialization, collection, state judgment, display, striking arc and welded subprogram. The cellulose type welding is also a function of the welding source. Thus the welding source offers two choices of cellulose type welding and self-shielded flux-cored wire.

The feedback voltage and current in welding collected by A/D converter channel are stored in variable value before data processing. The predetermined values of voltage and current input by knob are converted from analog signals to digital signals. Here, the first step is judging which mode of welding has been selected. Secondly, if flux-core welding mode had been selected, the program would access in corresponding subroutine. The host program figure is shown in figure 3.

Here, according to feedback digital values, it can be judged whether the state is idling or arcing. If the arc was not burning, the program will call striking arc subroutine which adopts low feeding speed and heavy current. After arc burning, normal arcing program will be executed of normal feeding speed and preset voltage value.

The voltage preset is converted to simulated value with the D/A converted chip. In order to stabilize the output, the preset voltage and the feedback voltage make the adjustment through the PI controller. Then the output is used to control SG3526 chip which generates a PWM waveform, to drive IGBT. So according PI controller, the constant-voltage output keep stable. Flux-cored wire welding subroutine is illustrated in figure 4.

5.2 Anti-jamming Design of Software

Built-in watchdog timer in LF2407A DSP will overflow when the program is disordered because of disturbing. Then a reset signal generated by watchdog will restart the running program.

In order to obtain real-time data collecting and system controlling, the disturbing signal in channels must be eliminated, ensuring the reliability and rationality of the system design. The digital filtering approach is selected in the system. In

the light of analyses of the data selected, a median average filtering approach has been successfully developed, which reduces the influence of the random disturbance. Median average filtering, which has been used in both filtering pulse interference and smoothing wave, focuses on the merits of media filtering and average filtering. That is to say, it has an effect on both rapid and slow interference. The median average filtering approach may be described like this. Got rid of the max and min value in multiple date in one sampling, the arithmetic mean value of rest date is taken as reference value in one sampling cycle.

6. Experiments and Analyses

The static external characteristic of self-shielded flux-cored arc welding measured on the basis of experiment is shown in figure 5. As a result of the preset voltage and feedback regulation of PI, the voltage is stabled in preset value, to which meet the requirement of self-shielded flux-cored arc welding. The voltage may be adjusted by knob on the panel to apply to various welding conditions.

The voltage and current oscillogram traced by an oscillograph is shown in figure 6, which apply to self-shielded flux-cored wire with a diameter of 1.6 millimeters. The upside line denotes voltage, and the other current. As shown in figure 6, the voltage fluctuating steadily, ensure the welding process stable. The current is in direct proportion to feeding speed. Thus the current stability is determined by feeding speed. The current will be adjusted swiftly owing to arc self-regulation, for restoring the arc changes in length caused by interference.

7. Conclusions

- (1) A new control circuit based on DSP and feeding wire system are designed, which runs stably and securely.
- (2) Constant voltage external characteristic can be obtained by design of hardware and software, and it meet the process of self-shielded flux-cored arc welding.
- (3) Using software to control is an agile approach. Multiple functions may be obtained by modifying software only.

References

Liu,Jing, Jiang,Guoqing & Luo Qimin. (2006). Application of Flux Cored Arc Welding to Long Distance Transmission Pipeline. *Welding Technology*, 3(6), 34-35.

Wang, Wenyan, Zeng, Jiuling, Sun, Wei & Xie Xinwen. (2007). Application of Flux Cored Arc Welding to Long Distance Transmission Pipeline. *Pipeline Technique and Equipment*, 3 (5), 23-34.

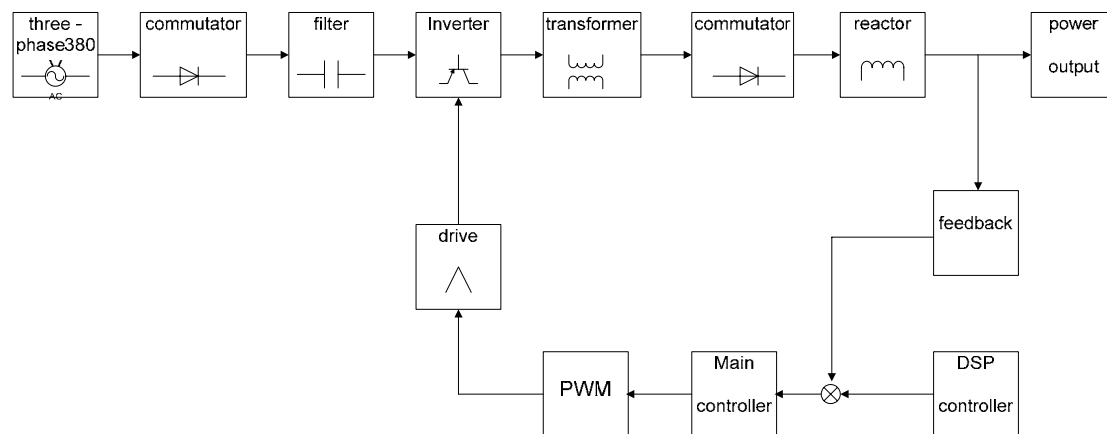


Figure 1. The integrated structural design

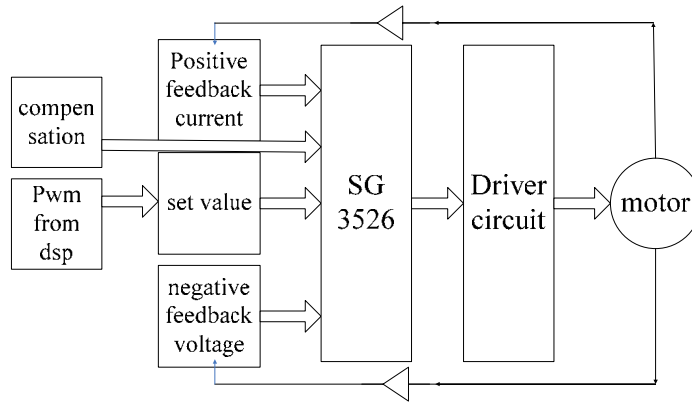


Figure 2. Scheme of feeding system

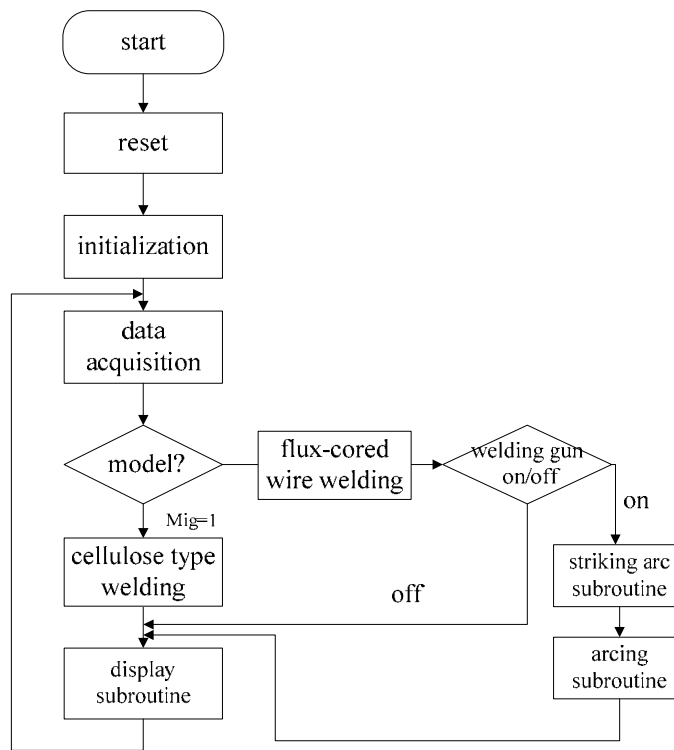


Figure 3. Main program layout

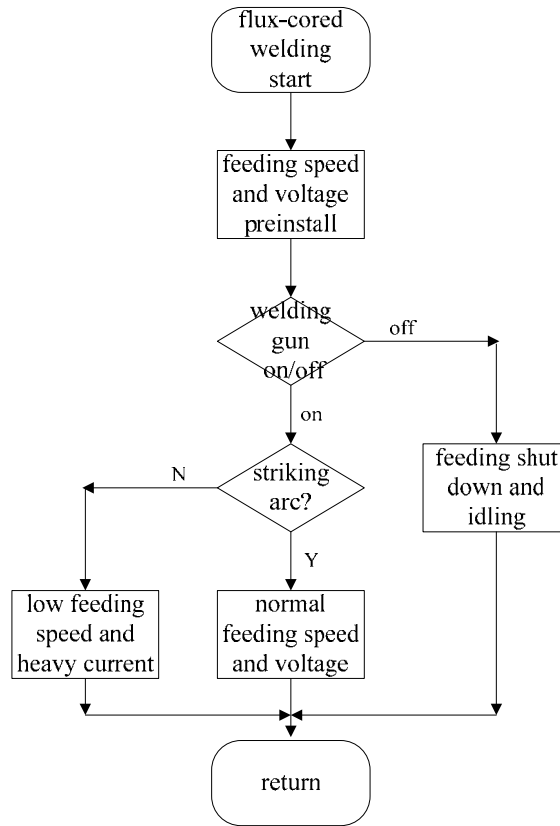


Figure 4. Flux-cored welding subroutine layout

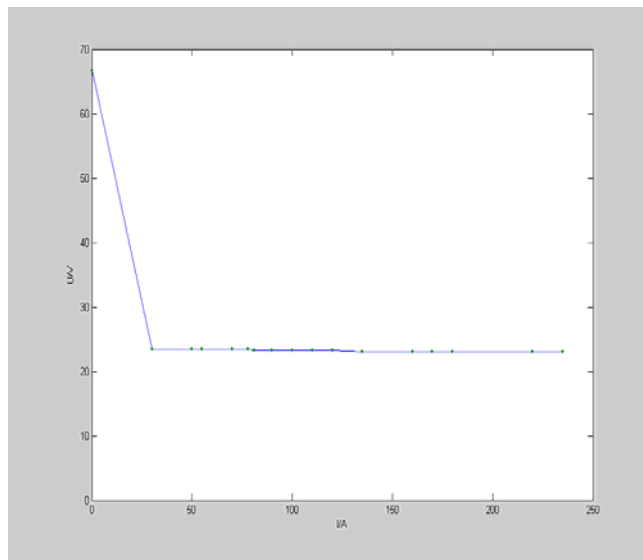


Figure 5. Scheme of constant-voltage external characteristic

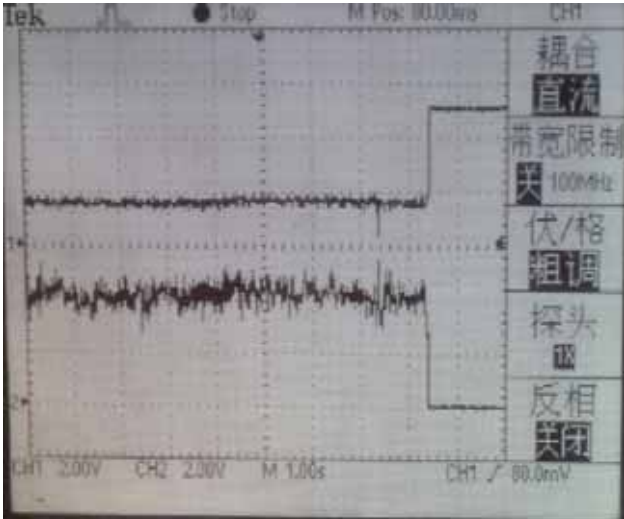


Figure 6. The oscillogram of voltage(23.8V) and current(200A)



Synthesis, Structure and Biological

Activity of Some Diorganotin(IV) with Benzamidomethionine

Yang Farina & Abdualbasit Graisa

School of Chemical Science & Food Technology, Faculty of Science, University Kebangsaan Malaysia 43600 UKM
Bangi, Selangor D.E., Malaysia

Emad Yousif (Corresponding author)

Department of Chemistry, College of Science, Al-Nahrain University, Baghdad, Iraq

E-mail: emad_yousif@hotmail.com

Abstract

New series of diorganotin(IV) complexes of the type Ph_2SnL_2 , Bu_2SnL_2 and Me_2SnL_2 of the ligand benzamidomethionine (L_H). Ligand formed by reaction of benzoyl chloride with methionine in presence of sodium hydroxide. The prepared complexes were characterized by elemental analysis, infrared, conductance measurements and nuclear magnetic resonance (^1H NMR and ^{13}C NMR) spectral data. From the spectral measurements, monomer structures for the complexes were proposed. Bidentate and Octahedral geometry was proposed for the complexes prepared. Preliminary in vitro tests for fungicidal activity show that all prepared compounds display good activity to *Gibberela*, *Cercospora arachidicola*, *Physalospora piricola* and *Fusarium oxysporum*. Moreover, the Ph_2SnL_2 show a higher inhibition percentage than diorganotin carboxylate.

Keywords: Diorganotin(IV), Carboxylate, Spectral studies, Biological activity

1. Introduction

The chemistry of organotin(IV) complexes has developed considerably during the last 30 years, organotin compounds in general and organotin carboxylates in particular continues to grow because of their biological activity and potential antineoplastic and antituberculosis agents (Zhang et al., 2007; Tian et al., 2005; Nathm et al., 2005), PVC stabilizers (Arks et al., 2005; Thoonen et al., 2004; Kuzelova and Vymazal 1999) and anti-tumour drugs (Tabassum and Pettinari 2006) as well as polymer catalysts (Angiolini et al., 2008).

Vast studies have been focused on organotin carboxylates and many of them have been characterized recently either by single crystal structure determination or by spectroscopy (Katsoulakou et al., 2008; Baul et al., 2007). This paper describe the preparation and characterization of benzamidomethionine (L_H) and its complexes, Diphenyltin(IV) bis(benzamidomethionine) (Ph_2SnL_2), Dibutyltin(IV) bis(benzamidomethionine) (Bu_2SnL_2) and Dimethyltin(IV) bis(benzamidomethionine) (Me_2SnL_2).

2. Materials and methods

2.1 Synthesis of benzamidomethionine

A one gram of methionine was dissolved in (25ml) of 5% NaOH solution in a conical flask. To this mixture benzoyl chloride (2.25ml) was added in a five portions and shaken vigorously until all the chloride has reacted. Acidified with diluted hydrochloric acid and the crude product was washed with cold ether. Finally, the desired product was recrystallized from Ethanol.

2.2 Preparation of Complexes

Complexes were synthesized by dissolving the free ligand (2 mmol) in hot toluene and adding the diorganotin salts (1 mmol) to the solution. The solution was refluxed for 6 hours with magnetic stirrer and then cooled and filtered. The filtrate was reduced under vacuum to a small volume and solid was precipitated by the added of petroleum ether, dried at 60 °C and recrystallized from Ethanol.

3. Instrumentation

Elemental C, H and N analysis were carried out on a Fison EA 1108 analyzer, the FTIR spectra in the range (4000-370) cm^{-1} cut were recorded as potassium bromide discs using a Perkin-Elmer spectrophotometer GX, molar conductance measurements were made in anhydrous DMF at 25 °C using Inolop-Cond Level 1 WTW, atomic absorption measurements of the prepared complexes were obtained using Shimadzu 680cc-flame. The ^1H and ^{13}C nuclear magnetic

resonance spectra were recorded on a jeol 400 MHz spectrometer, relative to the internal standard tetramethylsilane (TMS). Melting points were determined in open capillary tubes using an electrothermal 9300 digital melting point apparatus.

4. Results and discussion

The ligand was prepared by the reaction of benzoyl chloride with methionine in presence of sodium hydroxide. Table (1) shows the physical data for the ligand and the prepared complexes. The purity of the ligand and its complexes were checked by TLC using silica gel-G as adsorbent. The conductance of these complexes has been recorded in DMF at room temperature in the range 8-20 $\text{ohm}^{-1} \text{cm}^2 \text{mol}^{-1}$, suggesting their non-electrolytic nature. The data of CHNS and Tin analysis were obtained using flame atomic absorption technique. The calculated values were in a good agreement with the experimental values.

4.1 Infra-Red Spectroscopy

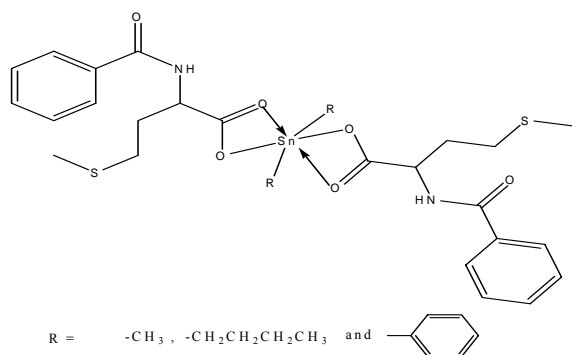
The FTIR spectrum of the ligand, shows a characteristic stretching absorption bands at 3784 cm^{-1} , 3334 cm^{-1} , 1732 cm^{-1} , 1021 cm^{-1} and 800 cm^{-1} assigned to hydroxyl, N-H, carbonyl, C-O and C-S group respectively. The reaction between this ligand with Diorganotin(IV) gave different types of complexes. In the free ligand, the bands at 1732 cm^{-1} and 1021 cm^{-1} were assigned to the stretching of C=O and C-O of the hydroxyl in the carboxylate group. On complexation these bands were shifted to a lower frequency region (Masood et al., 2004). This shift is probably due to the complexation of the metal to the ligand through oxygen of the carbonyl group, the disappearance of the hydrogen from hydroxyl group on complexation indicate the complexation is through the oxygen atom. The bands for $\nu(\text{Sn-C})$ and $\nu(\text{Sn-O})$ are assigned in the range of (551-573) and (445-494) cm^{-1} respectively (Shahid et al., 2002). The IR data of the complexes are shown in Table (2). The Table lists the stretching frequency (ν) for some of the characteristics groups exhibited by the ligand and complexes.

4.2 Nuclear magnetic resonance

The ^1H NMR spectra for all compounds were recorded in $[\text{D}_2\text{H}_6]$ DMSO using tetramethylsilane as the internal standard. The data are compiled in Table 3. The conclusion drawn from ^1H NMR studies of a few compounds lend further support to suggested formation of benzamidomethionine chelate. Ligand (L_H) give a single resonance near δ 8.69 ppm attributable to the N-H proton. The spectra also exhibit a singlet -OH peaks at 9.21 ppm due to hydroxy group. The hydroxy resonances is absent in the spectra of the complexes indicating deprotonation and coordination of Tin to the oxygen. There is a small upfield shift of the aromatic protons resonances of the ligand upon chelation with the diorganotin(IV) moiety (Shahid et al., 2002).

Table 4 shows the most relevant ^{13}C NMR data. Due to scant solubility of the ligand and its complexes, their spectra were recorded in $[\text{D}_2\text{H}_6]$ DMSO. The C=O resonance group of the complexes at (159.64-160.64) ppm where shifted downfield compared with the position in the free ligand which appeared at 169.64 ppm. It is most likely that shift is due to the decrease of electron density at carbon atoms when oxygen is bonded to metal ion (Masood et al., 2004). This observation lends further evidence that the complexation occurred through the oxygen atoms of the carboxylate group.

On the basis of the preceding discussion, the structure of the complexes suggested as follows:



4.3 Biological activity

Preliminary in vitro tests for fungicidal activity of ligand and complexes have been carried out by the fungi growth inhibition method (Junich et al., 1991). These compounds are dissolved in DMF at a concentration of 50 ppm. The data are summarized in Table 5, and show that all compounds display certain activity to *Physalospora piricola* at a low concentration. Moreover, the Ph_2SnL_2 are more active than the other diorganotin derivatives. In addition, Ph_2SnL_2 shows the highest inhibition percentage for *Physalospora piricola* (88.4%) in vitro.

5. Conclusion

The ligand benzamidoacetic acid was successfully synthesized. The ligand was treated to different diorganotin(IV) oxide metal salts to afford the corresponding complexes. It may be concluded that the ligand coordinated through carboxylate to the Tin atom leading to the formation of four membered ring chelate. Octahedral geometry was proposed for the prepared complexes. Biological activity data have shown that the reported complexes have a significant biological activity against *Gibberella*, *Cercospora arachidicola*, *Physalospora piricola* and *Fusarium oxysporum*.

Acknowledgments

Authors acknowledge the financial support provided by the University Kebangsaan Malaysia for carrying out this work.

References

- Angiolini, L., D. Caretti, L. Mazzocchetti, E. Salatelli, R. Willem and M. Biesemans. (2006). "Triorganotin-4-vinylbenzoates: Assessment of their catalytic activity in transesterification reactions". *Journal of Organometallic Chemistry*, 691: 3043–3052.
- Arks, E. and D. Balko. (2005). "Thermal stabilisation of poly(vinyl chloride) by organotin compounds". *Polymer Degradation and Stability*, 88: 46-51.
- Baul, T., C. Masharing, G. Ruisi, R. Jira'sko, M. Holcapek, D. de Vos, D. Wolstenholme and A. Linden. (2007). "Self-assembly of extended Schiff base amino acetate skeletons, 2-[[[(2Z)-(3-hydroxy-1-methyl-2-butenylidene)]amino]phenylpropionate and 2-[[[(E)-1-(2-hydroxyaryl)alkylidene]amino]phenylpropionate skeletons incorporating organotin(IV) moieties: Synthesis, spectroscopic characterization, crystal structures, and in vitro cytotoxic activity". *Journal of Organometallic Chemistry*, 692: 4849–4862.
- Junich, F., U. Yasuhiko, I. Kouzou. (1991). "Method of Pesticide Experiment-Fungicide, Agricultural", Press of China, Beijing.
- Katsoulakou, E., M. Tiliakos, G. Papaefstathiou, A. Terzis, C. Raptopoulou, G. Geromichalos, K. Papazisis, R. Papi, A. Pantazaki, D. Kyriakidis, P. Cordopatis and E. Zoupa. (2008). "Diorganotin(IV) complexes of dipeptides containing the α -aminoisobutyryl residue (Aib): Preparation, structural characterization, antibacterial and antiproliferative activities of $n\text{-Bu}_2\text{Sn}(\text{H}_2\text{L})$ (LH = H-Aib-L-Leu-OH, H-Aib-L-Ala-OH)". *Journal of Inorganic Biochemistry*, 102: 1397–1405.
- Kuzelova, K. and Z. Vymazal. (1999). "Contribution to the study of the thermal stabilization of PVC/SAN blends". *European Polymer Journal*, 35: 361-364.
- Masood, H., S. Ali, M. Mazhari, S. Shahzad and K. Shahidi. (2004). " ^1H , ^{13}C , ^{119}Sn NMR, Mass, Mossbauer and Biological Studies of Tri-, Di- and Chlorodiorganotin(IV) Carboxylates". *Turk. J. Chem.*, 28: 75 – 85.
- Nathm M., R. Jairath, G. Engb, X. Songb and A. Kumarc. (2005). "Synthesis, spectral characterization and biological studies of some organotin(IV) complexes of l-proline, trans-hydroxy-l-proline and l-glutamine". *Spectrochimica Acta Part A*, 62: 1179–1187.
- Shahid, S., S. Ali, M. Hussain, M. Mazhar, S. Mahmood and S. Rehman. (2002). "Synthesis, Characterization and Thermal Analysis of Organotin(IV) Derivatives of 4-(N-Maleoyl)Butanoate". *Turk. J. Chem.*, 26: 589 – 597.
- Tabassum, S., and C. Pettinari. (2006). "Chemical and biotechnological developments in organotin chemotherapy". *Journal of Organometallic Chemistry*, 691: 1761–1766.
- Tian, L., Y. Sun, H. Li, X. Zheng, Y. Cheng, X. Liu and B. Qian. (2005). "Synthesis, characterization and biological activity of triorganotin 2-phenyl-1,2,3-triazole-4-carboxylates". *Journal of Inorganic Biochemistry*, 99: 1646–1652.
- Thoonen, S., B. Deelman and G. Koten. (2004). "Synthetic aspects of tetraorganotins and organotin(IV) halides". *Journal of Organometallic Chemistry*: 689:2145–2157.
- Zhang, X. Yan, H. Song, Q. Li, X. Liu and L. Tang. (2007). "Synthesis, structure and biological activity of organotin derivatives with pyridylmethylthiobenzoic acid". *Polyhedron*, 26: 3743–3749.

Table 1. Physical data for preparation ligand and the complexes prepared.

compound	Color	%Yield	M.P, °C	Found(Calcd.)%				
				C	H	N	S	Sn
L _H	White	77	178-179	59.56 (56.90)	5.87 (5.97)	5.76 (5.53)	12.54 (12.66)	-
Ph ₂ SnL ₂	White	87	130-132	56.12 (55.61)	4.93 (4.93)	4.54 (4.20)	8.43 (8.25)	15.75 (15.17)
Bu ₂ SnL ₂	White	86	114-116	51.32 (52.11)	6.25 (6.29)	3.865 (3.80)	9.21 (8.96)	15.96 (16.10)
Me ₂ SnL ₂	White	83	121-123	47.55 (47.79)	4.89 (5.24)	4.33 (4.29)	9.74 (9.81)	18.21 (18.17)

Table 2. Characteristic absorption bands of benzamidomethionine and its complexes

compound	O-H	N-H	C=O	C-O	C-S	C-H aromatic	Sn-C	Sn-O
L _H	3784	3334	1732	1021	800	3071	-	-
Ph ₂ SnL ₂	-	3330	1719	1018	800	3074	573	491
Bu ₂ SnL ₂	-	3301	1720	1017	801	3069	551	445
Me ₂ SnL ₂	-	3325	1721	1016	802	3073	570	494

Table 3. ¹H NMR spectral data (δ,ppm) of the ligand and complexes

compound	O-H	N-H	C-H aromatic	C-(2)H aliphatic
L _H	9.11	8.69	7.46-7.85	3.92
Ph ₂ SnL ₂	-	8.68	7.41-7.78	3.81
Bu ₂ SnL ₂	-	8.68	7.39-7.79	3.87
Me ₂ SnL ₂	-	8.65	7.36-7.81	8.88

Table 4. ¹³C NMR spectral data (δ,ppm) of the ligand and complexes

compound	C=O amide	C=O acid	C-H aromatic	C-H ₂ aliphatic
L _H	163.49	169.64	124.77-130.43	43.44
Ph ₂ SnL ₂	163.24	161.75	126.70-133.56	41.07
Bu ₂ SnL ₂	164.29	158.75	124.34-131.75	42.31
Me ₂ SnL ₂	161.30	162.24	127.35-132.54	41.54

Table 5. Fungicidal activities of prepared compounds

Compound	Inhibition Ratio (%) (50ppm)			
	L _H	Me ₂ SnL ₂	Bu ₂ SnL ₂	Ph ₂ SnL ₂
<i>Gibberela</i>	14.3	24.4	30.2	33.4
<i>Cercospora arachidicola</i>	12.4	54.2	67.5	41.3
<i>Physalospora piricola</i>	31.5	66.4	76.5	88.4
<i>Fusarium oxysporum</i>	10.5	33.6	40.3	65.3

A journal archived in Library and Archives Canada
A journal indexed in CANADIANA (The National Bibliography)
A journal indexed in AMICUS
A journal indexed in Zentralblatt MATH
A journal included in DOAJ (Directory of Open-Access Journal)
A journal included in Google Scholar
A journal included in LOCKSS
A journal included in PKP Open Archives Harvester
A journal listed in Journalseek
A journal listed in Ulrich's
A peer-reviewed journal in applied science research

Modern Applied Science

Monthly

Publisher Canadian Center of Science and Education

Address 4915 Bathurst St. Unit # 209-309, Toronto, ON. M2R 1X9

Telephone 1-416-208-4027

Fax 1-416-208-4028

E-mail mas@ccsenet.org

Website www.ccsenet.org

Printer William Printing Inc.

Price CAD.\$ 20.00

